Atmospheric Mercury: Recent advances in theoretical, computational, experimental, observational and isotopic understanding to decipher its complex redox transformations in the upper and lower atmosphere and interaction with Earth surface reservoirs

5 Jonas O. Sommar[1], Xueling Tang[1,2], Xinyu Shi[1,2], Guangyi Sun[1], Che-Jen Lin[1,3] and Xinbin Feng[1,4].

[1]State Key Laboratory of Environmental Geochemistry, Institute of Geochemistry, Chinese Academy of Sciences, Guiyang 550081, China.
[2]University of Chinese Academy of Sciences, Beijing 100045, China.
[3]Center for Advances in Water and Air Quality, Lamar University, Beaumont, Texas 777100, United States.
[4] Center for Excellence in Quaternary Science and Global Change, Chinese Academy of Sciences, Xian 710061, China.

10 *Correspondence to*: Jonas O. Sommar (jonassommar@icloud.com)

Abstract

Mercury is a volatile heavy element with no known biological function. It is present in trace amounts (on average, ~80 ppb) but is not geochemically well-blended in the Earth's crust. As a result, it sometimes occurs in extremely high concentrations (up to a few %) in certain locations. It is found along tectonic plate faults in deposits of sulfide ores (cinnabar), and it has been extensively

15 mobilized during the Anthropocene. Mercury is currently one of the most targeted global pollutants internationally, with methylmercury compounds being particularly neurotoxic. Over 5,000 tons of mercury are released into the atmosphere annually through primary emissions and secondary re-emissions. Much of the re-emitted mercury, resulting from exchanges with surface reservoirs, is considered to be related to (legacy) human activities, as are the direct releases. Understanding the dynamics of the global Hg cycle is critical to assessing the impact of emission reductions under the UN Minamata Convention, which became legally binding

20 in 2017. This review of atmospheric mercury focuses on the fundamental advances in field, laboratory, and theoretical studies, including six stable Hg isotope analytical methods, that have contributed fairly recently to a more mature understanding of the complexity of the atmospheric Hg cycle and its interactions with the Earth's surface ecosystem.

1 Introduction

Mercury (Hg) is a potent neurotoxin that via methylmercury ($MMHg^+$) food exposure poses global health impact (e.g. IQ decrement

25 and heart attack) (Zhang et al., 2021b). The atmosphere plays a pivotal role in the Hg biogeochemical cycle, functioning as the most important transient reservoir, a conduit for transport and transformation, and a site of rich redox chemistry. In part due to concerns about global Hg transport, the multilateral UN-Environment Convention on Hg was negotiated and entered into force in 2017 with a mandate to reduce intentional use and emissions of Hg (UNEP, 2018). Research on the Hg biogeochemical cycling gained momentum after an outbreak of mass $MMHg^+$ poisoning severely affected the population of Minamata Bay, Japan, in the 1950s and 1960s through the

30 consumption of contaminated seafood, and it became clear that $MMHg^+$ was present at chronically high levels in predatory fish in many lakes, particularly those in the boreal forest belt, through long-range transport and biomagnification (Lindqvist et al., 1991). The earliest known series of measurements on airborne elemental Hg, possibly the first systematic study of its kind, was conducted in Pacific North America during the second half of the 1960s (Williston, 1968). It was recognized as early as the 1970s that Hg circulates globally through the atmosphere (Nriagu, 1979). Somewhat later, Slemr et al. (1985) published an influential paper whose results on the distribution, speciation and budget

35 of atmospheric Hg reproduce fairly well the qualitative features of the atmospheric Hg cycle, such as atomic vapor (Hg^0) dominating the atmospheric pool and showing an interhemispheric difference with higher concentrations in the northern hemisphere, and being relatively well mixed vertically through the troposphere with an extensive residence time (concept as "global pollutant").

The knowledge of the physical and chemical processes that govern the dynamics of Hg in the atmosphere has developed gradually. Over time, through technological leaps (stable isotope sampling in natural probes, refined methods in the theoretical and experimental field,

40 etc.), its full complexity began to be appreciated. In earlier research, there was a prevailing view that water phase oxidation by ozone could be the primary mechanism initiating the removal of tropospheric Hg^0 (Pleijel and Munthe, 1995; Seigneur et al., 1994). However,

newer data indicated that gaseous oxidized mercury (GOM) could also be present in the atmosphere (Xiao et al., 1997; Lindberg and Stratton, 1998), in addition to the particulate form (PBM). Specifically, the observation that Hg^0 was periodically depleted in the planetary mixing layer during the polar spring (Schroeder et al., 1998) prompted a reassessment of Hg chemistry in favor of homogeneous gas-

45 phase chemistry (Hynes et al., 2009). The two-step gas-phase oxidation of Hg^0 initiated by Br atoms has emerged as the most important global channel for tropospheric conversion to Hg^{II} (Donohoue et al., 2006; Holmes et al., 2010). It used to be thought that gas-phase O_3 was an oxidizing agent for Hg^0 to Hg^{II}. However, it has now been found to effectively oxidize intermediate Hg^I species (Gómez Martín et al., 2022). This suggests that OH- and less certain I-initiated oxidation of Hg^0, which produces more unstable intermediates than Br and Cl, may also be important for Hg turnover in parts of the troposphere and beyond (Dibble et al., 2020; Lee et al., 2024). A novel

50 finding is that major $Hg^{I,II}$ species, which are expected to be formed in the atmosphere upon oxidation of Hg^0, are themselves photolabile and undergo gas-phase reduction (Francés-Monerris et al., 2020; Saiz-Lopez et al., 2019). The complexity of rapid redox Hg chemistry involving multiple gas phase oxidation states (0, +1 and +2) is further compounded by the impact of multi-phase interactions, including reactive uptake and homogeneous and heterogeneous processes in condensed phase media, on the dynamics of atmospheric Hg. An indicator of the maturation of our understanding of atmospheric Hg chemistry is the inclusion of its bromine chemistry in critically

55 evaluated data sets for use in atmospheric studies (Burkholder et al., 2019). Over the past two decades, measurements of Hg stable isotope ratios in natural samples have emerged as a valuable tool for gaining insights into the atmospheric Hg cycle. One notable outcome of isotope analysis is the recognition that Hg^0 dry deposition exerts a more pronounced influence on a global scale than was previously understood, with wet and dry deposition of the atmospheric Hg^{II} fraction being of lesser importance.

Hg in the atmosphere has been the subject of reviews over the past 45 years (Hynes et al., 2009; Lindqvist and Rodhe, 1985;

60 Schroeder and Munthe, 1998; Jackson, 1997; Lin et al., 2011; Lin and Pehkonen, 1999; Bash et al., 2007; Ariya et al., 2015; Ariya et al., 2009; Ariya et al., 2008; Si and Ariya, 2018; Subir et al., 2011, 2012; Lin et al., 2006; Lin et al., 2007; Zhang et al., 2009; Gaffney and Marley, 2014; Gustin et al., 2015; Mao et al., 2016; Lyman et al., 2020a; Ariya and Peterson, 2005; Sprovieri et al., 2010; Schroeder et al., 1991). This review is based on the perspective of atmospheric scientists, with synthesis and a fairly comprehensive account of the results of fundamental research, including field, laboratory, and theoretical studies, that have

65 contributed to a reductionist understanding down to a molecular level of the complexity of the atmospheric Hg cycle and its interactions with the Earth's surface ecosystem. This work does not address several topics related to Hg in the atmosphere. These include anthropogenic and natural emission inventories, corresponding top-down constraints and inverse modeling from atmospheric observations, account of long-term air data series and their temporal and spatial trends, observations of PBM and its particle size distributions, wet deposition, future scenarios for the effects of regulatory measures (Minamata Convention) and the

70 ongoing climate change and many more topics. Our goal is to provide a comprehensive review of the atmospheric chemistry of both inorganic and organic Hg in the lower and upper atmosphere, coupled with tabulations of updated, critically evaluated kinetic, thermochemical, photochemical, and isotopic fractionation data. Where appropriate, we introduce the topic with basic concepts and fundamental aspects of Hg chemistry, including that of condensed phases. In atmospheric Hg isotope chemistry, our approach is comprehensive, encompassing a range of activities from field observations of air and of Hg^0 gas exchange with natural surfaces

75 to laboratory studies of processes that may be of value to the atmosphere. We also highlight areas of persistent uncertainty or lack of consensus, such as measurement methods for atmospheric Hg speciation, partitioning of Hg^{II} in atmospheric water between inorganic and organic ligands, and several other areas.

2 Physical chemistry of elemental mercury

Hg is the only metal that is a liquid at standard temperature and pressure (freezing point of -38.8°C and boiling point of 356.7°C),

80 and its vapor is monatomic. Under these conditions, the mixing ratio of neurotoxic Hg vapor in equilibrium with metallic liquid is already at the hazardous level of about 1.7 ppm (Huber et al., 2006). Liquid Hg possesses properties which have given it a wide range of applications in the past despite its known toxicity, including exceptional surface tension (nearly seven times of water at 25ºC), high specific gravity, high electrical conductivity (reference substance for the measure of the SI-unit Ω), low compressibility, and a constant volume of expansion in the liquid state. Hg forms solid alloys (amalgams) with most metals except iron. This property

85 enables its applications in gold panning (HgAu), dental fillings (HgAg), or as an electrode material in the chlor-alkali industry (NaHg). Its electronic configuration with filled f and d orbitals and a high density of 6s electrons near the nucleus ($[Xe]4f^{14}5d^{10}6s^2$),

contracts the orbital as the electron approaches a significant fraction of the speed of light. This shrinking cascade effect makes Hg less reactive than Zn and Cd in the same group (Pyykkö, 1988). It also follows that oxidation states 0 and +2 (mercuric ion, d^{10} metal ion) are the most stable for Hg. Nevertheless, Hg differs from other metals in its propensity to readily form a polycation in the aqueous

90 phase, the mercurous ion, Hg_2^{2+}, which is, however, only meta-stable in the gaseous phase (Strömberg and Wahlgren, 1990). The solubility of Hg^0 in water is limited to 0.3 μM (Sanemasa, 1975) and the gas-water equilibrium is governed by Henry's law. The Henry's law constant for Hg^0 is 0.11 M atm^{-1} at 25 °C (Andersson et al., 2008) while the parameter is more than seven orders of magnitude higher for the $HgCl_2$ molecule at the same temperature (Sommar et al., 2000).

3 The atmospheric environment

95 **3.1 Atmospheric measurements of mercury species**

Hg is the only trace gas with the exception of the noble gases (Burnard, 2013) that is widely present as a free atom (Hg^0) in the atmosphere, making this pollutant exceptional in terms of low detection limits by optical measurement techniques. This makes it possible to measure Hg vapor emissions in real time, for example from mining, chlor-alkali production and geothermal activities, as has been done in Europe for decades using Light Detection and Ranging (LIDAR) in the differential absorption mode by mobile laser systems

100 (Svanberg, 2002). If the optical path length in the measuring cell of an instrument is sufficiently long (i.e. using multi-path techniques such as cavity ring-down), then the conditions exist for continuous measurement of Hg^0 in ambient filtered air (at sub-ppt level, ~5×10^6 atoms cm^{-3} in the northern hemisphere) using atomic absorption spectroscopy (AAS) with Zeeman background correction (Osterwalder et al., 2020). The application of Zeeman AAS in Hg stable isotope analysis has also been described (Lu et al., 2019). As an alternative to Zeeman splitting of the Hg(6^3P) level for sensitive selective detection of Hg^0 (Sholupov et al., 2004), sequential two photon laser-

105 induced fluorescence schemes have been used (Bauer et al., 2002; Bauer et al., 2014; Hynes et al., 2017). For initial excitation of the Hg(6^1S_0) → Hg(6^3P_1) transition at 253.7 nm, a light beam from a Hg discharge lamp or the frequency-doubled output of a dye laser pumped by the third harmonic of an Nd:YAG laser is used. As shown in **Fig 1a**, further excitation involves the sequential excitation of different atomic transitions by two laser systems, both starting from the Hg(6^3P_1) state, followed by the detection of the emission of blue-(Hg(6^1P_1) → Hg(6^1S_0) at 184.9 nm) or redshifted (e.g. at 578.9 nm) fluorescence. Detection of Hg^0 with such a sophisticated apparatus

110 is an exception to the usual measurements, which are typically made by cold vapor atomic fluorescence spectroscopy (CV-AFS) after preconcentration sampling on gold (Ambrose, 2017). The smaller non-Hg^0 portions of atmospheric Hg are challenging to speciate due to their low concentrations. Instead, they are fractionated operationally based on their oxidation state (Hg^0 versus GOM) or phase state (GOM versus PBM). Since gold does not selectively trap Hg^0 but also captures other Hg species (Dumarey et al., 1985; Gačnik et al., 2024), GOM and PBM must be individually collected upstream of the sample air to accurately measure the triad Hg^0 – GOM – PBM.

115 The KCl-coated annular denuder has been utilized for fractionating ambient GOM by gas-phase diffusion for over two decades. Nonetheless, upon the development of techniques to regularly assess its accuracy in measuring ambient air, the method was found to be biased in a non-systematic manner towards lower values (Jaffe et al., 2014; Lyman et al., 2010; McClure et al., 2014). The automated
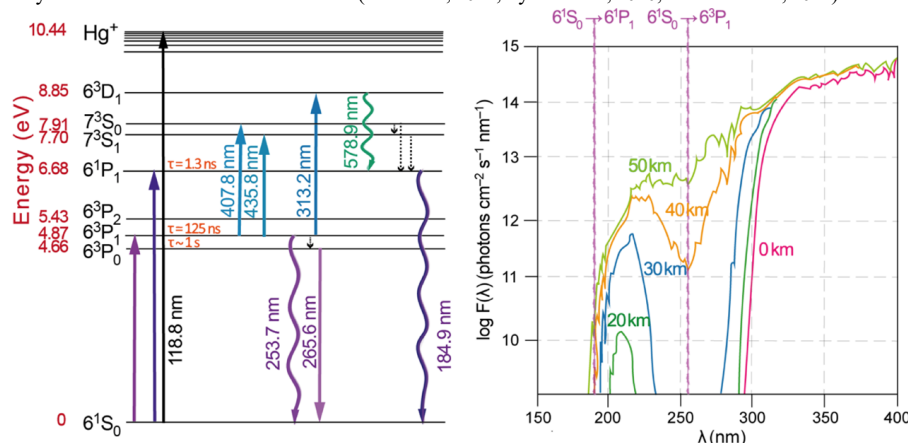
Figure 1: Left (a). Energy level diagram of Hg atom. The wave-shaped arrows represent resonant radiation. Right (b): Actinic fluxes as a function of altitude. The wavelengths of the Hg($^1S_0$) → Hg($^3P_1$) and → Hg($^1P_1$) transitions at 253.7 and 184.9 nm, respectively, are given.

120 KCl denuder method, with its variable efficiency, can thus lead to serious underestimation of GOM, while the refluxing mist chamber method, which is an alternative, carries the risk of artifact formation of Hg^{II} by co-sampling GOM with PBM (Gustin et al., 2021). However, the KCl-covered denuder does not have full penetration of PBMs < 2.5 µm, but aerosols of a hundred nm or less are increasingly trapped by the salt surface (Ghoshdastidar et al., 2019). When compared, refluxing mist chambers yielded ambient GOM concentrations that were 3 to 4 times higher on average than those obtained with KCl-coated annular denuders (Landis et al., 2002).

125 A decade later, the capture and retention efficiency of the KCl denuder method for GOM was evaluated, which was close to 95% in synthetic Hg^0-free air, but dropped drastically to between 20 and 54% when exposed to ambient air, where ozone and humidity in particular were found to cause severe reductive losses as Hg^0 (McClure et al., 2014). In fact, ozone gas can heterogeneously reduce particle-bound Hg^{II} halides, as recent experiments have shown (Ai et al., 2023). In high-humidity marine applications, KCl denuder technology operates at very low efficiency; for example, He and Mason (2021) reported average losses of 80% during oceanographic

130 expeditions in the Pacific. By determining total airborne mercury (TAM) (Steffen et al., 2002; Slemr et al., 2018) and Hg^0 in air, a measure of reactive mercury (RM) is obtained as the sum of GOM + PBM by subtracting Hg^0 from TAM. In turn, Hg^0 is obtained by passing an air stream through a filter and a cation exchange membrane (CEM) in series, while TAM is measured as Hg^0 after a pyrolysis unit held at 800 ºC converts all Hg in the sample air to elemental vapor (Lyman et al., 2020b). CEM has the ability to quantitatively capture and retain Hg^{II} over long storage periods, but has no affinity for Hg^0 (Miller et al., 2019). However, by

135 subtracting two quantities that are usually close to each other, the precision of the RM determination is low. Hynes et al. (2017) used two-photon laser-induced fluorescence as an online detection method for RM (by switching between ambient and pyrolyzed air as the source for the Hg^0 analyte) and concluded that the variability in ambient Hg^0 severely limits the sensitivity of dual-channel difference RM measurement. For the separation of the semi-volatile GOM fraction from PBM in ambient air, the use of various membranes has been implemented, but has recognized limitations (Dunham-Cheatham et al., 2023; Gustin et al., 2023). The

140 realization of NIST-traceable GOM calibration systems has recently progressed (Gacnik et al., 2022). Several studies have been carried out with the aim of experimentally deciphering the molecular identities (speciation) of the GOM pool in ambient air. Most are based on a pre-concentration process of GOM on a substrate, which is then thermo-desorbed in a gas stream following a programmed temperature ramp and detected as Hg^0 after pyrolysis (Gustin et al., 2015), alternatively focused on a capillary column and analyzed by different types (chemical ionization CI; electron impact ionization) of mass spectrometry (MS) (Deeds et al., 2015;

145 Jones et al., 2016). In the former case, standards are used in the form of a number of commercially available Hg chemicals (such as $HgBr_2$, $HgCl_2$, HgO, $Hg(NO_3)_2$, and $HgSO_4$) that are assumed to be a representative surrogate for GOM (Huang et al., 2017; Sexauer Gustin et al., 2016). As inferred by Khalizov et al. (2020), this speciation is indirect, as it has not been confirmed that the GOM molecule adsorbed on the substrate can be desorbed in the same chemical form as it was in air.

On the contrary, studies show that aerosol reactions lead to the re-speciation of mercuric halides on surfaces (Mao et al., 2021; Mao

150 and Khalizov, 2021). These authors also report that their ion-drift (ID) CI-MS system, which is sensitive enough for detection in laboratory studies, can achieve an LOD at 1 amu resolution of $(0.8 – 2.0) \times 10^5$ molecules cm^{-3} towards ambient GOM by switching to multi-stage atmospheric pressure ID-CI-MS. The feasibility of using proton transfer reaction mass spectroscopy (PTR-MS) to study the reaction products (GOM) of Br-initiated Hg^0 oxidation has been evaluated by Dibble et al. (2014), but is not recommended with respect to its inapplicability to multi-stage atmospheric pressure systems (Khalizov et al., 2020). In summary, direct

155 measurements of ambient GOM have not yet been achieved. No straight-forward method exists for chemically characterizing the GOM fraction, which is semi-volatile and may contain species that are photolytically unstable. Since an almost exclusive part of the previous GOM measurements are considered unreliable (Lyman et al., 2020a; Slemr et al., 2016) and the emerging RM data (Lyman et al., 2020b; Slemr et al., 2018; Swartzendruber et al., 2009; Gratz et al., 2015; Lyman and Jaffe, 2012) are still too sparse and spatially limited, it is not possible to draw far-reaching conclusions on atmospheric Hg^{II}. Sampling methods for organic Hg

160 (dimethylmercury (He et al., 2022) and monomethylated Hg^{II} species (Lee et al., 2003)) in ambient air, as opposed to inorganic Hg species, are more unambiguous. The speciation of Hg in atmospheric waters are discussed in **Section 4.6**. Hg measurement data in air and precipitation, ground-based or aircraft (Slemr et al., 2018; Slemr et al., 2016) observations that fall outside the scope of this

review, including those reported from continental- (Cole et al., 2014; Cole et al., 2013; Schmolke et al., 1999; Wängberg et al., 2001; Gay et al., 2013; Fu et al., 2015) to hemispherical-scale (Bencardino et al., 2024; Szponar et al., 2020; Slemr et al., 2020; Sprovieri
165   et al., 2017; Sprovieri et al., 2016) monitoring networks, some of which have been in operation since before the turn of 2000 (Custódio et al., 2020), have been reviewed elsewhere (Mao et al., 2016; Lyman et al., 2020a; Howard et al., 2017; Angot et al., 2016; Kim et al., 2012; Zhang et al., 2017). In the case of the isotopic characterization of atmospheric Hg, however, we feel justified in compiling, analyzing, and discussing the considerable body of recent observations (**Section 8.2**).

3.2 Stability of atmospheric Hg[0]

170   Atomic vapor (Hg[0]) dominates the atmospheric Hg pool, shows an interhemispheric difference with higher concentrations in the northern hemisphere (Bencardino et al., 2024), and is relatively well mixed vertically through the troposphere (Weigelt et al., 2016). When crossing the intertropical convergence zone, Hg[0] is subject to convective uplift that allows entry to the stratosphere. In the upper troposphere of the Pacific Ocean, there is evidence of augmented interhemispheric Hg exchange (Koenig et al., 2022). It is well accepted that the tropospheric Hg pool is close to 4000 Mg (Saiz-Lopez et al., 2025) and that direct anthropogenic emissions to
175   the troposphere, excluding biomass burning, are around 2200 Mg yr^{-1} worldwide (Sonke et al., 2023; Horowitz et al., 2017), while estimates of e.g. oceanic re-emissions (Zhang et al., 2023b; Zhang et al., 2019b; Soerensen et al., 2010) and vegetation uptake (Zhou and Obrist, 2021; Obrist et al., 2021; Jiskra et al., 2018; Yuan et al., 2023a) of Hg[0] vary widely. Based on a synthesis of RM measurements at various heights in the atmosphere, it has been estimated that the atmospheric burden of Hg[II] up to 20 km is approximately 360 Mg (Saiz-Lopez et al., 2020). This value significantly deviates from the values predicted by global models (~100
180   Mg, Shah et al., 2021; Zhang and Zhang, 2022; ~500 Mg, Saiz-Lopez et al. 2025) for the troposphere proper, values that are associated with significant uncertainties. Hg[I] species are intermediates in the Hg[0]/Hg[II] redox cycle, but their tropospheric mass is negligible (Shah et al., 2021). With scientific progress and new data, it has become clear that the magnitude of bidirectional mass fluxes through gas exchange (emission-deposition) and chemical transformation (reduction-oxidation) is much larger than previously thought. For transferring Hg[0] from the oceans into the atmosphere, the mass transfer rate is usually parameterized using wind speed dependencies
185   that have been tested for CO_2 emissions. However, recent evidence (Osterwalder et al., 2021) suggests that Hg[0], which is less soluble than CO_2, behaves rather similarly to O_2 and N_2, where the impact of bubble-mediated transfer is greater. As a result, ocean emissions have an increased role in the global Hg budget, accounting for approximately 60% of total Hg emissions to the atmosphere due to a wind speed dependence with a cubic power exponent instead of quadratic in model simulations (Zhang et al., 2023b). The greater gross emissions from seawater are balanced by the deposition of Hg[0], which is of comparable magnitude to that of Hg[II] deposition
190   (Jiskra et al., 2021) - and much higher than previously assumed (Soerensen et al., 2010). This also applies to the magnitude of Hg[0] dry and wet deposition (throughfall; Wang et al., 2020b) to vegetation (forests). A comprehensive overview of the understanding of the gas exchange of Hg[0] between the atmosphere and the Earth's surface has been presented elsewhere (Sommar et al., 2020).

Hg[0] is estimated to have a global tropospheric lifetime of 3.8 - 7 mo. and a chemical lifetime against oxidation (to Hg[I,II]) of 2.7 - 4.5 mo. (Shah et al., 2021; Horowitz et al., 2017; Zhang et al., 2023b; Shah et al., 2016; Saiz-Lopez et al., 2025), the differences between
195   the two values being largely due to significant redox cycling in the gas phase and aerosols before deposition. Atmospheric Hg deposition persists for terrestrial ecosystems overall with a predominance of Hg[0] compared to Hg[II] (Zhou and Obrist, 2021; Wang et al., 2020b; Feinberg et al., 2022), while the situation appears opposite for cryospheric and marine systems. The total atmospheric Hg deposition is estimated to be 4800 - 6700 Mg yr^{-1} Hg[II] (Sonke et al., 2023; Zhang et al., 2019b; Feinberg et al., 2022) and 3600 - 6750 Mg yr^{-1} Hg[0] (Shah et al., 2021; Sonke et al., 2023; Zhang et al., 2023b). Hg in the stratosphere is estimated to account for about 20%
200   of the total atmospheric Hg mass, with an exchange with the troposphere in the range of 176-300 Mg yr^{-1} (Shah et al., 2021; Lyman and Jaffe, 2012), where Hg is mainly removed from the stratosphere as Hg[II] on aerosols (Murphy et al., 2006) or, to a lesser extent, as the most photostable gas-phase mercurial species (Saiz-Lopez et al., 2022 & 2025). Based on correlations between Hg[0] and N_2O in the stratosphere within 4 km above the thermal tropopause, Slemr et al. (2018) provided a lifetime estimate of 74 ± 27 yr., while Lyman and Jaffe (2012) inferred a relatively short lifetime for Hg[0] in intercepted descending air with stratospheric origin. Saiz-Lopez

205 et al. (2022) estimate the lifetime of Hg^0 in the lower stratosphere against surface deposition of 3 – 9 years and Saiz-Lopez et al. (2025) a mean atmospheric (troposphere + stratosphere) lifetime of 8.2 mo. Hg^0 in the planetary boundary layer can be consumed at a surprisingly high rate, leading to low concentration levels bordering on complete depletion. Thus, chemical oxidation by reactive bromine species in a catalytic cycle ("bromine explosion", Toyota et al., 2014; Gao et al., 2022) can explain atomic Hg depletion events (AMDEs) during the polar spring after sunrise (Schroeder et al., 1998; Sommar et al., 2007; Nerentorp Mastromonaco et al.,

210 2016) and those observed over the Dead Sea (Obrist et al., 2011) (**Fig. 2**). Br-controlled oxidation via the intermediate $^\bullet Hg^I Br$ is also
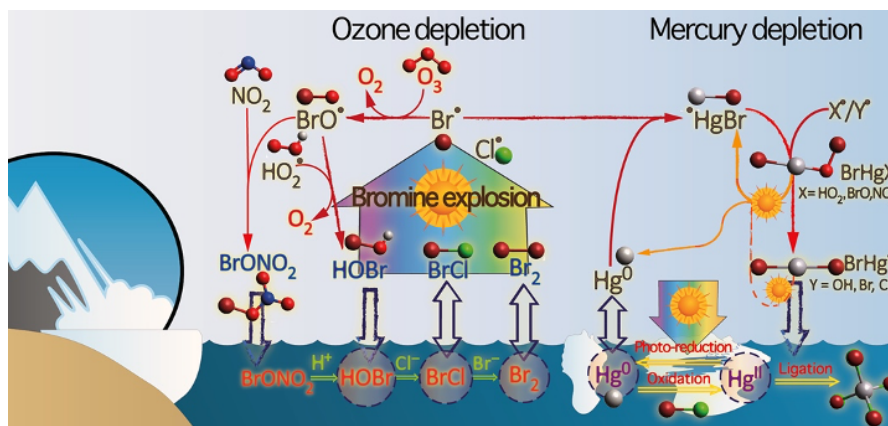
Figure 2. The chemistry behind bromine explosion events and related surface layer ozone and mercury depletion events.

critical for tropospheric oxidation of Hg^0, as described later in the section on gas-phase oxidation. Upon entry into the stratosphere, thermal oxidation with $Br^\bullet$ remains important for conversion to Hg^{II}, but with increasing altitude in the lower stratosphere, Cl

215 chemistry becomes the most important role, with OH-directed chemistry in second place at a slow net oxidation rate.

With the maximum concentration of the O_3 layer (~25 km) as the dividing line, there is a strong dichotomy between the Hg chemistry in the upper and lower stratosphere. The former is UVC driven (Sun et al., 2022) (The UV-window > 30 km provides a substantial photon flux at $\lambda = 253.7$ nm, **Fig. 1b**), involving optically excited Hg^0 states with a strong electrophilic character. The electronic excitation of Hg^0 from the ground state (singlet, $^1S_0$) at 253.7 nm is spin-forbidden (leading to a triplet state, $^3P_1$ with a radiative

220 lifetime of ~125 ns, **Fig. 1a**). The metastable dark $Hg(^3P_0)$ state cannot be produced directly from $Hg(^1S_0)$ by light absorption, but by spin-orbit relaxation of $Hg(^3P_1)$ atoms involving energy transfer to surrounding (air) molecules. In N_2, the equilibrium constant between the $^3P_0$ and $^3P_1$ states at room temperature (297 K) is 1.87×10^3 (Callear and Shiundu, 1987), but in the presence of O_2 their distribution changes profoundly. Although O_2 is a slightly less effective quencher for $Hg(^3P_0)$ than for $Hg(^3P_1)$ (Callear, 1987), their effective lifetimes in air at atmospheric pressure differ by only one order of magnitude (~1.1 ns and ~0.2 ns, respectively, Saiz-Lopez

225 et al., 2022). In addition to physical quenching to the ground state, both $Hg(^3P_0)$ and $Hg(^3P_1)$ may undergo chemical oxidation to mercury oxide(s) (Callear et al., 1959), although metastable atoms are expected to be less reactive. It is the chemical conversion of excited Hg atoms by O_2 that releases Hg^{II}, which can further react to more stable species, giving Hg^0 in the upper stratosphere a tiny lifetime against oxidation compared to transfer to the lower atmosphere (Saiz-Lopez et al., 2022). In the uppermost stratosphere, there appears to be access to deeper UVC (**Fig. 1b**) that at 184.9 nm allows a spin-allowed electronic transition from $Hg(^1S_0)$ to

230 $Hg(^1P_1)$ with a light absorption cross-section of nearly two orders of magnitude greater than for the $Hg(^1S_0) \rightarrow Hg(^3P_1)$ transition (Morton, 2000). Like $Hg(^3P_1)$, the more energetic $Hg(^1P_1)$ reacts with O_2 at a rate approaching the collision frequency, but the HgO product formed in the latter case is so vibrationally hot that it promptly decays into Hg and O atoms. As a result, the chemistry of $Hg(^1P_1)$ is expected to play a minor role in the turnover of Hg in the upper stratosphere. The calculated lifetime of Hg^0 in the mid to upper stratosphere is altitude-dependent in the range of a fraction of up to a few hundred hours (Saiz-Lopez et al., 2022) and is most

235 comparable to that of Hg^0 during AMDEs, but the underlying governing physicochemical processes are completely different.

4 Kinetics, thermodynamics and general chemistry

4.1 Fundamental kinetics and thermodynamical principles

A chemical process can be decomposed into a sequence of one or more single-step processes as elemental reactions. Elementary processes involve a transition between two atomic or molecular states separated by a potential energy barrier. The barrier represents the activation energy and determines the rate at which it occurs. The rate of a reaction is determined by the interaction between kinetics, a rate process, and thermodynamics that describes the energetics of the process. Processes that release heat as products and increase the entropy of the system favor the reaction. The balance between enthalpy (ΔH) and entropy (ΔS) is given by the Gibbs free energy equation, where T is the absolute temperature in Kelvin: $\Delta G = \Delta H - T\Delta S$. If the Gibbs free energy is negative, the reaction is spontaneous from a thermodynamic perspective. The index is used to distinguish the enthalpy of reaction (ΔH_R) from, say, the enthalpy of formation of a substance (ΔH_f). We can calculate the equilibrium constant, K, using $\ln K = -\Delta G_R/RT$ and determine the ratio of the forward and reverse rate coefficients from $K = k_f/k_r$. Examples of important types of reaction are as follows:

Reaction order	Type	Unit
Unimolecular step	Thermal dissociation	s^{-1}
Bimolecular step	Recombination	$cm^3 molecule^{-1}s^{-1}$, $L\ mol^{-1}s^{-1}$
Termolecular step	Recombination assisted by a third body ($M = N_2/O_2$)	$cm^6 molecule^{-2}s^{-1}$, $L^2 mol^{-2}\ s^{-1}$

Termolecular reactions are pressure (M) dependent at low pressures with an effective rate coefficient (k) of third order, but becomes pressure independent at high pressures. The transition from third to second order behavior is known as the fall-off region. For most atmospheric reactions, we can expect that rate coefficient is at the low pressure-limit. However, there are exceptions which are listed in **Table 1**. While *two-body* collisions are common in the gas phase, *three-body* collisions are much less probable and *four-body* collisions can be ignored because of their low probability. An *overall* reaction includes two or more *elementary* reactions. The temperature dependence of rate coefficients can be fit over a relatively narrow temperature range by the empirical *Arrhenius equation*: $k(T) = A \exp(-E_a/RT)$, where E_a is the activation energy and R the gas constant. The pre-exponential factor A, a constant in the original Arrhenius equation, is weakly temperature dependent for most reactions (varying as the square root of T according to collision theory). For a wider temperature range, the modified expression $k(T) = (T/300)^n \cdot \exp(-E_a/RT)$ provides a better fit to the experimental data. If the activation energy is high enough, there is a large endothermic barrier that prevents even a reaction with a strongly negative ΔG^0 from occurring at measurable rates. In select cases, the experimental data show a negative activation energy, suggesting that the reaction proceeds by the addition of reactants to form an intermediate species with excess energy that must be dissipated before decomposing into the final products. The rate constant for termolecular reactions between small molecules in the atmosphere can usually be well approximated by a combination of three parameters k_0 ($cm^6 molecule^{-2}\ s^{-1}$), k_∞ ($cm^3 molecule^{-1}\ s^{-1}$) and F_C. The first two correspond to the low- and high-pressure limits, and F_C is a form factor describing the transition region.

$$k = \frac{k_0 \cdot k_\infty \cdot [M]}{k_\infty + k_0 \cdot [M]} F_C^{\left(1 + [\log(k_0 \cdot [M]/k_\infty)]^2\right)^{-1}} \qquad (1)$$

The temperature dependence of k is expressed by parameterizing k_0 and k_∞ as a function of temperature with the following expression:

$$k_0^T = k_0^{300}(T/300)^{-n} \text{ and } k_\infty^T = k_\infty^{300}(T/300)^{-m} \qquad (2)$$

4.2 Surface kinetics

Atmospheric aerosols possess a high surface-to-volume ratio, which enables most of their constituents being concentrated at the surface. Furthermore, the influence of surface chemistry is enhanced with decreasing particle size. Gas-to-particle reactions, among other heterogeneous reactions, begin with adsorption, which links molecules from the gas phase to the surface of a solid or liquid. This process can be physical, with low adsorption energy (*physisorption*, van der Waals forces), chemical (*chemisorption*), when chemical bonding occurs as molecules approach the surface and overcome the activation energy barrier, and become reactive when the adsorbent reacts with sites on the surface. It is crucial to recognize that gases and solutes adsorbed at an interface frequently exhibit physicochemical

properties that diverge from their bulk properties, including reactivity and spectral shifts. Surface reaction kinetics are often expressed by the uptake probability (γ), which represents the fraction of gas collisions with a substrate surface that yield uptake or reaction. The net uptake of gas γ_{net} is quantified in terms of conductances (Γ), which are normalized to the rate of gas surface collisions:

$$\gamma_{net}^{-1} = \Gamma_g^{-1} + \alpha^{-1} + (\Gamma_{rxn} + \Gamma_{sol})^{-1} \tag{3}$$

where Γ_g, Γ_{rxn}, and Γ_{sol} represent the processes of gas-phase diffusion to the surface, solubility, and reaction in the bulk liquid phase,

275   respectively, and α represents the (reversible) mass accommodation ("sticking") across the gas-particle interface. In addition to α, these processes are related to the diffusion constants in gas (D_g) and liquid (D_l) phases, Henry's law coefficient (k_H), and the rate constant of the (first order) reaction in the condensed phase bulk (Finlayson-Pitts and Pitts, 2000). For solids, bulk diffusion is generally too slow to allow bulk solubilities or bulk kinetics to control uptake. To justify the use of the formulation of additive kinetic conductances (**Eq. 3**) to solve the continuity equation and thus to be sufficient in laboratory studies to measure the net loss of a gas

280   over a condensed phase of known volume and surface area, it is preferable to conduct experiments at low pressure. These experiments are typically performed in a tube reactor (radius r) with fast laminar flow conditions (FF). To vary the reaction time, a moving injector is employed to change the exposed surface length in this technique. The net flux of the gas X into the condensed phase (J_x) can in this case be expressed as **Eq. 4**:

$$J_X = \frac{2 \cdot k_{obs}}{r}\left([X]_{g,\infty} - \frac{[X]_{surf}}{H}\right) \tag{4}$$

where k_{obs} is the experimentally observed first-order rate coefficient and the indices g,∞ and surf represent the gas bulk and surface,

285   respectively. In turn, k_{obs} relates approximately to γ_{net} by **Eq. 5**:

$$k_{obs} = r^{-1}\left(\frac{r}{3.66 \cdot D_g} + \frac{2\gamma_{net}}{\bar{v}_X}\right)^{-1} \tag{5}$$

where D_g is the diffusivity of the gas and $\bar{v}_X$ its mean thermal velocity. The value of γ_{net} changes as the surface is covered by molecules and depends on the concentrations of the reactants and the reaction time. The initial phase is denoted by γ_{net}^0, while the steady state phase is denoted by γ_{net}^∞. The calculated γ_{net} can be employed to estimate the lifetime of the gas X (τ_X) with respect to reactive uptake on particles. The following formula has been applied to the uptake on aerosols with a polydisperse distribution (Mao et al., 2021; Sander, 1999; Schwartz, 1986):

$$\tau_X = \left[\sum 4\pi r^2 \left(\frac{\Delta N}{\Delta \log r}\right)\Delta \log r \left(\frac{r}{D_g} + \frac{4}{\gamma_{net} \cdot \bar{v}_X}\right)\right]^{-1} \tag{6}$$

290   The uptake of the only Hg^{II} species studied so far, $HgCl_2$, follows a Hinselwood-Langmuir mechanism (Pankow, 2007), where $HgCl_2(g)$ must first be adsorbed to a site (∥) on the surface and can then react as a surface complex with a reactive center (e.g., anions) R on the surface, forming a product which is released from ∥, which becomes vacant again:

$$HgCl_2(g) \underset{K=k_{ads}/k_{des}}{\overset{}{\rightleftharpoons}} \parallel-HgCl_2 \overset{R}{\rightarrow} product(s) + \parallel \tag{7}$$
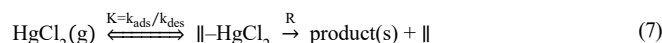
where K in the above equation is referred to as the Langmuir constant. Deposition velocities and partitioning coefficients are an older empirical framework for parameterizing heterogeneous atmospheric processes. A coefficient for absorptive partitioning of compound

295   X onto existing aerosol, K_{gp}, was proposed as Pankow (2007):

$$K_{gp} = \frac{[X]_p/PM}{[X]_g} \tag{8}$$

where the index gp is the gas-particle partitioning, $[X]_p$ and $[X]_g$ are the mass concentrations of compound X in the gas phase and particle phase, respectively, in a unit volume of air, and PM is the total mass concentration of particles.

4.3 Aqueous redox equilibria

The Gibbs free energy change (ΔG) presented previously is related to the electrode potential (E) by the formula:

300   $$\Delta G = -nFE \tag{9}$$

where n is the number of moles of electrons transferred in the reaction and F is the Faraday constant (96485 C mol⁻¹). The standard

potentials for the mercury-mercurous-mercuric free cation couples are:

$$Hg_2^{2+}(aq) + 2\ e^- \rightleftarrows 2\ Hg^0(aq)\quad E^0 = 0.789\ V \qquad \text{(Rxn 1)}$$
$$2\ Hg^{2+}(aq) + 2\ e^- \rightleftarrows Hg_2^{2+}(aq)\quad E^0 = 0.908\ V \qquad \text{(Rxn 2)}$$
$$Hg^{2+}(aq) + 2\ e^- \rightleftarrows Hg^0(aq)\quad E^0 = 0.854\ V \qquad \text{(Rxn 3)}$$

These positive potential indicates that the reduction of Hg^{2+}/Hg_2^{2+} to Hg is favored under standard conditions. It is also evident that Hg^0 can be oxidized to Hg_2^{2+}(aq) rather than Hg^{2+}(aq) only by agents with potential from –0.79 to –0.85 V. None of the common

305 oxidizing agents meet this narrow potential range. Therefore, in excess of oxidizing agent, Hg^0 is completely oxidized to Hg^{2+}(aq). Only when the excess of Hg^0 exceeds 50% does the oxidation leads to Hg_2^{2+}(aq). Ligation and hydrolysis have a major impact on standard potentials, including those listed in **Rxn 1 – 3**. For example, $Hg(OH)_2 + 2\ e^- \rightleftarrows Hg^0 + 2\ HO^-$, analogous to **Rxn 3**, has an E^0 value of 0.206 V.

4.4 Chemical properties of aqueous $Hg^{I,II}$

310 The Hg^{2+} aqua ion, $[Hg(H_2O)_6]^{2+}$, exists only in distinctly acidic aqueous solutions containing a weakly coordinating anion (e.g., ClO_4^-). It undergoes hydrolysis readily at pH > 1 (log K $([Hg(OH)]^+ = 10.3$, Powell et al., 2005). Depending on its size and stable electron configuration, Hg^{2+}(aq) can be easily polarized by ligands and, therefore, has the potential to form strong covalent bonds. This property allows Hg^{2+}(aq) to interact with organic C to readily form Hg–C bonds through mercury-hydrogen substitution (*mercuration*), addition (*oxy-* and *amino-mercuration, etc.),* and decarboxylation reactions. An example is aniline, which form

315 covalent complex with Hg^{2+} readily in aqueous solution at room temperature:
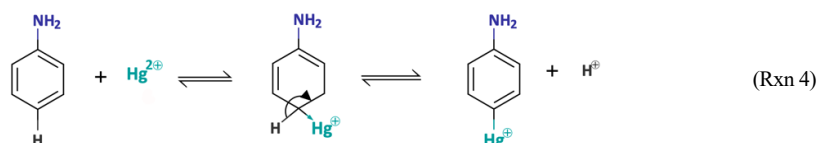
The formation of organomercurials by mercuration in aqueous solution is generally slow due to the reduced electrophilicity of Hg^{2+} caused by the metal center's hydrolysis. However, the presence of a polar solvent has little influence on other processes of organomercurial formation, such as decarboxylation. Therefore, abiotic Hg methylation can occur in aqueous solution with the assistance of, e.g., light carboxylic acids (Deacon et al., 1986). In the case of keto-enolic organic compounds such as acetylacetone

320 (R = H) and malonate (R = OH), the mercuric ion can, in principle, adopt a C-bond, an O-bond or a chelate structure:
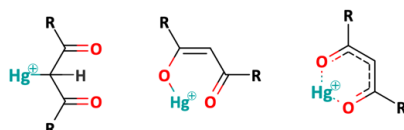
Highly toxic CH_3Hg^+ (MMHg$^+$) species are by far the most abundant organic Hg in the environment and are formed from inorganic Hg^{II} mainly by the action of Fe^{III} and SO_4^{2-} reducing bacteria. Besides monomethylation, permethylation can also occur anaerobically (Sommar et al., 1999). $(CH_3)_2Hg$ (DMHg) is detected mainly in deep sea waters, but via upwelling waters (Conaway et al., 2009), it may reach the mixed layer, where gas exchange with the atmosphere can occur. DMHg has also been detected in landfill (Lindberg

325 et al., 2005; Feldmann et al., 1994) and sewage gas (Sommar et al., 1999), flood plains (Wallschläger et al., 1995) and rice paddies (Wang et al., 2019c). The binding affinity of Hg^{2+} to ligands is often qualitatively rationalized by Lewis' acid-base theory with the message that mercurials (type B metal) prefer soft ligands such as heavier halides and hydrochalcogenides (e.g. I^- and SH^-, respectively) to hard ones (e.g. OH^- and F^-). In fact, Hg^{2+} is the softest of all metal ions acting as Lewis's acids. The preference for low coordination numbers (≤ 4, typically linear two-coordination) in Hg^{II} complexes is related to the fact that relativistic effects come

330 into play for the heaviest elements (Tossell and Vaughan, 1981). The interaction between Hg^{2+}(aq) and inorganic ligands and low molecular weight organics are given as stability constants. The tables show that Hg^{2+} also binds strongly to nitrogenous bases. The interaction with inorganic ones, such as ammonia, is extensive and complex (Breitinger and Brodersen, 1970). For organic nitrogen

ligands, there is a parallel between the basicity of the ligand and the stability of the Hg-ligand complex (e.g. guanidine). Heterocyclic nitrogen compounds, such as histidine, also form strong complexes with the mercuric ion. The hard-soft acid-base principle applies

335   only to highly polar solvents, such as in aqueous solution, a result of solvation (hydrolysis) effects (Riccardi et al., 2013). In the gaseous phase, an inverse relationship prevails (Riccardi et al., 2013) and can be illustrated by the fact that gaseous $Hg(OH)_2$ is a stable molecule, whereas in aqueous solution, Hg^{2+} and 2 OH^- can form the intermediate molecule $Hg(OH)_2$ (Yang et al., 2020b), which eliminates H_2O and precipitates solid HgO. Therefore, solid $Hg(OH)_2$ is not known (Wang and Andrews, 2005). Furthermore, in the aqueous phase, the univalent state (mercurous species) is represented by the metal-metal bound ion Hg_2^{2+}(aq) that is ordinarily

340   stable. Like Hg^{2+}(aq), Hg_2^{2+}(aq) is a soft Lewis acid.

Hg-ligand complexation is ubiquitous in the environment. This process involves a significant energy shift due to solvation effects, which result in a reduction in the number of solvating water molecules and an increase in the interaction between ligands/anions in the complexes and water. As opposed to the dimer cation, the discrete $Hg^{\bullet+}$ cation is paramagnetic and was detected for the first time using electron spin resonance (Symons and Yandell, 1971). The free $Hg^{\bullet+}$ is a highly potent reducing agent with a one-electron

345   reduction potential, $E^0(Hg^{2+}/Hg^{\bullet+})$, estimated to be well below -2.0 V (Gårdfeldt and Jonsson, 2003). However, hydrolyzed or ligated forms are less reactive (Gårdfeldt and Jonsson, 2003; Kozin and Hansen, 2013). The dissociation Hg_2^{2+}(aq) $\rightleftarrows$ 2 $Hg^{\bullet+}$(aq) is considerably less significant than the disproportionation Hg_2^{2+}(aq) $\rightleftarrows$ Hg^0(aq) + Hg^{2+}(aq), with a conservative upper bound for the ratio $[Hg^{\bullet+}]/[Hg_2^{2+}]$ of 10^{-7} (Moser and Voigt, 1957). Free cation acidity decreases in the order of Hg^{2+} (pK 3.4), Hg_2^{2+} (pK 4.9) and $Hg^{\bullet+}$ (pK 5.1). Hg_2^{2+}(aq) $\rightleftarrows$ Hg^0(aq) + Hg^{2+}(aq) has an equilibrium constant of 5.5 x 10^{-9} M (Moser and Voigt, 1957), which

350   indicates that a solution of initially only Hg_2^{2+} in pure water will contain only a single percent Hg^{2+} in the absence of ligands that form complexes with Hg^{2+}. However, in the presence of ligands that form complexes with Hg^{2+}, disproportionation is rapid and Hg_2^{2+} is consumed. The same applies when Hg^0(aq) is removed from the solution, e.g., by a gas stream. Hg_2^{2+} can be a major speciation component in heavily polluted waters (Fang et al., 2024), but is insignificant in the atmosphere.

4.5. Chemical equilibria data

355   For a general complex equilibrium with Hg^{2+} and the ligand L, Hg^{2+} + q L + r H_2O $\rightleftarrows$ $\left[HgL_q(OH)_r\right]^{(2-r)+}$ + r H^+, a stability constant β_{qr} is defined as $\left[M_pL_q(OH)_r\right]\left[H^+\right]^r/([M]^p[L]^q)$. When the complex is not hydrolyzed β_{qr} is reduced to $\beta_q =$ $\left[ML_q\right]/([M][L]^q)$. For the equilibrium obtained by adding a ligand (L) to a metal complex in a stepwise manner, K_q is used, which is related to β_q by $\prod_{i=1}^{q} K_q$. **Tables 1** and **2** present the equilibrium constants for Hg^{2+} associated with a range of inorganic and organic natural ligands, respectively, without purporting to be comprehensive. The reader's attention should also be drawn to

360   the open-access AQUAMER database and web server dedicated to Hg, which provides direct speciation results by combining web-based interfaces to a speciation calculator, thermodynamic constants databases, and a computational chemistry toolbox for input to other software to estimate missing constants. (Lian et al., 2020).

4.6 The speciation of Hg^{II} in atmospheric waters

Hg^{II} speciation in atmospheric waters such as clouds and fog is governed by interaction with inorganic nucleophiles, low molecular

365   weight organics (LMWO), and high molecular weight dissolved organic matter (DOM). Identified LMWOs typically make up a smaller mass fraction of the DOM in ambient cloud and fog droplets. Despite its limited abundance (0.5 - 3% in freshwater), sulfurized DOM exerts control over Hg cycling in terrestrial aquatic systems by forming predominantly strong HgL (logK ~21.9 – 23.6) and HgL_2 (logK ~30.1–31.6) complexes (Dong et al., 2011), where L represents functional groups with reduced sulfur. Although sulfur-containing DOM (with the elemental composition CHSO and CHNSO) is also relatively ubiquitous in atmospheric

370   organic matter (AOM), it is mainly in hexavalent form, with reduced sulfur being a rare occurrence (Zhao et al., 2013; Bianco et al., 2018; Jiang et al., 2022). In contrast to sub-zero valence S, whose presence in AOM is thus not universal, conjugate bases of strong oxo acids that are common in AOM, such as organic nitrates and sulfates, form weak complexes with Hg^{II}, which is not relevant in this context. It is therefore questionable to apply speciation by geochemical equilibrium modeling to assess the interaction between

atmospheric DOM and Hg^{II} as in some studies (Li et al., 2018; Zhen et al., 2023). Bittrich et al. (2011) used pH, a confined set of
375 inorganic ions (NH_4^+, NO_3^-, SO_4^{2-} and Cl^-), and LMWO acids to speciate observations of dissolved Hg^{II} in a study of cloud and fog
water. Strongly dependent on pH, at < 5 even moderate Cl^- levels can control speciation ($HgCl_2$), whereas in more alkaline waters
(e.g. influenced by NH_3) speciation is controlled by $Hg(OH)_2$, $Hg(OH)Cl$ and to some extent by $[Hg(NH_3)_2]^{2+}$. A more realistic
approach is to include DOM in the speciation. In this regard, Yang et al. employed Hg^{II} complexation with fulvic acids under
conditions of binding to mainly O-donors (1:2 complexes with logK = 5.6, Haitzer et al., 2002) as surrogates for AOM interaction.
380 It was found to dominate in the Hg^{II} speciation of rainwater samples in rural and urban France (Yang et al., 2019). Studies of cloud
water in eastern China show a remarkable change in acidity and other chemical composition in the post-2008 period, where Hg^{II},
although the concentration is unchanged over time, in the former acidic environment is mainly bound by DOM (~79%) (Li et al.,
2018) and in the later more neutral environment is more homogeneously distributed in addition to DOM among hydrolyzed and
halide (X = Cl, Br) bound species ($Hg(OH)_2$, $HOHgX$, and HgX_2, Zhen et al., 2023). In conclusion, it is clear that as long as the
385 complexation of Hg^{II} with AOM is less constrained, there is considerable uncertainty regarding the partitioning of aquatic Hg^{II}
between stable and reduction-labile complexes in the photic atmosphere.

Table 1. Hg^{2+} – inorganic ligand complexes. Omitted in the table is, e.g., interactions with reduced sulfur (HS–, R–S–) that can be found in e.g. Skyllberg (2011).

Ligand/ion		log β_{10} / pKa$_1$	log β_{20} / pKa$_2$	log β_{30}	log β_{40}	log β_{11}	Reference
Elemental mercury	Hg^0	8.46					Hietanen and Sillén, 1956
Hydroxide	HO^-	10.3	21.4				Powell et al., 2005
Fluoride	F^-	1.6 / 3.17					Martell and Smith, 1976
Chloride	Cl^-	7.3 / < 0	14.0	14.9	15.5	18.0	Powell et al., 2005
Bromide	Br^-	9.0 / < 0	17.1	19.4	21.0		Martell and Smith, 1976
Iodide	I^-	12.87 / <0	23.82	27.6	29.8		Martell and Smith, 1976
Ammonia/amide	$NH_3/-NH_2$	8.8 / 9.25	17.4	18.4	19.1		Martell and Smith, 1976
Carbonate	CO_3^{2-}	10.7 / 6.35	14.5/15.7 / 10.33			5.47[1]	Puigdomenech, 2013
Cyanide	$C\equiv N^-$	17.0 / 9.21	32.8	36.3	39.0		Martell and Smith, 1976
Thiocyanate	$N\equiv CS^-$	9.08 / 0.9	17.3	20.0	21.8		Martell and Smith, 1976
Selenocyanate	$N\equiv CSe^-$	— / —	—	26.4	28.9		Martell and Smith, 1976
Sulfite	SO_3^{2-}	13.3 / 1.81	24.1 / 6.97	26.0			Martell and Smith, 1976; van Loon et al., 2001
Selenite	SeO_3^{2-}	/ 2.35	12.5 / 7.94				Martell and Smith, 1976
Sulfate	SO_4^{2-}	1.34 / < 0	2.4 / 1.99				Martell and Smith, 1976
Thiosulfate	$S_2O_3^{2-}$	/ 1.6	29.23	30.6			Martell and Smith, 1976
Selenosulfate	$SeSO_3^{2-}$		36.8				Martell and Smith, 1976
Selenide	Se^{2-}	51.2[2] / 3.89	61.0[3] / 15.0			52.8[4]	Foti et al., 2009
Nitrate	NO_3^-	0.11 / < 0					Martell and Smith, 1976

[1] $Hg^{2+} + HCO_3^- \rightleftarrows (HgHCO_3)^+$
[2] $Hg^{2+} + HO^- + HSe^- \rightleftarrows HgSe$
[3] $Hg^{2+} + 2 HO^- + 2 HSe^- \rightleftarrows HgSe_2^{2-}$
[4] $Hg^{2+} + HO^- + 2 HSe^- \rightleftarrows HgHSe_2^-$
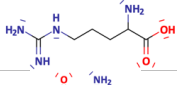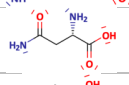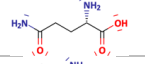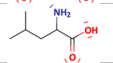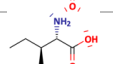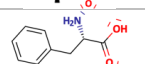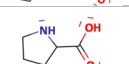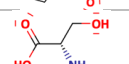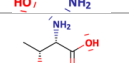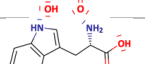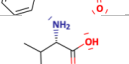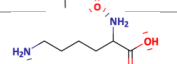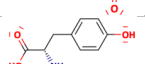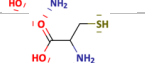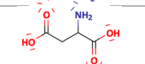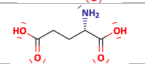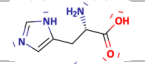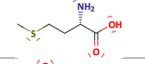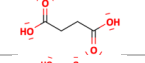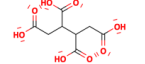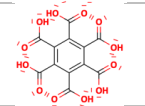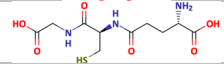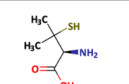
Table 2. Hg^{2+} –organic ligand complexes.

Ligand/ion	Structure formula	log β_{10}	log β_{20}	log β_{30}	log β_{40}	log β_{11}	Reference
		pKa$_1$	pKa$_2$				
Oxalate		9.66/10.5					Bartels-Rausch et al., 2011; Martell and Smith, 1982
		1.25	4.27				
Formate		3.66/3.55	7.10/7.35				Martell and Smith, 1982
		3.55	—				
Acetate		3.74/4.3	7.01/8.7				Martell and Smith, 1982
		4.5	—				
Pivalate		5.92					Martell and Smith, 1977
		5.03	—				
Monochloroacetate		2.95.	5.61				Martell and Smith, 1977
		2.87	—				
Trichloroacetate		3.08					Martell and Smith, 1977
		0.66	—				
Glycolate		3.6	7.05				Martell and Smith, 1982
		3.83					
Mercaptoacetate		34.2	42.6			36.3	Cardiano et al., 2011
		3.43	10.1				
Metoxyacetate		3.54	6.91				Martell and Smith, 1982
		3.57					
Acetylacetonate		12.9	20.1				van der Linden and Beers, 1975
		9.00					
Phtalate		4.9					Martell and Smith, 1977
		2.7	4.9				
D-tartarate		5.4				15.5	Kornev and Kardapol'tsev, 2008
		2.8	3.9				
Thiomalate		9.94	18.07				Martell and Smith, 1977
		3.3	4.6				
Iminodiacetate		13.1	20.2				van der Linden and Beers, 1975
		2.65					
Dimercaprol (BAL)		25.7	34.3				Martell and Smith, 1982
		8.76	10.78				
Citrate (Cit^{3-})		4.1	6.1	11.1	15.0	17.8	van der Linden and Beers, 1975; Kornev and Kardapol'tsev, 2008
		3.0	4.1				
Ascorbate		4.2	8.7				Kleszczewska, 1999
		4.1					
Urea		2.1					Martell and Smith, 1977
Thiourea		11.4	21.7	24.6	26.4		Martell and Smith, 1982
Selenourea			24.0	30.2	32.9		Martell and Smith, 1977
Semicarbazide			11.6	15.2			Martell and Smith, 1977
		3.53					
Thio-semicarbazide			22.4	24.8	25.8		Martell and Smith, 1977
		1.6					
Seleno-semicarbazide			26.9	30.4	32.4		Martell and Smith, 1977
		0.8					
Guanidine			24.5				Martell and Smith, 1982
		13.5					
Ethylenediamine (en)		13.85	23.3			10.2	Martell and Smith, 1982
		9.79	16.82				
Alanine		12.4	19.6				van der Linden and Beers, 1974
		2.50	9.80				

Compound	Structure								Reference
Arginine		11.5	18.8						van der Linden and Beers, 1974
		2.19	9.21						
Asparagine		11.4	18.6						van der Linden and Beers, 1974
		2.14	8.85						
Glycine (Gly)		12.2	19.2			18.82	31.42	6.98	van der Linden and Beers, 1974
		2.44	9.68						
Glutamine		11.5	18.7						van der Linden and Beers, 1974
		2.27	9.16						
Leucine		11.9	19.5						van der Linden and Beers, 1974
		2.37	9.62						
Iso-leucine		12.4	19.6						van der Linden and Beers, 1974
		2.40	9.66						
Phenylalanine		12.4	19.6						van der Linden and Beers, 1974
		2.21	9.18						
Proline		12.2	20.1						van der Linden and Beers, 1974
		2.04	10.52						
Serine		11.7	19.1						van der Linden and Beers, 1974
		2.21	9.13						
Threonine		11.7	18.7						van der Linden and Beers, 1974
		2.24	8.86						
Tryptophan		13.9	21.4						van der Linden and Beers, 1974
		2.39	9.43						
Valine		11.7	18.7						van der Linden and Beers, 1974
		2.38	9.59						
Lysine		11.3	18.7						van der Linden and Beers, 1974
		2.18	9.18	10.72					
Tyrosine		12.3	19.5						van der Linden and Beers, 1974
		2.34	9.11	10.16					
Cysteine			39.4						van der Linden and Beers, 1974
		1.96	8.48	10.55					
Aspartic acid		14.86	19.15			33.1		7.4	van der Linden and Beers, 1975; Kornev and Kardapol'tsev, 2008
		1.94	3.70	9.62					
Glutamic acid		12.8	19.2						van der Linden and Beers, 1974
		2.39	4.21	9.54					
Histidine		15.75	20.48			34.4		7.4	Martell and Smith, 1982
		1.79	6.00	9.16					
Methionine		12.8	19.5						van der Linden and Beers, 1974
		2.26	9.13						
Succinic acid Succinate (suc^{2-})		9.46	14.22					3.3	Martell and Smith, 1982
		5.20	9.17						
1,2,3,4-butane tetracarboxylic acid (btc^{4-})		11.61	17.14			21.5		4.8	Martell and Smith, 1982
		6.42	11.67						
1,2,3,4,5,6-benzene hexacarboxylic acid (mlt^{6-})		18.4	22.6			25.6		14.3	Martell and Smith, 1982
		6.55	12.11						
Glutathione (H_2GsH)		26.0	33.4					32.4	Smith et al., 2004
		2.12	3.53	8.66	9.12				
Penicillamine		18.9	25.0						Strand et al., 1983
		1.8	7.83						

4.7 Chemical reactions data

The subsequent two principal sections address the chemical redox reactions in the gaseous phase (**Section 5**) and in the aqueous phase (**Section 6**), respectively. **Table 3** summarizes the gas-phase reactions with the corresponding rate coefficients and reaction enthalpies. The reaction numbers are designated with the prefix G (G1, G2, etc.). The aqueous phase reaction numbers are designated with the prefix W and are listed in **Table 4** with the corresponding rate coefficients. It should also be noted that several chemical

395 reactions appear in the text that are not labeled with G or W and are not assigned to **Tables 3** and **4**. This is particularly the case for heterogeneous (multi-phase) processes (**Section 7**), such as reactive uptake and reduction on surfaces, which consequently have no prefix and follow the sequential numbering throughout the document.

5 Gas-phase atmospheric Hg chemistry

5.1 Inorganic species

400 **5.1.1 Initial reactions of ground state Hg^0**

The homogeneous gas-phase oxidation of Hg^0 in the electronic ground state of atmospheric importance is limited to a few reactive species formed by the action of actinic light. In the atmosphere, multi-step reactions involving both Hg^I and Hg^{II} species are crucial for Hg transformations. Atmospheric oxidation of Hg^0 occurs largely in the gas phase, whereas the rates of aqueous phase reactions in deliquescent aerosols are relatively slower on a unit air volume basis and are inherently limited by the low water solubility of Hg^0.

405 Oxidation of Hg^0 vapor by closed-shell molecules, such as halogenation chemistry with reference to the gas phase, has been studied in the laboratory at various temperatures (Hall, 1992; Qu et al., 2009; Chi et al., 2009; Ariya et al., 2002; Sumner et al., 2005; Raofie and Ariya, 2004; Raofie et al., 2008; Wilcox, 2009) since Ogg et al. (1936). Direct oxidation by the free halogens (X_2) via the insertion reaction $Hg + X_2 \rightarrow XHg^{II}X$ is highly exothermic but very slow under atmospheric conditions due to large energy barriers (Auzmendi-Murua et al., 2014), whereas the abstraction $Hg + X_2 \rightarrow {}^\bullet Hg^I X + X^\bullet$ proceeds at significant rates only at high

410 temperatures (Niksa et al., 2001). Thus, free halogen chemistry is of great importance for the conversion of Hg in the flue gas from power generation systems (Wilcox, 2009), such as the coal-fired (CFPP) type but not in the atmosphere. The same applies to the $Hg + NO_2$ reaction, which is barrierless and whose pathway to $Hg^{II}(ONO)_2$ shows a negative temperature dependence (Li et al., 2022c). However, reactions that are only important in combustion and flue gas cleaning systems are outside the scope of this review.

$Hg + XO$ ($X = O_2$, NO_2 and Br)

415 Although oxidation of Hg^0 vapor by common atmospheric oxidants O_3 (Sumner et al., 2005; Hall, 1995; Pal and Ariya, 2004b; Snider et al., 2008), $BrO^\bullet$ (Raofie and Ariya, 2004; Spicer et al., 2002) and $NO_3^\bullet$ (Sommar et al., 1997; Sumner et al., 2005) has been observed in the laboratory, the identity and phase of the product(s) are in doubt. Laboratory studies of gas-phase oxidation of ppb levels of Hg^0 (the atmospheric level is sub-ppt) have observed product particles in the accumulation mode, suggesting that gas-to-particle conversion takes place (Raofie and Ariya, 2004; Sun et al., 2016). These data attributed to the gas phase are almost certainly

420 compromised by complex kinetics including reactions at the reactor wall (Hynes et al., 2009). In all cases, gas-phase oxidation pathways leading to HgO by O atom transfer are endothermic (**Rxn G5 – G7**, **Table 3**). Furthermore, experimentally measured pre-exponential factors for the Hg–O_3 reaction, $\sim 10^{-16} – 10^{-18}$ cm^3 molecule^{-1} s^{-1} (Hall, 1995; Pal and Ariya, 2004b), are very much smaller than expected for a simple O atom transfer (Calvert and Lindberg, 2005). Alternative O_3 oxidation via a weakly bound (~16 kJ mol^{-1}) adduct HgO_3 lacks exothermic dissociation pathways (i.e., $HgO + O_2$, **Rxn G5a**) and is therefore unlikely to occur in the

425 atmosphere but in laboratory experiments can conceivably diffuse to surfaces and be deposited as solid HgO possibly via oligomerization (Tossell, 2006). Recombination of Hg^0 with $NO_3^\bullet$ results in the weakly bound ${}^\bullet Hg^I NO_3$ (~27 kJ mol^{-1}), which dissociates in the lower troposphere before oxidation to Hg^{II} species of the type $O_2NOHgO^\bullet$ or O_2NOHgY can occur (Edirappulige et al., 2023a). Abstractions (e.g., $Hg + BrO^\bullet \rightarrow HgO + Br^\bullet$ or $Hg + BrO^\bullet \rightarrow {}^\bullet Hg^I Br + O$, **Rxn G7a & b**) are endothermic, whereas direct insertion reactions (e.g., $Hg + BrO^\bullet \rightarrow BrHg^{II}O^\bullet$, **Rxn G7c**) is exothermic (–84 kJ mol^{-1}, Shepler 2006) but affected by large

430 barriers (170 kJ mol^{-1}) and therefore unlikely to proceed (Balabanov and Peterson, 2003). The remaining exit channels, namely the recombination of Hg and $BrO^\bullet$ (**Rxn G7d**) leading to the formation of the geometric isomers of $BrHg^{II}O^\bullet$ (${}^\bullet Hg^I BrO$ and ${}^\bullet Hg^I OBr$),

are also inconceivable as these adducts are thought to be very weakly bound (Shepler, 2006). Stable Hg^I species of this type have been reported in one laboratory suggesting that $BrO^\bullet$ is important during AMDEs (Raofie and Ariya, 2004). However, other studies both in the field (Wang et al., 2019a) and in the form of models (Xie et al., 2008; Ahmed et al., 2023) show that the synchronous

435 disappearance of Hg^0 and O_3 during AMDEs can best be described solely as the action of Br atoms, with an upper limit for $k_{Hg + BrO}$ of 1×10^{-15} cm^3 $molecule^{-1}$ s^{-1}, but that the reaction product $^\bullet Hg^I Br$ (**Fig. 2**) rapidly adds $BrO^\bullet$, presumably mainly to $BrHg^{II}OBr$, which is 117 kJ mol^{-1} more stable than the isomer $BrHg^{II}BrO$ (Jiao and Dibble, 2017a). Despite its thermal stability, $BrHg^{II}OBr$ is rapidly photolyzed (**Figs. 2** and **4**), and therefore does not constitute a significant component of the Hg^{II} pool following an AMDE.

Table 3. Atmospheric gas-phase reactions. Except where otherwise noted in the reference column, the thermodynamic data have been compiled from
440 the following sources of information: CRC Handbook of Chemistry and Physics (Lide, 2008), Hepler and Olofsson (1975), Chemical Kinetics and Photochemical Data for Use in Atmospheric Studies (Burkholder et al., 2019), Guzman and Bozzelli (2019), Saiz-Lopez et al. (2020; 2022), Balabanov and Peterson (2003; 2004), and Shepler (2006).

ID	Elementary reaction	Rate coefficient[5]	ΔH_R (kJ mol^{-1})[6]	Reference	Remarks
	Initial reactions of ground state Hg^0				
G1	$Hg + Br^\bullet \xrightarrow{M} BrHg^\bullet$	$1.46 \times 10^{-32} \times (T/298)^{-1.86} \times [M]$	−69	Donohoue et al., 2006	
G2	$Hg + HO^\bullet \xrightarrow{M} HOHg^\bullet$	$3.34 \times 10^{-33} \times exp(43/T) \times [M]$	−60 to −30	Sommar et al., 2001; Pal and Ariya, 2004a; Dibble et al., 2020; Bauer et al., 2003	
G3	$Hg + Cl^\bullet \xrightarrow{M} ClHg^\bullet$	$2.2 \times 10^{-33} \times exp(680/T) \times [M]$	−104	Donohoue et al., 2005	
G4	$Hg \xrightarrow{h\nu} Hg(^3P_1)$		471	Saiz-Lopez et al., 2022	Only significant in the stratosphere
G5	$Hg + O_3 \begin{array}{l}\rightarrow HgO + O_2 \\ \xrightarrow{M} HgO_3\end{array}$		93	Hall, 1995; Pal and Ariya, 2004b; Hynes et al., 2009	Thermo-dynamically unfeasible or adducts weakly bound
G6	$Hg + NO_3^\bullet \rightarrow HgO + NO_2$		195	Sommar et al., 1997; Spicer et al., 2002; Edirappulige et al., 2023a	
G7	$Hg + BrO^\bullet \begin{array}{l}\rightarrow HgO + Br^\bullet \\ \rightarrow BrHg^\bullet + O \\ \xrightarrow{M} BrHgO^\bullet \\ \xrightarrow{M} HgBrO\end{array}$		219 166 114 −85	Shepler, 2006; Raofie and Ariya, 2004	
G8	$Hg + ClOO^\bullet \rightarrow ClHg^\bullet + O_2$		−80	Hynes et al., 2009	
	Reactions of excited state Hg^0				
G9	$Hg(^3P_1) \rightarrow Hg + h\nu$	8.4×10^6		Kramida et al., 2023	Only significant in the stratosphere
G10	$Hg(^3P_1) + N_2 \rightarrow Hg(^3P_0) + N_2$	$5.1 \times 10^{-11} \times exp(-701/T)$	−21	Callear and Shiundu, 1987	
G11	$Hg(^3P_0) + O_2 \rightarrow Hg + O_2(^3\Sigma_u^+)$	$1.8 \times 10^{-10} \times (T/300)^{0.167}$	−27	Callear, 1987	
G12a	$Hg(^3P_1) + O_2 \rightarrow Hg + O_2(^3\Sigma_u^+)$	$1.3 \times 10^{-10} \times (T/300)^{-0.29}$	−6	Saiz-Lopez et al., 2022	
G12b	$Hg(^3P_1) + O_2 \rightarrow HgO(^3\Pi) + O$	$1.7 \times 10^{-10} \times (T/300)^{0.53}$	−48		
G13	$Hg(^3P_1) + H_2O \rightarrow HOHg^\bullet + H^\bullet$		−37		
	Hg^I & Hg^{II} bromine chemistry				
G14a	$BrHg^\bullet \xrightarrow{M} Hg + Br^\bullet$	$1.6 \times 10^{-9} \times exp(-7801/T) \times [M]$	69	Saiz-Lopez et al., 2019; Dibble et al., 2012	
G14b	$BrHg^\bullet \xrightarrow{h\nu} Hg + Br^\bullet$	4.3×10^{-2}		Shah et al., 2021	
G15a	$BrHg^\bullet + Br^\bullet \rightarrow Hg + Br_2$	3.90×10^{-11}	−124	Balabanov et al., 2005	
G15b	$BrHg^\bullet + Br^\bullet \xrightarrow{M} HgBr_2$	$2.5 \times 10^{-10} \times (T/298)^{0.57}$	−301	Goodsite et al., 2004	
G16	$BrHg^\bullet + HO^\bullet \xrightarrow{M} HOHgBr$	$2.5 \times 10^{-10} \times (T/298)^{0.57}$	−314	Goodsite et al., 2004	
G17	$BrHg^\bullet + Cl^\bullet \xrightarrow{M} ClHgBr$	3.00×10^{-11}	−338	Shah et al., 2021	
G18	$BrHg^\bullet + NO \rightarrow Hg + BrNO$	$7.0^{+1.2}_{-0.9} \times 10^{-12}$	−56	Wu et al., 2022	
G19	$BrHg^\bullet + O_2 \rightleftarrows BrHgOO^\bullet$	$1.4 \times 10^{-26} \times exp(3650/T)[7]$	−30	Wu et al., 2022	
G20	$BrHg^\bullet + NO_2 \begin{array}{l}\xrightarrow{M} BrHgONO \\ \rightarrow Hg + BrNO_2\end{array}$	$k_0 = (4.3 \pm 0.5) \times 10^{-30} \times (T/298)^{-(5.9\pm0.8)}$ $k_\infty = 1.2 \times 10^{-10} \times (T/298)^{-1.9}$ $F_C = 0.6$ 3.0×10^{-12}	−176 −45	Jiao and Dibble, 2017b; Wu et al., 2020	

---

[5] The basics of gas phase kinetics have been introduced in section 3.2. Unimolecular rate coefficients are in s^{-1} (photolysis frequencies refer to excitation energies at lambda >290 nm calculated according to J = $\int \phi(\lambda, T) \cdot \sigma(\lambda, T) \cdot F(\lambda) d\lambda$, where ϕ is the quantum yield (≤1), σ is the absorption cross section (cm^2 $molecule^{-1}$), F is the photon flux (photons cm^2 s^{-1}), λ is the wavelength and T is absolute temperature), bimolecular reaction rate coefficients are in cm^3 $molecule^{-1}$ s^{-1} (expressed as a rate constant or as a coefficient with an Arrhenius or other type of temperature dependence) and three-body reactions according to Eq. 1, i.e. k = $\frac{k_0[M]}{1 + k_0[M]/k_\infty} \cdot F_C^{\left[1 + [\log_{10} k_0[M]/k_\infty]^2\right]^{-1}}$ are in cm^6 $molecule^{-2}$ s^{-1} (where [M] is the number density of air molecules, k_0 (cm^3 $molecule^{-1}$ s^{-1}) is the low-pressure limiting rate coefficient, k_∞ (cm^6 $molecule^{-2}$ s^{-1}) is the high-pressure limiting rate coefficient. The temperature dependence of k_0 and k_∞ is expressed with Eq. 2.

[6] Refers to the calculated enthalpy (0 K) or to the experimental ditto (298 K).

[7] Equilibrium coefficient (unit: cm^3 $molecule^{-1}$)

G21	$BrHg^\bullet + HO_2^\bullet \overset{M}{\to} BrHgOOH$	$k_0 = 4.3 \times 10^{-30} \times (T/298)^{-5.9}$ $k_\infty = 6.9 \times 10^{-11} \times (T/298)^{-2.4}$ $F_C = 0.6$	−167	Jiao and Dibble, 2017b	
G22	$\to BrHgO^\bullet + O_2$ $BrHg^\bullet + O_3 \to BrHg^\bullet + O_2 + O_2$ $\to BrHgOO^\bullet + O_2$	$(7.5 \pm 0.6) \times 10^{-11}$	−140 −143 −171	Gómez Martín et al., 2022	
G23	$BrHg^\bullet + O \to Hg + BrO^\bullet$	$(5.3 \pm 0.4) \times 10^{-11}$	−168	Gómez Martín et al., 2022	
G24	$BrHg^{II}O^\bullet + O \to BrHg^\bullet + O_2$	$(9.1 \pm 0.6) \times 10^{-11}$	−252	Gómez Martín et al., 2022	
G25	$BrHg^{II}O^\bullet + O_3 \begin{array}{l}\to {}^\bullet Hg^I Br + O_2 + O_2\\\to BrHg^{II}OO^\bullet + O_2\end{array}$	$< 5 \times 10^{-12}$	−143 −171	Gómez Martín et al., 2022	
G26	$BrHgO^\bullet + CH_4 \to BrHgOH + CH_3^\bullet$	$4.1 \times 10^{-12} \times \exp(-856/T)$	−10	Lam et al., 2019a	
G27	$BrHgO^\bullet + CO \to HgBr^\bullet + CO_2$	$6.0 \times 10^{-10} \exp(-550/T)$	−282	Khiri et al., 2020	
G28	$BrHgO^\bullet + HCHO \to BrHgOH + CO + H^\bullet$	$(4.7 - 5.5) \times 10^{-11}$ [8]	−109	Lam et al., 2019a	
G29	$BrHgO^\bullet + NO \overset{M}{\to} BrHgONO$	2.9×10^{-11} [9]	−226	Lam et al., 2019b	
G30	$BrHgO^\bullet + NO_2 \overset{M}{\to} BrHgONO_2$	1.7×10^{-11} [10]	−242	Lam et al., 2019a	
G31	$BrHgO^\bullet \overset{hv}{\to} 0.56 \, HgO + 0.44 \, Hg + Br^\bullet + 0.44 \, O$	2.9×10^{-2}		Francés-Monerris et al., 2020	
G32	$HgBr_2 \overset{hv}{\to} 0.6 \, BrHg^\bullet + 1.4 \, Br^\bullet + 0.4 \, Hg$	1.5×10^{-6}		Shah et al., 2021	
G33	$BrHgOH \overset{hv}{\to} 0.35 \, HOHg^\bullet + 0.85 \, Br^\bullet + 0.5 \, Hg + 0.65 \, HO^\bullet + 0.15 \, BrHg^\bullet$	1.3×10^{-5}		Shah et al., 2021	
G34	$BrHgCl \overset{hv}{\to} 0.6 \, BrHg^\bullet + Cl^\bullet + 0.4 \, Br^\bullet + 0.4 \, Hg$			Sitkiewicz et al., 2019	Only significant in the stratosphere
G35	$BrHgONO \overset{hv}{\to} 0.9 \, BrHgO^\bullet + 0.1 \, NO_2 + 0.9 \, NO + 0.1 \, BrHg^\bullet$	1.1×10^{-3}		Shah et al., 2021	
G36	$BrHgOOH \overset{hv}{\to} 0.31 \, BrHgOH + 0.66 \, Br^\bullet + 0.66 \, Hg + 0.69 \, HO_2^\bullet + 0.03 \, BrHg^\bullet$	1.5×10^{-2}		Shah et al., 2021	
Hg^I & Hg^{II} chlorine chemistry					
G37a	$ClHg^\bullet \overset{M}{\to} Hg + Cl^\bullet$	$9.0 \times 10^{-11} \times \exp(-8980/T) \times [M]$	104	Khalizov et al., 2003; Donohoue et al., 2005	
G37b	$ClHg^\bullet \overset{hv}{\to} Hg + Cl^\bullet$	2.5×10^{-2}		Shah et al., 2021	
G38	$ClHg^\bullet + Br^\bullet \to ClHgBr$	3.0×10^{-11}	−307	Shah et al., 2021	
G39	$ClHg^\bullet + Cl^\bullet \to HgCl_2$	$3.0 \times 10^{-11}, (4 \pm 1) \times 10^{-12}$ [11]	−346	Shah et al., 2021; Taylor et al., 2005	
G40	$ClHg^\bullet + HO^\bullet \to ClHgOH$	3.0×10^{-11}	−315	Shah et al., 2021	
G41	$ClHg^\bullet + NO_2 \overset{M}{\to} ClHgONO$	$k_0 = 4.3 \times 10^{-30} \times (T/298)^{-5.9}$ $k_\infty = 1.2 \times 10^{-10} \times (T/298)^{-1.9}$ $F_C = 0.6$	−165	Shah et al., 2021	
G42	$ClHg^\bullet + HO_2^\bullet \overset{M}{\to} ClHgOOH$	$k_0 = 4.3 \times 10^{-30} \times (T/298)^{-5.9}$ $k_\infty = 6.9 \times 10^{-11} \times (T/298)^{-2.4}$ $F_C = 0.6$	−183	Shah et al., 2021	
G43	$ClHg^\bullet + O_3 \to ClHgO^\bullet + O_2$	$1.0 \times 10^{-10} \times (T/300)^{0.5}$	−151	Saiz-Lopez et al., 2022	
G44	$ClHgO^\bullet + CH_4 \to ClHgOH + CH_3^\bullet$	$1.5 \times 10^{-11} \times \exp(-1290/T)$	−23	Shah et al., 2021	
G45	$ClHgO^\bullet + CO \to ClHg^\bullet + CO_2$	$6.0 \times 10^{-11} \times \exp(-550/T)$	−275	(Shah et al., 2021)	
G46	$ClHgO^\bullet + HCl \to HgCl_2 + HO^\bullet$	$7.9 \times 10^{-11} \times (T/300)^{-0.916}$	−84	Saiz-Lopez et al., 2022	
G47	$ClHgOH + HCl \to HgCl_2 + H_2O$	$1.3 \times 10^{-12} \times (T/300)^{-1.6}$	−122	Saiz-Lopez et al., 2022	
G48	$ClHgO^\bullet \overset{hv}{\to} 0.673 \, HgO + 0.327 \, Hg + Cl^\bullet + 0.327 \, O$			Saiz-Lopez et al., 2022	Only significant in the stratosphere
G49	$HgCl_2 \overset{hv}{\to} 0.6 \, ClHg^\bullet + 1.4 \, Cl^\bullet + 0.4 \, Hg$			Saiz-Lopez et al., 2022	
G50	$ClHgOH \overset{hv}{\to} 0.063 \, HgOH + 0.969 \, Cl^\bullet + 0.906 \, Hg + 0.937 \, HO^\bullet + 0.031 \, ClHg^\bullet$	1.3×10^{-5}		Shah et al., 2021	
G51	$ClHgONO \overset{hv}{\to} 0.9 \, ClHgO^\bullet + 0.1 \, NO_2 + 0.9 \, NO + 0.1 \, ClHg^\bullet$	1.1×10^{-3}		Shah et al., 2021	
G52	$ClHgOOH \overset{hv}{\to} 0.31 \, ClHgOH + 0.66 \, Cl^\bullet + 0.66 \, Hg + 0.69 \, HO_2^\bullet + 0.03 \, ClHg^\bullet$	1.5×10^{-2}		Shah et al., 2021	
Hg^I & Hg^{II} HO$_x$ chemistry					
G53a	$HOHg^\bullet \overset{M}{\to} Hg + HO^\bullet$	$3.5 \times 10^{-9} \times \exp(-5269/T) \times [M]$	30 to 60	Saiz-Lopez et al., 2022	
G53b	$HOHg^\bullet \overset{hv}{\to} Hg + HO^\bullet$	1.6×10^{-2}		Saiz-Lopez et al., 2019	
G54	$HOHg^\bullet + Br \overset{M}{\to} BrHgOH$	3.0×10^{-11}	−306	Shah et al., 2021	
G55	$HOHg^\bullet + Cl \overset{M}{\to} ClHgOH$	3.0×10^{-11}	−273	Shah et al., 2021	
G56	$HOHg^\bullet + HO^\bullet \overset{M}{\to} Hg(OH)_2$	3.0×10^{-11}	−321	Shah et al., 2021	
G57	$HOHg^\bullet + NO_2 \overset{M}{\to} HOHgONO$	$k_0 = 3.69 \times 10^{-17} \times T^{-4.75}$ $k_\infty = 1.26 \times 10^{-5} \times T^{-2.04}$ $F_C = 0.6$	−189	Jiao and Dibble, 2017b	
G58	$HOHg^\bullet + HO_2 \overset{M}{\to} HOHgOOH$	$k_0 = 7.68 \times 10^{-19} \times T^{-4.25}$ $k_\infty = 1.24 \times 10^{-4} \times T^{-2.53}$ $F_C = 0.6$	−184	Jiao and Dibble, 2017b	

[8] Over the interval 333 K to 200 K.

[9] Estimated value from $CH_3O + NO$

[10] Estimated value from $CH_3O + NO_2$

[11] Valid for 395-573 K

G59	$HOHg^\bullet + O_3 \rightarrow HOHgO^\bullet + O_2$	$10^{-10} \times (T/300)^{0.17}$	-162[12]	Saiz-Lopez et al., 2022; Castro Pelaez et al., 2022	
G60	$HOHgO^\bullet + H_2O \rightarrow Hg(OH)_2 + HO^\bullet$	$5.3 \times 10^{-12} \times \exp(-2894/T)$	-26[13]	Saiz-Lopez et al., 2022	
G61	$HOHgO^\bullet + HO_2 \rightarrow Hg(OH)_2 + O_2$	$7.2 \times 10^{-11} \times (T/300)^{-0.436}$	-282	Saiz-Lopez et al., 2022	
G62	$HOHgO^\bullet + CH_4 \rightarrow Hg(OH)_2 + CH_3^\bullet$	$4.4 \times 10^{-12} \times \exp(-1650/T)$	-40	Saiz-Lopez et al., 2022	
G63	$HOHgO^\bullet + CO \rightarrow HOHg^\bullet + CO_2$	$6.0 \times 10^{-11} \times \exp(-550/T)$	-252	Edirappulige et al., 2023b	
G64	$HOHgO^\bullet + HCHO \rightarrow Hg(OH)_2 + CO + H^\bullet$	$\leq 4.7 \times 10^{-11}$	-109	Edirappulige et al., 2023b	
G65	$HOHgO^\bullet + NO \xrightarrow{M} HOHgONO$	2.9×10^{-11}[14]	-226	Edirappulige et al., 2023b	
G66	$HOHgO^\bullet + NO_2 \xrightarrow{M} HOHgONO_2$	1.7×10^{-11}[15]	-242	Edirappulige et al., 2023b	
G67	$Hg(OH)_2 + HCl \rightarrow HOHgCl + H_2O$	$1.5 \times 10^{-12} \times (T/300)^{-2.14}$	-125	Saiz-Lopez et al., 2022	
G68	$HOHgCl + HCl \rightarrow HgCl_2 + H_2O$	$1.3 \times 10^{-12} \times (T/300)^{-2.14}$	-122	Saiz-Lopez et al., 2022	
G69	$Hg(OH)_2 \xrightarrow{h\nu} 0.5\ HOHg^\bullet + 1.5\ HO^\bullet + 0.5\ Hg$			Saiz-Lopez et al., 2022	Only significant in the stratosphere
G70	$HOHgONO \xrightarrow{h\nu} HOHg^\bullet + NO_2$	1.1×10^{-3}		Shah et al., 2021	
G71a	$HgO \xrightarrow{M} Hg + O$	$8.4 \times 10^{-11} \times \exp(-3150/T) \times [M]$	27.6	Saiz-Lopez et al., 2022	
G71b	$HgO \xrightarrow{h\nu} Hg + O$	0.54		Francés-Monerris et al., 2020	
G72	$HgO + H_2O \xrightarrow{M} Hg(OH)_2$ $\rightarrow HOHg^\bullet + HO^\bullet$		-240[16] 40	Saiz-Lopez et al., 2022	
G73	$HgO + HCl \rightarrow ClHg^\bullet + HO^\bullet$	$7.1 \times 10^{-11} \times (T/300)^{-1.6}$	-61	Saiz-Lopez et al., 2022	
G74	$HgO + O_2 \rightarrow Hg + O_3$	$3.4 \times 10^{-13} \times \exp(-1993/T)$	-300	Saiz-Lopez et al., 2022	
Dimethylmercury chemistry					
G75	$CH_3HgCH_3 + Cl^\bullet$ $\rightarrow CH_3HgCl + CH_3^\bullet$ $\rightarrow CH_3HgCH_2^\bullet + HCl$ $\rightarrow CH_3Hg^\bullet + CH_3Cl \rightarrow CH_3^\bullet + Hg + CH_3Cl$	$(2.8 \pm 0.3) \times 10^{-10}$	-121 -21 -9	Niki et al., 1983b	
G76	$CH_3HgCH_3 + HO^\bullet$ $\rightarrow CH_3HgOH + CH_3^\bullet$ $\rightarrow CH_3HgCH_2^\bullet + H_2O$ $\rightarrow CH_3Hg^\bullet + CH_3OH \rightarrow CH_3^\bullet + Hg + CH_3OH$	$(2.0 \pm 0.2) \times 10^{-11}$	-39[17] -88 -177	Niki et al., 1983a	
G77	$CH_3HgCH_3 + NO_3^\bullet$ $\rightarrow CH_3HgONO_2 + CH_3^\bullet \rightarrow HgO + 2\ CH_3^\bullet + NO_2$ $\rightarrow CH_3HgCH_2^\bullet + HNO_3$ $\rightarrow CH_3Hg^\bullet + CH_3OH \rightarrow CH_3^\bullet + Hg + CH_3OH$	$3.2 \times 10^{-11} \times \exp((-1760 \pm 400)/T)$	-93 -98 -100	Sommar et al., 1996; Sommar et al., 1997	

Hg + X$^\bullet$ (X = Br, Cl, OH and I)

Besides bromine atoms (Br$^\bullet$), hydroxyl radicals (HO$^\bullet$) and, to lesser extent, chlorine (Cl$^\bullet$) and possibly iodine (I$^\bullet$) atoms have been
445 proposed to globally initiate the gas-phase oxidation of Hg^0 in the ground state in the atmosphere:

$$Hg + X^\bullet \xrightarrow{M} {}^\bullet Hg^I X \qquad\qquad (Rxn\ G1 - G3)$$

The reaction rate for X = Cl (**Rxn G2**, Donohoue et al., 2005; Taylor et al., 2005) and Br (**Rxn G1**, Donohoue et al., 2006) has been
determined by pulsed laser photolysis-laser induced fluorescence (PLP-LIF) for a range of pressures and temperatures. The reaction
is apparently termolecular, i.e. it shows a linear dependence on pressure (M), a slightly negative temperature dependence and a
450 significant difference in deactivation efficiency with N$_2$ and He as third bodies (Donohoue et al., 2005). There are also several
experimental static studies of the halogen atom reactions carried out at 1-atm pressure, which, with the exception of the studies by
Horne et al. (1968) and Greig et al. (1970), have used the relative rate (RR) technique at room temperature (Ariya et al., 2002; Spicer
et al., 2002; Sun et al., 2016; Guérette, 2011). The Hg + X$^\bullet$ rate expression determined absolutely by Donohoue et al. over 0.26 –
0.79 atm and 243 – 293 K by the preferred PLP-LIF technique gives a rate coefficient of 5.4 ×10^{-13} (Donohoue et al., 2005) and 3.6
455 × 10^{-13} (Donohoue et al., 2006) cm^3 molecule^{-1} s^{-1} at 298 K and 1-atm pressure in air for the Cl$^\bullet$- and Br$^\bullet$- reactions, respectively.
Although the rate constant of the chlorine atom reaction is at STP 50% greater than that of the bromine atom reaction, the significance
of the former is small in the remote troposphere, taking into account the low concentration of chlorine atoms. It should also be added
that a significant increase in the apparent recombination rate coefficient of Hg + Cl$^\bullet$ was observed in the presence of air. This result
has been rationalized on the basis that secondarily formed ClO$_x$ species may also react rapidly with Hg^0 (Donohoue, 2008). A
460 plausible candidate is Hg + ClO$_2 \rightarrow {}^\bullet Hg^I Cl + O_2$ (**Rxn G8**), which is exothermic ($\Delta H_R = -80$ kJ mol^{-1}), but the channel has not been
investigated further. Byun et al. (2010) studied the Hg + ClO$_x$ gas phase system experimentally at 130 °C. Their results in favor of a

---

[12] Based on calculation on exit-channel complexes at SC-NEVPT2 level of theory

[13] Based on $\Delta_f H^0$(HOHgO$^\bullet$) = 63.2 kJ mol^{-1}

[14] Estimated value from CH$_3$O + NO

[15] Estimated value from CH$_3$O + NO$_2$

[16] refers to *singlet* Hg(OH)$_2$, but is 10 kJ mol^{-1} endothermic for formation of spin-conserving *triplet* Hg(OH)$_2$

[17] Assuming $\Delta_f H^0$(CH$_3$HgCl) = $\Delta_f H^0$(CH$_3$HgOH)

rapid reaction between Hg + ClO$^\bullet$ → products at 1.1 ×10^{-11} cm^3 molecule $^{-1}$ s^{-1} are surprising, but they also report Hg + Cl$^\bullet$ → products at 1.2 ×10^{-10} cm^3 molecule^{-1} s^{-1} and Hg + Cl$_2$ → products at 4.3 ×10^{-15} cm^3 molecule^{-1} s^{-1}, which may indicate that the results are strongly affected by surface reactions. Computational studies (Shepler et al., 2007; Goodsite et al., 2004; Goodsite et al.,

465 2012) gave a slightly larger rate constant (~10^{-12} cm^3 molecule^{-1} s^{-1}) for the Hg + Br$^\bullet$ reaction than the absolute PLP-LIF determination at STP. On the other hand, the experimental RR studies generally give rate constants that exceed the limit obtained from theoretical calculations, suggesting complex kinetics including reactions at the reactor wall.

The reaction with X = OH (**Rxn G3**) was studied with PLP-LIF using an excess of Hg^0 over $^\bullet$OH (generated from photolysis of HNO$_3$ at 266 nm) without evidence for a reaction, giving an upper rate limit of (<) 1.2 × 10^{-13} cm^3 molecule^{-1} s^{-1} (Bauer et al., 2003).

470 The rate constant of Hg + $^\bullet$OH → products determined by Sommar et al. (2001) relative to cyclohexane + $^\bullet$OH → products of 8.7 × 10^{-14} cm^3 molecule^{-1} s^{-1} falls below this limit at 295 K and 1 atm air, as does the temperature-resolved RR study of Pal and Ariya (2004a) extrapolated to 295 K (~1 × 10^{-13} cm^3 molecule^{-1} s^{-1}). External re-analysis of the Pal and Ariya (Calvert and Lindberg, 2005) and Sommar et al. (Dibble et al., 2020) data using kinetic modeling has shown that the fate of $^\bullet$Hg^{I}OH under their experimental conditions is exclusively reaction with NO$_2$ ($^\bullet$Hg^{I}OH + NO$_2$ → HOHg^{II}ONO, **Rxn G59**) rather than dissociation. The time resolution

475 in the PLP-LIF study also allowed a lower bound estimate of the equilibrium constant K$_{\bullet HgOH}$ = [$^\bullet$HgOH]/([Hg][HO$^\bullet$]) of 5 ×10^{-16} cm^3 molecule^{-1} (Bauer et al., 2003). This equilibrium constant has also been modeled by computational studies. A recent one using high-level quantum chemical calculations (Dibble et al., 2020), performed at 200 – 320 K yields a K$_{\bullet HgOH}$ of ~7 ×10^{-16} cm^3 molecule^{-1} at 298 K corresponding to a k$_{13}$ of 9.5 × 10^{-14} cm^3 molecule^{-1} s^{-1} at 1 atm. In contrast, Saiz-Lopez et al. (2022) arrive at a K$_{\bullet HgOH}$ more than an order of magnitude smaller (~5 ×10^{-17} cm^3 molecule^{-1}) at the corresponding temperature.

480 The kinetics of the reaction between Hg^0 and iodine atoms (by photolysis of CH$_2$I$_2$/CF$_3$I) was studied in an early work by monitoring $^\bullet$Hg^{I}I by absorption spectroscopy at 403 – 438 K (Greig et al., 1971), and in a later study by following the Hg^0 loss by MS at 296 K (Raofie et al., 2008). In the first study, sufficiently high $^\bullet$Hg^{I}I densities could not be generated to gauge a reaction, for which the rate constant is lower than that of the competing I$^\bullet$ + I$^\bullet$ $\overset{M}{\rightarrow}$ I$_2$ reaction of ~1 × 10^{-13} cm^3 molecule^{-1} s^{-1}. The latter study lacks conclusive results on Hg + I$^\bullet$ $\overset{M}{\rightarrow}$ $^\bullet$Hg^{I}I reaction but provides a limit on the rate constant for the reaction of Hg with molecular iodine vapor (≤ 1.3

485 × 10^{-19} cm^3 molecule^{-1} s^{-1}), a reaction that lacks any atmospheric significance. A rate coefficient of 4.0 × 10^{-13} (T/298)$^{-2.38}$ cm^3 molecule^{-1} s^{-1} was calculated for Hg + I$^\bullet$ $\overset{M}{\rightarrow}$ $^\bullet$Hg^{I}I reaction at 1 atm N$_2$ and T between 180 and 400 K using Rice-Ramsperger-Kassel-Markus (RRKM) theory, based on a calculated binding energy (46 kJ mol^{-1}) and molecular properties of $^\bullet$HgI($^2\sum$) (Goodsite et al., 2004).

5.1.2 Stability of $^\bullet$Hg^{I}X

The first step (termolecular reactions **G1 – G3**), which is exothermic, produces Hg^I radical intermediates ($^\bullet$Hg^{I}X), which can revert

490 to Hg^0 both thermally and photolytically:

$$^\bullet Hg^I X \underset{\overset{\rightarrow}{hv}}{\overset{\Delta}{\rightarrow}} Hg + X^\bullet \qquad\qquad\qquad (\text{Rxn G14a,b/G37a,b/G53a,b})$$

Photo- and thermal dissociation

The first excited electronic state of $^\bullet$Hg^{I}X (designated A$^2\Pi$ for halogenated radicals) is exclusively repulsive, resulting in dissociation with visible light for wavelengths exceeding ~460 nm, where the absorption maxima are predicted at ~480, ~575, ~650, and ~690

495 nm for $^\bullet$Hg^{I}OH, $^\bullet$Hg^{I}Cl, $^\bullet$Hg^{I}Br, and $^\bullet$Hg^{I}I, respectively (Saiz-Lopez et al., 2019; **Fig. 3**). While the bond strengths of Hg–Cl and Hg–Br are well-defined in relative terms (89.5 – 98.0 kJ mol^{-1}, Tellinghuisen et al., 1982; Shepler et al., 2005; Saiz-Lopez et al., 2022; Cremer et al., 2008 and 60.2 – 68.1 kJ mol^{-1}, Goodsite et al., 2004; Shepler et al., 2005; Cremer et al., 2008; Tellinghuisen and Ashmore, 1983, respectively), there is significant variation in the estimates of the bond strengths of $^\bullet$Hg^{I}I and $^\bullet$Hg^{I}OH, ranging from ~33 to 46 kJ mol^{-1} (Goodsite et al., 2004; Shepler et al., 2005; Cremer et al., 2008; Jordan et al., 1993; Salter et al., 1986) and ~23

500 to 55 kJ mol^{-1} (Dibble et al., 2020; Tossell, 2003; Goodsite et al., 2012; Guzman and Bozzelli, 2019; Cremer et al., 2008), respectively. Therefore, the stability of $^\bullet$Hg^{I}OH and $^\bullet$Hg^{I}I is uncertain, and it is debatable whether their thermal lifetimes in the atmosphere are long enough for these radicals to be further oxidized to mercuric species to any significant degree. The question has been raised recently since it was experimentally established that $^\bullet$Hg^{I}Br is kinetically oxidized by O$_3$ without a reaction barrier (**Rxn**

G22), which was also theoretically established to be true at least for •Hg^{I}Cl and •Hg^{I}OH (**Rxn G44 & G59**, respectively, **Section**

505 **5.1.3**). A study using RRKM theory suggests that the recombination rate coefficients of Hg with I• and HO• are similar in the free troposphere, while the thermal dissociation of •Hg^{I}I gradually exceeds that of •Hg^{I}OH at lower temperatures (Goodsite et al., 2004). •Hg^{I}I is the •Hg^{I}X species with the shortest photolytic lifetime in the troposphere globally (~17 s), according to computational chemistry theory (Saiz-Lopez et al., 2019). Recently, Dibble et al. estimated the HO–Hg binding energy to be 46 kJ mol^{-1} using high-level quantum chemical calculations (Dibble et al., 2020). Compared to a global photolytic lifetime of just over one minute (Shah et

510 al., 2021), the thermal lifetime of •Hg^{I}OH in the lower troposphere is significantly shorter (according to data from Dibble et al., 2020 ~10 ms at the surface up to about ten seconds at the tropopause). For the lighter mercurous halides (i.e., excluding •Hg^{I}I), the relationship is reversed with respect to the importance of photolytic versus thermal dissociation. The lifetime of the former channel is globally ~20 and ~40 s for •Hg^{I}Br and •Hg^{I}Cl, respectively, while the thermal decay is slower for •Hg^{I}Br above the planetary boundary layer and •Hg^{I}Cl is much less thermally unstable.

515
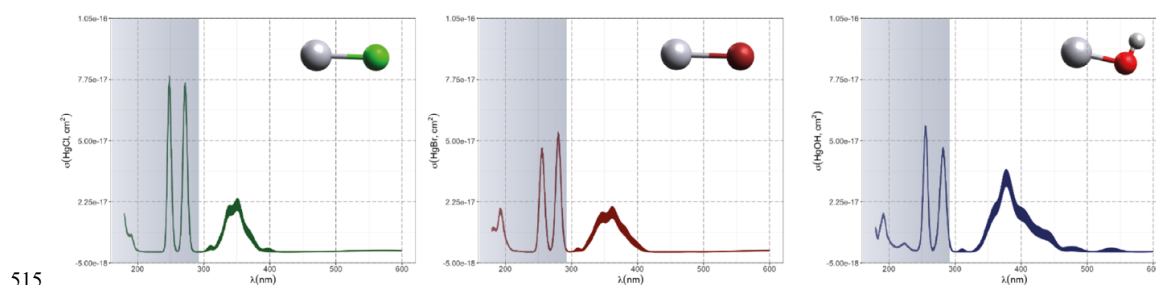
Figure 3. Computed absorption spectra of the atmospherically important mercurous chloride, bromide, and hydroxyl radicals. Wavelengths accessible in the troposphere are to the right of the colored area. Data from Saiz-Lopez et al. (2019).

5.1.3 Bimolecular reactions of •Hg^{I}X

In addition to thermal and photolytic decomposition, the fate of •Hg^{I}X in the atmosphere is controlled by further oxidation to

520 thermally stable mercuric species molecules. Experimental studies of specific bimolecular reaction kinetics of •Hg^{I}X are limited to X = Br and Cl (**Rxn G15 & G39**). Taylor et al. (2005) studied the reaction of •Hg^{I}Cl with Cl$_2$, HCl and Cl• at temperatures characteristic of post-combustion conditions. The observed reaction with free chlorine to form HgCl$_2$ was rapid (1.2×10^{-11} cm^3 molecule^{-1} s^{-1}) and temperature independent. Jiao and Dibble (2017b) determined the rate constant and product yield for the reactions of •Hg^{I}Br with abundant atmospheric NO$_2$ (**Rxn G20**) and HOO (**Rxn G21**) radicals using computational chemistry. Analogous to

525 the experimental •Hg^{I}Cl study, these reactions were calculated to be rapid with the rate constant for oxidation by NO$_2$ being approximately twice that for oxidation by HOO•. This theoretical study indicated that the •Hg^{I}Br + NO$_2$ reaction occurs along two competing channels (**Rxn G20a, b**), one proceeding by oxidative addition resulting in BrHg^{II}ONO and another operating by reductive displacement resulting in Hg^0 + BrNO$_2$. The dichotomy occurs depending on the fact that •Hg^{I}Br ($^2\Sigma^+$) possesses a delocalized electron that spreads more equivalent spin density over the molecule (•Hg^{I}Br ↔ Hg^{I}Br•), whereas the spin density of HgOH (^{1}A')

530 radical is most localized on the Hg atom. Reaction with another radical center occurs for •Hg^{I}OH when the reactant is oriented towards Hg, leading to addition, while for HgBr reductive displacement is also possible when the collision involves the Br atom (Castro Pelaez et al., 2022). The existence of a branching ratio was also confirmed by an experimental study of •Hg^{I}Br + NO$_2$ reaction by Wu et al. (2020) using PLP-LIF, who found that the computed rate coefficients for both reduction and oxidation were greatly overestimated. This study deduced that the importance of the reductive channel increases slowly with altitude from ground level to

535 the tropopause but is only ~10% as fast as the oxidation reaction. Wu et al. (2022) have also experimentally studied the interaction between NO and •Hg^{I}Br, leading to Hg^0 + BrNO. •Hg^{I}Br + O$_2$ → BrHg^{II}OO• (**Rxn G19**) is slightly exothermic while that leading to Hg^0 + BrOO• is less feasible due to endothermicity. •Hg^{I}Br + O$_2$ reaction is thus described by •Hg^{I}Br + O$_2$ ⇌ BrHg^{II}OO• with an equilibrium constant that decreases dramatically with temperature (Wu et al., 2022). To the extent that BrHg^{II}OO• can be attributed significance, it is a reservoir for •Hg^{I}Br at low temperatures, with an upper limit of ~50% stored at 220 K. Wu et al. (2022) argued

540 that $BrHg^{II}OO^\bullet$ behaves like a peroxyl radical ($HOO^\bullet/ROO^\bullet$) in reactions with atmospheric radicals. Recently, Saiz-Lopez et al. (2020) implied missing oxidation pathways to better reconcile their GEOS-Chem global atmospheric chemistry model simulations with field observations. Suggested by Shepler (2006) och later Lam (2019) as a potential pathway of Hg^I oxidation, the Saiz-Lopez group has carried out theoretical (Saiz-Lopez et al., 2020) and experimental (Gómez Martín et al., 2022) investigations of the system $^\bullet Hg^I Br + O_3$. In addition, Castro Palaez et al. (2022) have carried out theoretical calculations for rate constants and product yields,

545 including $^\bullet Hg^I OH + O_3$. $^\bullet Hg^I X + O_3 \rightarrow XHg^{II}O^\bullet + O_2$ (**Rxn G22a, G43** and **G59**) is highly exothermic (172 kJ mol⁻¹ for X = Br) and proceeds without a substantial activation barrier and is currently considered to be of great importance for the atmospheric oxidation of $^\bullet Hg^I X$, with $XHg^{II}O^\bullet$ as a key intermediate. Being a radical, $XHg^{II}O^\bullet$ is relatively thermally stable with a strong Hg-O bond (333 and 294 kJ mol⁻¹ for X = Cl & Br, respectively, Balabanov and Peterson, 2003). Gómez Martin et al. (2022) determined the rate coefficient of the $^\bullet Hg^I Br + O_3$ reaction at 295 K using a PLP-LIF system. To generate $^\bullet Hg^I Br$ (photolysis of $HgBr_2$ at 248

550 nm by a KrF excimer laser), it was inevitable that the introduced O_3 would be photolyzed to some extent before it could react with $^\bullet Hg^I Br$. This led to complications due to the following potential chemistry:

$$^\bullet Hg^I Br + O_3 \rightarrow BrHg^{II}O^\bullet + O_2 \qquad\qquad (\text{Rxn G22a})$$

$$^\bullet Hg^I Br + O(^3P) \begin{array}{l} \rightarrow BrHg^{II}O^\bullet \\ \rightarrow Hg^0 + BrO^\bullet \end{array} \qquad\qquad (\text{Rxn G23})$$

$$BrHg^{II}O^\bullet + O(^3P) \rightarrow {}^\bullet Hg^I Br + O_2 \qquad\qquad (\text{Rxn G24})$$

555 $$BrHg^{II}O^\bullet + O_3 \begin{array}{l} \rightarrow {}^\bullet Hg^I Br + O_2 + O_2 \\ \rightarrow BrHg^{II}OO^\bullet + O_2 \end{array} \qquad\qquad (\text{Rxn G25})$$
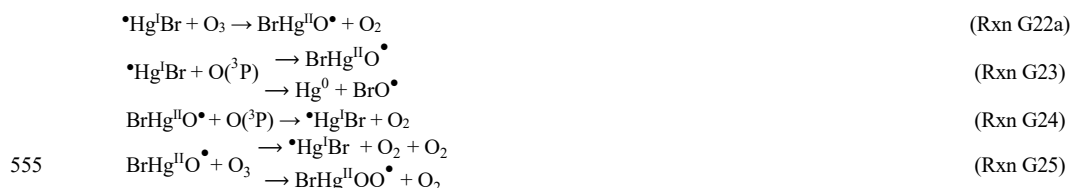
By performing experiments at different KrF laser energies and the ozone concentrations and by numerical modeling of the data, Gómez Martin et al. isolated k($^\bullet HgBr + O_3$), k($^\bullet HgBr + O$) and k($BrHgO^\bullet + O$) as 7.5, 5.3 and 9.1 (all × 10⁻¹¹ cm³ molecule⁻¹ s⁻¹), respectively. They presented an upper limit for $BrHg^{II}O^\bullet + O_3$ (k < 5 × 10⁻¹² cm³ molecule⁻¹ s⁻¹), which, however, was considered obsolete by theoretical calculations as sterically hindered. Instead of leading primarily to $BrHg^{II}O^\bullet$ as is the case for the $^\bullet Hg^I Br + O_3$

560 reaction, $^\bullet Hg^I Br + O$ results in reductive elimination ($Hg^0 + BrO^\bullet$) for all collision geometries. Hg^0 is also produced in the rapid reaction between $BrHg^{II}O^\bullet + O$. In the lower atmosphere (≤ 25 km), the content of free O atoms is low, and therefore, its role as an oxidant is minor (Calvert et al., 2015). The energetic $O(^1D)$, formed primarily by photolysis of O_3 by UV light (< 340 nm), is rapidly consumed through two competitive channels: deactivation to $O(^3P)$ by collision with air molecules or reaction with the ubiquitous water vapor to form OH radicals. $O(^3P)$, also formed by photolysis of NO_2 (< 430 nm), reacts rapidly thermally with O_2 in the

565 atmosphere to form ozone (Calvert et al., 2015). It is important to note that k($^\bullet HgBr + O_3$) is more than twice as fast as k($^\bullet HgBr + NO_2$) when the experimental results are extrapolated to the atmospheric surface layer (1 atm, 295 K). The combination of a high k($^\bullet HgBr + O_3$) and the abundance of ozone relative to other radicals such as NO_2 and HOO suggests that $^\bullet Hg^I Br + O_3$ is of ultimate significance in the conversion of Hg^I to Hg^{II} in the atmosphere. The experimentally determined k($^\bullet HgBr + O_3$) is close to the upper limit of 1 × 10⁻¹⁰ cm³ molecule⁻¹ s⁻¹ estimated by Saiz-Lopez et al. (2020), which excludes steric effects. For an updated chemical

570 mechanism in the global atmospheric model GEOS-Chem, Shah et al. (2021) used a conservative rate constant of 3 × 10⁻¹¹ cm³ molecule⁻¹ s⁻¹ for oxidation of $^\bullet Hg^I X$ with O_3 (X = Cl, Br and OH). By postulating k($^\bullet HgOH + O_3$) = k($^\bullet HgBr + O_3$), simulations by Shah et al. (2021) showed that the OH-initiated pathway accounts for one-third of the global Hg^{II} production. In contrast, by not including $^\bullet Hg^I OH + O_3$ in their model, Dibble et al. (2020) found the OH-initiated channel to be largely irrelevant, with only some regional significance in areas with high levels of photochemical smog. More recently, however, they (Castro Pelaez et al., 2022)

575 compared $^\bullet Hg^I Br + O_3$ and $^\bullet Hg^I OH + O_3$ systems by computational chemistry and found that the former has a slight tendency (≤ 0.1%) to undergo reductive elimination ($Hg + BrO^\bullet + O_2$) rather than oxidation ($BrHg^{II}O^\bullet + O_2$) when the orientation of the terminal oxygen in ozone is towards the Br atom. There is no such tendency for $^\bullet Hg^I OH + O_3$. It was also found that k($^\bullet HgBr + O_3$) and k($^\bullet HgOH + O_3$) are likely to be similar with a computational value for the latter at 298 K in the range (6.6 - 8.5) x 10⁻¹¹ cm³ molecule⁻¹ s⁻¹. The positive covariation of O_3 and $^\bullet OH$, as opposed to $^\bullet Br$ and O_3 (O_3 titrates $^\bullet Br$, **Fig. 2**), suggests precedence for the OH-

580 initiated Hg oxidation in air with secondary pollutants (Rutter et al., 2012). Field observations of speciated Hg in urban air speculate

radical-initiated $Hg^0 \rightarrow Hg^{II}$ gas-phase transformation, which is claimed to be completed by certain radicals (Peleg et al., 2015; Hong et al., 2016). An interesting case is urban Jerusalem with episodes of elevated daytime and nighttime gaseous Hg^{II} levels co-varying with O_3 (max 250 $\mu g\ m^{-3}$) and NO_3 (430 $ng\ m^{-3}$), respectively (Peleg et al., 2015). To the east of the city lies the Dead Sea basin, where effective bromine-controlled oxidation of Hg^0 has been observed (Tas et al., 2012). Finally, in discussing the reactivity of

585 $^\bullet Hg^I X$, it can be concluded that it is low viz-á-viz volatile organic compounds in that the species neither abstracts H atoms (e.g. from CH_4) nor adds significantly to double bonds ($C = C$) (Dibble and Schwid, 2016).

5.1.4 Stability of $Hg^{II}XY$

Photoreduction and stoichiometric yields

Atmospheric Hg^{II} species are more stable than Hg^I species. Not all Hg^{II} molecules are stable, but the atmospheric pool contains mercury

590 species with different thermal and photolytic stability. Most of the atmospherically relevant gas-phase species have well-defined absorption bands in deep UV, in some cases extending into the UV-B and UV-A regions. Early theoretical studies (Strömberg et al., 1989; Strömberg et al., 1991), at a time when knowledge of the atmospheric chemistry of Hg was rudimentary, indicate that the photoreduction of $HgCl_2$ and $Hg(CN)_2$ in actinic light at the Earth's surface is negligible, while that of $Hg(OH)_2$ and $Hg(SH)_2$ is extremely slow. The UV absorption spectra for mercuric halides become increasingly red-shifted as the halogen becomes heavier. $HgCl_2$ vapor absorbs only radiation below

595 240 nm (**Fig. 8a**), $HgBr_2$ absorbs mainly in the deep UV with a tiny tail ($< 10^{-19}\ cm^2$ molecule^{-1}, **Fig. 8c**) into UV-B, while HgI_2 has a significant absorption in the entire UV region (Maya, 1977; Sitkiewicz et al., 2019). However, binary compounds such as $HgBr_2$ or $HgCl_2$ do not completely dominate the atmospheric $Hg^{II}(g)$ speciation. Mixed compounds such as $BrHg^{II}Y$ (Y= ONO, OOH, OH, OCl, OBr etc.) and $XHg^{II}O^\bullet$ (X = Br, OH) are also predicted to be important. Saiz-Lopez et al. (2018) computed the absorption spectra of mixed compounds and found that abundant $BrHg^{II}Y$ molecules absorb in UV-B. The rapidly photolyzed Hg^{II} species identified include

600 BrHgONO (**Rxn G35**), BrHgOOH (**Rxn G36**) and BrHgOBr (with lifetimes of a few min. to less than a second, **Fig. 4a-c**), with BrHgOH being comparatively long-lived (> 1 day, **Fig. 4d**) in terms of photodissociation. $HgCl_2$ and $Hg(OH)_2$ were estimated to be photolytically stable in the troposphere by Shah et al. (2021) in their modeling study, while the photolysis frequency of $HgBr_2$ was calculated to be just over an order of magnitude lower than that of BrHgOH (1.2×10^{-6} and $1.3 \times 10^{-5}\ s^{-1}$, respectively).
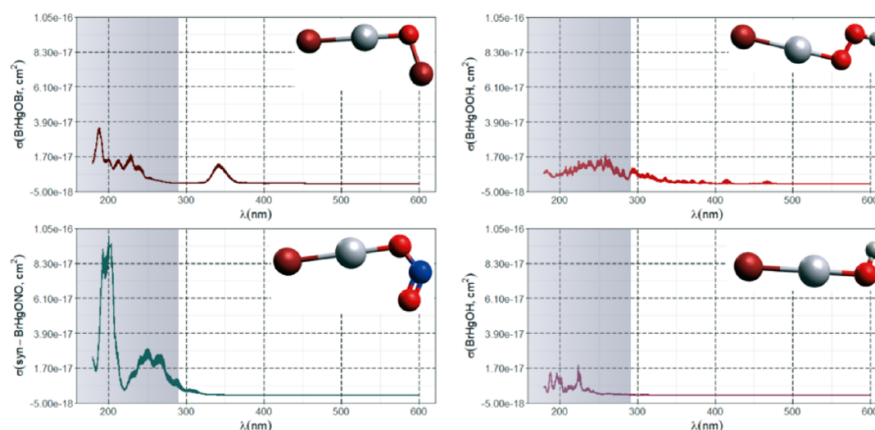
605 **Figure 4.** Computed absorption spectra of the atmospherically important (a) BrHgOBr, (b) BrHgOOH, (c) syn-BrHgONO and (d) BrHgOH. Wavelengths accessible in the troposphere are to the right of the colored area (Francés-Monerris et al., 2020).

The photodissociation mechanism (quantum and product yield) of $BrHg^{II}Y$ has been studied using computer-assisted theoretical calculations, with the result that photodynamics leads to different channels in which the Hg-containing products can exhibit +II, +I and 0 oxidation states (Francés-Monerris et al., 2020; Lam et al., 2019b). Photolysis of $BrHg^{II}ONO$, forms NO_2 and $BrHg^{II}O^\bullet$ in

610 90% of cases, while the remainder reverts to $^\bullet Hg^I Br$ and NO_2 (Francés-Monerris et al., 2020). Consistently, a large dominance of the photoproducts $BrHg^{II}O^\bullet$ + NO was predicted by calculations of Lam et al. (2019b), in contrast to an early work by Saiz-Lopéz et al. (2018) that favors $^\bullet Hg^I Br$ and Hg^0 formation. During the photolysis of $BrHg^{II}OOH$, the Hg-Br, Hg-O and O–O bonds can be broken,

resulting in three main exit channels:

$$BrHg^{II}OOH \xrightarrow{h\nu} \begin{array}{l} Hg + Br + {}^\bullet OOH \ (66\%) \\ BrHg^{II}O^\bullet + {}^\bullet OH \ (31\%) \\ {}^\bullet Hg^I Br + O{\sim}O{\sim}H \ (2\%) \end{array} \qquad\qquad \text{(Rxn G36)}$$

615 Thus, the photodissociation of BrHg^{II}OOH produces Hg^0, $^\bullet$Hg^{I}Br and BrHg^{II}O$^\bullet$ to varying degrees (Francés-Monerris et al., 2020). In the case of BrHg^{II}OH, the photolytic formation of BrHg^{II}O$^\bullet$ is negligible, while in half of the cases (49%), reduction to elemental Hg occurs, and in the other half, $^\bullet$Hg^{I}Br or $^\bullet$Hg^{I}OH is formed, with the former being predominant (~70%) (Francés-Monerris et al., 2020). Photolysis of BrHg^{II}ONO and BrHg^{II}OOH thus results in significant yields of BrHg^{II}O$^\bullet$, the radical form of Hg^{II} described above as the major product of the rapid reaction between $^\bullet$Hg^{I}Br and O$_3$. In this series of reported compositional chemical results, it

620 should be noted that the only YHg^{II}O$^\bullet$ species that has been experimentally characterized is the fluorine analog that is formed along with FOHg^{II}F when excited Hg atoms react with OF$_2$ (Andrews et al., 2012). Although FHg^{II}O$^\bullet$ has no atmospheric significance, its experimentally determined properties are important as a benchmark for other homologs in the series. YHg^{II}O$^\bullet$ has two strong bonds (the dissociation energy for YHg-O is ~250 kJ mol^{-1}) and is thermally stable in gas phase. However, YHg^{II}O$^\bullet$ is photolabile in UV-VIS (cf. **Fig. 5**) and decompose photolytically along two channels. The calculated branching ratio for both Y = Cl and Br is in favor

625 of the formation of HgO (67% and 56%, respectively, Saiz-Lopez et al., 2022) over a splitting into atoms, as shown below:

$$YHg^{II}O^\bullet \xrightarrow{h\nu} \begin{array}{l} HgO + Y^\bullet \ (56\%) \\ Hg + O + Y^\bullet \ (44\%) \end{array} \qquad\qquad \text{(Rxn G31 \& G48)}$$

For HOHg^{II}O$^\bullet$, there are no stoichiometric calculations for the photoproducts. The main product generated, HgO with a $^3\Pi$ ground state, as a monomer in the gas phase (Sun et al., 2022), possesses a weak Hg-O bond of disputed magnitude (15 –30 kJ mol^{-1}, Tossell, 2006; Balabanov and Peterson, 2003; Cremer et al., 2008; Filatov and Cremer, 2004; Shepler and Peterson, 2003; Peterson et al.,

630 2007), which is only ≤ 10% as strong as in YHg^{II}O$^\bullet$. HgO can be reduced to Hg^0 by reaction with O$_2$ and by thermal- and photo-dissociation:

$$HgO \xrightarrow{M} Hg + O \qquad\qquad \text{(Rxn G71a)}$$
$$HgO \xrightarrow{h\nu} Hg + O \qquad\qquad \text{(Rxn G71b)}$$
$$HgO + O_2 \rightarrow Hg + O_3 \qquad\qquad \text{(Rxn G74)}$$

635 The HgO + O$_2$ reaction is exothermic but is subject to a barrier which, using transition state theory, gives a rate coefficient of 3.4 × 10^{-13} exp (−1993/T) cm^3 molecule^{-1} s^{-1} (Saiz-Lopez et al., 2022). The enthalpy of thermal decay of HgO is weakly endothermic and therefore favored by high temperature with a dependence of 8.4 × 10^{-11} exp (−3150/T) cm^3 molecule^{-1} s^{-1} calculated by RRKM theory (Saiz-Lopez et al., 2022). In addition, HgO is more photolabile than $^\bullet$Hg^{I}OH, with a calculated global annual mean J(HgO) of 0.54 s^{-1} for the troposphere (Saiz-Lopez et al., 2018, absorption spectrum in **Fig. 5a**). Taken together, this information indicates that gas-

640 phase HgO is highly unstable in the troposphere, but that the thermal lifetime is extended at cryogenic conditions (T < 250 K) in the
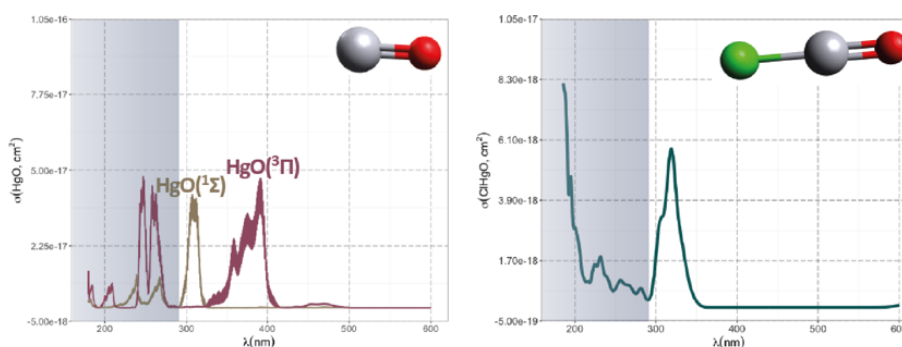
Figure 5. Computed absorption spectra of (a) HgO (low lying $^3\Pi$ and $^1\Sigma$ states) and (b) ClHgO radical (Saiz-Lopez et al., 2018; Saiz-Lopez et al., 2022). Wavelengths accessible in the troposphere are to the right of the colored area.

stratosphere where HgO has more abundant sources than that controlled by Hg^{II} radical species photolysis (see below). Analogous to the photolysis of Hg^{I} compounds, the quantum yield for the photo-dissociation of Hg^{II} compounds is assumed to be at unity.

645 **Thermochemistry of $YHg^{II}O^\bullet$**

Experimental data on the kinetics and mechanisms of the atmospheric chemistry of $YHg^{II}O^\bullet$ are marginal (the reaction $BrHg^{II}O^\bullet$ + O_3 to $^\bullet Hg^I Br$ and O_2 has been described above, Gómez Martín et al., 2022). The computational calculations focus on $BrHg^{II}O^\bullet$. Dibble and colleagues (Lam et al., 2019b; Khiri et al., 2020; Lam et al., 2019a) have concluded that the bimolecular reaction with CH_4 is of primary importance for the disappearance of $BrHg^{II}O^\bullet$: $BrHg^{II}O^\bullet$ + $CH_4 \rightarrow BrHg^{II}OH$ + $^\bullet CH_3$ (**Rxn G26**). Unlike $^\bullet Hg^I X$,

650 $BrHg^{II}O^\bullet$ readily abstracts hydrogen atoms from saturated hydrocarbons, overcoming a modest energy barrier with a rate expression of $4.1 \times 10^{-12} \times \exp(-856/T)$ cm^3 molecule^{-1} s^{-1} for $BrHg^{II}O^\bullet$ + CH_4. Computational modeling suggests that $BrHg^{II}O^\bullet$ mimics the OH radical in terms of reaction selectivity. In addition to that $BrHg^{II}O^\bullet$ abstracts H from aliphatic hydrocarbons, it adds to unsaturated bonds of olefins (such as the biogenic isoprene), NO (**Rxn G29**) and NO_2 (**Rxn G30**) and interacts with CO (**Rxn G27**). The addition of NO produces $BrHg^{II}ONO$ is susceptible to photolytic decomposition to predominantly $BrHg^{II}O^\bullet$, while the addition of NO_2

655 promptly produces peroxynitrites of $BrHg^{II}OONO$ type which are likely to be isomerized to $BrHg^{II}ONO_2$. Whether bromomercuric nitrate is photolabile in the troposphere is not yet known. Another source of $BrHg^{II}OH$ is the reaction of $BrHg^{II}O^\bullet$ with aldehydes (e.g. HCHO, **Rxn G28**). The pathway for the $BrHg^{II}O^\bullet$ + HCHO reaction bifurcates into two processes leading to different products (Khiri et al., 2020). The dominant reaction is H-abstraction leading to $BrHg^{II}OH$ and a formyl radical. The alternative route involves the addition of the oxygen atom in $BrHg^{II}O^\bullet$ to the carbon center in HCHO to form a methoxy radical, which eliminates a hydrogen

660 atom unimolecularly or in the presence of O_2 to form a formate salt ($BrHg^{II}OCHO$). Secondary chemistry initiated by O_2 after the addition of $BrHg^{II}O^\bullet$ to a carbon double bond (such as in ethene) also involves alkoxy radicals formed after titration of the primarily formed peroxyl radical by NO. The atmospheric fate of these mercuric alkoxy and alkyl peroxyl radicals (with one Hg–O bond) is similar to the general characteristics of organic oxidation in the atmosphere described in detail elsewhere (Finlayson-Pitts and Pitts, 2000). However, apart from the CH_4 reaction, the interaction between $BrHg^{II}O^\bullet$ and VOCs is considered limited in the atmosphere.

665 By analogy with $^\bullet OH$ + CO, the reaction between $BrHg^{II}O^\bullet$ and CO is not a simple bimolecular reaction. However, the intermediate BrHgOCO is much less stable than HOCO with respect to the release of CO_2. The very weakly bound BrHgOCO promptly dissociates in $^\bullet Hg^I Br$ + CO_2 (Khiri et al., 2020). The above reaction is highly exothermic (> 280 kJ mol^{-1}), and therefore, the product $^\bullet Hg^I Br$ can be chemically activated to the extent that it increasingly decomposes in atoms. The importance of this Hg reduction channel has been identified as difficult to constrain theoretically, as the shape of the potential energy surface is unfavorable for the

670 application of standard kinetic simulation methods. Nevertheless, by using an inverse Laplace transformation method, Khiri et al. (2020) calculated the range for the rate coefficient at two temperatures: $(9.4-52) \times 10^{-12}$ cm^3 molecule^{-1} s^{-1} at 298 K and $(3.8-29) \times 10^{-12}$ cm^3 molecule^{-1} s^{-1} at 220 K. These data are the basis for the current inclusion of the reaction $YBr^{II}O^\bullet$ + CO $\rightarrow ^\bullet Hg^I Y$ + CO_2 in chemical models (Shah et al., 2021; Saiz-Lopez et al., 2022) with the averaged expression of $6.0 \times 10^{-11} \times \exp(-550/T)$ cm^3 molecule^{-1} s^{-1}. With this numerical characterization, the $YHg^{II}O^\bullet$ + CO reaction becomes profoundly important when implemented

675 in simulations, as it largely counteracts the effect of the $^\bullet Hg^I X$ + O_3 reaction, thereby extending the predicted lifetime of Hg^0 in the troposphere. However, other candidates have emerged that, like CH_4, may react with $HOHg^{II}O^\bullet$ to directly form very stable $Hg(OH)_2$ molecule, namely water vapor. The reaction $HOHg^{II}O^\bullet$ + $H_2O \rightarrow Hg(OH)_2$ + $^\bullet OH$ (**Rxn G60**) is nearly thermoneutral due to the stability of $Hg(OH)_2$ ($\Delta H_f = -226$ kJ mol^{-1}, Wang and Andrews, 2005) and Saiz-Lopes et al. (2022) give the temperature dependent rate constant expression of $5.3 \times 10^{-12} \times \exp(-2894/T)$ cm^3 molecule^{-1} s^{-1} without further details. Since both the calculated $HOHg^{II}O^\bullet$

680 + H_2O rate coefficient and the $H_2O(g)$ mixing ratio vary considerably across the troposphere, the $HOHg^{II}O^\bullet$ loss due to this channel may largely exceed or fall below the more monotonic rate of hydrogen abstraction by $HOHg^{II}O^\bullet$ from CH_4, depending on the circumstances. The fate of $HOHg^{II}O^\bullet$ is thus influenced by several exit channels (Edirappulige et al., 2023b), none of which have been investigated experimentally and especially the uncertainty of the CO and H_2O reaction makes it difficult to determine the importance of the OH-initiated oxidation to the atmospheric Hg^{II} pool.

685 **Gas to nucleation**

Oxidized Hg species have properties that make them suitable for nucleation processes, such as being ionic solids at equilibrium under atmospheric conditions, which makes them improbable to evaporate from nucleating clusters (Ariya et al., 2015). They can condense, either homogeneously or onto pre-existing nuclei of subcritical or critical size. A particle formation event associated with polar spring partial AMDE has been observed in the East Antarctic pack ice, where 3 nm particle formation lags the phase of gaseous Hg^0 loss in

690 the air mass (Humphries et al., 2015). Observations over a decade in the Canadian High Arctic region clearly show that PBM transmitted by KCl-coated denuders dominate Hg^{II} fractionation over GOM during the early period of AMDEs, where the highest frequencies of depleted Hg^0 occur between –45 and –40 °C, while during the late period of higher temperatures and lower particulate concentrations (AMDEs then occur most frequently between –25 and –20 °C) the Hg^{II} fractionation has shifted to a clear dominance of GOM (Steffen et al., 2014). The KCl-denuder technique used cannot selectively separate nano- to submicron-sized mercuric halide

695 clusters completely from GOM (Ghoshdastidar and Ariya, 2019), which, along with the other nonsystematic bias of the method previously mentioned, makes the separation into Hg^{II} fractions tentative. The measurement methodology deficiencies make it highly uncertain to establish empirical gas-particle partitioning schemes (Amos et al., 2012; Rutter and Schauer, 2007b, a). This complicates the assumption and verification of model parameterization, which relies on accurate atmospheric concentration measurements. For example, assuming that the release of Hg^{II} from aerosols into the gas phase is entirely in the form of the tropospherically stable $HgCl_2$

700 molecule (Shah et al., 2021). Coupling an oxidized Hg vapor source or a reactor where oxidized Hg is formed by gas phase oxidation of Hg^0 to particle characterization instruments (such as scanning mobility or optical particle sizers) provides conclusive evidence that mercuric halide molecules readily form clusters that undergo particle growth (Ghoshdastidar and Ariya, 2019). In experimental studies of the vapor-phase oxidation of the volatile Hg forms Hg^0 and $(CH_3)_2Hg$, aerosol-phase products have been detected (Raofie et al., 2008; Raofie and Ariya, 2004; Sun et al., 2016; Niki et al., 1983a; Niki et al., 1983b). For example, using a scanning mobility

705 particle sizer, Sun et al. (2016) found that well below saturation pressure of HgX_2, reaction products from X (Cl and Br)-initiated Hg^0 vapor oxidation began to generate particles that grew from the Aitken nuclei range (few tens of nm) into the accumulation range (> 100 nm) over the course of a few hours (**Fig. 6**). **Fig. 7** summarizes the main elements of Hg gas phase chemistry in troposphere.
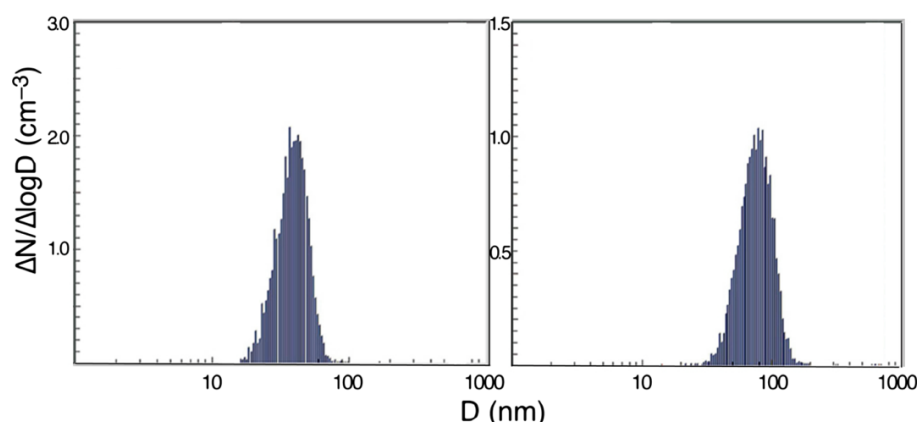
Figure 6. Particle growth of reaction products (yield of $HgX_2 > Hg_2X_2$) from the halogen atom (X = Cl, Br). Induced oxidation of Hg^0 vapor studied after the same degree of Hg^0 conversion (~75%, 5 – 8 ppb) but at different reaction times a and b (~45 min, Hg^0 + Br and ~4 h, Hg^0 + Cl, respectively).

710 **5.1.5 Lower stratospheric conditions**

In the lower stratosphere, the chlorine atom and hydroxyl radicals initiate most of the oxidation of Hg^0. This is because the concentrations of these species increase with altitude and the channels in which they are contained produce more photostable products such as $Hg(OH)_2$ and $HgCl_2$ (**Fig. 8a,b**). However, the increasing photon flux as one moves up through the ozone layer increases the photolysis rate of $Hg(OH)_2$ and $HgCl_2$, so that the lifetime of Hg^0 above the ozone maximum extends and approaches

715 10 years (Saiz-Lopez et al., 2022).
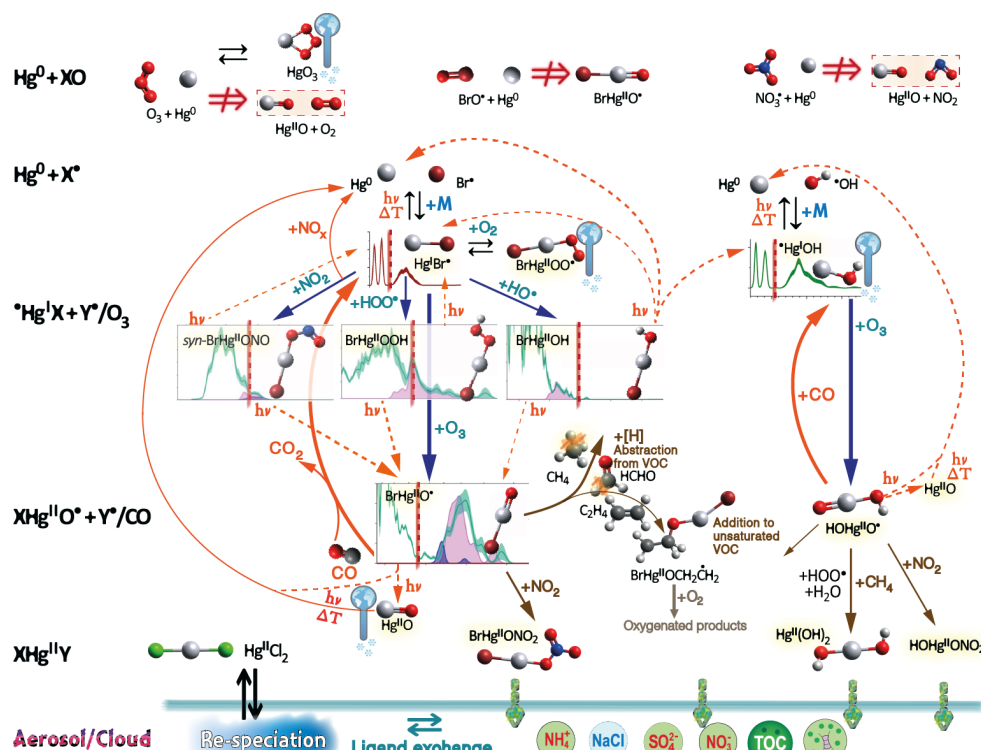
Figure 7. Outline of tropospheric gas-phase Hg chemistry. Reactions of the type Hg + XO• (X = O₂, Br and NO₂) directly leading to mercuric species are, for the (varying) reasons given in the text, impossible processes in the homogeneous gas phase. In the troposphere, gas phase oxidation of Hg⁰ in termolecular reactions is initiated by a few radicals of which Br atoms and with some uncertainty OH radicals have the greatest importance leading to
720 the formation of thermally and photolytically labile mercurous radical species (i.e. •HgᴵBr and •HgᴵOH). These Hgᴵ species are further oxidized to Hgᴵᴵ by the action of mainly ozone but also by abundant inorganic radicals such as NO₂, HOO, BrO, OH etc. It should be noted that NOₓ (NO and to a lesser extent NO₂) cannot efficiently oxidize Hgᴵ to Hgᴵᴵ but instead induce thermal reduction, e.g. •HgᴵBr + NO → Hg + BrNO. As O₃ is a closed shell species, it directly oxidizes •HgᴵBr/•HgᴵOH to mercuric radical species YHgᴵᴵO• while for example HOO• and BrO• are added to linear mercuric molecules (e.g. BrHgᴵᴵOOH) that are photolytically labile while those resulting from e.g. NO₂, •OH and Br• are more photostable. The photolysis of many of the major
725 thermally more stable Hgᴵᴵ species such as syn-BrHgᴵᴵONO, BrHgᴵᴵOOH and BrHgᴵᴵOH leads as shown to several species-specific photoproducts (potentially Hg⁰, Hgᴵ species or YHgᴵᴵO•) with various yields (**Table 3**). The remarkably thermally stable YHgO radical exhibits versatile thermochemistry, such as abstracting hydrogen from VOCs, adding to double bonds and being reduced by CO. Some of its bimolecular reactions, such as with CH₄ and NO₂, directly form fairly stable Hgᴵᴵ compounds such as Hg(OH)₂, BrHgᴵᴵOH and YHgᴵᴵONO₂. When these encounter hydrometeors, they dissolve and are re-speciated by rapid equilibrations with major aqueous ligands. This leads to the formation of strong complexes, e.g. by Cl⁻ to
730 chloromercurates HgCl₂, HgCl₃⁻ and HgCl₄²⁻. Thus, molecular HgCl₂ is released into the gas phase when the particle dries up. HgCl₂ is completely photostable and is enriched in the troposphere (a major Hgᴵᴵ species) with dry and wet deposition as the only sink processes.

5.1.6 Reactions of electronically excited state Hg⁰

The presence of UVC radiation above the ozone layer maximum opens completely new reaction pathways for redox cycling of stratospheric Hg. New insights into its conceptual stratospheric chemistry (Saiz-Lopez et al., 2022; 2025) and the associated
735 anomalous isotope fractionation (Sun et al., 2022; Fu et al., 2021) have been presented. The gas-phase oxidation of Hg⁰ is rapid (10³ –10⁴ times faster than in the troposphere, Saiz-Lopez et al., 2022) and is entirely driven by the oxidation of electronically excited Hg atoms by one of the major constituents of air, O₂.

Hg⁰(³P) reaction with molecular oxygen

Already involved in the discovery of the element oxygen towards the end of the 18th century, the chemistry of the system Hg + O₂
740 exhibits intricate complexity. These early observations, made independently in northern and western Europe, address an important aspect of the thermochemistry of the system. A direct combination of liquid Hg and O₂ occurs just below the boiling point of Hg to form HgO, but the reaction is reversed above 400 °C. While the reaction of ground-state Hg vapor (Hg(¹S)) with O₂ is negligibly slow (Hall et al., 1995), deep UV light excitation of singlet to triplet Hg atoms (Hg(³P)) leads to significant homogeneous reactions with O₂. In contrast, excitation of Hg(¹P₁) further out in the blue and subsequent reaction with O₂, as discussed above, is unlikely to
745 result in the net formation of mercury oxides. The gas-phase reactions of Hg(³P) have been studied in the laboratory since 1922

(Cario and Franck, 1922). In particular, those with O_2/air as a route to ozone synthesis since the mid-1920s (Dickinson and Sherrill, 1926). While larger quantities of ozone are produced by Hg photochemistry (photo-sensitization), the elemental vapor is oxidized more slowly, resulting in the deposition of a yellow-brown film of solid HgO on the reactor walls downstream of the irradiation zone (Volman, 1953). However, the $Hg(^3P) + O_2$ mechanism is still unelaborated due to the controversy regarding the molecular

750   intermediates and whether there is a direct route from $Hg(^3P)$ to gaseous HgO or the oxidation starts from the $Hg(^1S)$ state remains undetermined (Callear et al., 1959; Volman, 1953; Hippler et al., 1978; Morand and Nief, 1968). A dark homogeneous reaction $Hg(^1S) + O_3 \rightarrow HgO + O$, supported by early researchers (Callear et al., 1959; Volman, 1953; Pertel and Gunning, 1959) as driving the oxidation in the photochemical experiments can now be rejected for the reasons discussed above in **Section 5.1.1**. In any case, considering more recent results (Wang and Andrews, 2005; Hall, 1995), e.g., obtained by refined computational chemistry, the

755   following mechanism seems to be the most plausible:

$$Hg(^1S_0) + h\nu\ (\lambda=253.7\ nm) \rightarrow Hg(^3P_1) \tag{Rxn G4}$$
$$Hg(^3P_1) \rightarrow Hg(^1S_0) + h\nu\ (\lambda=253.7\ nm) \tag{Rxn G9}$$
$$Hg(^3P_1) + N_2 \rightarrow Hg(^3P_0) + N_2 \tag{Rxn G10}$$
$$Hg(^3P_1) + O_2 \xrightarrow{M} HgO_2^* \xrightarrow{M} OHgO \begin{matrix} \rightarrow Hg(^1S_0) + O_2(^3\Sigma_u^+) \\ \rightarrow HgO(^3\Pi) + O(^3P) \end{matrix} \tag{Rxn G12a,b}$$

760
$$Hg(^3P_0) + O_2 \rightarrow Hg(^1S_0) + O_2^* \tag{Rxn 5}$$
$$O_2^* + O_2 \rightarrow O_3 + O(^3P) \tag{Rxn 6}$$
$$O_2 + O(^3P) \rightarrow O_3 \tag{Rxn 7}$$
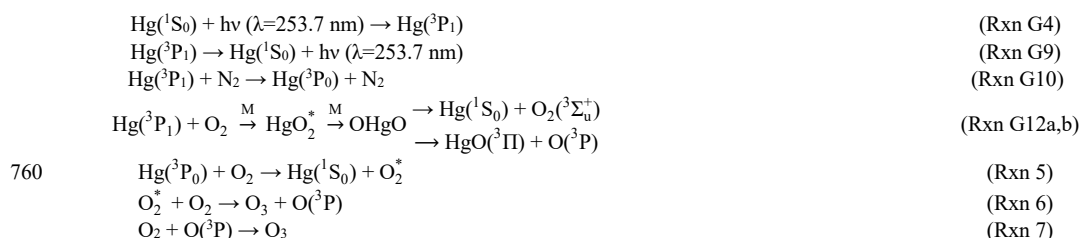
The photoexcitation (**Rxn G4**) has already been discussed, but its reverse (**Rxn G9**), i.e. the spontaneous emission of a photon that brings $Hg(^3P_1)$ to the ground state, is spin-forbidden and the radiative lifetime is relatively long (0.12 µs corresponding to k = 8.4 ×

765   10^6 s^{-1}). The quenching of $Hg(^3P)$ (i. e. **Rxn G6 & G10 – G12a**) for a number of gases has been carefully studied, with $Hg(^3P_1)$ atoms being 21.3 kJ mol^{-1} more energetic than $Hg(^3P_0)$ atoms. The two main constituents of air play different roles in the quenching process, with N_2 almost exclusively deactivating $Hg(^3P_1)$ to $Hg(^3P_0)$ with $k_{G10} = 5.1 \times 10^{-11}$ exp $(-701/T)$ cm^3 molecule $^{-1}$ s^{-1}, while O_2 quenches both $Hg(^3P_1)$ and $Hg(^3P_0)$ directly to $Hg(^1S_0)$ with k_{G12a} and k_{G11} of 1.3×10^{-10} (T/300)$^{-0.29}$ and 1.8×10^{-10} (T/300)$^{0.167}$ cm^3 molecule $^{-1}$ s^{-1}, respectively. In the stratosphere (T = 240 K), the ratio k_{G12a}/k_{G10} is ~50 suggesting that O_2 is a much better

770   physical quencher than N_2, which is true throughout the atmosphere. Of primary interest here, however, is the spin-conserving **Rxn G12b**, which allows the oxidation of Hg, and is overall nearly thermoneutral (exothermic by ~6 kJ mol^{-1}), yielding HgO ($^3\Pi$) with low vibrational energy, as noted by Saiz-Lopez et al. (2022), which is important for increasing the lifetime of this weakly bound molecule. First tentatively identified as an intermediate in a low-temperature UVC-irradiated matrix consisting of Hg, O_2 and H_2 yielding discrete $Hg(OH)_2$ molecules (Wang and Andrews, 2005), linear OHg^{II}O as the initial product is calculated to be 275 kJ mol^{-}

775   ^{1} less energetic than the reactants $Hg(^3P) + O_2$ and therefore sufficiently stable over time to participate in barrier rearrangement to $Hg(^1S) + O_2^*$ alongside with dissociation to HgO and O. Experimental data suggest that the branching ratio between **Rxn G12b** and **G12a** is low, making oxidation the minor process. Sun et al. observed a quantum yield of up to a few % for the oxidation step in experiments using synthetic air at 46 – 88 kPa and 233 – 298 K (Sun et al., 2022). Callear et al. (1959) observed a faster reaction in air than in O_2, suggesting that $Hg(^3P_0)$ may also react with O_2 to form HgO, analogous to $Hg(^3P_1)$.
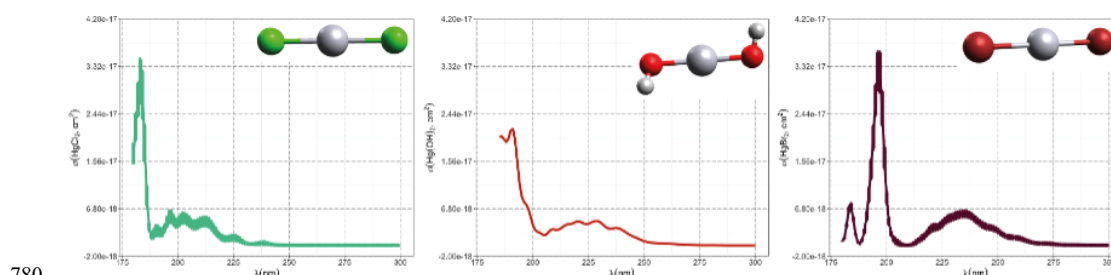
780
Figure 8. Computational absorption spectra of $HgCl_2$, $Hg(OH)_2$ and $HgBr_2$. Data from Saiz-Lopez et al. (2022) and Sitkiewicz et al. (2019).

Chemical turnover of HgO in the stratosphere. Formation of $HgCl_2$

The instability of the HgO molecule and its unimolecular decay to elemental Hg has been discussed earlier. Produced in larger quantities by the rapid photosensitized but nearly thermoneutral oxidation, the initially vibrational cold stratospheric HgO is more

785 likely to survive in the colder part of the upper stratosphere until it can react further into less unstable oxidized forms. The most abundant trace gases in this part of the stratosphere are water vapor, hydrochloric acid and ozone (Calvert et al., 2015). H_2O can oxidize $Hg(^3P)$ (Gunning and Strausz, 1963; Gruss et al., 2017) and may react with HgO:

$$Hg(^3P) + H_2O \rightarrow {}^{\bullet}Hg^IOH + H^{\bullet} \qquad \text{(Rxn G13)}$$

$$HgO(^3\Pi) + H_2O \begin{array}{l} \xrightarrow{M} Hg(OH)_2 \\ \rightarrow {}^{\bullet}Hg^IOH + HO^{\bullet} \end{array} \qquad \text{(Rxn G72)}$$
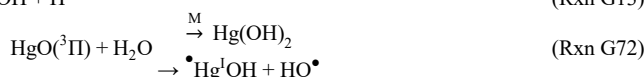
However, the reaction $Hg(^3P) + H_2O$ is so exothermic (~200 kJ mol^{-1}) that the product ${}^{\bullet}Hg^IOH$ can be expected to be vibrational hot and dissociate rapidly with less time for further bimolecular oxidation. A possible reaction between water vapor and HgO is strongly

790 exothermic if the final product is singlet $Hg(OH)_2$ but weakly endothermic if the triplet form is formed instead. Nevertheless, there is currently no evidence to suggest that HgO can be converted to $Hg(OH)_2$ in a direct reaction with moisture. According to Saiz-Lopez et al. (2022), the reaction between stratospheric HgO and HCl is fast enough (close to the collision limit) to allow some Hg^{II} to be converted to ${}^{\bullet}Hg^ICl$ rather than being reduced to elemental vapor:

$$HgO + HCl \rightarrow {}^{\bullet}Hg^ICl + {}^{\bullet}OH \qquad \text{(Rxn G73, } \Delta H_R = -61 \text{ kJ mol}^{-1}\text{)}$$

795 As with ${}^{\bullet}Hg^IOH$ and ${}^{\bullet}Hg^IBr$, the reaction between ${}^{\bullet}Hg^ICl$ and O_3 is barrierless and rapid, in this case producing $ClHg^{II}O^{\bullet}$:

$${}^{\bullet}Hg^ICl + O_3 \rightarrow ClHg^{II}O^{\bullet} + O_2 \qquad \text{(Rxn G43)}$$

Of the versatile tropospheric chemistry presented for $YHg^{II}O^{\bullet}$, hydrogen abstraction (**Rxn G44**) is still important in the stratosphere, which is again dominated by CH_4 (which is not photolyzed and remains the reaction with the OH radical as the main sink). The product $ClHg^{II}OH$, like $ClHg^{II}O^{\bullet}$, is further converted by reaction with HCl to $HgCl_2$ (**Rxn G46 & G47**), which is the most thermally

800 and photolytically stable of the Hg^{II} molecules present. The photolytic lifetime of $HgCl_2$ in the upper stratosphere is close to one hour and about twice that of Hg^0, so the oxidized Hg species dominate (of which $\geq$ 90% is $HgCl_2$). From insignificant, the Hg^I concentration rises rapidly above 50 km with the increasing UVC photon flux, so the ratio ${}^{\bullet}Hg^ICl/Hg^{II}Cl_2$ approaches unity at 60 km. An overview of the gas-phase Hg chemistry in the upper stratospheric is given in **Fig. 9** below.
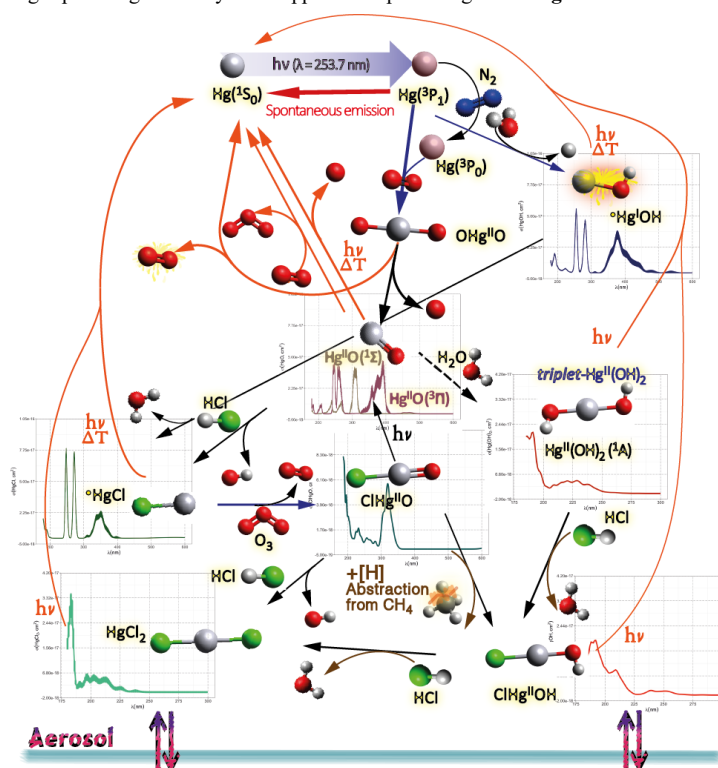
805 **Figure 9.** At about 35 km, the stratosphere begins to contain actinic radiation, which can electronically excite Hg (at 253.7 nm), but below this it is absorbed by O_3 in the Hartley bands (with a maximum at 254 nm). Electronically excited Hg^0 reacts primarily with O_2, with one of the exit channels leading to the formation of HgO via the intermediate $OHg^{II}O$. Before HgO can fully decay into the elements, it reacts further via secondary HCl-driven fast chemistry to

HgCl$_2$, the major constituent of Hg in the mid-upper stratosphere. A 2:1 steady state between HgCl$_2$ and Hg^0 occurs because the former photo dissociates more slowly than photosensitized Hg oxidizes, both at significant rates.

5.2 Organic species

5.2.1 Dimethylmercury

In addition to Hg^0, the "supertoxic" DMHg is another volatile Hg species that exists in nature, namely DMHg classified as a 'supertoxic' chemical (Siegler et al., 1999). In fact, DMHg has a boiling point below 100 °C, a high vapor pressure and a Henry's Law constant equivalent to Hg^0 (Schroeder and Munthe, 1998). Both DMHg and MMHg$^+$ species have been detected in ambient air (Lee et al., 2003; Bloom et al., 2005; Weiss-Penzias et al., 2018; Baya et al., 2015; Zhang et al., 2019a). DMHg has no known sources in the atmosphere. Its occurrence is mainly due to volatilization from surface waters where it is transported by upwelling conditions from the deep sea where it is formed under anoxic conditions (Conaway et al., 2009; Pongratz and Heumann, 1999). Polar sea ice harbors Hg-methylating microbes and is thought to be a source of DMHg that can be degassed as the ice melts (Schartup et al., 2020). Recently, DMHg has been automatically measured in marine air and corresponding surface water and shows an air-sea gas flux that is 1/30 of the magnitude of the simultaneously measured Hg^0 flux (He et al., 2022). The atmospheric transformation of DMHg is the main source of atmospheric MMHg$^+$ species (Sommar et al., 1997). DMHg vapor does not absorb actinic light (Terenin, 1934; Terenin and Prileshajewa, 1935) and is, therefore, not photolyzed in the planetary boundary layer, where it is only expected to be found (Sommar et al., 1996). DMHg appears to be prone to rapid gas phase transformation and, depending on the products formed, could be an important source of atmospheric MMHg$^+$ on a regional scale. However, in addition to MMHg$^+$ species (Niki et al., 1983a; Niki et al., 1983b), inorganic Hg compounds (Thomsen and Egsgaard, 1986; Sommar et al., 1997) have also been reported as products of radical reactions with DMHg. Aware of its acute toxicity (Siegler et al., 1999), it has been more than a quarter of a century since any laboratory kinetic and reaction mechanistic studies of the atmospheric gas-phase chemistry of DMHg have been reported and, in retrospect, some comments are worth making. There are three thermodynamically accessible bimolecular pathways that potentially can initiate the gas phase transformation of DMHg, where X$^\bullet$ below denotes a radical oxidant:

$$CH_3HgCH_3 + X^\bullet \begin{cases} \rightarrow CH_3HgX + CH_3^\bullet \\ \rightarrow CH_3HgCH_2^\bullet + HX \\ \rightarrow CH_3Hg^\bullet + CH_3X \end{cases}$$

(Rxn G75 – G77)

The existence of the CH$_3$Hg radical formed in the latter reaction was tentatively demonstrated in a matrix isolation study (Snelson, 1970). The small dissociation energy of the methylmercury bond of the radical (Kominar and Price, 1969) together with a predicted barrierless CH$_3$Hg$^\bullet \rightarrow {}^\bullet$CH$_3$ + Hg reaction (Kallend and Purnell, 1964) suggest a rapid decomposition to metallic Hg without time for e.g. reaction with O$_2$ to form a methylmercury peroxyl radical (CH$_3$HgOO$^\bullet$). In contrast, a composite reaction such as CH$_3$HgCH$_3$ + X$^\bullet \rightarrow {}^\bullet$Hg^{I}X + 2 CH$_3^\bullet$ directly producing inorganic Hg are endothermic and, therefore, less plausible. In a high-pressure study of the gas phase reaction between atomic F and DMHg, of low atmospheric relevance, it was reported that ~10% of the reacted DMHg is converted to CH$_3$F via the above substitution reaction (McKeown et al., 1983). However, a static FT–IR study of the Cl-initiated gas-phase reaction in the presence and absence of O$_2$ at atmospheric pressure shows the importance of the displacement reaction that generates CH$_3$HgCl. The remaining CH$_3$ group is converted to CH$_3$Cl in N$_2$ as a bath gas in a chain reaction that regenerates Cl atoms, while the end-products of the group in air can be attributed to the self-reaction of the CH$_3$OO radical. The reaction CH$_3$HgCH$_3$ + $^\bullet$OH studied with the same static method by photolysis of a mixture of CH$_3$HgCH$_3$, ethyl nitrite, and NO in air, also primarily follows the displacement reaction. The rate constant of ~2 × 10^{-11} cm^3 molecule^{-1} s^{-1} indicates that the lifetime of DMHg in the planetary boundary layer with respect to the OH channel active during the day is a few up to tens of hours. In the nocturnally active DMHg + NO$_3^\bullet$ reaction, studied by fast flow discharge technique with Hg/CI–MS detection (Sommar et al., 1996) and by a static long path FT–IR system (Sommar et al., 1997), both CH$_3$ groups contained in DMHg are accounted to react. A small but significant yield of Hg^0 was detected along with a product with m/z = 78 (CH$_3$ONO$_2$) after the reaction of DMHg and NO$_3^\bullet$ under fast flow discharge conditions, indicating that substitution has occurred. Assessment of the stability of HgO(Shepler and Peterson, 2003) suggests that although the quantitative carbon balances for non-Hg-containing reaction products are close to unity for both the

X = O (Thomsen and Egsgaard, 1986) and NO₃ (Sommar et al., 1997) studies, thermodynamic considerations suggest that the main

850 reaction proceeds by displacement and subsequent decomposition of a tentative intermediate $CH_3HgO^{\bullet}$ to HgO, which is stabilized by rapid oligomerization (Jayasekharan and Sahoo, 2014). In the DMHg + O study, ~95% of the Hg in the converted DMHg was recovered as HgO downstream of the injector in the fast flow experiments. In the DMHg + $NO_3^{\bullet}$ batch reactor study, carbon and nitrogen mass balances ruled out the formation of $MMHg^+$ entities and no Hg compound other than HgO could be considered as an end product. The rate constant of the nitrate radical reaction (**Rxn G77**) evaluated in the temperature range 258–358 K can be

855 described by the Arrhenius expression $3.2 \times 10^{-11} \times \exp[-(1760 \pm 400)/T]$ cm³ molecule⁻¹ s⁻¹ and the reaction is fast enough to put the lifetime of DMHg during the night in the same time range as for $^{\bullet}OH$ initiated degradation during the day (Sommar et al., 1997). To summarize this section, the degradation of DMHg in the atmosphere has been illustrated in **Fig. 10**.
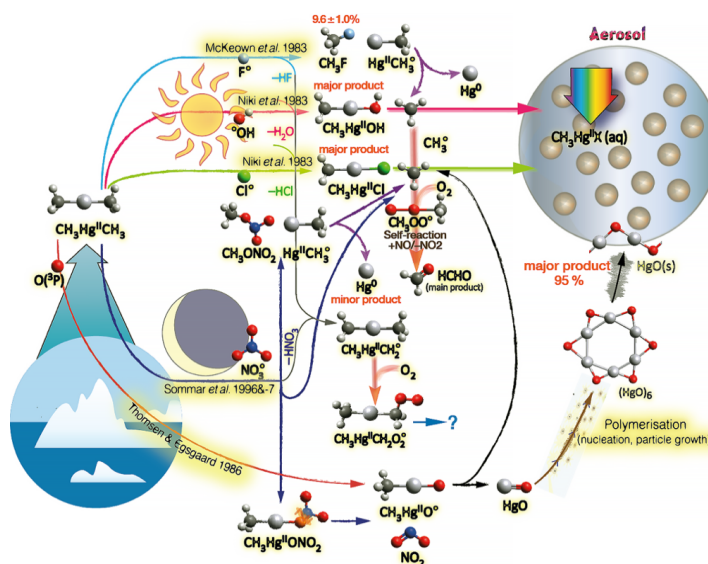
Figure 10. Schematics of the atmospheric destiny of DMHg. The fate of HgO indicated is uncertain.

860 **5.2.2 Monomethylmercury species**

Although there is a lack of experimental data, gaseous $MMHg^+$ species are expected to react with atmospheric radicals, which leads to demethylation similar to the process that occurs when in the reaction of CH_3HgCH_3 and OH/Cl radicals. However, it is probable that the rate constant is lower, and the uptake of particles is of greater significance for the atmospheric fate of $MMHg^+$ species.

6. Red-ox transformations in the aqueous phase

865 **6.1 Inorganic Hg species**

Aqueous redox of Hg^{II} complexes can include primary (intramolecular) processes involving direct electron transfer and secondary (intermolecular, usually bimolecular) reactions caused by reactive intermediates. Atmospheric aerosols serve as microreactors for the redox Hg reactions (Lin and Pehkonen, 1999). Both oxidation and reduction occur in the aqueous phase. Since $Hg^{2+}(aq)$ has a rapid ligand exchange rate, the formation of Hg^{II} hydrated complexes does not limit the redox reaction rates, and can therefore be

870 treated separately as chemical equilibria. The aqueous speciation of Hg^{II}, where pH is often a critical parameter, is of great importance for the reaction kinetics, not least for the reduction pathways. Thus, it appears that aerobic reduction pathways in principle require the formation of specific complexes, since Hg^0 cannot be formed from Hg^{2+} by successive bimolecular (single-electron) reduction steps, since dissolved O_2 instantaneously reoxidizes $Hg^{\bullet+}$:

$$XHg^{\bullet} + O_2 \rightleftarrows {}^{\bullet}OOHgX \rightleftarrows HgX^+ + O_2^{\bullet-} \qquad \text{(Rxn W11)}$$

875 The overall forward rate constant for **Rxn W11** is at the diffusion limit (k~10⁹ M⁻¹ s⁻¹, Nazhat and Asmus, 1973). In contrast, Hg^0 can be formed by fragmentation of a ligand bound to Hg^{II} (reductive elimination, van Loon et al., 2000). Such photo- or thermolabile

Hg^{II} complexes are characterized by low-energy ligand-to-metal charge transfer (LMCT) excited states, which tend to induce internal redox processes leading to oxidation of a ligand and reduction of the mercuric ion. There is evidence that Hg^{2+} complexes can undergo both one- and two-electron LMCT. An example is mercuric oxalate, where 2e-LMCT is photoinduced and occurs as part of a

880   concerted series of electron rearrangements (heterolytic cleavage of σ-bonds in the complex), resulting in the oxalate ligand being eliminated as two molecules of CO_2 and the oxidation state of the metal ion decreasing by two units. This mechanism occurs without any detectable intermediates such as free radicals:

(Rxn W16a)

As described in **Section 8**, 1e- and 2e-LMCT reactions produce isotopic effects, the specific fractionation of which can be used to identify the reaction mechanism. In addition to the quenching of triplet complex states, the presence of dissolved O_2 leads to the

885   scavenging of radicals such as $Hg^{\bullet+}$ produced by the 1e-LMCT mechanism, resulting in reoxidation to Hg^{2+} (**Rxn W11**, Zhao et al., 2021). As has been previously noted (Pehkonen and Lin, 1998), in certain laboratory experiments, such as reduction experiments, sufficiently elevated Hg concentrations are employed such that the Hg^0 formed exceeds its solubility, thereby existing predominantly as a colloidal form. **Table 4** below outlines the potentially significant redox reactions occurring in the aqueous phase, which are then elaborated upon in the subsequent text.

890   **Table 4.** Aqueous phase redox chemistry

ID	Reaction type	Reactant	Co-reactant	Reaction mechanism		Technique/ Comments	Rate coefficient $(M^{-1} s^{-1})$[18]	References
W1			Ozone (O_3)	$Hg^0 + O_3 \xrightarrow{H^+} Hg^{2+} + OH^- + O_2$	pH 5.2–6.2	Relative rate[19]	$(4.7 \pm 2.2) \times 10^7$	Munthe, 1992
W2			Hydroxyl radical (•OH)	$Hg^0 + HO^\bullet \rightarrow HOHg^\bullet \xrightarrow{H^+, O_2} Hg^{2+} + O_2^{\bullet-}$	pH 5.6 – 5.9	Steady-state[20]	2.0×10^9	Lin & Pehkonen, 1997
					pH 7.9	Relative rate[21]	$(2.4 \pm 0.3) \times 10^9$	Gårdfeldt et al., 2001
W3			Carbonate radical ($CO_3^{\bullet-}$)	$Hg^0 + CO_3^{\bullet-} \longrightarrow$ products	pH 8	Relative rate[22]		He et al., 2014
W4	Oxidation, bimolecular		Hypochloric acid (HOCl)	$Hg^0 + HOCl \longrightarrow Hg^{2+} + Cl^- + HO^-$	pH 6.5 – 8.4	Steady-state concentration of reactant by hydrolysis of the precursor NH_2Cl	$(2.1 \pm 0.1) \times 10^6$	Lin & Pehkonen, 1998b
			Hypochlorite (ClO^-)	$Hg^0 + ClO^- \xrightarrow{H^+} Hg^{2+} + Cl^- + HO^-$	pH 6.5 – 8.4		$(2.0 \pm 0.1) \times 10^6$	
W5		Hg^0 (aq)	Hypobromic acid (HOBr)	$Hg^0 + HOBr \longrightarrow Hg^{2+} + Br^- + HO^-$	pH 6.7 – 6.8	Steady state disproportionation of Br_2	0.28 ± 0.02	Wang & Pehkonen, 2004
			Hypobromite (BrO^-)	$Hg^0 + BrO^- \xrightarrow{H^+} Hg^{2+} + Br^- + HO^-$	pH 11.7 – 11.8		0.27 ± 0.04	
			Bromine (Br_2)	$Hg^0 + Br_2 \longrightarrow Hg^{2+} + 2 Br^-$	pH 2.0 – 2.1		0.20 ± 0.03	
W6			Peracids (peracetic and perbenzoic acid)			Screening study		Wigfield & Perkins, 1985a
W7	Oxidation, complexation		2–mercapto propionic acid		pH 7, anoxic	Absolute	0.61	Zheng et al., 2013
W8	Comprop., bimolecular		Mercuric ion (Hg^{2+})	$Hg^0 + Hg^{2+} \longrightarrow Hg_2^{2+}$	pH 3 – 4	e_{aq}^- (pulse radiolysis)	5.9×10^8	Buxton et al., 1995
W9	Dimerization, bimolecular		Mercurous ion radical ($Hg^{\bullet+}$)	$2 Hg^{\bullet+} \longrightarrow Hg_2^{2+}$			$\geq 10^9$	
W10	Disprop., bimolecular	$Hg^{\bullet+}$ (aq)		$2 Hg^{\bullet+} \longrightarrow Hg^{2+} + Hg^0$	pH 3.15		2.6×10^9	
W11	Oxidation, bimolecular		Oxygen (O_2)	$XHg^\bullet + O_2 \rightleftarrows {}^\bullet OOHgX \rightleftarrows HgX^+ + O_2^{\bullet-}$			$(1-4) \times 10^9$ [23]	Jungbluth et al., 1976
W12			p–benzoquinone		pH 5.0 – 5.5		$(1-4) \times 10^9$	
W13	Reduction, 2e–LMCT, thermal		Sulfite (SO_3^{2-})	$Hg^{2+} + SO_3^{2-} \rightleftarrows HgSO_3 \longrightarrow Hg^0 S^{VI} O_3 \longrightarrow Hg^0 + S(VI)$	pH 3.0 – 4.8	Absolute[24]	$0.6 \ s^{-1}$	Munthe et al., 1991
					280 – 307 K		$T \cdot exp \frac{(31.971 \cdot T - 12595)}{T}$	

[18] Unless otherwise stated.
[19] with SO_3^{2-} as reference.
[20] using C_6H_6 as •OH scavenger. NO_3^- photolysis as •OH source.
[21] with CH_3Hg^+ as reference. NO_3^- photolysis as •OH source.
[22] The loss of Hg^0(aq) was followed, but neither •OH nor $CO_3^{\bullet-}$, which co-occur in the solution, were quantified. NO_3^- photolysis as •OH source, •OH reaction with carbonate anion as a source of $CO_3^{\bullet-}$
[23] Concerns various mercuric halide and pseudohalide radicals ${}^\bullet HgX$ (X = Cl, Br, I, SCN and CN)
[24] Followed by decay of $[Hg(SO_3)_2]^{2-}$ absorption ($\lambda = 230$ nm)

				pH 3, 298 K	Absolute[25]	0.0106 ± 0.0009 s^{-1}	van Loon et al., 2000 Feinberg et al., 2015
W14	Reduction, bimolecular	Hg^{II}(aq)	Carbon dioxide anion radical (CO$_2^{\bullet-}$)	HgCl$_2$ + CO$_2^{\bullet-} \longrightarrow$ ClHg$^{\bullet+}$ + CO$_2$ + Cl$^-$	pH 1 – 2, anoxic	Relative rate[26]	1.8×10^8	Berkovic et al., 2010
W15			Superoxide anion radical (O$_2^{\bullet-}$)	HgCl$_2$ + O$_2^{\bullet-} \longrightarrow$ ClHg$^{\bullet+}$ + O$_2$ + Cl$^-$	pH 6	Relative rate[27]	5×10^3	Gårdfeldt & Jonsson, 2003
			Hydroperoxy radical (HO$_2$)	C$_2$O$_4^{\bullet-} \to$ CO$_2$ + CO$_2^{\bullet-}$, CO$_2^{\bullet-}$ + O$_2 \to$ CO$_2$ + O$_2^{\bullet-}$, H$^+$ + O$_2^{\bullet-} \rightleftarrows$ HO$_2^{\bullet}$, Hg^{2+} + HO$_2^{\bullet} \longrightarrow$ products	pH 3.9	Absolute[28]	1.7×10^4	Pehkonen and Lin, 1998
W16	Reduction, 2e$^-$ and 1e$^-$ LMCT, photolytic	Hg^{II}(aq)	Oxalate	Hg^{2+}+C$_2$O$_4^{2-} \rightleftarrows$ HgC$_2$O$_4$ $\xrightarrow{h\nu}$ Hg^0 + 2 CO$_2$ HgC$_2$O$_4$ $\xrightarrow{h\nu}$ Hg$^{\bullet+}$+C$_2$O$_4^{\bullet-}$ Hg^{2+} + C$_2$O$_4^{\bullet-} \to$ Hg$^{\bullet+}$ + 2 CO$_2$, Hg$^{\bullet+}$ + C$_2$O$_4^{2-} \to$ Hg^0 + C$_2$O$_4^{\bullet-}$	pH 3 – 6, anoxic — pH 3, anoxic	Absolute[29]	15.7 ± 2.8 [30] — $(1.2 \pm 0.2) \times 10^4$ [31]	Zhao et al., 2021 — Si & Ariya, 2008
			Malonate (R = CH$_2$), Succinate (R = C$_2$H$_4$)	Hg^{2+}+ R(COO)$_2^{2-} \rightleftarrows$ Hg(OOC)$_2$R $\xrightarrow{h\nu}$ Hg^0 + CO$_2$ + HORCOOH – H$_2$O Hg(OOC)$_2$R $\xrightarrow{h\nu}$ Hg$^{\bullet+}$+ $^{\bullet}$OOCRCOO$^-$, Hg^{2+} + $^{\bullet}$OOCRCOO$^- \xrightarrow{H_2O}$ Hg$^{\bullet+}$ + CO$_2$ + HORCOOH Hg$^{\bullet+}$ + R(COO)$_2^{2-} \to$ Hg^0 + $^{\bullet}$OOCRCOO$^-$	pH 3, anoxic		$(4.9 \pm 0.8) \times 10^3$ — $(2.8 \pm 0.5) \times 10^3$	Si & Ariya, 2008
	Reduction, thermal		Ascorbate (H$_2$asc, Hasc$^-$) (enolic acids)	HOHg(Hasc) $\longrightarrow$ Hg^0 + H$_2$O + dehydroascorbate	pH 4 – 5.5		2.8×10^{-3} s^{-1}	
	Reduction, photolytic		Salicylic acid		pH 4.3		1.0×10^{-4} s^{-1}	This work
			p-aminobenzoic acid p-hydroxybenzoic acid	See Rxn 8	pH 4.9 pH 5.6		3.1×10^{-4} s^{-1} 1.1×10^{-5} s^{-1}	
W17	1e$^-$ LMCT, followed by bimolecular reduction, photolytic		Anthraquinone–2,6–disulfonate (AQDS)		UVB, pH 3.4	Absolute[32]	$(9.9 \pm 2.7) \times 10^{-4}$ s^{-1}	Zhao et al., 2021
W18	Reduction, photolytic		1–alkanethiols	Hg(RS)$_2$ $\xrightarrow{h\nu}$ Hg^0 + RS–SR	UV–VIS, pH 7	Absolute	$(2.0 \pm 0.2) \times 10^{-7}$ s^{-1} (R = C$_3$H$_7$) $(1.4 \pm 0.1) \times 10^{-7}$ s^{-1} (R = C$_4$H$_9$) $(8.3 \pm 0.5) \times 10^{-8}$ s^{-1} (R = C$_5$H$_{11}$)	Si & Ariya, 2011
	Reduction etc. Photolytic		Thioglycolic acid	Hg(O(=O)CCH$_2$S) $\xrightarrow{h\nu}$ Hg^0 + products $\xrightarrow{h\nu}$ HgS + products	UV–VIS, pH 4		$(2.3 \pm 0.4) \times 10^{-5}$ s^{-1}	Si & Ariya, 2015

6.1.1 Oxidation channels

The mass transfer (diffusion) of gas-phase Hg^0 into typical size regimes of aerosols (radius of 0.1 – 10 µm) does not limit the rate of aqueous Hg^0 oxidation. The concentration of dissolved Hg^0 in the droplet is at a steady state governed by Henry's Law (Lin and Pehkonen, 1998a).

895 **Elemental mercury**

Inorganic oxidants

Rxn W1. Ozone (O₃)

The presence of O$_3$ in atmospheric water is mainly from the scavenging of gaseous O$_3$ (Henry's constant = 0.013 M atm^{-1} at 298 K). An early study of the oxidation of Hg^0 by O$_3$ in the aqueous phase was carried out by Iverfeldt and Lindqvist (1986) using a flowing

900 system in which 70-200 ppb O$_3$ was introduced. Their results suggested a conversion rate of 1-4% h^{-1} when applied to atmospheric conditions. Munthe and co-worker (Mcelroy and Munthe, 1991; Munthe, 1992) studied the ozone reaction with mercurous cation in acidic solution (pH = 1 - 3) in a stopped-flow system and with elemental Hg using the relative rate technique (sulfite as reference

---

[25] Followed by the formation of of Hg$_2^{2+}$ (λ = 236 nm)

[26] Methyl viologen as reference. S$_2$O$_8^{2-}$ photolysis in the presence of HCOOH.

[27] Methyl viologen as reference. Reduction of O$_2$ by e$_{aq}^-$ (pulse radiolysis). Determination of K = 2.5 for WO8/WR4 and using WO8 for calculating WR4.

[28] Dithizone colorimetric quantification of Hg^{II} decay. HO$_2^{\bullet}$ produced by C$_2$O$_4^{2-}$ photolysis with air bubbling. [HO$_2^{\bullet}$] estimated from production of H$_2$O$_2$.

[29] After analytically determining the initial Hg^{II} concentration, the reduction process was studied by measuring the production of Hg^0 by CV-AFS.

[30] The oxalate ion (C$_2$O$_4^{2-}$) was identified as the sole reducing agent (complexing ligand), hence k = k$_{obs}$/[C$_2$O$_4^{2-}$].

[31] Based on the total concentration, the second-order rate coefficient is expressed as k = k$_{obs}$/([H$_2$C$_2$O$_4$] + [HC$_2$O$_4^-$] + [C$_2$O$_4^{2-}$]).

[32] AQDS is not the reductant rather photohydroxylated reduced AQDS forms.

compound, pH 5.2 - 6.2) and obtained pH-independent rate constants of $(9.2 \pm 0.9) \times 10^6$ and $(4.7 \pm 2.2) \times 10^7$ M^{-1} s^{-1}, respectively.

Rxn W2. Hydroxyl radical ($^\bullet$OH)

905 The OH radical in atmospheric water can come from the air (equilibrium at 30 M atm^{-1}) or from aqueous phase production via pathways including photolysis of H_2O_2, HONO, O_3 and NO_3^- (Finlayson-Pitts and Pitts, 2000). The reaction rate of $Hg^0 + {}^\bullet$OH in the aqueous phase was determined by Lin and Pehkonen (1997) using a steady-state technique with photolysis of NO_3^- as $^\bullet$OH source and C_6H_6 as $^\bullet$OH scavenger to 2.0×10^9 M^{-1} s^{-1} at pH 5.6 – 5.9. Like the first step ($Hg^0 + {}^\bullet$OH $\rightarrow {}^\bullet Hg^I$OH), the second step mediated by dissolved O_2 (reaction 6) is near the diffusion limit. Gårdfeldt et al. (2001) later studied the same reaction at pH 7.9, but with the

910 reaction between CH_3Hg^+ and $^\bullet$OH as a reference, but with similar results (2.4×10^9 M^{-1} s^{-1}).

Rxn W3. Carbonate radical ($CO_3^{\bullet-}$)

In water, the carbonate system (HCO_3^- and CO_3^{2-}) can react with OH radicals to form the strongly oxidizing carbonate radical ($CO_3^{\bullet-}$) in fast reactions (8.5×10^6 and 3.9×10^8 M^{-1} s^{-1}, respectively). In a comparative study, He et al. (2014) studied the disappearance of Hg^0 in aqueous solutions where NO_3^- was photolyzed in UV-VIS in the absence and presence of CO_3^{2-} at pH = 8. When both NO_3^- (0.23

915 mM) and CO_3^{2-} (2.75 mM) were present in the irradiated solutions (electron paramagnetic resonance spin trapping analysis detected the presence of $^\bullet$OH and $CO_3^{\bullet-}$), the rate of oxidation of Hg^0 (aq) (1.44 h^{-1}) was 8 times faster than that observed when only NO_3^- (which produces $^\bullet$OH) was irradiated. The carbonate radical is a single-electron oxidant and reacts according to: $Hg^0 + CO_3^{\bullet-} \rightarrow Hg^{\bullet+} + CO_3^{2-}$. In addition to identifying the carbonate radical as an effective oxidant of Hg^0 dissolved in water alongside the hydroxyl radical, the study also investigated the role of $^1\Delta_g O_2$ (singlet oxygen) as an oxidant for Hg^0 (aq). However, the latter species, an excited state of O_2, does

920 not initiate any measurable oxidation. It should also be noted that the absolute rate constant for $Hg^0 + CO_3^{\bullet-}$ remains to be determined.

Rxn W4. Aqueous chlorine (HOCl/ClO$^-$)

Aqueous chlorine is mainly formed by the scavenging of gaseous Cl_2 (Henry's constant $= 7.61 \times 10^{-2}$ M atm^{-1} at 298 K) into the aqueous phase and the oxidation of the chloride ion by $^\bullet$OH. Once incorporated into the aqueous phase, it dissociates to form HOCl/ OCl$^-$ (pK$_a$ = 7.5) and Cl$^-$, the former being the primary oxidants and increasing the solubility of total chlorine. It is a nocturnal oxidant as both Cl_2

925 and HOCl are readily photolyzed by solar radiation. The prospects for Hg^0 oxidation by aqueous chlorine were investigated by Kobayashi (1987) and Munthe and McElroy (1992). In the former, rapid dissolution of Hg was reported when a gas stream containing Hg^0 was passed through a solution containing dissolved chlorine (HClO), while in the latter, Hg_2^{2+}(aq) was used as a proxy for Hg^0, whose oxidation was observed to be "relatively fast" in a solution containing HClO. A detailed kinetic study (Lin and Pehkonen, 1998b) of the reaction between Hg^0 and HClO/ClO$^-$ was carried out using a steady-state method with chloramine as a reservoir of free hypochlorous

930 acid formed by hydrolysis: $NH_2Cl + H_2O \rightarrow NH_3 + HClO$. The turnover of Hg^0 was studied in the pH range 6.5 - 8.5 around pK$_a$ (HClO) to investigate the influence of HClO (aq) and ClO$^-$ (aq), which were found to be closely equivalent according to the rate constants for $Hg^0 + HClO$ and $Hg^0 + ClO^-$ of $(2.09 \pm 0.06) \times 10^6$ and $(1.99 \pm 0.06) \times 10^6$ M^{-1} s^{-1}, respectively. The products of both reactions (2 electrons are transferred) are chloride and hydroxide anions with a stoichiometry of 1:1 together with a mercuric cation which rapidly forms a strong complex (logβ_{11} = 18.0).

935 **Rxn W5. Aqueous bromine (HOBr/BrO$^-$/Br$_2$)**

Bromine has a higher Henry's constant (0.725 atm M^{-1}) than chlorine, but the disproportionation of Br_2 to HBrO/BrO$^-$ (pK$_a$ = 8.7) and Br$^-$ is slow and the equilibrium is shifted in favor of Br_2. In contrast, Br^{+1} is formed by the action of O_3 on bromide ions and exists in the presence of Cl$^-$ largely as BrCl (Liu and Margerum, 2001). Aqueous bromine (Br_2, HOBr) oxidizes Hg^0 only slowly (0.2 – 0.3 M^{-1} s^{-1}, Wang and Pehkonen, 2004). However, BrCl is likely important as it is used as an oxidant for Hg in current analytical

940 methods, although the kinetics have not been investigated.

Organic oxidants

Rxn W6. Peroxides

H_2O_2 cannot oxidize Hg^0 (aq) itself (Kobayashi, 1987), but participates in the metal-catalyzed oxidation of Hg^0 as in the Fenton's system. The Fenton's reagent itself $Fe^{2+} + H_2O_2$ produces OH radicals for which Hg^0, Fe^{2+} and H_2O_2 are in competition for oxidation.

945 The latter reaction, $H_2O_2 + {}^\bullet OH$, produces the HO_2 radical which propagates a chain reaction (Fenton's reaction) supported by Fe^{3+} acting as a catalyst to decompose H_2O_2 to O_2 and H_2O, during which a stable concentration of Fe^{2+} is produced as a source of ${}^\bullet OH$. Hg^0 oxidation is most pronounced when the ferrous part of the Fenton reaction dominates over the ferric part, corresponding to a higher concentration of OH radicals (Liu, 2011). The -OOH functional group in organic hydroperoxides, like that in hydrogen peroxide, lacks the ability to oxidize Hg^0, whereas that in peroxocarboxylic acids (peracetic and perbenzoic acid) seems to possess

950 it, tentatively forming a mercuric carboxylate by a cyclic mechanism (Wigfield and Perkins, 1985b; Wigfield and Perkins, 1985a).

Rxn W7. Thiocarboxylic acids

Thiol compounds, as substituted carboxylic acids including cysteine and glutathione, can oxidize $Hg^0(aq)$ both thermally under anoxic conditions (Gu et al., 2011). For example, Zheng et al. (2013) observed that 2-sulphanylpropanoic acid in greater excess (1000:1) oxidized Hg^0 at a rate of 2.18 ± 0.13 h^{-1}. The presence of an electron acceptor (such as quinones) further enhanced the

955 reaction rate. The reaction mechanism has been described as oxidative complexation. Hg^0, which is polarizable, interacts with a thiol group, leading to ligand-induced oxidative complexation in which the hydrogen participates in charge transfer (Cohen-Atiya and Mandler, 2003).

Mercurous radical species (${}^\bullet Hg^I X$)

Inorganic oxidants

960 **Rxn W11. Oxygen (O_2)**

The reaction between $Hg^{\bullet+}$ and O_2 has been studied for a variety of ligands and over a range of pH values well into the alkaline range using pulse radiolysis with a homogeneous kinetic result (Nazhat and Asmus, 1973; Jungbluth et al., 1976; Fujita et al., 1975; Fujita et al., 1973; Liu et al., 1983; Pikaev et al., 1975). Mercurous species are formed by the reduction of corresponding mercuric species by the action of solvated electrons and H atoms derived from H_2O radiolysis: $HgX_2 + e_{aq}^- \rightarrow {}^\bullet Hg^I X + X^-$ and $HgX_2 + H^\bullet \rightarrow {}^\bullet Hg^I X + H^+ + X^-$.

965 All types of ${}^\bullet Hg^I X$ species react rapidly ($\geq 1 \times 10^9$ M^{-1} s^{-1}) with O_2 (aq): $Hg^{\bullet+} + O_2 \rightleftarrows {}^\bullet OOHg^+ \rightleftarrows Hg^{2+} + O_2^{\bullet-}$, where the equilibrium is very strongly shifted to the right. In one case (X = CN, Jungbluth et al., 1976) the reaction takes place without clear formation of a peroxyl radical intermediate. In an air-saturated solution (~0.2 mM O_2), the lifetime of ${}^\bullet Hg^I X$ is about 1 μs (Jungbluth et al., 1976).

Organic oxidants

Rxn W12. Quinones

970 Both $Hg^{\bullet+}$ and ${}^\bullet OOHg^+$ are rapidly oxidized by benzoquinone ($\gtrsim 10^9$ and $\lesssim 10^9$ M^{-1} s^{-1}, Jungbluth et al., 1976), which accepts an electron to form a semiquinone anion. Lalonde et al. (2001) observed that Hg^0 is oxidized (~0.6 h^{-1}) in UVB-irradiated aqueous solutions containing both benzoquinone (32 nM) and chloride ions (0.5 M), without being able to fix the mechanism.

6.1.2 Reduction channels

Mercuric compounds (Hg^{II})

975 **Inorganic reductants**

Rxn W13. Sulfite (SO_3^{2-})

SO_2 dissolves in water (Henry's constant 1.36 M atm^{-1}) to form the weak acid H_2SO_3 (aq), which can be deprotonated to HSO_3^- and SO_3^{2-}. Oxidation of sulfite to sulfate is rapid in the atmosphere, taking a few hours under typical oxygenated conditions in atmospheric droplets. SO_3^{2-} is a soft ligand that forms strong complexes with Hg^{2+} (**Table 1**), such as $HgSO_3$ and $[Hg(SO_3)_2]^{2-}$, the latter completely

980 dominating under natural conditions where the sulfite content greatly exceeds that of Hg^{2+}. The reduction of aqueous Hg^{II} by the sulfite system was first investigated by Munthe et al. (1991). $[Hg(SO_3)_2]^{2-}$ is stable, whereas $HgSO_3$ decomposes readily to Hg^0 and sulfate with first order rate constants of $<10^{-4}$ s^{-1} and 0.6 s^{-1}, respectively. Scott and co-workers (van Loon et al., 2001, 2000) carried out a thorough re-examination and confirmed that the bis-sulfite complex is not thermally unstable, but that the reduction of $HgSO_3$, which is strongly temperature dependent (k approximately quadruples with each 10 °C increase in temperature) and weakly pH dependent, is more than

985 50 times slower than reported by Munthe et al. (0.011 vs. 0.6 s^{-1} at 25ºC). The reaction mechanism is intramolecular with 2e-LMCT and heterolytic cleavage of the Hg-S bond: $Hg^{2+} + SO_3^{2-} \rightarrow Hg^{II}S^{IV}O_3 \rightarrow Hg^0 S^{VI}O_3 \xrightarrow{H_2O} Hg^0 + SO_4^{2-}$.

Rxn W14. Carbon dioxide anion radical ($CO_2^{\bullet-}$)

The carbon dioxide radical ($CO_2^{\bullet-}$) can be formed in nature by the oxidation of carboxylic acids (see above under oxalic acid). It is strongly reducing and occurs in anaerobic environments. Berkovic et al. (2010) studied the $CO_2^{\bullet-}$–mediated reduction of Hg^{2+} at low

990   pH by laser flash photolysis of a dilute mixture of $HgCl_2$, formic acid and sodium peroxydisulfate at 266 nm. The one-electron reaction $Hg^{2+} + CO_2^{\bullet-} \rightarrow Hg^{\bullet+} + CO_2$ is exothermic with a rate constant of 1.8×10^8 M^{-1} s^{-1}. The $Hg^{\bullet+}$ formed can only be further reduced to Hg^0 in the absence of O_2.
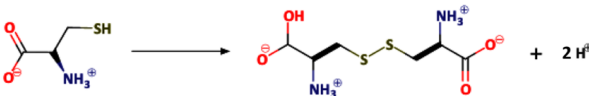
Rxn W15. Superoxide anion/hydroperoxy radical ($O_2^{\bullet-}/HO_2^{\bullet}$)

$HO_2^{\bullet}/O_2^{\bullet-}$ (pK_a 5.5) is a one-electron reductant of Hg^{2+} to $Hg^{\bullet+}$. Gårdfeldt and Jonsson (2003) determined the one-electron

995   reduction potential for the pair $HgCl_2/^{\bullet}HgCl$ vs. NHE at $[Cl^-] = 0.05$ M to be –0.47 V, which together with that for $O_2/O_2^{\bullet-}$ vs. NHE of –0.155 V gives an equilibrium constant for $HgCl_2 + O_2^{\bullet-} \rightleftarrows \,^{\bullet}HgCl + O_2 + Cl^-$ of 5 x 10^{-6} at the aforementioned $[Cl^-]$. Given the rate constant for the reaction $^{\bullet}Hg^I Cl + O_2$ is ~10^9 M^{-1} s^{-1} (**Rxn W11**), the bimolecular rate constant between $HgCl_2$ and $O_2^{\bullet-}$ can be estimated to be 5 x 10^3 M^{-1} s^{-1}. Pehkonen and Lin (1998) carried out a study of the photoreduction of mercuric ion to Hg^0 with nitrate or chloride as counterion in the presence of formic, acetic or oxalic acid at neutral (7.0) and acidic (3.9) pH in

1000   aerated solutions. Only in the presence of oxalic acid does a significant photoreduction occur and, as in the later studies by Zhao et al. (2021) and Si and Ariya (2008), an increase in the reaction rate is observed with increasing ratios of oxalic acid to Hg^{II}. It is also observed that the reduction is suppressed in the presence of Cl^-. Photoreduction results in an exponential increase in H_2O_2 formation, which is due to the presence of hydroperoxyl radicals in solution (2 $HO_2^{\bullet} \rightarrow H_2O_2 + O_2$). In retrospect (see above), this follows from the homolytic decomposition of $Hg(\eta^2\text{-}C_2O_4)$ into radicals in an aerated solution ($CO_2^{\bullet-} + O_2 \rightarrow O_2^{\bullet-} + CO_2$)

1005   and does not necessarily mean that $HO_2^{\bullet}/O_2^{\bullet-}$ can reduce Hg^{II} to Hg^0.

Organic reductants

In the atmospheric environment, Hg^{II} complexation by natural organic matter (NOM) plays a pivotal role in the redox chemistry of Hg (Åkerblom et al., 2015). The chemical-reducing effect of dissolved NOM (humic substances) on Hg^{II} has been recognized for nearly 50 years (Alberts et al., 1974). These heterogeneous macromolecular ligands contain not only building blocks that can for complexes with Hg^{II}, but also redox-active aromatic chromophores that can photolytically convert Hg. The fractions of NOM

1010   contributing to Hg^{II} photoreduction include the fulvic- and flavin-like fractions that contain more quinone and flavin moieties, than usual (Yang et al., 2020a). Furthermore, NOM contains several functional groups that can reduce complex-bound mercuric ions to Hg^0 by a 2e-LMCT reaction (**Table 5**).

Table 5. Main functional groups of NOM that can (photo)reduce ligated Hg^{2+}.

Binding atom	Ligand oxidation process
Oxygen (O)	$R-CH_2OH \longrightarrow R-CHO + 2\,H^+$ $R-COOH \longrightarrow R-H + O=C=O$
Nitrogen (N)	$H_2C(NH_2)-CH_2(NH_2) \longrightarrow H_3C-CH_3 + N\equiv N + 2\,H^+$
Sulfur (S)	cysteine $\longrightarrow$ cystine-type disulfide $+\ 2\,H^{\oplus}$

1015   **Rxn W16. Organic acids**

Low molecular-weight organic acids present in the atmosphere can reduce Hg^{II} to Hg^0 in the presence of O_2. These include dicarboxylic acids, ortho-substituted aromatic carboxylic acids, and enolic acids. It has been known since 1880 (Eder, 1880) that the salt of the lightest dicarboxylic acid, oxalate, can reduce Hg^{II} in daylight. Oxalic acid is formed from, e.g., ethylene or acetylene by atmospheric oxidation over several reaction cycles (chemical aging, Warneck, 2003). Mercuric ion forms a complex with oxalate in

1020   a 1:1 ratio ($Hg(\eta^2\text{-}C_2O_4)$), characterized by log β = 9.66, which is most photolabile under UVB irradiation. Si and Ariya (2008) studied the kinetics and products of the photoreduction of Hg^{II} in a series of experiments with different concentrations of the lightest

dicarboxylic acids C_2–C_4 at an initial pH of 3.0 and temperature of 296 ± 2 K, while the kinetic, product and isotopic study of Zhao et al. (2021) involved the system Hg^{II} + oxalic acid with ClO_4^- as counterion in the pH range of 2.7 – 6.3 and a small temperature range of 295 – 303 K. The pH-resolved experiments show that in the $C_2O_4^{2-}$, $HC_2O_4^-$, $H_2C_2O_4$ – system, only the oxalate ion reduces

1025 Hg^{2+} with a $k_{Hg^{2+}+C_2O_4^{2-}}$ of 15.7 ± 2.8 M^{-1} s^{-1} at 295 ± 1 K. Si and Ariya reported a strongly divergent bimolecular rate constant between Hg^{2+} and total oxalic acid concentration of 1.2×10^4 M^{-1} s^{-1} at pH 3.0. The magnitude is surprisingly large and is comparable to the rate constant between Hg^{2+} and HO_2/O_2^- radicals (see below). When this higher rate constant based on total oxalic acid concentration is implemented in regional air quality models, the impact is significant (Bash et al., 2014). However, on the reaction mechanism, there is more consensus that it follows branched routes. $Hg(\eta^2\text{-}C_2O_4)$ undergoes photolysis followed by partial reductive

1030 elimination in one step (which is insensitive to the presence of O_2): $Hg(\eta^2\text{-}C_2O_4) \xrightarrow{h\nu} Hg^0 + 2 CO_2$ and partly by homolysis of an Hg–O bond, which initiates a chain reaction: $Hg(\eta^2\text{-}C_2O_4) \xrightarrow{h\nu} Hg^{\bullet+} + C_2O_4^{\bullet-}$. Hg^0 should form from the reaction of $Hg^{\bullet+}$ with the bulk ligand $C_2O_4^{2-}$, where $Hg^{\bullet+}$ is reformed from the reaction between bulk Hg^{2+} and the oxalyl ($C_2O_4^{\bullet-}$) or carbon dioxide anion ($CO_2^{\bullet-}$) radical. Reduction to Hg^0 in the chain reaction is inhibited by O_2, which reacts rapidly with both $C_2O_4^{\bullet-}$ and $CO_2^{\bullet-}$ and also re-oxidizes $Hg^{\bullet+}$ to Hg^{2+}. As with dicarboxylic acids, aqueous solutions of aromatic ortho- and para-substituted carboxylic acids

1035 exposed to UVB can oxidize Hg^{2+} to Hg^0 by elimination of CO_2 and the $Hg^{2+} \rightarrow Hg^0$ photoreduction is attenuated but not completely inhibited by the presence of dissolved O_2 and competing counterions. Previously, He et al. (2012) studied the aqueous photoreduction of Hg^{2+} coupled with a series of aromatic carboxylic acid derivatives in the absence of O_2 at pH 4.3 and suggested that the reaction proceeds by a radical mechanism. However, studies of the same reactants in our laboratory (unpublished results, shown in **Table 4**) show that Hg^0 is formed even in the presence of dissolved O_2, suggesting the existence of an additional non-radical reduction pathway.

1040 We propose that this channel requires solvo-mercuration to an arylmercurial intermediate followed by photolytically induced 2e-LMCT as part of a concerted series of electron rearrangements including cleavage of a Hg-C bond yielding Hg^0, CO_2 and a decarboxylated aromatic as end products. Taking p-aminobenzoic acid as an example:

(Rxn 8)
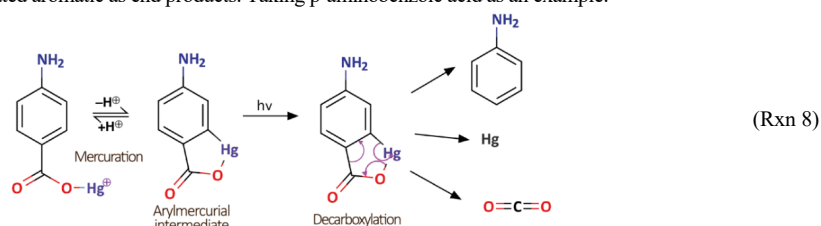
Photo-reduction has also been observed in the presence of dissolved O_2 when Hg^{2+} is mainly bound to the amino acid serine (HSer) as $HgSer_2$ (Motta et al., 2020b), which can be explained as the result of reductive elimination with CO_2 and 2-aminoethanol as by-

1045 products besides Hg^0 and involving an intermediate with a photolabile Hg-C bond (Zhao et al., 2021). In the cysteine-mediated photoreduction (Motta et al., 2020b; Zheng and Hintelmann, 2010b), the ligand is converted from a thiol to a disulfide (**Table 5**). Ascorbic acid, as a representative of the enolic acids, can readily reduce inorganic divalent Hg in aqueous solution to Hg^0. Studies in our laboratory show that the reaction is thermal and not affected by actinic light. When ascorbic acid is in excess (>10:1) relative to Hg^{2+}, the reaction rate is not significantly affected by increasing ascorbic acid concentration. The reaction rate is highest in the pH

1050 range where the hydrogen ascorbate ion ($HAsc^-$) is dominant and the hydrolysis of Hg^{2+} is not complete, i.e., typical pH values for atmospheric hydrometeors (≤ 5.5). Presumably, $HgOH^+$ (aq) forms a reactive complex with $HAsc^-$, $Hg(HAsc)^+$, which is labile to the elimination of water in a heterolytic process, forming Hg^0 and dehydroascorbate as the final product. Enols act as atmospheric intermediates and it is doubtful whether they are present in high concentrations that would make them interesting as reducing agents for atmospheric Hg^{2+}. In any case, $k_{Hg^{2+} + HAsc^-}$ is relatively high (~ 0.17 min^{-1}, **Rxn W16b**, **Table 4**).

1055 **Rxn W17. Hydroquinones and polyphenols**

The quinonic (Zheng et al., 2012) and fulvic (Yang et al., 2020a) units in NOM act as key red-ox centers. How this happens at the molecular level is being investigated by studying model compounds that contain the redox-active group but lack other functional groups (Zhao et al., 2021). The simplest quinone forms a red-ox pair with the corresponding hydroquinone in the half-reaction:

(Rxn 9)
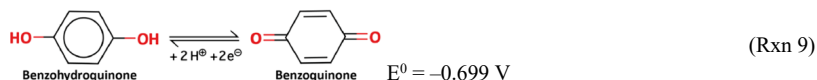
Combined with the half-reaction in **Rxn 3**, this gives a $\Delta E^0 > 0$ for $Hg^{2+} + C_6H_4(OH)_2 \rightarrow Hg^0 + C_6H_4(=O)_2 + 2\ H^+$, i.e.
1060 thermodynamically feasible. Relatively slow reduction of Hg^{2+} to Hg^0 by hydroquinone occurs in the dark in dilute aqueous solution
$(8.2 \pm 2.4) \times 10^{-5}\ s^{-1}$). The results are consistent with a reaction mechanism involving a hydroxyphenoxymercuric complex or via
ipso-mercuration followed by electron shuttling and elimination of Hg^0 and H_2O:

(Rxn 10)
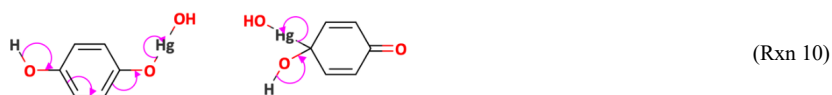
The aqueous photochemistry of quinones is complicated and can involve both ground and excited state reactions as well as free radicals
(Görner, 2019). Concerning the interaction of benzoquinone with Hg under actinic light, one study shows a significant oxidation (~0.6
1065 h^{-1}) of Hg^0 in Cl$^-$ enriched water (see above, Lalonde et al., 2001), whereas another study shows a photoreduction of $Hg^{II} \rightarrow Hg^0$ of
about the same magnitude (~0.8 h^{-1}) under anaerobic conditions and in the absence of strongly complexing inorganic ligands (Zhao et
al., 2021). An anthraquinone (AQ) derivative (AQ-2,6-disulfonate) is an effective electron shuttle that facilitates electron transfer from
metal-reducing bacteria (MRB) to Hg^{II} (Lee et al., 2018), as well as from Hg^0 (aq) to organic thiols (R-SH) during oxidative complexation
to form $Hg(SR)_2$ (Zheng et al., 2013). Zheng et al. (2013) reported that AQDS(aq) alone is unable to oxidize Hg^0 or reduce Hg^{II} under
1070 dark and anaerobic conditions. AQDS-assisted biotic Hg^{II} reduction by the MRB *Shewanella oneidensis* MR-1 is associated with
negative charge scavenging, which temporarily increases the content of reduced AQDS species, such as AQH$_2$DS and semiquinone
radicals (Lee et al., 2018). The reduced species AQH$_2$DS alone is a potent reductant of Hg^{II} in the dark. On the other hand, Hg^{II} is
efficiently reduced to Hg^0 in a UVB-irradiated aqueous solution containing dissolved AQDS (~10^{-3} M^{-1} s^{-1}). The reactive species is
tentatively photohydrated AQDS (AQH$_2$(OH)DS) interacting with Hg^{II} by forming a photolabile bidentate O–coordinated mercuric
1075 complex. In conjunction with a strong isotope effect (**Section 8.4**), photoreaction is likely to occur via a paramagnetic intermediate (a
mercurous semiquinone biradical complex). The reaction rate decreases to ~0.2 h^{-1} in the presence of dissolved O_2 (Zhao et al., 2021).
Hg^{II} interacts with ortho-QH$_2$ moieties such as those in natural polyphenols of humic substances and tannins (Jerzykiewicz, 2013). A
direct reaction yields redox-active Hg^I complexes with ligands of semiquinone radical character that eventually may decompose into
Hg^0 (Jerzykiewicz et al., 2015). Reaction kinetic and mechanistic studies more applicable to the environment are not available.

1080 **Rxn W18. Thiols**

Hg^{2+} and CH_3Hg^+ bind extremely strong to heavier hydrochalcogenide groups (such as RSH and RSeH) and other corresponding groups
of reduced chalcogenides, such as sulfides and disulfides, etc. (Skyllberg, 2011). Most relevant, both inorganic (e.g. H_2S, CS_2) and
organic (CH_3SH, CH_3SCH_3), low molecular weight reduced sulfur compounds have short lifetimes (Warneck, 1988) and therefore have
no effect on aqueous Hg speciation. It is questionable whether reduced sulfur/thiol groups associated with macromolecular organic
1085 compounds in aerosols influence internal Hg speciation. Photo-reduction of divalent Hg by lighter aliphatic thiols is slow (< 10^{-7} s^{-1}, Si
and Ariya, 2011), while that by thioglycolic is slightly faster (2.3 x 10^{-5} s^{-1}, Si and Ariya, 2015), but hardly significant in the atmosphere.

6.2 Organic mercury

6.2.1 Demethylation channels

Biogenically produced organo-Hg in the environment is almost exclusively methylated Hg, although there are a few reports of the
1090 presence of ethyl Hg (Wu et al., 2023b), which must have a natural source. However, only methylated Hg has been detected in air. As
mentioned above, DMHg is a major source of MMHg$^+$ compounds in the atmosphere through gas-phase degradation. Gaseous MMHg$^+$
species (Lee et al., 2003) can potentially react homogeneously to inorganic Hg, but as MMHg$^+$ species are only semi-volatile and have
a high Henry's constant, they are more likely to be rapidly absorbed on aerosols. MMHg$^+$ species have been detected in cloud water (Li
et al., 2018; Weiss-Penzias et al., 2018), fog water (Weiss-Penzias et al., 2012), rain water (Conaway et al., 2010; Won et al., 2019) and
1095 snow (St Louis et al., 2007). Photolytic demethylation of dissolved DMHg occurs in pure water (Chen et al., 2024) incubated with

sunlight ($CH_3HgCH_3 \xrightarrow{h\nu, +H^+} CH_3Hg^+ + CH_4$, ~0.32 ± 0.07 d^{-1}, West et al., 2022). Acidolytic demethylation of DMHg to MMHg$^+$ species is of very minor importance and only occurs at low pH (Maguire and Anand, 1976; Wolfe et al., 1973). A theoretical study of $CH_3HgOH_2^+$ and CH_3HgOH, which dominate the speciation of MMHg$^+$ in natural waters without significant levels of Cl$^-$ and reduced sulfur ligands including NOM, indicates that $CH_3HgOH_2^+$ can be excited to the triplet state by sunlight, and this state dissociates into CH$_3$

1100   and Hg^I radicals (Tossell, 1998). An experimental room temperature study of the photo-degradation of CH_3HgOH (aq) when irradiated by a Xe lamp with a filter blocking wavelengths < 290 nm gave a rate constant of (2.2 ± 0.2) × 10^{-4} s^{-1} (Gårdfeldt et al., 2003). Rapid indirect demethylation of MMHg$^+$ species by a bimolecular process with the OH radical occurs at the limit of what diffusion allows (9.83 ± 0.66) × 10^9 M^{-1} s^{-1}, Chen et al., 2003). In natural waters, select reactive oxygen species, such as singlet oxygen (see above, Suda et al., 1993; Zhang and Hsu-Kim, 2010), have been suggested to cause Hg^{II} demethylation, but their reactivity has not been directly

1105   quantified. Instead, its presence has been suggested based on the results of added scavenger/promoter tests, some of which may give misleading results for some water compositions (Han et al., 2017). Chen et al. (2003) concluded that OH-initiated demethylation is comparable to the rates of MMHg$^+$ photodegradation reported in situ in natural waters. These researchers found that, in addition to inorganic Hg^{II}, Hg^0 was a by-product of OH-initiated degradation in an O$_2$-saturated system, presumably by homolytic substitution.

6.2.2 Methylation channels

1110   The paucity of empirical data renders the budget of tropospheric MMHg$^+$ species highly uncertain. A recent estimate of the MMHg$^+$ pool size is 5.5 Mg, associated with a lifetime of 1.9 d, of which one of the major sources is inferred to be in-cloud methylation (Wu et al., 2024b). The potential for atmospheric biotic methylation is considered limited, despite the presence of pathogens and bacteria in aerosols and hydrometeors, because Hg methylating microbes (possessing two important methylation genes, hgcA and hgcB, Parks et al., 2013) usually thrive in anaerobic environments, in contrast to the distinctly oxic environment of atmospheric waters. However, many

1115   unknowns about the potential for Hg^{II} methylation under oxic conditions need to be resolved (Sonke et al., 2023). There have been extensive studies on the abiotic methylation of Hg^{2+} (Ullrich et al., 2001). Methylating agents that have been discussed as important for MMHg$^+$ formation in the atmosphere are oxygenated hydrocarbons containing a methyl group (Yin et al., 2012; Hammerschmidt et al., 2007). Some of them have properties that allow competitive photochemical reduction and methylation of Hg^{2+} (Yin et al., 2012). Earlier studies have investigated photochemical Hg^{2+} methylation by irradiation in deep UV (Yin et al., 2012; Akagi et al., 1974; Hayashi et al.,

1120   1977), making it impossible to generalize these results to the lower atmosphere. Formation of MMHg$^+$ species was observed in the dark in dilute Hg^{II} solutions (1 nM) containing an excess of acetic acid (100:1 M/M) with an apparent first-order rate constant of 5.4 × 10^{-6} s^{-1} in artificial rainwater (pH 4.9, Gårdfeldt et al., 2003). When the system is exposed to sunlight, photo-demethylation occurs which counteracts MMHg$^+$ formation mediated by acetic acid/acetate and within hours the MMHg$^+$ concentration enters a steady state (~2.5% of inorganic Hg^{II}). Hammerschmidt et al. (2007) have pointed out that the average ratio of MMHg$^+$ to reactive Hg^{II} measured in North

1125   American continental precipitation (2.5 ± 0.6%) is in agreement with the findings of the above laboratory study. The methylation takes place intramolecularly in the acetato-mercuric complexes present in solution concerted with decarboxylation (Gårdfeldt et al., 2003; Yin et al., 2012; Akagi et al., 1974): $\left[Hg(CH_3COO)_n\right]^{2-n} \rightarrow CH_3Hg^+ + CO_2 + (n-1)\, CH_3COO^-$.

7 Multi-phase transformations

Multiphase transformations deal with the dynamics and chemistry at various interfaces and media, such as aerosol particles and cloud

1130   droplets, interacting heterogeneously with gases and solute species. Although there is a significant amount of literature in this field (Ariya et al., 2015; Subir et al., 2011, 2012), it is mostly irrelevant to the atmosphere.

7.1 Gas-particle partitioning and reactive gas uptake

The behavior of gaseous Hg^0 atoms and Hg^{II} molecules in interacting with the atmospheric condensed phase differs. The dominant Hg^0 pool is of limited water solubility, and the uptake of Hg^0 vapor is low to aerosol surfaces, to the limited extent that it has been investigated.

1135   Gas phase Hg^{II} molecules, "GOM", have Henry's coefficients several orders of magnitude greater than that of Hg^0, favoring the liquid phase. Heterogeneous processes that keep GOM adsorbed, reversibly or irreversibly, modified by ligand exchange, or dissociated to Hg^0 by reduction on surfaces are key parameters that need to be characterized to appropriately parameterize chemical transport models.

7.1.1 HgCl₂

Understanding the transformation from GOM to PBM through gas phase processes (condensation, **Section 5.1.4**) and aerosol surface
interaction (**Section 3.2**) is crucial for parameterizing deposition. Since the separation of GOM from PBM with current methods is tentative,
the accuracy of studies of Hg^{II} distribution between gas and condensed phase, performed by preconcentration in laboratory experiments with
nebulized aerosol (Rutter and Schauer, 2007b, a) and in the field (Amos et al., 2012), is retrospectively ambiguous. Fitting observational
data to an equilibrium $GOM + PM_{2.5} \overset{1/T}{\Longleftrightarrow} PBM$ according to a van't Hoff type relationship $\log_{10}(K_{gp}^{-1}) = a + b/T$ is used in models
to calculate the volatilization of GOM from atmospheric aerosols, where K_{gp} (**Eq. 8**) is here weighted by the inverse of the mass
concentration of fine particulate matter ($PM_{2.5}$, Shah et al., 2021). The partitioning expression does not consider that the interaction between
GOM and a surface is significantly influenced by the composition of the surface layer. $HgCl_2(g)$ has a high partitioning for particles
consisting of typical alkali metal salts such as chlorides, nitrates, and sulfates (Mao et al., 2021; Malcolm et al., 2009). To compensate, global
Hg models treat the uptake of GOM onto sea salt particles separately as an irreversible first-order process parameterized by wind speed and
humidity. The equilibrium studies conducted at atmospheric pressure do not provide insights into the dynamics of the system, as the
experiments are limited by mass transport, which negates the possibility of obtaining quantitative information on reactive uptake. As an
alternative (Liu et al., 2022), partition coefficients have been calculated for individual GOM species on the basis of theoretical predictions
of both adsorption and absorption (Wu et al., 2024a). The reactive uptake of $HgCl_2(g)$ on surfaces representative of inorganic and organic
primary and secondary atmospheric aerosols has recently been studied using the fast flow technique coupled to an ion drift chemical
ionization mass spectrometer, (ID-CI-MS). The reported data (Mao et al., 2021; Khalizov and Mao, 2023) are summarized in **Table 6**.

Table 6. Reactive uptake of $HgCl_2(g)$ on surfaces

Chemical	Structural formula[33]	γ_{net}[34]		Surface coverage (θ, %)	Lifetime (τ, days)
		γ_{net}^0,	γ_{net}^∞		
Inorganic aerosol surrogates					
Na_2SO_4		3.1×10^{-2}	1.7×10^{-3}	98	0.1
NaCl		2.2×10^{-2}	1.9×10^{-3}	65	0.1
$(NH_4)_2SO_4$		1.4×10^{-2}	7.0×10^{-4}	5.6	0.2
NH_4NO_3		3.6×10^{-3}	3.3×10^{-4}	0.3	0.7
Primary organic aerosol (POA) surrogates					
Levoglucosan		1.1×10^{-2}	2.9×10^{-4}	9.6	0.2
Pyrene		2.1×10^{-3}	5.0×10^{-4}	1.3	1.2
Perylene		3.0×10^{-3}	5.2×10^{-4}	3.8	0.8
Soot		8.9×10^{-5}		0.1	20.2
Secondary organic aerosol (SOA) surrogates					
Citric acid (H_3cit)		$< 1 \times 10^{-5}$	$< 1 \times 10^{-5}$	< 0.02	> 242
NaH_2cit		6.9×10^{-5}	5.0×10^{-5}	< 0.02	35
Na_2Hcit		2.4×10^{-3}	2.3×10^{-4}	1.2	1.0
Na_3cit		8.4×10^{-3}	6.6×10^{-4}	7.5	0.3
Pimelic acid (H_2pim)		1.1×10^{-3}	1.8×10^{-4}	1.0	2.2
NaHpim		2.2×10^{-3}	3.1×10^{-4}	1.4	1.1
Na_2pim		8.2×10^{-3}	8.0×10^{-4}	11.6	0.3
Succinic acid (H_2suc)		9.3×10^{-4}	1.0×10^{-4}	0.02	2.6
NaHsuc		2.0×10^{-3}	3.6×10^{-4}	0.7	1.2
Na_2suc		8.3×10^{-3}	6.6×10^{-4}	6.2	0.3
Dioctyl sebacate		2.6×10^{-2}	7.1×10^{-3}	153	0.1

---

[33] For soot, a clichéd structure is used that does not claim to be accurate.
[34] Calculated by Eq. 5

The data in **Table 6** are for dry surfaces, where γ_{net}^0 is the initial uptake coefficient, which is relevant throughout the lifetime of the aerosol as the surface coverage by atmospheric $HgCl_2$ remains unchanged and low. In the presence of sea salt aerosols (>0.6 μm, initially at pH 8) that dominate in the marine air, where NaCl represents >95% of its mass, the lifetime of $HgCl_2$ (g) is expected to be between 4 and 20 h depending on aerosol loading (Mao et al., 2021). When the relative humidity exceeds ~75%, a hygroscopic sea salt droplet is formed as the salt deliquesces, and a highly mobile surface phase in which Hg^{II} is equilibrated in ionic form as $HgCl_4^{2-}$ may contribute to a more rapid GOM loss in marine air (Holmes et al., 2009). Ammonium salts such as nitrates and sulfates are primarily found in secondary particles, typically in urban and agricultural-rural air. Although $HgCl_2$ uptake is lower here, its lifetime is comparative due to the higher particle number and the large surface area they generally represent. These semi-volatile ammonium salts do not occur in isolation but coexist with oxygenated organics formed through photochemical activity, seeding the formation of secondary aerosols, which constitute the primary fraction of the atmospheric burden of organic aerosols (OA, Jimenez et al., 2009). The acidity of secondary organic aerosols (SOA), a dominant component of $PM_{2.5}$, affects $HgCl_2$ uptake by controlling the acid-base equilibria of characteristic chemical species such as aliphatic dicarboxylic acids, aromatic polycarboxylic acids, and other oxygenated multi-functional organics in the aerosol. Of the diprotic acids in **Table 6**, the reactivity becomes noticeable only after the first deprotonation step at pH 4.5 - 5.5. For the triprotic citric acid, it occurs after the second step at pH 6.5. The adsorption of $HgCl_2$ on primary organic aerosol (POA) surfaces is significant in the presence of levoglucosan, an anhydrosugar, which is a fingerprint of fire activity. Nevertheless, the interaction between $HgCl_2$ and polyaromatic hydrocarbons (PAHs) derived from carbonaceous fuel combustion is more constrained, occurring between the electrophile $HgCl_2$ and the π electrons delocalized over the aromatic fused ring skeleton. The observed adsorption on fresh soot, porous of the graphitic type with a high specific surface area, is more than one order of magnitude lower than for the PAHs of the minor type studied (pyrene, perylene). If morphology affects uptake, so does the state of the surface phase, as a diester of sebacic acid (close homologue of pimelic acid), octyl sebacate, a lubricant, is more reactive to $HgCl_2$ than the microcrystaline pimelic acid film. The adsorption of $HgCl_2$ on mineral surfaces (dust aerosols) represented by iron (hydr)oxides has not been studied experimentally, but calculations indicate a partition coefficient (K_{gp}) for α-Fe_2O_3 that exceeds that for NaCl by three orders of magnitude (Tacey et al., 2018b). The studies listed in **Table 6** were performed without observing redox chemistry (i.e., no Hg^0 was detected being emitted from the $HgCl_2$-exposed surfaces when heated up to 120°C), but a combined study using FF-ID-CIMS and Raman spectroscopy shows that exchange reactions between gaseous mercuric compounds are catalyzed by surfaces, such that $HgCl_2$ and $HgBr_2$ molecules in the presence of a deactivated surface produce the mixed BrHgCl molecule (Mao and Khalizov, 2021), which is also volatile. Due to the rapid exchange reactions, the prospect of accurately speciating GOM by pre-concentration on filters and cation exchange membranes, as discussed previously (**Section 4.1**), is unlikely.

7.1.2 Hg^0

A challenge in studying gas-phase or liquid-phase initiated reactions is the potential for side reactions and phase changes to occur during experiments. Thus, a portion of the loss of gas-phase Hg^0 in laboratory experiments designed to study homogeneous oxidation (e.g. by O_3, Snider et al., 2008; $NO_3^\bullet$, Sommar et al.,1997 etc.) has been linked to a heterogeneous rate component (k_{surf}) occurring on new surfaces that form during experiments (product clusters undergoing particle growth in free suspension, **Section 5.1.4**) and/or on initially deactivated existing surfaces (reactor walls) that begin to catalyze Hg^0 surface oxidation as deposits form (Sommar et al., 1997; Medhekar et al., 1979). For example, in a series of spherical reactors of varying surface-to-volume ratios (S/V), Pal and Ariya (2004b) observed the loss of Hg^0 by reaction with an excess of O_3 in N_2 following:

$$-d[Hg^0]/dt = \left\{ k_{gas} + \frac{S}{V} \cdot k_{surf} \right\} \cdot [Hg^0] \cdot [O_3] = k_{net} \cdot [Hg^0] \cdot [O_3] \qquad (10)$$

where k_{gas} (cm^3 $molecule^{-1}$ s^{-1}) is the gas-phase reaction rate, S/V (cm^{-1}), k_{surf} (cm^4 $molecule^{-1}$ s^{-1}) is the surface rate loss, and [O_3] (molecules cm^{-3}) is the gas-phase O_3 concentration. In the S/V range 0.28 - 0.93 cm^{-1}, k_{net} increased by 30% simultaneously with the formation of particles (Snider et al., 2008) during the experiments, which started homogeneously. Using a fluorocarbon film smog chamber (9 m^3, S/V = 0.03 cm^{-1}), Rutter et al. (2012) studied the influence of SOA (yielding a ~100-fold increase in the surface area

of the system) and secondarily formed $^\bullet$OH (at ambient level due to added scavenger) generated from an irradiated mixture of O_3 and various biogenic and anthropogenic VOCs (at a level ~one order of magnitude higher than ambient) on the oxidation of Hg

1200 atoms (at a level ~two order of magnitude higher than ambient). Neither Rutter et al. nor subsequent researchers (Lyman et al., 2022) have been able to identify evidence that interaction with photochemical smog particles significantly contributes to the oxidation of Hg^0. Nevertheless, few studies concerning Hg^0 uptake have been conducted to a sufficiently rigorous standard, employing techniques used in the specific studies of heterogeneous processes, to produce a kinetic formalism that can be related to atmospheric models. These studies, conducted with a coated-wall laminar flow tube reactor, concern the light and moisture dependent uptake of Hg^0

1205 (detected by CV-AFS) that may be photocatalytic, on the major metal oxides (TiO_2, Fe_2O_3, FeOOH, Al_2O_3) present in mineral dust aerosols (Kurien et al., 2017; Lee et al., 2022). The first three metal oxides have semiconductor properties with band gaps that allow photoexcitation in the UVA (≤ 395 nm) and visible (≤590 nm) regions, while Al_2O_3, the second most abundant mineral oxide in the Earth's crust after SiO_2, is an insulator but has some thermal conductivity. It has been established for over half a century that Hg^0 vapor in the presence of O_2 over an irradiated TiO_2 surface is consumed by reactive uptake (Kaluza and Boehm, 1971) via the

1210 following tentative mechanism:

$$TiO_2 \xrightarrow{h\nu} e_{CB}^- + h_{VB}^+$$
$$e_{CB}^- + O_2 \,(ads) \rightarrow O_2^{\bullet-} \,(ads)$$
$$h_{VB}^+ + H_2O|OH^- \,(ads) \rightarrow HO^\bullet \,(ads) + (H^+(ads))$$
$$Hg^0 \,(ads) + HO^\bullet \,(ads) \rightarrow \; ^\bullet Hg^I OH \,(ads) \qquad\qquad (Rxn\ 11a\text{-}g)$$
$$^\bullet Hg^I OH \,(ads) + O_2 \,(ads) \rightarrow HgO \,(ads) + HO_2^\bullet \,(ads)$$
$$HO^\bullet \,(ads) + HO_2^\bullet \,(ads) \rightarrow H_2O \,(ads) + O_2 \,(ads)$$
$$HO_2^\bullet \,(ads) + O_2^{\bullet-} \,(ads) \xrightarrow{H^+} H_2O_2 \,(ads) + O_2 \,(ads)$$
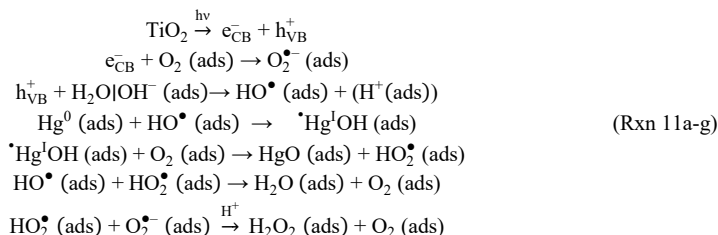
When excited by light of a wavelength shorter than the band gap energy, the generation of electron-hole pairs (e_{CB}^-, h_{VB}^+) occurs in the conduction and valence bands (**Rxn 12a**). Electrons and holes transported to the particle surface initiate redox chemistry by reacting with H_2O and O_2 molecules to form reactive oxygen species (ROS, **Rxn 11b, c**). The oxidation potential of h_{VB}^+ exceeds +2.27 eV in the TiO_2, Fe_2O_3 and FeOOH cases, which is sufficient to generate hydroxyl radicals from surface water (**Rxn 11c**) that can oxidize

1215 adsorbed Hg^0 (**Rxn 11d**). The reported uptake coefficients are in the range of $<10^{-10}$ to $>10^{-4}$ (based on BET surface area), with the relative reactivities $Fe_2O_3 \lesssim FeOOH < Al_2O_3 < TiO_2$, where γ_{net}^∞ without irradiation is below the detection limit. The uptake of Hg^0 on the iron (hydr)oxides is less than 10^{-8} under both UV and visible light, and inhibited by humidity, as was the case for Al_2O_3, which shows measurable uptake under UV irradiation ($\gamma_{net}^\infty = 1.2 \times 10^{-8}$). The photo-initiated uptake of Hg^0 on TiO_2 is significant, especially in UV light at low humidity ($\gamma_{net}^\infty > 3 \times 10^{-5}$, diffusion-controlled limit). However, as with Al_2O_3, it shows reversibility (desorption of Hg^0) in

1220 the presence of water vapor during darkness (Lee et al., 2022), while Hg^0 exhibits almost irreversible binding to iron (hydr)oxides at the temperatures studied (< 150ºC, Kurien et al., 2017). Based on the limited published data, only under conditions of low humidity and very high mineral dust aerosol loading can the uptake of Hg^0 be discussed as having any effect on the atmospheric cycling of Hg^0. It is worth noting that there is no corresponding experimental data for $HgCl_2$ uptake on mineral dust surrogates.

The uptake of Hg^0 on ice, studied by migration of radioactive Hg isotopes into ice spheres in a packed bed flow tube exposed to a strong

1225 temperature gradient, can be described by reversible adsorption without significant solvation. The observations were in accordance with a Langmuir isotherm, where the adsorption equilibrium can be described thermodynamically by Bartels-Rausch et al. (2008):

$$-RT\ln K = \Delta H_{ads}^0 - T\Delta S_{ads}^0 = -28000 + 38\cdot T \qquad\qquad (11)$$

where K is the Langmuir absorption constant (**Eq. 7**), R is the gas constant, T is absolute temperature, ΔH_{ads}^0 and ΔS_{ads}^0 are the enthalpy and entropy of adsorption, respectively. Compared to the Henry's law equilibrium for Hg^0 (0.18 at 5 ºC), the Langmuir adsorption coefficient on ice, both expressed in a dimensionless way, is much smaller even at temperatures lower than its freezing

1230 point (2.2×10^{-5} at 220 K), which is most relevant for polar regions and the upper troposphere. Therefore, in the atmospheric and polar environment, uptake of Hg^0(g) on ice surfaces is negligible.

7.2 Reduction of mercurial species on surfaces

Computational chemistry studies report that adsorption of mercuric halides on dry salt- or mineral-like surfaces reduces the energy required for reduction to Hg^0 (Tacey et al., 2016), and that reduction of $HgCl_2$ and $HgBr_2$ to Hg^0 on iron oxide aerosols requires the
1235 presence of actinic light (Tacey et al., 2018a). Breaking the first Hg–X bond is possible either thermally or photolytically, while the second requires photons with $\lambda \leq 461$ nm. To release Hg^0 from the surface, an excitation energy of 2.59 eV ($\lambda \leq 479$ nm) is required in a photoinduced charge transfer process between the surface and the adsorbate.

The photoreduction of particle-bound Hg^{II} has been the subject of experimental investigation (Tong et al., 2013; Tong et al., 2014). In these experiments, aerosolized surrogates, doped with $HgCl_2$, were generated and dried in laboratory air and subsequently captured on
1240 filters, which were then exposed to light with three spectral options in a flow-through reactor. Photoreduction on NaCl aerosols occurs in actinic light (both in UV and visible light, with approximately 2.5% and 2.0% of Hg^{II} reduced, respectively, during a 30-minute exposure, normalized per 100 W m^{-2} irradiation). However, the presence of iron species (mainly Fe^{III} rather than Fe^{II}) has been observed to exert some inhibitory effects (Tong et al., 2013). In contrast, photoreduction on carbon-based synthetic aerosols has been demonstrated to be more significant but also more variable. For example, Hg^{II} on adipic acid aerosols exhibits a comparatively 8% reduction (per same
1245 time unit and normalization as above), while on levoglucosan it is less than 2% (Tong et al., 2014). It should be noted, however, that these experiments were carried out without O_2 in the carrier gas stream.

The reduction of Hg^{II} in ice in the presence of organics has been studied in an ice-coated flow tube at atmospheric pressure under irradiation with light between 300 nm and 420 nm (Bartels-Rausch et al., 2011). O_2-free ice matrices containing 60 nM Hg were doped with a stoichiometric excess (up to 50:1 M/M) of either benzophenone (a strong photosensitizer), oxalic acid-oxalate (forming
1250 photolabile Hg^{II} complexes), or humic acid (ditto photolabile complexes), which upon irradiation accelerated the release of Hg^0 with a maximum rate constant of $\sim 5 \times 10^4$ M^{-1} s^{-1} observed for benzophenone at high pH. The presence of O_2 (20% in the gas stream), the introduction of sea ice-like conditions, or a large drop in temperature (from 270 to 250 K) or pH (to 4) resulted in diminished photoreduction. The mechanism by which the Hg^{II} reduction is sensitized by benzophenone is challenging to ascertain. One potential mechanism involves the dissociation of an excited state of the major species, $Hg(OH)_2$, which has been reported to be photolabile as a
1255 solute in water (Xiao et al., 1994). A controlled laboratory study of light-irradiated natural snow samples at a temperature of -10°C revealed that the release of Hg^0 follows first-order kinetics with a coefficient between 0.18 and 0.25 h^{-1}, corresponding to a natural lifetime of $4 - 5.6$ h (Dommergue et al., 2007). However, no monitoring of Hg^{II} in the condensed phase was conducted. Given that light does not penetrate the entire snowpack, it can be assumed that a Hg^{II} gradient towards depletion at the top is established.

Brominated mercurials that are present in the Arctic environment during AMDE may play a role in light-induced Hg re-emission from
1260 the cryosphere to the atmosphere (cf. **Fig. 2**). A computational study (Carmona García, 2024) suggests that $HgBr_2$ in solution has an increased absorption cross section for wavelengths longer than 290 nm compared to $HgBr_2$ in the gas phase, while the bromomercurate anions ($Hg^{II}Br_3^-$ and $Hg^{II}Br_4^{2-}$) have a comparatively even higher absorption in actinic light. The low-energy excited states of $HgBr_2$, $Hg^{II}Br_3^-$, and $Hg^{II}Br_4^{2-}$ in solution are characterized by electronic transitions in which the electron density is mainly transferred from the Br atoms to the Hg atom, indicating a significant photoreductive character upon light absorption leading to generation of Hg^I species
1265 ($^\bullet Hg^I Br$, $^\bullet Hg^I Br_2^-$ and $^\bullet Hg^I Br_3^{2-}$) and a bromine atom. The photoreductive character is also recognized for the aforementioned Hg^I species in their electonically excited states, which plausibly dissociate via an LMCT mechanism with Hg^0 as end product. Predicted peak photolysis constants for the polar spring (March, ~80 °N) are 3.9 x 10^{-6}, 3.8 x 10^{-4} and 7.9 x 10^{-5} s^{-1} for $HgBr_2$, $HgBr_3^-$ and $HgBr_4^{2-}$, respectively.

For pure heterogeneous reduction, there is experimental evidence that $SO_2(g)$ can reduce HgO(s) at room temperature via $Hg_2^I SO_4$
1270 (Zacharewski and Cherniak, 1987) to Hg^0, HgS and $HgSO_4$ as stable products (Scott et al., 2003), and that $O_3(g)$ in the presence of actinic light can reduce $HgCl_2/HgBr_2(s)$ to mercurous species (Ai et al., 2023, which may tentatively undergo Hg^0/Hg^{II} disproportionation). In the latter exploratory study, single-particle reactors, 10–50 μm in size, synthesized from mercuric halides in a single-walled carbon nanotube, were prepared and made to levitate during the experiments using optical means. The turnover of HgX_2 by breaking an Hg–X bond was measured by time- and position-resolved Raman spectroscopy, which also showed that

1275 the decomposed X atom was bound to the carbon material (X = Cl, Br). Heterogeneous reactions of this type, i.e.,

$$O_3 \xrightarrow{h\nu} O_2 + O(^3P)$$
$$HgX_2 \text{ (s)} + O(^3P) \rightarrow \ {}^\bullet Hg^I X \text{ (s)} + XO^\bullet \text{ (g)}$$
$$XO^\bullet + O(^3P) \rightarrow X^\bullet + O_2$$
$$2 \ {}^\bullet Hg^I X \text{ (s)} \rightarrow Hg_2X_2 \text{ (s)} \rightleftarrows Hg^0 \text{ (ads)} + HgX_2 \text{ (s)}$$

(Rxn 12)
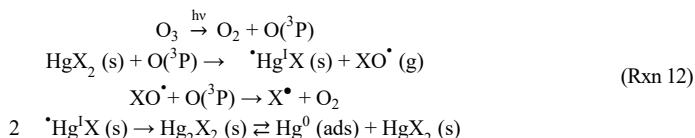
may explain why KCl coated denuders do not work as a robust quantitative method for measuring GOM in ambient air (Lyman et al., 2010). Since a gas-phase reaction $HgX_2 + O/O_3 \rightarrow \ ^\bullet Hg^I X + XO^\bullet (+ O_2)$ is endothermic (≥ 66 kJ mol^{-1}) and therefore unlikely, the results of a steady-state study (Tong et al., 2021) claiming gas-phase photoreduction of HgX_2 in the presence of O_3 and light can instead be attributed to the above-mentioned heterogeneous reactions.

1280 Additionally, voltammetry can provide valuable insights into the redox chemistry of mercury. Hg^0 is frequently employed as the working electrode, exhibiting a high overpotential for the reduction of H_3O^+ to H_2. This enables the utilization of standard potentials as negative as -1 V in acidic solutions and -2 V in basic solutions. The surface of the hanging mercury drop electrode (HMDE) can be readily renewed by extruding a new drop. In a study by Giannakopoulos et al. (2012), the interfacial adsorption mechanism of gallic acid onto HMDE was investigated, and a series of easily reducible Hg^{II} complexes with mono-, di-, or tridentate gallic acid

1285 ligation were identified.

7.3 Dark oxidation of Hg⁰ accelerated by freeze-concentration effects

Slow oxidation of dissolved Hg^0 by O_2 occurs in aquatic systems in the presence of Cl^- ions (Amyot et al., 2005; Wang et al., 2023). However, upon freezing, most of the solutes are separated from the forming ice phase and concentrated in the remaining liquid at a significantly reduced pH (Bartels-Rausch et al., 2011). In experimental mimics of the micro-pockets of solution that occur in ice,

1290 experiments in the presence of O_2, H_2O_2, and HONO each result in significant Hg^0 oxidation. It has been postulated that protonated forms, $HO-OH_2^+$ and $ONOH_2^+$, are responsible for the oxidation processes, which can be classified as strongly exothermic based on the provided thermodynamic data (O'concubhair et al., 2012). It should be added that neither dilute H_2O_2 (aq) nor HONO (aq) will oxidize Hg^0 (aq) to any significant extent at room temperature (Kobayashi, 1987).

7.4 Surface-catalyzed reduction of Hg^{II} in aqueous solution

1295 In the presence of a solid phase of ferric (hydr)oxide and dissolved di- or monocarboxylic acids under oxic conditions, reduction of Hg^{II} in aqueous solution to Hg^0 occurs upon UV irradiation (Lin and Pehkonen, 1997). Systems studied that show photoreduction of Hg^{II} are goethite (α-FeOOH) + oxalate/formate, hematite (α-Fe$_2$O$_3$) + oxalate, and maghemite (γ-Fe$_2$O$_3$) + oxalate. The experiments with filtered Xe light were conducted with 10 μM HgCl$_2$, 1 mM organic acid, and 0.1 g L^{-1} ferric hydr(oxide) suspension, with a starting pH of 3.9. During some of the experiments, the pH increased substantially, resulting in the dominance of oxalate over

1300 hydrogen oxalate. Unlike oxalate, formate alone is not capable of reducing Hg^{II} to Hg^0 in actinic light. It requires irradiation in the deep UV by processes such as (Leonori and Sturgeon, 2019):

$$Hg^{2+} + 2\ HCOO^- \rightleftarrows Hg(OOCH)_2 \xrightarrow{h\nu} Hg^0 + 2\ CO_2 + H_2$$
$$Hg^{2+} + HCOO^- \rightleftarrows Hg^{II}(OOCH)^+ \xrightarrow{h\nu} Hg^{\bullet+} + HCO_2^\bullet \text{ and } Hg^{\bullet+} + HCOO^- \rightarrow Hg^0 + HCO_2^\bullet$$

(Rxn 13)
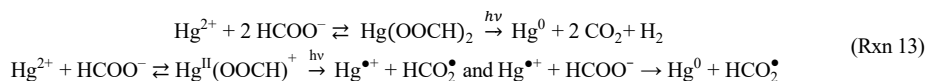
One study describes Hg^{II} reduction mediated by the carbon dioxide radical anion ($CO_2^{\bullet-}$) generated from formic acid via photosensitization by visible light-excited naphthoquinone (Berkovic et al., 2012). Iron(III) complexes with formate and oxalate are photolabile in the UVA and into the visible, where a fast 1e$^-$ LMCT step generates Fe^{2+} and eventually $CO_2^{\bullet-}$ that initiates a chain

1305 process (Mangiante et al., 2017; Baxendale and Bridge, 1955):

$$\equiv Fe^{III}-OH + HC_2O_4^-|HCOO^- \rightleftarrows \ \equiv Fe^{III}-C_2O_4^-|OOCH + H_2O$$
$$\equiv Fe^{III}-C_2O_4^-|OOCH \xrightarrow{h\nu} \ \equiv Fe^{II} + C_2O_4^{\bullet-}|HCO_2^\bullet$$
$$\equiv Fe^{II} \rightleftarrows \ \equiv + Fe^{2+} \text{ and } HCO_2^\bullet \rightleftarrows H^+ + CO_2^{\bullet-}$$
$$C_2O_4^{\bullet-} \rightarrow CO_2 + CO_2^{\bullet-}, CO_2^{\bullet-} + O_2 \rightarrow CO_2 + O_2^{\bullet-} \text{ and } H^+ + O_2^{\bullet-} \rightleftarrows HO_2^\bullet \rightarrow \tfrac{1}{2}\ O_2 + \tfrac{1}{2}\ H_2O_2$$
$$Fe^{2+} + H_2O_2 \rightarrow Fe^{III} + HO^- + HO^\bullet$$

(Rxn 14)

$$Hg^{II} + CO_2^{\bullet-}|Fe^{2+}{\equiv}Fe^{II} \rightarrow Hg^{I} + CO_2|Fe^{III}{\equiv}Fe^{III} \, , \, Hg^{I} + CO_2^{\bullet-}|Fe^{2+}{\equiv}Fe^{II} \rightarrow Hg^{0} + CO_2|Fe^{III}{\equiv}Fe^{III} \, (red.)$$
$$2\,Hg^{I} \rightleftarrows Hg^{0} + Hg^{II} \, (disprop.)$$
$$Hg^{0/I} + HO^{\bullet} \rightarrow Hg^{I/II} + HO^{-} \, , \, Fe^{2+} + HO^{\bullet} \rightarrow Fe^{III} + HO^{-} \, and \, H_2O_2 \, + HO^{\bullet} \rightarrow HO_2^{\bullet} + H_2O \, (ox.)$$
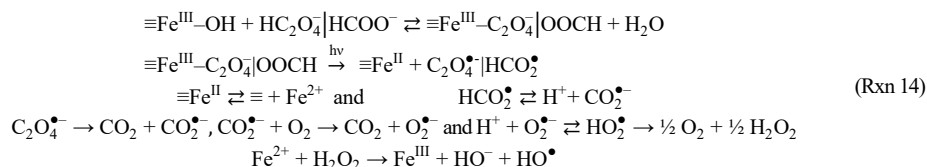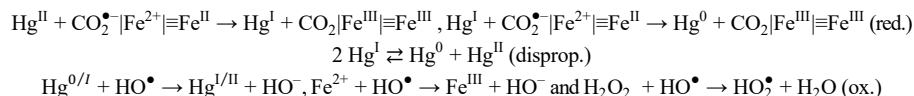
The oxic reaction system described by **Rxn 14** reaction formulas contains a number of ROS with different designations, such as the strongly reducing $CO_2^{\bullet-}$ and the strongly oxidizing $HO^{\bullet}$ as extreme cases. One subsystem is the Fenton's reagent (**Section 6.1.1**, **Rxn W6**), which produces $HO^{\bullet}$ for which each of $Hg^{0/I}$, Fe^{2+}, and H_2O_2 competes to be oxidized. Except for the heterolytic photolysis of $Hg(\eta^2\text{-}C_2O_4)$, which produces Hg^0 from Hg^{II} in a single step (**Section 6.1.2**, **Rxn W16**), the remaining redox steps involving metals

1310 are of the single-electron type. The reduction of Hg^{II} occurs by reaction with the $HCO_2^{\bullet}|CO_2^{\bullet-}$ nucleophiles (**Section 6.1.2**, **Rxn W14**), and both homogeneously and heterogeneously with dissolved and adsorbed ferrous species, respectively. A second-order homogeneous reaction coefficient of ~120 to 313 $M^{-1}\,s^{-1}$ has been determined in the near neutral pH range, with $Hg(OH)_2$ and $FeOH^+$ identified as the reactive species in solution (Amirbahman et al., 2013; Schwab et al., 2023). In anoxic conditions, the rate of Hg^0 production derived from the surface-catalyzed reduction on hematite and goethite has been described by the expression

1315 $k_{het}[{\equiv}Fe^{II}][Hg(OH)_2]$, with k_{het} of ~89 and ~78 $M^{-1}\,s^{-1}$, respectively (Amirbahman et al., 2013). In an O_2-saturated, non-bubbled solution, a photo-stationary state between Hg^{II} and Hg^0 occurs, indicating the reduction pathways (**Rxn 14 red.**) are gradually balanced by the oxidation pathways (**Rxn 14 ox.**, Ababneh et al., 2006). In the absence of Hg^0 removal, solubility limitations are easily exceeded during experiments (Lin and Pehkonen, 1997; Ababneh et al., 2006), resulting in the precipitation of colloidal Hg^0. The removal of dissolved Hg^0 by sorption on hydrous iron oxides, which is relevant here, is also documented (Richard et al., 2016).

1320 In the presence of competing anions, such as chloride, the rate of reduction decreases, in part due to the formation of metastable poorly soluble dimeric mercurous salts that compete with the disproportionation of Hg^I to Hg^0 and Hg^{II} (Pasakarnis et al., 2013).

7.5 Field observations of photoreduction in precipitation, cloud and fog

In precipitation and clouds, a strong correlation between Hg and total organic carbon was observed (Li et al., 2018; Åkerblom et al., 2015), suggesting that Hg-organics complexes are also important in aerosols. Authentic rain samples, where Hg-organics complexes

1325 dominate, show photoreduction rates in the range of $0.02 - 0.2\,h^{-1}$ (Yang et al., 2019; Saiz-Lopez et al., 2019; Fu et al., 2021). There have been a handful of measurements of Hg in cloud water (Li et al., 2018; Weiss-Penzias et al., 2018; Malcolm et al., 2003; Gerson et al., 2017; Huang et al., 2016a), but so far there seems to be only a few studies of the photoreduction rate in this category of waters (Li et al., 2018; Zhen et al., 2023; Gao et al., 2023). Photolysis rates in cloud water samples of $0.07 - 0.21\,h^{-1}$ measured in situ under actinic light and in the laboratory under UV (> 290 nm) light are consistent with those observed in precipitation. Whether the

1330 photoreduction rates observed in rain- or cloud water are representative of atmospheric aerosols is questionable. Hg^{II} in snowfall or in freshly fallen snow has been reported to be labile for photoreduction (Steffen et al., 2008; Faïn et al., 2013). In temperate urban and pristine rural snow, it has been demonstrated that within 24 h, approximately 50% (Lalonde et al., 2003; Lalonde et al., 2002) and within 48 h, up to 90% (Poulain et al., 2004) of the newly deposited Hg can be effectively recycled back to the atmosphere. Reduction is reportedly strong even in cloudy conditions and is not limited by light (Faïn et al., 2013). In general, less than 5% of the

1335 Hg content of a snowpack is in the elemental form (Hg^0), which is concentrated stratigraphically in the first few centimeters. Nevertheless, if the rates are implemented as a mean value (~0.07 h^{-1}), determining the lifetime of atmospheric Hg against wet deposition, then modelled wet deposition underestimates the observations by an average of 25% globally. Current global chemistry and transport models (GMOS-Chem) consider photoreduction on particles with the pool of Hg^{II} complexed with organic ligands as the reactant (Shah et al., 2021).

1340 ### 8 Mercury isotope systematics and fractionation

Natural Hg contains seven stable isotopes with the mass numbers 196, 198, 199, 200, 201, 202 and 204. In the 1920s, a significant separation of Hg into its isotopes was achieved through vaporization in a vacuum (Harkins and Mulliken, 1921; Mulliken, 1923; Brønsted and De Hevesy, 1921), a process that is conducted on a preparative scale through electromagnetic (Love, 1973) and photochemical (Vyazovetskii, 2012) methods. When the feed flow is in the form of DMHg, total gram quantities of highly enriched

1345   Hg isotopes can be obtained through cascade centrifugation (Babaev et al., 2010). The longest-lived radioisotope is ^{194}Hg at 444 y.
Since it does not occur naturally, it cannot be used in the dating typical of ^{14}C. Two additional unstable isotopes (^{197}Hg and ^{203}Hg
with a half-life of 64.1 h and 46.6 d, respectively) are of value in instrumental neutron activation analysis and radio-labeled Hg
compounds, due to their decay by emission of readily detectable γ rays. It was not until after the turn of the century, 80 years later,
with the development of high-precision analytical instruments such as multi-collector inductively coupled plasma mass spectrometry

1350   (MC-ICP-MS), that it became possible to measure differences in the natural stable Hg isotope composition in the environment
(Jackson, 2001; Lauretta et al., 2001). Natural processes can alter the isotopic composition, i.e., causing stable isotope fractionation,
such as redox reactions, complexation, sorption, precipitation, dissolution, evaporation, diffusion and biological processes. Stable
isotope analyses can, therefore, provide a previously untapped source of valuable information on the sources and biogeochemical
cycling of natural and anthropogenic Hg. Isotopic fractionation refers to the division of a sample into two (or more) parts with

1355   different ratios of "heavy" and "light" isotopes than the original ratio. In isotopic jargon, if one part contains more heavy isotopes, it
is said to be "enriched," while the other part is said to be "depleted". Hg has an extremely large isotopic variation in nature, which,
when normalized by the relative mass difference between isotopes, approaches that of the traditional light element isotopes
(Wiederhold, 2015). However, the overlapping signals from different fractionation processes can be a major challenge in deciphering
natural isotope signatures when tracing sources. It is important to determine the Hg stable isotope fractionation for *individual* key

1360   processes, which can be done, inter alia, through controlled laboratory and field experiments. Stable isotope variations are reported
as relative values compared with a reference standard (NIST SRM 3133 Hg solution, Blum and Bergquist, 2007):

$$\delta^{xxx}\text{Hg} = 1000 \cdot \left(R^{xxx/198}_{\text{sample}} / R^{xxx/198}_{\text{NIST3133}} - 1 \right) \qquad (12)$$

where R is the ratio of the isotopes with mass numbers xxx and 198. Parenthesized:^{196}Hg is not an alternative because of its low
occurrence of only 0.15%. The standard unit for δ values is per mill (‰). The fractionation factor α determines the distribution of
isotopes between any two parts (A and B) of a system as follows:

$$\alpha_{A-B} = \frac{1000 + \delta_A}{1000 + \delta_B} \qquad (13)$$

1365   Actual δ-values are usually very close to unity. Therefore, it is usually more practical to use an enrichment factor:

$$\varepsilon_{A-B} = \delta_A - \delta_B = 1000 \cdot (\alpha_{A-B} - 1) \cong 1000 \cdot \ln\alpha_{A-B} \qquad (14)$$

The last similarity is only valid for δ values less than 10‰. Many kinetic processes can be described as Rayleigh fractionation, which
is an irreversible process in an open system involving the progressive removal of a fraction of a trace substance from a larger reservoir.
It is described by the following differential equation:

$$d \ln R = (\alpha - 1) \cdot d \ln f_R \qquad (15)$$

If the fractionation factor is constant, the differential equation can be integrated directly into the expression:

$$R/R_0 = f_R{}^{\alpha-1} \qquad (16)$$

1370   where R_0 is the isotope ratio of the initial reservoir (when $f_R = 1$), R is the isotope ratio of the reservoir at a given time when the
fraction of initial material remaining in the reservoir is defined by f_R. In the literature, the following expression is often used to
evaluate the fractionation factor:

$$\ln \frac{1000 + \delta}{1000 + \delta_0} = \left(\alpha^{xxx/198} - 1 \right) \ln f_R \qquad (17)$$

The process tends to enrich the heavier isotopes in the reservoir (α < 1, normal kinetic isotope effect) rather than remove the heavier
isotopes from the reservoir more rapidly (α > 1, inverse KIE).

1375   **8.1 Conventional mass-dependent and mass-independent fractionation**

Scaling factor β describes the relationship between the fractionation factors as follows:

$$\alpha_{xxx/198} = \alpha_{202/198}^{\beta} \qquad (18)$$

where β for mass-dependent equilibrium fractionation ($\beta_{\text{EIE-MDF}}$) and kinetic fractionation ($\beta_{\text{KIE-MDF}}$) are as follows (Young et al.,
2002):

$$\beta_{\text{EIE-MDF}} = \frac{1/m_{198} - 1/m_{xxx}}{1/m_{198} - 1/m_{202}} \qquad (19)$$

$$\beta_{\text{KIE\_MDF}} = \frac{\ln(m_{198}/m_{xxx})}{\ln(m_{198}/m_{202})} \qquad (20)$$

The equilibrium MDF resulting from the differences in zero-point vibrational energy (ZPE) distances and the kinetic MDF resulting

1380 from the differences in dissociation energies between the isotopologues and their respective effects can be expressed in two rules of thumb: the heavier isotopes are concentrated in the compounds in which the element is most stiffly bound (with the highest force-constant), and compounds with heavier isotopes have greater potential energy, so less energy is required to break the bonds of compounds with lighter isotopes, which therefore preferentially enter the chemical reaction and are enriched in the product (Criss, 1999). By combining kinetic and equilibrium MDF, a limit of ~10‰ fractionation is possible (Sun et al., 2022).

1385 Properties of nuclei, such as nuclear size and shape or the presence of non-zero nuclear spin may trigger isotope fractionation that does *not* follow the expected MDF relationships. The first effect, called nuclear field shift (NFS, Rosenthal and Breit, 1932), detected in atomic spectra, results from the interaction of nuclear volume on electrons (also called nuclear volume effect, NVE, Schauble, 2007) and is highly relevant for the very heavy metals, which besides Hg also include, e.g., Tl, Pb and U. NFS is a shift in the ground electronic energy of an atom or molecule due to differences in nuclear size and shape between isotopes. The shift caused by an odd

1390 (neutron number) nucleus scales non-linearly between those of the even isotopes of the next higher and lower atomic mass. The odd neutron isotope level is shifted towards the next lower even nucleus (*odd-even staggering*). Due to its smaller size and greater surface charge density, the electronic energy of a light isotope is lower than that of a heavier isotope. The amount of shift is a product of two factors: The electron density at the nucleus and the charge, size and shape of the nucleus and the change in the latter two between isotopes. Hg 6s-orbital electrons significantly overlap with the nucleus, whereas 5p-, 5d- and 4f-orbitals do not, although f-electrons

1395 in inner shells have a smaller screening effect on 6s-valence electrons (Bigeleisen and Wolfsberg, 1957). The lowest energy of a system occurs when the heavier isotopes of Hg are enriched in the chemical species with the lowest number of s-electrons in the bonding or the valence orbital. The largest shifts, therefore, occur when the number of Hg 6s electrons is greatly reduced by the formation of a bond of an ionic nature (to an electronegative element), while the influence of a more covalent bond is less significant. Examples of Hg species in the former category are chloro- or aqua-complexes with high coordination numbers ($HgCl_4^{2-}$ and

1400 $[Hg(H_2O)_6]^{2+}$) and the latter category includes soft ligands with typical linear bi-coordination ($Hg(SH)_2$ and $(CH_3)_2Hg$).The scale factor of nuclear volume fractionation (β_{NFS}) is defined:

$$\beta_{\text{NFS}} = \frac{\langle r_{198}^2 \rangle - \langle r_{xxx}^2 \rangle}{\langle r_{198}^2 \rangle - \langle r_{202}^2 \rangle} \qquad (21)$$

where $\langle r^2 \rangle$ describes the mean-square nuclear charge radii of different isotopes. Coincidentally, MDF and NFS with ^{198}Hg, ^{200}Hg and ^{202}Hg show almost identical β-values, but ^{199}Hg, ^{201}Hg and ^{204}Hg and to a lesser extent ^{196}Hg show distinct non-mass dependent signatures due to NFS. Only a small proportion of the NFS is mass-independent because it creates a deviation from MDF (Yang and

1405 Liu, 2015). The mass-dependent part of the two effects can be synergistic (increasing total fractionation) or antagonistic (decreasing total fractionation), the former being dominant for Hg redox chemistry (Hintelmann and Zheng, 2011; Jiskra et al., 2012). Regular MDF scales are proportionate to $1/T^2$, whereas NVF scales are proportionate to $1/T$ and more prominent than regular MDF for the Hg red-ox reactions studied (Schauble, 2007). Among the commonly measured isotopes 198-202, a minor to moderate level of MIF has been experimentally observed isolated in the odd isotopes 199 ($\leq 0.6‰$) and 201 as a result of NFS. NFS has been described for

1410 equilibrium exchange reactions but has never been extended to kinetic processes. In contrast to the small magnitude observed in natural samples, the possibility has recently been suggested that nonequilibrium isotopic effects of NFS in photodissociation may give rise to a significant magnitude of MIF (Motta et al., 2020b).

The only effect that has been documented to lead to significant odd-mass number Hg MIF (odd-MIF) in present-day surface ecosystems is the magnetic isotope effect (MgIE). MgIE is a purely kinetic effect triggered by the formation of a long-lived radical

1415 pair after a primary process that causes homolysis of a Hg - ligand bond upon photolytic excitation. (**Fig. 11**). Among the stable

isotopes of Hg, only [199]Hg and [201]Hg (odd mass numbers) have non-zero nuclear spin and momentum, with half-integer ($\frac{1}{2}$ and $\frac{3}{2}$, respectively) spins. MgIE arises when hyperfine coupling (HFC) acts on a spin-coherent solvent-separated radical pair after dissociation by changing the rate of intersystem crossing from singlet to triplet (S↔T) or vice versa (T↔S) in the odd Hg isotopes. Radical pairing and MgIE are suppressed in mercuric complexes with strong spin-orbit coupling (containing bromine and iodine ligands), favoring spin mixing and return to the ground state, while S-, Cl- and C-bonded complexes with generally weak spin-orbit coupling favor strong MgIE (Motta et al., 2020a). If the radical pair is born in the triplet state (lower panel of **Fig. 11**), HFCs are induced, enriching odd isotopes in the resulting singlet state. The singlet radical pair can then recombine to the ground state, resulting in an odd isotope enrichment in the reactant, expressed as (+)MgIE. When the radical pair is in the singlet state (top panel of **Fig. 11**), the overall effect is to deplete odd isotopes in the reactant, as expressed by (–)MgIE, because mainly the odd isotopes with the majority in the triplet radical pair dissociate into free radicals. A computational study has provided an explanation as to why photodissociation of monomethyl Hg species in nature is observed to yield only (+)MgIE, whereas photolysis of inorganic mercuric complexes may yield positive or negative MgIE, depending on the reaction conditions and the complex ligation (**Section 8.4**).

Thus, odd-MIF results from both the MgIE and NFS mechanisms. MgIE is most effective in a viscous solvent, where a "solvent cage" environment is possible (Turro, 1983). In addition, a seemingly enigmatic even mass number Hg isotope MIF (even-MIF) has been observed in samples of atmospheric origin or deposition. However, an analog atmospheric photochemical anomalous isotope fractionation is well known for the lighter (traditional) elements for which MIF (containing three or more stable isotopes) can be detected, such as oxygen and sulfur. However, understanding the underlying causes of multi-isotope anomalous fractionation is limited because the investigation requires detailed quantum mechanical calculations at the molecular isotope level for, e.g., photo absorption and photodissociation. Recently, rock records have revealed significant even-MIF in the Archean atmosphere, which lacked an ozone (O_3) layer to filter UVC from actinic light, suggesting that contemporary UVC-induced atmospheric chemistry may be responsible for the coupled changes in even-MIF for both Hg and sulfur (Zerkle et al., 2020). Correlations between these entities have also been observed in marine aerosols in the southern hemisphere (Auyang et al., 2022).

MIF (denoted with capital delta, Δ) is defined as the difference between the measured δ-value and that predicted from the measured δ^{202}Hg value and the scale factor for kinetic MDF ($\beta_{KIE-MDF}$) and is approximated for δ-values < 10‰ according to:
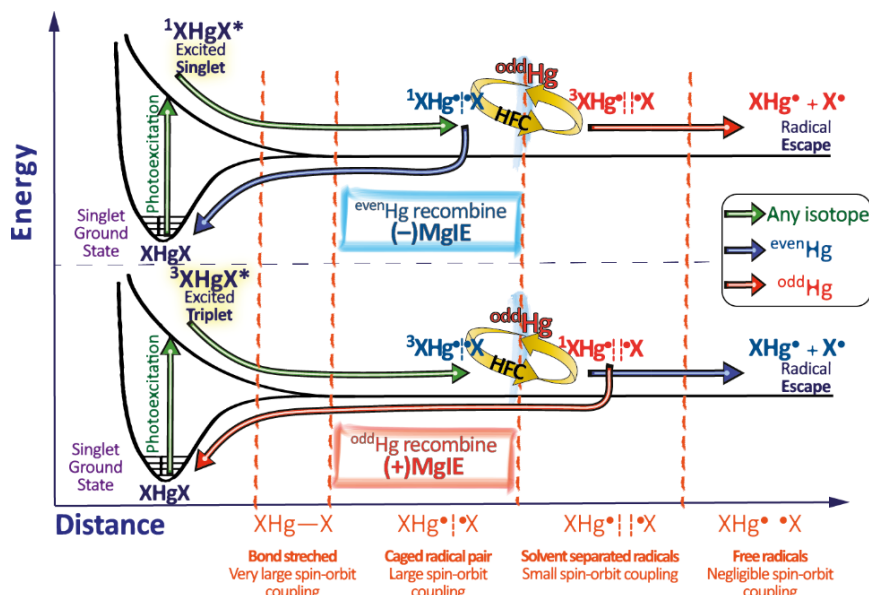
Figure 11. General scheme for the photolysis of a molecule to produce a spin-correlated radical pair (RP). The singlet and triplet RPs can be interconverted by intersystem crossing. Both the singlet and triplet RPs can escape from the solvent cage. Only the singlet RP can recombine. Adopted from Turro (1983) and Motta et al. (2020a).

$\Delta^{196}Hg = \delta^{196}Hg + 0.508 \cdot \delta^{202}Hg$, $\Delta^{199}Hg = \delta^{199}Hg - 0.252 \cdot \delta^{202}Hg$, $\Delta^{200}Hg = \delta^{200}Hg - 0.502 \cdot \delta^{202}Hg$, $\Delta^{201}Hg = \delta^{201}Hg - 0.752 \cdot \delta^{202}Hg$ and $\Delta^{204}Hg = \delta^{204}Hg - 1.493 \cdot \delta^{202}Hg$. The MIF enrichment factor $E^{xxx}Hg$ for a process is calculated by:

$$E^{xxx}Hg = \varepsilon^{xxx}Hg - \varepsilon^{202}Hg \cdot 0.252 \qquad (22)$$

where xxx is the mass number.

The non-mass-dependent odd isotope fractionation observed in nature spans a range of more than 12‰ (Kwon et al., 2020).

8.1.1 MIF Signatures as Additional Tracer

The isotopic measurement of Hg results in up to six useful isotopic signatures ($\delta^{202}Hg$, $\Delta^{196}Hg$, $\Delta^{199}Hg$, $\Delta^{200}Hg$, $\Delta^{201}Hg$ and $\Delta^{204}Hg$). In addition, pairs of these signatures have been utilized to distinguish between fractionation mechanisms. The relationship between these signatures is typically illustrated using a three-isotope plot. To interpret experimental results satisfactorily, specific robust linear regression methods are recommended (Stephan and Trappitsch, 2023). Based on early results (Bergquist and Blum, 2007), it was assumed that photoreduction of Hg^{II} to Hg^0 would result in a $\Delta^{199}Hg/\Delta^{201}Hg$ ratio of unity. Several investigated photoreactions exhibit just a ratio of 1 within the margin of error (refer to **Table 4**, **Section 8.4**). However, further data has shown that this is not always the case, as the slope depends on factors such as the complexing ligand and reaction conditions. Clearly, the odd-MIF signature for the photolysis of organomercurials is different from that stipulated for inorganic Hg. The photolytic degradation of MMHg$^+$ species exhibits a variation of $\Delta^{199}Hg/\Delta^{201}Hg$ ranging from 1.17 to 1.38 depending on reaction conditions (Bergquist and Blum, 2007; Chandan et al., 2015; Rose et al., 2015; Malinovsky et al., 2010). NFS gives rise to a generally much weaker MIF than for MgIE with a larger anomalous fractionation of ^{199}Hg compared to ^{201}Hg, approaching a ratio of ~1.6. However, confirmation of the NFS should be done using alternative methods when the experimentally measured NFS is too limited to determine a definitive odd-MIF ratio (Motta et al., 2020b). Another commonly used parameter is $\Delta^{199}Hg/\delta^{202}Hg$, which describes the degree of odd-MIF in relation to conventional MDF. The even-MIF signature of $\Delta^{200}Hg$ to $\Delta^{204}Hg$, which is negative in natural samples (air, rainfall and fish), is discussed in **Section 8.2.4**.

8.2 Isotopic characteristics of atmospheric mercury

Fig. 13 summarizes the magnitude of isotopic observations reported in the literature on the main fractions of Hg in the atmosphere, namely gaseous Hg dominated by Hg^0, particle-bound Hg and Hg associated with hydrometeors (rain, snow and water from clouds and fog). Here, $\delta^{202}Hg$, $\Delta^{199}Hg$, and $\Delta^{200}Hg$ are shown to describe MDF, odd-MIF, and even-MIF, respectively. The number of isotopically resolved samples has increased dramatically in recent years, and the reader should consult the literature regularly to keep up to date. On the other hand, this development justifies revisiting the topic, even though it has been dealt with satisfactorily in the recent past (Kwon et al., 2020). It should be noted that the spatial distribution of available data is heavily skewed toward North America, Europe, and East Asia, and observations from large parts of the world are missing (**Fig. 13**). However, as far as the marine remote regions are concerned, recent oceanographic expeditions have contributed to an increasing amount of data. Further below, the in situ and laboratory experiments performed so far to study the gas exchange of Hg^0 between air and water, soil and foliage in terms of isotope fractionation are discussed.

8.2.1 Gaseous Hg

The following part excludes an early series of measurements where the air was not filtered prior to sampling (Rolison et al., 2013). The referenced series of measurements should be considered as total airborne Hg, not total gaseous mercury (TGM). TGM shows a significant spread for $\delta^{202}Hg$ (–3.75 to 1.52‰) and $\Delta^{199}Hg$ (–0.62 to 1.32‰), but is more limited for $\Delta^{200}Hg$ (–0.22 to 0.11‰). Analogous to Hg^{II} deposited in biomass and fossil fuels such as coal (Sun et al., 2014), Hg^0 in natural gas (Washburn et al., 2018) and in smoke from spontaneous combustion in coal fields (Sun et al., 2023) has strongly negative $\delta^{202}Hg$-values. This differs from the majority of Hg^0 in ambient air, which is isotopically heavy (often with positive $\delta^{202}Hg$ values). Terrestrial background air (rural, subpolar and forest in **Fig. 13a**) has higher $\delta^{202}Hg^0$ values because it is modified by vegetation, which preferentially incorporates lighter isotopes of Hg^0 into the foliage. Foliar uptake of Hg^0 is discussed in more detail in **Section 8.6.2**. The estimate of atmospheric

Hg⁰ dry deposition to vegetation has recently been revised upward and constrained to about 2300 Mg yr.$^{-1}$ (Feinberg et al., 2022), and together with the large negative $\varepsilon_{foliage/air}$ of the process, the global atmospheric Hg⁰ pool is estimated to have a δ^{202}Hg mean of 0.5‰, in contrast to that of Hg⁰ from anthropogenic sources (global bulk mean of –0.7‰, Sun et al., 2019). Specific studies of the

1485 vertical distribution of Hg⁰ concentration from near the ground to above the canopy for different forest types show clear gradients averaging 10 (Wang et al., 2022) and 20% (Fu et al., 2016b) of ambient Hg⁰, respectively. Under stable conditions, such as during summer nights, Hg⁰ levels were observed to be strongly depleted below the canopy (Fu et al., 2016b; Mao et al., 2008; Poissant et al., 2008; Lan et al., 2012; Fu et al., 2019a). Thus, isotopic measurements of above-canopy air versus in-canopy air (Wang et al., 2022; Fu et al., 2016b) and daytime air versus nighttime air in the forest (Kurz et al., 2020) show statistically significant differences

1490 (p < 0.01) in δ^{202}Hg⁰. For a deciduous forest in northeast China, Fu et al. (2019a) observed that δ^{202}Hg⁰ in biweekly air samples during the growing season was 0.35 to 0.99‰ higher than during the dormant season. In a subtropical perennial forest in southwest China with little seasonal variation in photosynthetic activity of the vegetation, the existing seasonal variation in δ^{202}Hg⁰ (amplitude 0.4‰) can be related to the influence of long-range transported anthropogenic emissions, which occur mainly during the warmer seasons. However, in the last 5 to 7 years the air concentrations of Hg⁰ have been falling rapidly in the two mentioned forest reserves due to

1495 decreasing regional anthropogenic emissions, as can be seen in the median value of δ^{202}Hg⁰ shifting from 0.42 to 0.46‰ and from 0.17 to 0.57‰. The marine δ^{202}Hg⁰ data (n = 112) are significantly lower (Wilcoxon test, p < 0.01) than those from the forest (n = 113). Based on coastal measurements in the Gulf of Mexico, Demers et al. (2015) determined that the measured marine-influenced air isotopically represents background air modified by Hg⁰ emitted from the sea after being formed in surface water by photoreduction. Measurements in the marine boundary layer (MBL) of the offshore East China Sea indicated that airborne Hg⁰ is

1500 essentially a binary mixture of anthropogenic outflow from mainland China and air masses from the sea (significantly correlated δ^{202}Hg⁰ and Δ^{199}Hg⁰ vs. $C_{Hg^0}^{-1}$), with an extrapolated Δ^{199}Hg⁰ of –0.26‰ for the marine component. The extrapolated Δ^{199}Hg⁰-value agrees well with observations made in Hawaii with passive samplers (Szponar et al., 2020) as well as with the signatures of a larger number of samples from Mauna Loa (3397 m a s l) in the free troposphere (Tate et al., 2023; Yamakawa et al., 2024).

The generally negative Δ^{199}Hg⁰ in the background air can be considered to reflect Hg⁰ added to the pool after Hg^{II} photoreduction in

1505 Earth's surface reservoirs interacting with the atmosphere and aerosols (of the variant that induces (+)MgIE in the reactant and complements it by depleting the product Hg⁰ isotopically in odd isotopes). This is supported by atmospheric Hg⁰ exhibiting Δ^{199}Hg/Δ^{201}Hg slopes close to unity (Kwon et al., 2020), similar to aqueous photoreduction of inorganic Hg^{II}. However, not all photo controlled Hg⁰ re-emissions from terrestrial ecosystems contribute to negative Δ^{199}Hg⁰ in the atmosphere. A branch-level study of air-foliage Hg⁰ gas exchange in a subtropical perennial beech forest revealed bidirectional fluxes, where leaf uptake of Hg⁰ from ambient

1510 air is balanced by reemission of Hg⁰ that was previously metabolized and bound as Hg^{II} in the leaf interior, but subsequently photo reduced and recirculated, and not as a retro flux of recently deposited Hg⁰ at the leaf surface (data in **Fig. 17a**). This re-emission is isotopically distinct in that it is enriched in odd isotopes compared to ambient air (Yuan et al., 2019b), indicating that leaf photoreduction induces (–)MgIE, as reported for Hg^{II} bound to organic ligands containing sulfur or nitrogen of low oxidation states (Motta et al., 2020b; Zheng and Hintelmann, 2010b). A mass balance based on isotope measurements indicates that re-emission from the beech foliage

1515 compared to uptake of Hg⁰ from the air gradually increases from emergence to senescence with an average of 30% (Yuan et al., 2019b). Observations from a temperate deciduous forest with 0.06 – 0.09 ‰ higher Δ^{199}Hg⁰ values during the growing season compared to winter suggest that foliar Hg⁰ efflux contributes to the enrichment of odd Hg isotopes in the atmosphere (Fu et al., 2019a).

The large spread in the odd-MIF shown by Hg⁰ in polar air (Araujo et al., 2022; Yu et al., 2021; Sherman et al., 2010, **Fig. 13a**) is due to the part of the collected data that includes AMDEs of Hg⁰ in the spring and summer period, when Hg⁰ is enhanced by a contribution

1520 of reemissions from the cryosphere. **Fig. 12** shows the isotopic composition of fractionated airborne Hg into Hg⁰ and Hg^{II} (RM) during the Arctic spring (at three stations) compared to the corresponding data from a background station in the Pyrenees (Fu et al., 2021). With respect to Δ^{199}Hg, a dichotomy between the polar and temperate data is striking for both Hg⁰ and Hg^{II} (RM), in that montane oxidized Hg is enriched in a limited range (0.14 to 0.77‰) while the polar is depleted in a greater range (–2.15 to –0.18‰), with a complementary relationship existing for Hg⁰ (–0.31 to –0.16‰ versus –0.22 to 1.32‰). This relationship could be caused by surface layer airborne Hg

1525 strongly influenced by the oxidation of Hg^0 to Hg^{II} controlled by halogen atoms during AMDEs, processes characterized by $E^{199}Hg$ of
–0.37‰ and –0.23‰ for Cl$^\bullet$-initiated and Br$^\bullet$-initiated oxidation (Sun et al., 2016). In this way, the remaining reactant is driven to higher
$\Delta^{199}Hg^0$ and the molecular products assume negative $\Delta^{199}Hg^{II}$ values. However, this interpretation is not supported by the measured
$\Delta^{199}Hg/\Delta^{201}Hg$ ratio in airborne Hg of close to unity, which is more typically a reflection of the Hg^{II} photo-reduction ((−)MgIE) taking
place in the snow, and it has been proposed that this process also operates in aerosols of the boundary layer, with Hg^0 reemissions giving

1530 such a strong positive imprint that the entire boundary layer of the Hg^0 pool becomes enriched in odd isotopes (Araujo et al., 2022).
Isotopic measurements of $Hg^{II}(g)$ separated from $Hg^{II}(p)$ using CEM have commenced and are anticipated to elucidate the mechanisms
underlying the pronounced fractionation of odd isotopes in airborne Hg^0 and Hg^{II}. Several such datasets are currently in preparation for
publication. Furthermore, Hg^0 in the Arctic during the dark period of the year and from the Antarctic Peninsula throughout the year (Yu
et al., 2021) share a consistently slightly negative $\Delta^{199}Hg^0$ with other background air (represented by montane air in **Fig. 13a**). In the late

1535 Arctic summer, minimum $\Delta^{199}Hg^0$ values (approaching –0.5 ‰) are observed uniformly without much variation from coastal stations
around the Arctic Ocean, which are thought to result from photoreduction of cryospheric Hg^{II}, a substrate which has been strongly
depleted of odd isotopes during months of long sunshine (Araujo et al., 2022).

$\Delta^{200}Hg^0$ is generally negative for the non-fossil/anthropogenic sources, while the remainder is significantly shifted to higher values
(Wilcoxon T-test, e.g., natural gas vs. arid data, p < 0.01). As mentioned above, even-MIF is generated exclusively by atmospheric

1540 chemical processes, which may be mainly limited to molecular $Hg^{I,II}$ photolysis processes (Sun et al., 2022), of which Hg^0 is a product.
The marine and polar $\Delta^{200}Hg^0$ data have the most negative values. For example, a recently published TGM record from Mauna Loa
(not shown in **Fig. 13**) in the Pacific Ocean has $\Delta^{200}Hg$ values down to –0.20‰ (Yamakawa et al., 2024). The polar pool as a unit
shows a significant shift towards lower $\Delta^{200}Hg^0$ values compared to the forest pool (Wilcoxon T-test, p < 0.05). One can only
speculate as to the reason, but it should be mentioned in the context of a halogen-rich environment that any presence of Cl-initiated

1545 Hg^0 oxidation in the gas phase will result in depletion of ^{200}Hg in the reactant pool ($E^{200}Hg \sim 0.06‰$, Sun et al., 2016). Due to its
relatively limited range, ambient $\Delta^{200}Hg^0$ & $\Delta^{204}Hg^0$ is considered a conservative tracer of atmospheric Hg^0 deposition, and terrestrial
surface and water $\Delta^{200}Hg$ & $\Delta^{204}Hg$ values can constrain the relative contribution of Hg^0 to Hg^{II} deposition. Throughout, a median
value of -0.05‰ (IQR –0.02 to –0.08‰) of $\Delta^{200}Hg^0$ was used to calculate this contribution in atmospheric transfer to soil
($\Delta^{200}Hg^{II}\sim0‰$, Enrico et al., 2016; Zhou et al., 2021; Zheng et al., 2016) and oceans ($\Delta^{200}Hg\sim0.04‰$, Jiskra et al., 2012). Quantitative

1550 AMDEs observed in Alaska are isotopically mass-balanced in that $\Delta^{200}Hg^{II}$ in snow (-0.06‰) corresponds, within the measurement
uncertainty, to that in ambient Hg^0 (-0.05‰).

8.2.2 Aerosol-bound Hg

While Hg^0 has a relatively long lifetime and $Hg^{II}(g)$ a short lifetime, the lifetime of particle-bound Hg (PBM, Hg_p^{II}) reflects that of
particles, which varies from days to months due to their size and composition. Isotopic analyses have been performed on airborne $PM_{2.5}$,

1555 PM_{10}, and TSP, as well as on particles in precipitation. In the literature, studies of urban air, regionally polluted air, and air associated
with anthropogenic emissions (CFPP, traffic and waste incineration, etc.) are well represented and strongly biased toward Asia. As
reviewed and discussed in Kwon et al. (2020), attempts to decipher the cause of seasonal variations etc. in urban and industrial air are
challenging in an environment with a plethora of local and regional emission sources. However, it is clear that primary particles from
fossil fuel and biomass combustion inherit the clearly negative but highly variable $\delta^{202}Hg^{II}(p)$ and the less negative $\Delta^{199}Hg^{II}(p)$ of the

1560 material. The large range in $\Delta^{199}Hg^{II}(p)$ (–0.93 to 1.5‰) around the origin depends on $Hg^{II}(p)$ photoreduction with (+)MgIE, halogen
atom-initiated Hg^0 oxidation or, more speculatively, $Hg^{II}(p)$ photoreduction with (–)MgIE, driving the data to extremes. In a series of
papers, including field measurements of particle-bound isotopic Hg in regionally polluted air (Huang et al., 2016b; Huang et al., 2019;
Qiu et al., 2022; Zhang et al., 2022) and laboratory experiments (Huang et al., 2021; Huang et al., 2015), Chen and colleagues have
drawn attention to the effect of (+)MgIE photoreduction, which is accelerated in the presence of a particle surface liquid layer (wet haze)

1565 and water-soluble organic carbon as a reducing agent (Zhang et al., 2022). Several peripheral monitoring stations in China, primarily
receptors of long-range particles transported domestically or transboundary, generally measure positive $\Delta^{199}Hg^{II}(p)$ (Fu et al., 2019b). A
strong anticorrelation between $\Delta^{199}Hg^{II}(p)$ (up to ~1.2‰) and the concentration of particle-bound Hg, rationalized as caused by photo

reduced Hg^0 loss from the aerosol that initially has a near-zero $\Delta^{199}Hg^{II}(p)$, was observed for the stations with northeastern China and the regions along the lower reaches of the Yangtze River to its mouth, respectively, as the major potential source area (Fu et al., 2019b). The

1570 results indicate that the globally modeled tropospheric lifetime of Hg^{II} against photoreduction in aerosols and clouds of nearly two weeks (Horowitz et al., 2017) is significantly shorter in the East Asian region plausibly due to a higher fraction of organic aerosol. As can be seen in **Fig. 13b**, there is a statistical anomaly in the PBM polar data for all reported isotopic signatures: positively shifted $\delta^{202}Hg^{II}(p)$, negatively shifted $\Delta^{199}Hg^{II}(p)$ and negatively shifted $\Delta^{200}Hg^{II}(p)$. It is represented in both Arctic (Araujo et al., 2022; Zheng et al., 2021) and Antarctic (Auyang et al., 2022; Li et al., 2020a) data in conjunction with AMDEs. In the high Arctic (~83ºN), there is good isotopic

1575 agreement between ambient Hg^0 and PBM associated with nearly complete AMDEs, as would be expected. At the same time, for less quantitative oxidation, PBM is found to be isotopically lighter than Hg^0, analogous to kinetic isotope fractionation during oxidation and subsequent uptake of $Hg^{II}(g)$ on particles (such as Arctic haze). As described above, halogen atom-driven gas-phase oxidation induces negative $\Delta^{199}Hg^{II}$ (Sun et al., 2016; Auyang et al., 2022), which is consistent with the observed signature in PBM. The interpretation of Zheng et al. (2021) that gas-phase oxidation uniquely shapes isotopic fractionation has been challenged by Araujo et al. (2022) who

1580 instead consider (–)MgIE photoreduction in the aerosol as the imprinting source. The uniquely high positive $\delta^{202}Hg^{II}(p)$ values (up to ~3‰ and anticorrelated with $\Delta^{199}Hg^{II}(p)$) measured in coastal Antarctica interpreted as originating from air masses transported by katabatic winds from the inland plateau, where oxidation of Hg^0 persists during summer (Li et al., 2020a). Under precipitation (**Section 8.3**), the high $\Delta^{200}Hg^{II}$ values measured in southern Canada are addressed, noting that this also applies to the particulate fraction in precipitation, which is included in the rural PBM category (**Fig. 13b**).

1585 ### 8.2.3 Hg in precipitation

Measurements of Hg isotopes in precipitation samples (including fog and cloud water) have been reported at sites in the Northern Hemisphere (map in **Fig. 13c**), most in North America. Precipitation samples show the largest scatter in both $\Delta^{199}Hg$ and $\Delta^{200}Hg$ compared to Hg^0 and PBM. Nevertheless, the isotopic distribution pattern in precipitation water is generically similar to that of PBM, which is scavenged in precipitation during rainout and washout processes. Precipitation in the vicinity of anthropogenic emission sources

1590 (such as CFPP) tends to be isotopically distinct with particularly negative $\delta^{202}Hg^{II}$ values (Sherman et al., 2012). Precipitation from more pristine areas has $\delta^{202}Hg^{II}$ that is shifted in a positive direction (significant for marine, polar and rural categories, Wilcoxon t-test, p < 0.01) compared to urban precipitation and precipitation near point sources. General differences between Hg^0 and precipitation/PBM in terms of MIF signatures (negative $\Delta^{199}Hg^0$ & $\Delta^{201}Hg^0$ vs. positive $\Delta^{199}Hg^{II}$ & $\Delta^{201}Hg^{II}$ and negative $\Delta^{200}Hg^0$ & positive $\Delta^{204}Hg^0$ vs. positive $\Delta^{200}Hg^{II}$ & negative $\Delta^{204}Hg^{II}$, respectively) are explained by atmospheric redox processes (Auyang et al., 2022; Kwon et al.,

1595 2020). In the case of even-MIF, chlorine atom-initiated gas-phase oxidation is known to induce a limited positive $\Delta^{200}Hg^{II}$ in the product. However, its observed magnitude definitely cannot explain the highest $\Delta^{200}Hg^{II}$ measured in precipitation (Kurz et al., 2021; Chen et al., 2012; Yuan et al., 2022) in North America. Cai and Chen (2015) reported a trend towards increasing $\Delta^{200}Hg^{II}$ in background precipitation as one moves northwards along the mid-latitudes of the Northern Hemisphere (~20–45ºN), but only with data from a unique station anomalous with higher statistical significance. A one-year measurement north of Lake Ontario (Chen et al., 2012), separated by a full

1600 decade from measurements at the same site limited to the colder parts of the year (Yuan et al., 2022), have together shown that precipitation in winter often contains high values of $\Delta^{200}Hg^{II}$ (and at the same time strongly negative $\Delta^{204}Hg^{II}$ values). During the full-year measurement in 2010, filtered precipitation samples showed $\Delta^{200}Hg^{II}$ in the range of 0.21 to 1.24‰, while during the colder months around the turn of the year 2020-21, the same category of samples contained between 0.25 to 1.19‰ and between –1.97 to –0.37‰ for $\Delta^{200}Hg^{II}$ and $\Delta^{204}Hg^{II}$ respectively. During the last campaign, isotopic analysis was also performed on precipitation particles, which showed

1605 comparatively significantly lower positive $\Delta^{200}Hg^{II}$ values (up to 0.37‰) and less negative $\Delta^{204}Hg^{II}$ values (down to –0.84‰). Intermittently, the particle phase has the opposite sign to the solute phase in the same precipitation sample with respect to both odd- and even-MIF. This, together with a time series of unrelated odd-MIF and even-MIF trends during events with large fluctuations in these values, has been interpreted as the influence of the circumpolar vortex with varying contributions of tropospheric and stratospheric air, with transport of the latter airmasses explaining more extreme even-MIF values (Yuan et al., 2022). Rain samples compared to snow samples from the

1610 Canadian station north of Lake Ontario generally show more moderately positive $\Delta^{200}Hg^{II}$ values, consistent with observations in the

mid-latitudinal USA (Kurz et al., 2021; Demers et al., 2013; Gratz et al., 2010; Sherman et al., 2015), Europe (Fu et al., 2021; Enrico et al., 2016), the Tibetan Plateau (Yuan et al., 2015) and over the Pacific Ocean (Motta et al., 2019; Washburn et al., 2021). Although cloud water (Fu et al., 2021; Zhen et al., 2024) and fog water (Washburn et al., 2021) have been isotopically analyzed, there are no apparent differences between them or significant differences with rain samples. In cloud water, Hg speciation with increasing complexation to DOM has been shown to correlate with odd-MIF (Zhen et al., 2024), consistent with the view that these mercuric complexes are photolabile. Polar precipitation samples (only those from AMDEs are reported in the literature, Araujo et al., 2022; Sherman et al., 2012; Zheng et al., 2021) consistently show slightly negative $\Delta^{200}Hg^{II}$, which differs from precipitation samples of all other provenances, which show positive median values. The reason for these observations is plausibly that oxidation is so advanced during these AMDEs that Hg^{II} scavenged by precipitation approaches the same isotopic values as Hg^0 in the polar air had before the AMDE.

8.2.4 Even-MIF ($\Delta^{200}Hg/\Delta^{204}Hg$) ratios in atmospheric samples

Early studies by Gratz et al. (2010) and Chen et al. (2012) showed that MIF anomalies of even mass number isotope ^{200}Hg are regularly present in atmospheric precipitation. Later, measurements (Demers et al., 2013) were also made at $\Delta^{204}Hg$, which is more challenging due to the limitations of ion beam collector designs (Blum and Johnson, 2017). The anomaly of $\Delta^{204}Hg$ was generally larger and of the opposite sign to that of $\Delta^{200}Hg$. The $\Delta^{200}Hg/\Delta^{204}Hg$ ratio has been calculated based on spatial averages and exclusively on precipitation samples, which are usually above measurement uncertainty. For example, a slope of –0.5 was previously reported (Blum and Johnson, 2017) and later adjusted to –0.4 (Kwon et al., 2020) using this method as more data became available. However, when all individual precipitation data up to 2020 were combined, Kwon et al. (2020) obtained a significantly lower regression slope of –0.24. **Fig. 14** shows the even-MIF data ($\Delta^{200}Hg$ vs. $\Delta^{204}Hg$) binned into geographical regions (categorized as Hg^0, rain/mist/cloud, PBM, RM, and snowfall samples). Linear regression of York type $\Delta^{200}Hg$ against $\Delta^{204}Hg$ gives slopes between –0.07 and –0.53 for data grouped by site and category for data of statistical significance ($p \leq 0.05$, indicated by *). When the global data grouped by sample type are analyzed separately, significant ($p < 0.001***$) slopes of –0.51±0.02 (n = 45, Kurz et al., 2021; Yuan et al., 2022), –0.41±0.03 (n = 108, Fu et al., 2021; Demers et al., 2015; Enrico et al., 2016; Sherman et al., 2012; Yuan et al., 2022; Demers et al., 2013; Donovan et al., 2013; Motta et al., 2019; Washburn et al., 2021), –0.29±0.06 (n = 58, Fu et al., 2019b) and –0.11±0.02 (n = 295, Fu et al., 2021; Kurz et al., 2020; Demers et al., 2015; Tate et al., 2023; Araujo et al., 2022; Enrico et al., 2016; Kurz et al., 2021; Demers et al., 2013; Yamakawa et al., 2017; Jiskra et al., 2019; Fu et al., 2016a; Wu et al., 2023a) are obtained for snowfall, rain and fog, particulate matter and Hg^0 respectively. The reaction mechanism triggering even-MIF could be due to photo-dissociation in the gas phase (Sun et al., 2022) or on surfaces (Fu et al., 2021). This should lead to varying fractionation depending on the species undergoing decomposition. As a result, atmospheric Hg^I and Hg^{II} species will differ in fractionation from one another, possibly explaining the divergent $\Delta^{200}Hg/\Delta^{204}Hg$ for $Hg^{II}(aq)$, $Hg^{II}(p)$, and $Hg^0(g)$.
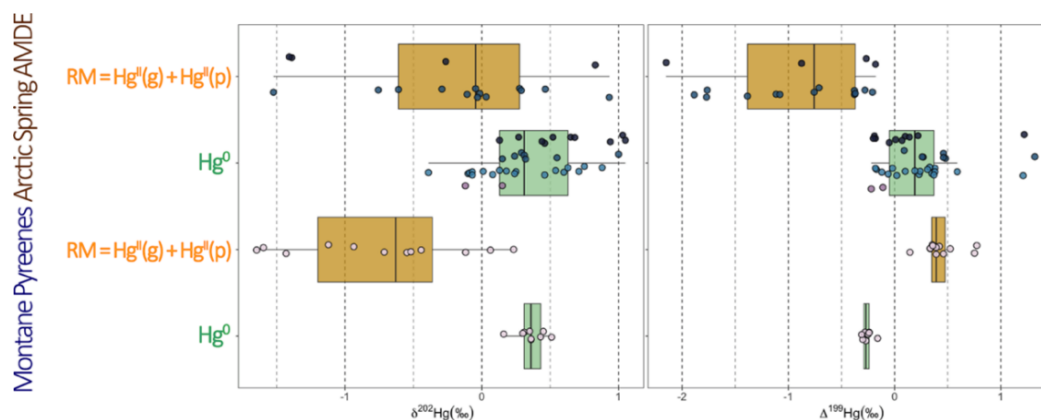
Figure 12. A comparison of the MDF and odd-MIF signatures for atmospheric Hg^0 and RM, measured during Arctic AMDEs and in the Pyrenees during winter, reveals notable contrasts.

Gaseous Hg
(~Hg⁰)
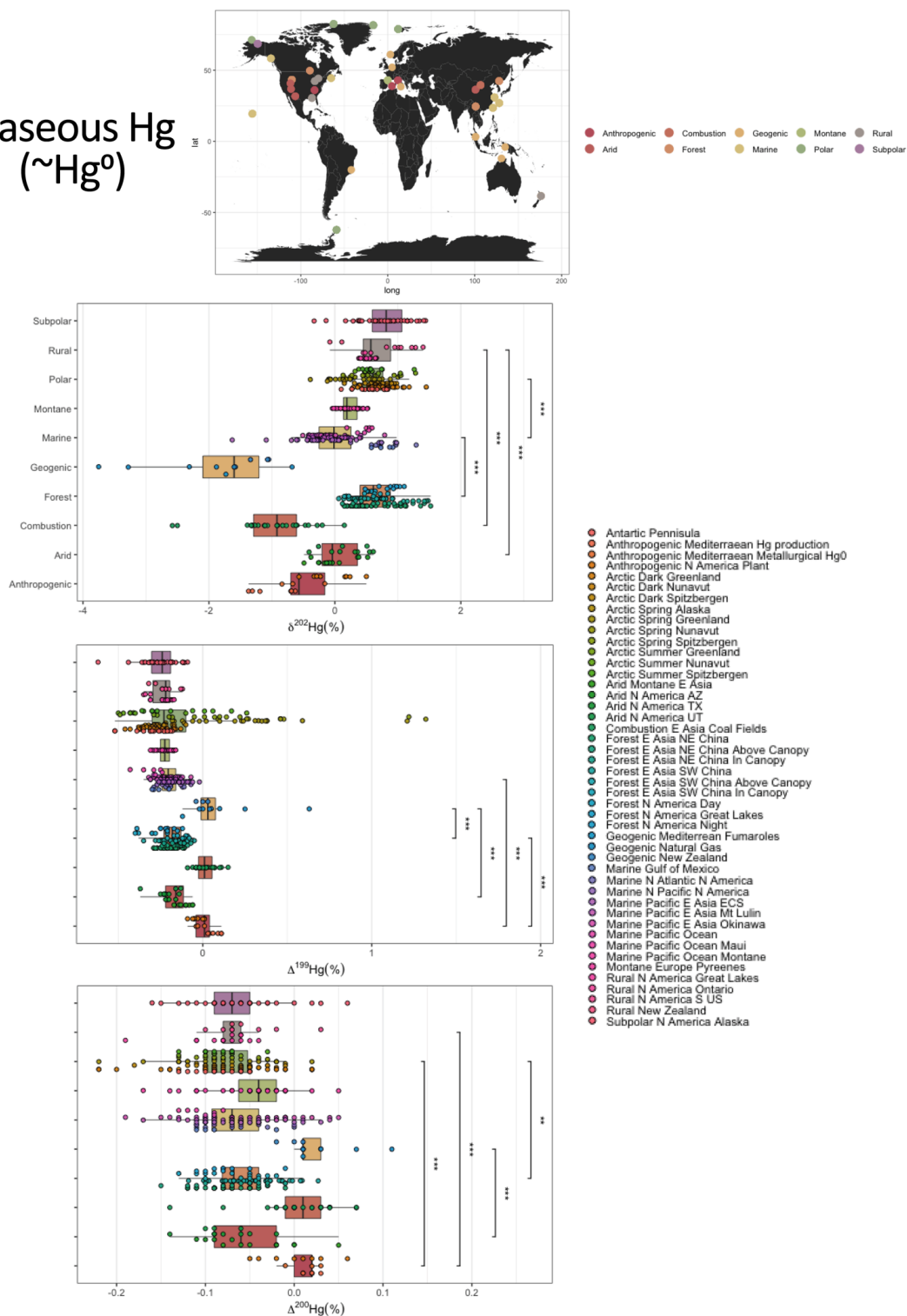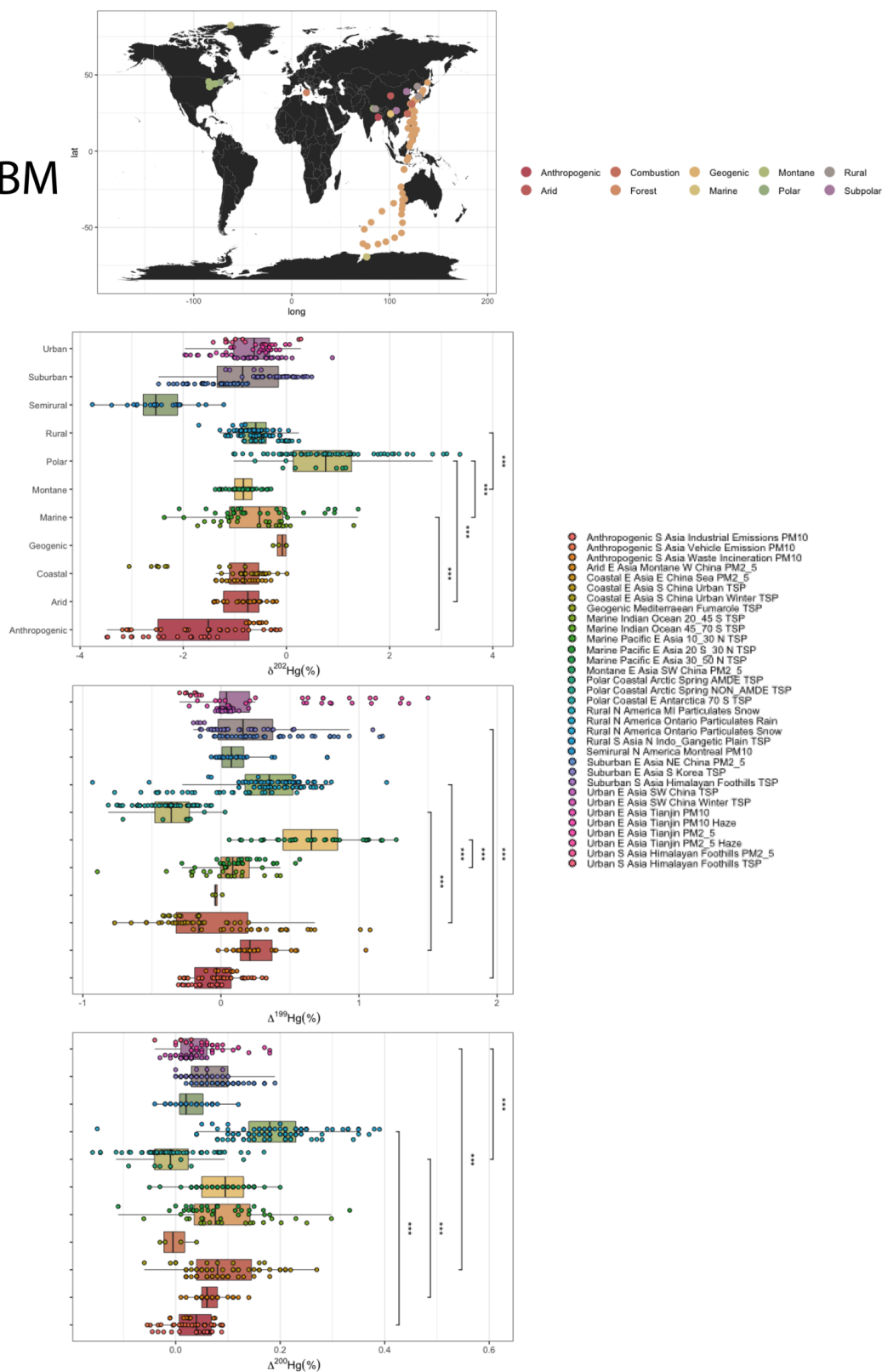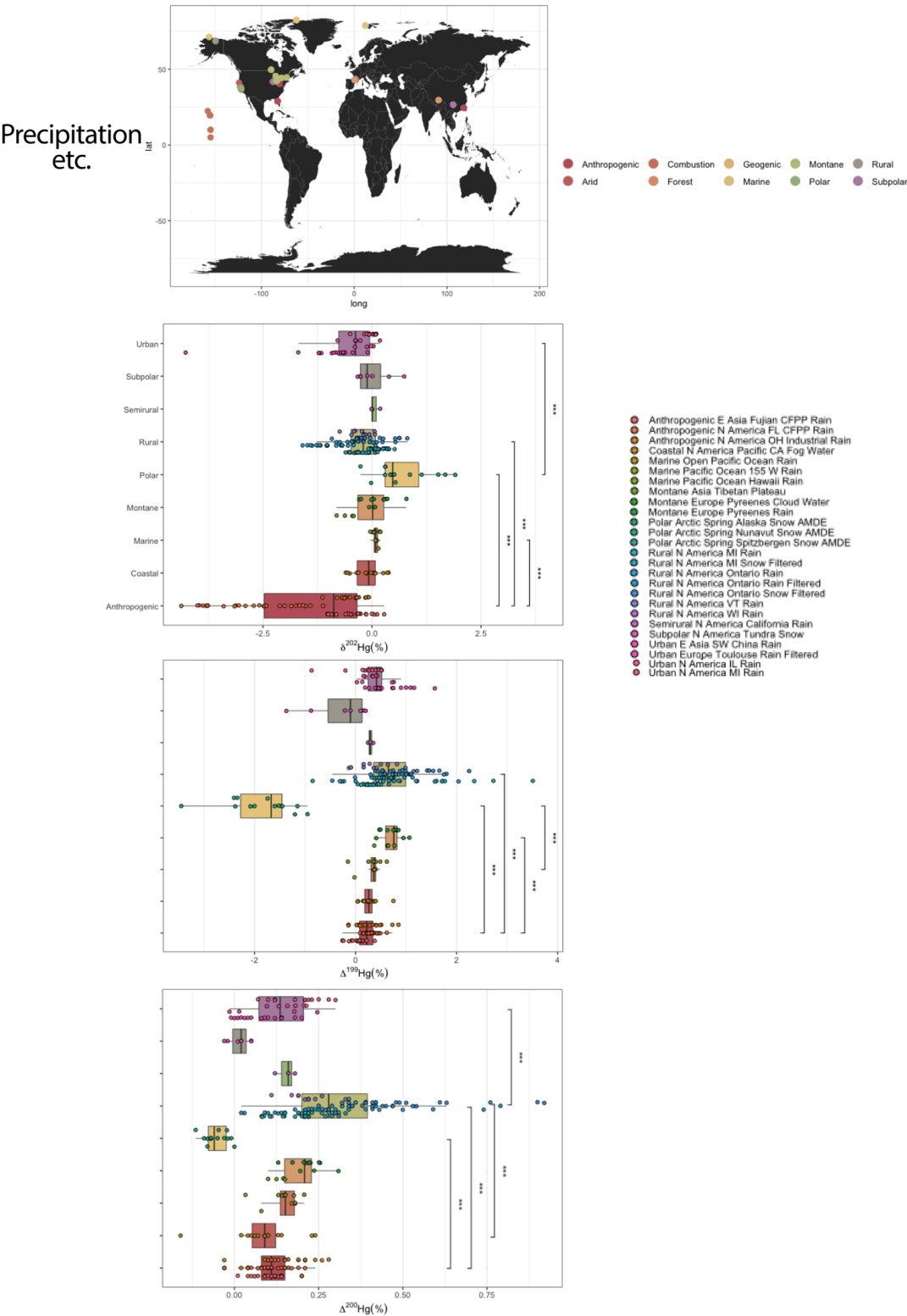
Figure 13. Global isotopic observations of gaseous Hg (~Hg^0) (a), particulate Hg (PBM) (b) and Hg in precipitation (c) divided into δ^{202}Hg (top), Δ^{199}Hg (middle) and Δ^{200}Hg (bottom).
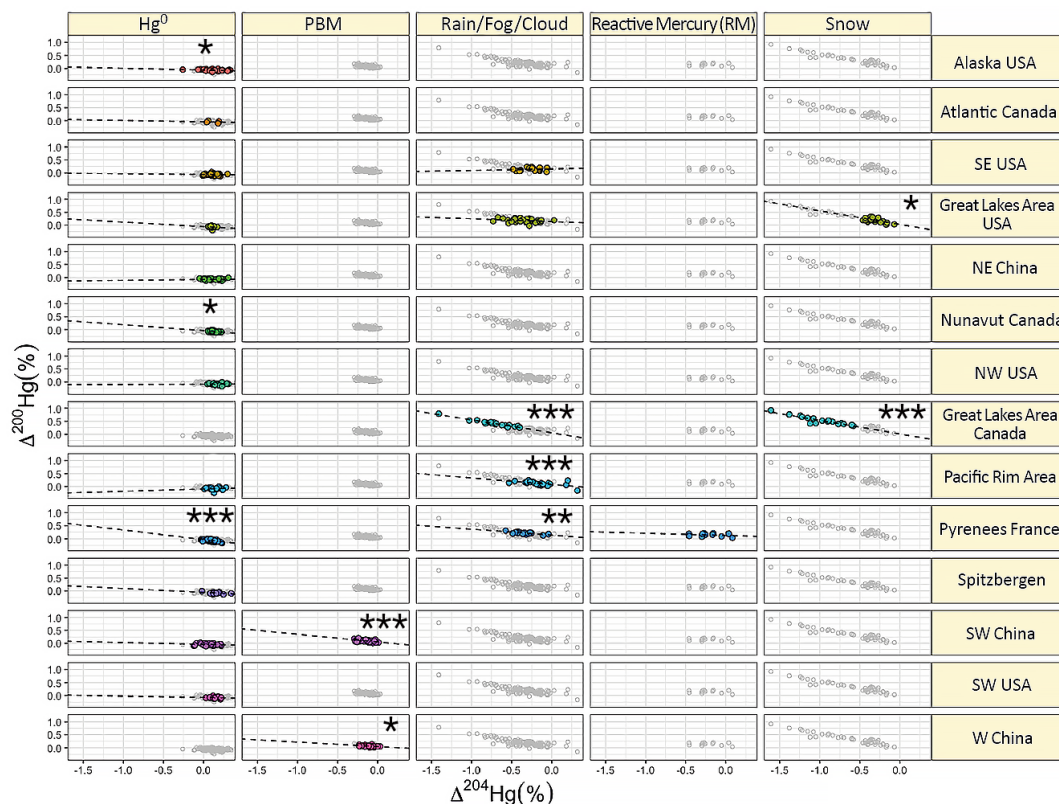
Figure 14. Global observations of even-MIF (Δ^{200}Hg vs. Δ^{204}Hg) by, from left, Hg^0, PBM, rain/fog/cloud, Reactive Mercury (RM), and snow.

1650 **8.3 Isotope fractionation during gas-phase oxidation**

Data on Hg stable isotopic fractionation during gas-phase chemical reactions of Hg are limited. However, in addition to the published studies on the fractionation during the oxidation of Hg^0 initiated by Cl and Br atoms (Sun et al., 2016) and during the oxidation of electronically excited Hg^0 in the presence of synthetic air (Sun et al., 2022), a thesis work of provides additional data (Sun, 2018), which are highlighted here.

1655 **8.3.1 Ground-state Hg^0 oxidation in air**

Isotope fractionation during the oxidation of Hg^0 vapor in the ground state has been studied for the reactions initiated by Cl$^\bullet$/Br$^\bullet$/$^\bullet$OH/O$_3$/BrO$^\bullet$ in air at 750 torr and 298 K as listed in **Table 7**. **Fig. 15** shows that the Br$^\bullet$ and $^\bullet$OH reactions produce a lighter isotope enrichment in the reactant, unlike the other reactions that follow the kinetic isotope effect (KIE). This deviation from KIE occurs because the Hg^0 to Hg^I step (**Rxn G1-G3**, **Table 3**) in the overall Hg^0 to Hg^{II} oxidation is reversible. The equilibrium isotope

1660 effect (EIE) is especially invoked for the $^\bullet$OH and Br$^\bullet$ channels being affected by thermal and photolytic dissociation (Br1, OH1), creating a cyclic replenishment of Hg^0 at higher temperatures, as discussed in **Section 5.1.2**. EIE predicts the enrichment of heavier isotopes in species with a stronger bonding environment (e.g., HgBr$_2$, Hg(OH)$_2$, Schauble, 2007). However, at temperatures in the upper atmosphere and during AMDEs in polar regions, the rate of Br1b/OH1b becomes much lower and the oxidation mechanism moves towards irreversibility, potentially leading to dominance of KIE at lower temperatures. The chlorine-atom-initiated reaction

1665 already displays KIE at 298 K, which is related to the relative thermal stability of the HgCl intermediate. All the atmospherically relevant reactions investigated (Cl$^\bullet$, Br$^\bullet$ and $^\bullet$OH) give rise to (+) odd-MIF, which is most pronounced for the Cl-initiated reaction (E^{199}Hg = –0.37‰) compared to the others (E^{199}Hg = –0.23‰ and –0.18‰ for the Br and OH reactions, respectively). Analogous to $^\bullet$OH + $^\bullet$OH recombination yielding H$_2$O$_2$ in the gas phase (Velivetskaya et al., 2016; Velivetskaya et al., 2018), odd-MIF plausibly occurs due to MgIE triggered by radical-radical ($^\bullet$Hg^{I}X + Y$^\bullet$) interactions that occur during reactions leading to the formation of

1670 XHg^{II}Y species. It should be noted that the diagnostic ratio of Δ^{199}Hg/Δ^{201}Hg ~1.9, which is observed for the Hg^0 + Cl$^\bullet$ system,

differs significantly from the ratios reported in the photoreduction of Hg^{2+} complexes in water (**Section 8.4.1**).
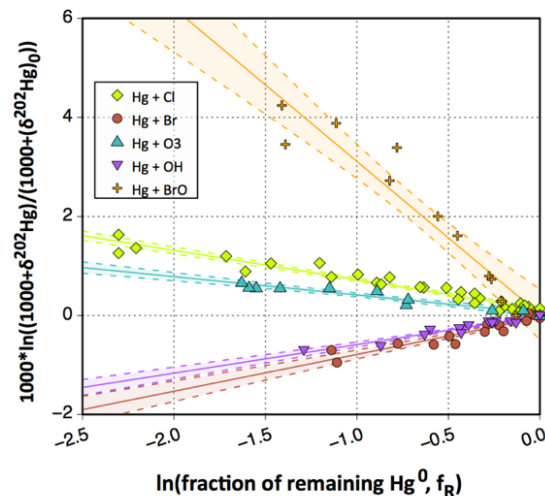
Figure 15. Linearized Rayleigh diagram for δ^{202}Hg in Hg^0 during Cl, Br, OH, O$_3$ and BrO oxidation experiments at ~298 K showing normal and inverse KIE. Each point represents a single experiment.

Table 7. Experimental fractionation factors (ε, E) determined in the gas-phase oxidation studies.

Oxidant	Precursor	Bath gas	ε^{202}Hg (‰)	E^{199}Hg (‰)	Even-MIF
Cl$^\bullet$	CCl$_3$C(O)Cl + hν	air	−0.590	−0.370	detected
Br$^\bullet$	CHBr$_3$ + hν	air	0.740	−0.230	
O$_3$	n/a	air	−0.370	−0.120	
$^\bullet$OH	H$_2$O$_2$ + hν	air	0.580	−0.180	
"BrO$^\bullet$"	CHBr$_3$ + O$_3$ + hν	air	−3.105	1.009	

1675 **8.3.2 Hg^0 oxidation initiated by photosensitized reactions**

Ancient rock samples show a significant occurrence of even-MIF in the Archean atmosphere (~2.5 Ga, Zerkle et al., 2020), which lacked an O$_3$ layer to filter out deep UV in the actinic light. However, in the modern atmosphere, even MIF does not appear to occur significantly in Hg redox processes at the Earth's surface. A current atmospheric budget reveals notable imbalances between the Δ^{200}Hg in Hg emissions from and deposition to the Earth's surface (0.025 ± 0.032‰ vs. 0.073 ± 0.019‰, Fu et al., 2021). To maintain
1680 a steady state, even-MIF sources in the atmosphere are necessary. Studies have shown that UVC-induced Hg^0 vapor in the electronically excited state, Hg(^{3}P$_1$), undergoes chemical transformation under both artificial (Mead et al., 2013) and modern (Sun et al., 2022) atmospheres, resulting in large MIF of both odd and even Hg isotopes. There are claims (Blum and Johnson, 2017; Mead et al., 2013) that the Δ^{200}Hg/Δ^{204}Hg ratios found in nature are similar to those present in the glass housing of compact fluorescent lamps (CFLs). However, the Δ^{199}Hg^{II}, Δ^{200}Hg^{II}, and Δ^{204}Hg^{II} in the CFL housing exhibit opposite signs to those observed in nature
1685 (cf. **Fig. 13 & 14**). Laboratory experiments have shown that the net oxidation of Hg^0 by reaction between excited state Hg^0 and atmospheric O$_2$, identical to the driving photosensitized reaction for the turnover of Hg^0 in the upper stratosphere (**Rxn G12b** counteracted by **Rxn G71, Table 3**), scrambles the systematics of all Hg isotopes in an entirely mass-independent manner. These laboratory experiments and atmospheric samples show similar observations for the Δ^{200}Hg/Δ^{204}Hg ratio, suggesting that photodissociation is a potential chemical mechanism for triggering even-MIF in the atmosphere (Sun et al., 2022). This review
1690 outlines new findings on atmospheric Hg chemistry, supporting the fundamental importance of photodissociation processes (**Sections 5.1.2 and 5.1.4**). In addition to the gas phase, surface-mediated photolysis of mercurous halide species has also been proposed to give rise to even-MIF (Fu et al., 2021). However, theoretical challenges still need to be solved at the quantum mechanics level to generically expand our understanding of anomalous isotope effects for traditional and non-traditional elements (Lin and Thiemens, 2024). Nevertheless, further research in this area should be encouraged, including both field studies and laboratory experiments.

8.4 Isotope fractionation during aqueous-phase red-ox transformation

Hg transformation in the aqueous phase has been reviewed extensively, including stable Hg isotope studies (Hintelmann and Zheng, 2011). This article will not focus on biotic processes, such as microbial reduction, methylation and demethylation, and phototrophic microbial reduction. Kritee et al. (2013) and Tsui et al. (2020) provide overviews of this field. The focus is on abiotic processes, excluding those involving coordination with macromolecular heterogeneous ligands such as dissolved organic matter or fractions, and instead on low molecular weight ligands, including those with N–, O–, S–, or (pseudo)halide donors. This includes inorganic and organic ligands, and oxidizing and reducing processes (**Section 6**).

8.4.1 Reduction

To recapitulate **Section 8.1**, in addition to conventional MDF, isotopic effects in NFS and MgIE occur for Hg during chemical transformation in the aqueous phase. MDF and NFS are present in all reactions to varying magnitude and in all mechanisms and have a thermodynamic nature. In contrast, MgIE is the kinetic effect and is indicative of spin-selective reactions involving a paramagnetic intermediate. Therefore, MgIE is the only isotope effect that detects the mechanism of the reaction. MgIE can be both thermally and photolytically induced and can be two-dimensional (+ or – depending on the reaction conditions, Zheng and Hintelmann, 2010b) or one-dimensional (exclusively +) depending on the identity of the Hg^{II} complex (Motta et al., 2020a). In cases where the spin-selective reaction can be induced thermally, the radical pair is generated almost exclusively as a singlet (Buchachenko, 2018), which is spin-forbidden to react (dissociate) further into products. For a singlet spin forbidden reaction compared to a triplet spin allowed reaction, the magnitude of the MgIE-MIF is more limited. However, many Hg^{II} complexes have a narrow energy separation of a variety of excited states, indicating that the intermediate radical pair can evolve in a triplet or singlet state. From studies of Hg^{2+} photoreduction in the presence of organic ligands (which consistently follow a pseudo-first-order kinetic pathway), it has been shown that, depending on the degree of Hg^{2+}(aq) turnover, weak MIF is initially induced by NFS and then, when most of the Hg^{2+}(aq) has been converted, there is a shift to strong MIF induced by MgIE, the onset of which coincides with strong suppression of MDF (Motta et al., 2020b; Zheng and Hintelmann, 2010b). One explanation why MgIE first appears closer to complete Hg^{II} reduction is, at least in part, that the termination radical-radical step when Hg^0 is split off (in a bimolecular reaction, such as $Hg^{+\bullet} + C_2O_4^{\bullet-}/CO_2^{\bullet-}$ in the photoreduction of $Hg(\eta^2\text{-}C_2O_4)$) is favored by a decreasing concentration ratio of oxidized Hg to bulk ligand (Zhao et al., 2021). As shown in **Fig. 11**, (–)MgIE is induced when the radical pair is generated in a singlet state and (+)MgIE is induced when the excitation occurs in a triplet state. Ligand field strength, in combination with atomic orbital hybridization theory, has been used to illustrate MgIE in the (photo)reduction of Hg^{II} complexes. This has been suggested to vary as a function of, among other things, the arrangement of the ligands around Hg^{2+}, the coordination strength of the ligands, and the presence/absence of light along with its wavelength (Epov, 2011a; Epov, 2011b). As discussed in **Section 4.2**, reduced S- and reduced N-containing groups are soft (strong field) ligands, whereas O-donating groups are hard (weak field) ligands. Epov (2011a) rationalized mercuric complexes with strong field ligands such as cysteine ($Hg(cys)_2^{2-}$) and ethylenediamine ($Hg(en)^{2+}$) as bright singlets (i.e. in the presence of light) with an sp-hybridization at the central atom Hg in two binding orbitals. To undergo a singlet-triplet evolution by hyperfine coupling between magnetic nucleus (^{199}Hg and ^{201}Hg) and electrons to a paramagnetic state, Hg must change its orbital hydridization from sp-linear to sp^2d-planar square so that the transfer of electrons from the soft ligand to Hg can be accomplished.
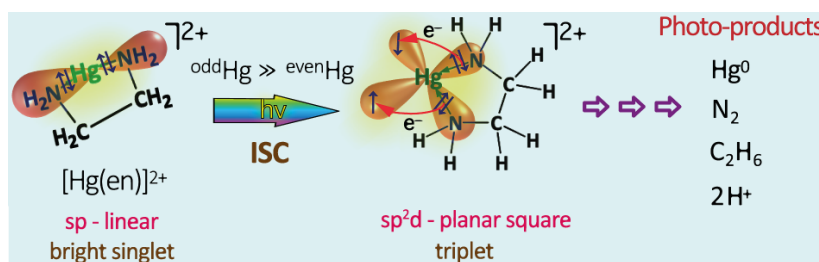
Figure 16. Mechanism proposed by Epov (2011b) for the photoreduction of $Hg(en)^{2+}$ via a bright singlet excited complex undergoing intersystem crossing preferentially for the odd isotope to the closest triplet state, which can dissociate following a complex reaction.

The figure above shows this schematically for Hg(en)$^{2+}$ + light showing (–)MgIE. Analogously, it is postulated that mercuric complexes with O-binding ligands possess a bright triplet state that is more likely (spin allowed) to undergo Hg reduction via 1e-LMCT with an imprint of (+)MgIE.

1735 For a change in spin state to occur, spin-orbit coupling (SOC) must be induced, but if SOC is elevated, spin relaxation or phosphorescence can be induced, which prevents the formation of a separating radical pair during dissociation, making MgIE less relevant (cf. **Fig. 11**). Coupling constants are known experimentally for only a few Hg-containing radicals (CH$_3$Hg$^\bullet$, Karakyriakos and Mckinley, 2004; $^\bullet$HgF, Knight Jr. et al., 1981; $^\bullet$HgCN, Knight Jr. and Lin, 1972; $^\bullet$HgH/$^\bullet$HgD, Stowe and Knight, 2002). Recently published theoretical electronic structure simulations have been performed on environmentally interesting Hg halides (Cl,

1740 Br, I) and pseudohalides (methanethiol). The study (Motta et al., 2020a) shows that the coupling for reactions involving $^\bullet$Hg^{I}Br and $^\bullet$HgI is so high that radical pair formation is inhibited, while for $^\bullet$Hg^{I}Cl and CH$_3$SHg$^{I\bullet}$ it is sufficient in the caged pair as well as at a low level in the separated pair geometries, allowing MgIE to form. Depending on the identity of the Hg–ligand bond that undergoes homolysis to a radical pair, either quadruple (X = Cl, S) or double (Y = C) degeneracy can occur between the low-lying electronically excited levels and the ground state in HgX$_2$ and HgXY compounds, respectively, allowing the photoreduction of HgX$_2$ to exhibit

1745 (+)MgIE or (–)MgIE while that of HgXY (i.e. MMHgX) exhibits only (+)MgIE. This is based on the premise that the photolysis of MMHgX is exclusively by cleavage of the weaker Hg–C bond rather than the stronger Hg–X bond. (+)MgIE is most evident for the photoreduction of MMHg$^+$ species, as its $^3\sigma\sigma^*$ 1e-LMCT state is energetically separated from other excited states in the paramagnetic intermediate, leading to maximization of MgIE (Motta et al., 2020a). Stable Hg isotopes provide insight into the dynamics and metabolism of inorganic and methylated Hg in biota. In particular, exposure to the former results in subtle odd-MIF with a

1750 Δ^{199}Hg/Δ^{201}Hg ratio close to unity at sampling, while for the latter this ratio is higher (~1.3) with large odd-MIF (up to ~5‰ in fish, Li et al., 2022b).

From **Table 8**, which summarizes the isotopic effects quantitatively observed in aqueous-phase laboratory studies, MgIE can have different signs for the same reactant depending on the reaction conditions, as exemplified by the Hg-cysteine-light system. Depending on the degree of photoconversion, reduction of Hg^{II} in the presence of water-soluble diesel soot (aromatic polyacids and humic-like

1755 structures) exhibits swings in the direction of MgIE (Huang et al., 2021). A further example of the influence of pH/complexation on the evolution of MgIE can be seen in the UVC photodegradation of MMHg$^+$ in acidic and alkaline (adjusted with NH$_3$) solution, where (+)MgIE is significant in the first case but very limited in the second. For traditional elements with the same reaction mechanism, the strength development of MgIE depends on various factors, including viscosity, triplet sensitizer, and excited state quenchers (Turro, 1983; Buchachenko, 2013). As in the laboratory experiments, both (+) and (–) net Hg MgIE have been observed

1760 in samples related to the natural atmosphere, as previously reported in **Section 8.2**. The reaction conditions also affect the degree of turnover of the Hg reactant at which the onset of MgIE occurs, which incidentally does not correlate with a change in the overall reduction rate. Experimental research is needed to better interpret odd-MIF signatures and systematically elaborate the roles of reaction parameters (pH, presence of O$_2$, light wavelength, Rose et al., 2015, etc.) in excited state kinetic isotope effects. For example, dissolved O$_2$ is a well-known quencher of excited triplet states, but radical-O$_2$ reactions have also been described to induce significant

1765 MgIE (Pliss et al., 2019). For the photoreduction of Hg in the presence of multifunctional ligands (such as NOM), stoichiometry (Hg:L ratio) has been shown to play an important role in the magnitude of MgIE induced. For the dissolved organic matter (DOM) fraction from Dorset Lake, Ontario, Zhang and Hintelmann (2009) observed in anoxic photo-experiments an –E^{199}Hg optimum ($\gtrsim$5‰) associated with a ligation mode where all S−bonding functional groups are saturated by Hg^{2+} cations and the proportion of Hg–O bonds increases, which increases the ratio of bright triplets to bright singlets and the MgIE becomes increasingly positive. As

1770 the Hg:L ratio is further increased, the reduction rate (driven by Hg–O complexes) is significantly affected. The triplet-singlet spin evolution is limited to fewer HgL radical pairs, resulting in a lower –E^{199}Hg (Epov, 2011a). Photo experiments with Hg^{II} in the presence of DOM extracted from marine phytoplankton give rise to (–)MgIE during reduction, in contrast to freshwater DOM (Kritee et al., 2018).

Table 8. Experimental fractionation factors determined for a variety of Hg red-ox transformations.

Initial Hg conc. (electrolyte)	Reactant	Experimental conditions: L/Hg ratio	Anoxic/Oxic	Major Hg species	$\varepsilon^{202}Hg$ (‰,±2σ)	$E^{199}Hg$ (‰)	$\Delta^{199}Hg/\Delta^{201}Hg$	Isotope effects	Reference
Photoreduction of Hg^{II}									
0.5 µM NIST-3133 (Cl⁻)	Cysteine (Hcys)	Quartz glass, ~2000:1 (M/M), Xe lamp (UVC-filter), pH 3.6	A	Hg(cys)₂	−1.32 ± 0.07	1.02	1.46 ± 0.03	MDF, NVE, (−)MgIE	Zheng & Hintelmann, 2010b
0.17±0.04 µM		FEP Teflon, ≳2000:1 (M/M), natural sunlight, pH 3.2	A			−	1.34 ± 0.03		Motta et al., 2020b
		FEP Teflon, ≳2000:1 (M/M), natural sunlight, pH 7.2			−1.04 ± 0.09	−0.25	0.99 ± 0.06	MDF, (+)MgIE	
		FEP Teflon, ≳2000:1 (M/M), natural sunlight, pH 7.2	O			−1.15	1.11 ± 0.09		
0.5 µM NIST-3133 (Cl⁻)	Serine (Hser)	Quartz glass, 2000:1 (M/M), Xe lamp (UVC-filter), pH 3.8	A	Hg(ser)₂	−1.71 ± 0.03	0.17	1.67 ± 0.28	MDF, NVE, (+)MgIE[35]	Zheng & Hintelmann, 2010b
0.17±0.04 µM		FEP Teflon, ≳2000:1 (M/M), natural sunlight	A/O		−1.81 ± 0.04	0.06 ~−1.3	~1.6 1.08 ± 0.01	MDF, NFS (+)MgIE[36]	Motta et al., 2020b
0.17±0.04 µM	Ethylenediamine (en)	FEP Teflon, ≳20000:1 (M/M), natural sunlight, pH 7.4	O	Hg(en)₂²⁺ HgOH(en)⁺	−0.9 ± 0.3	0.16	0.85 ± 0.14	MDF, (−)MgIE	Motta et al., 2020b
1 µM (ClO₄⁻)	Oxalate (ox²⁻)	Pyrex, 300:1 (M/M), UV-B light, pH 3.9 & 5.2	A/O	Hg-η-ox	−1.45 ± 0.06	0.15	1.39 ± 0.38	MDF, NVE[37]	Zhao et al., 2021
	AQDS	Pyrex, 300:1 (M/M), UV-B light, pH 3.4	A	?	−0.66 ± 0.10	−0.86	1.00 ± 0.02	MDF, (+)MgIE	
	Salicylic acid (Hsal)	Pyrex, 300:1 (M/M), UV-B light, pH 4.3	A	Hg(sal)⁺?	−1.79 ± 0.30				This work
	4-hydroxy-benzoic acid (HOBz)	Pyrex, 300:1 (M/M), UV-B light, pH 4.9	A	Hg(OBz)⁺?	−2.25 ± 0.10	~−0.10	1.53 ± 0.02	MDF, NVE	
	4-aminobenzoic acid (HNBz)	Pyrex, 300:1 (M/M), UV-B light, pH 5.9	A	Hg(NBz)⁺?	−2.75 ± 0.40				
0.3−0.5 µM	Suwannee River fulvic acid	Quartz glass, ~10−17 (m/m), sunlight	O		−0.60	−0.45	1.00 ± 0.02	MDF, (+)MgIE	Bergquist & Blum, 2007
~10 µM	NIST-3133 (Cl⁻) Dorset Lake bulk DOM pH 6.5	Quartz glass, ~29000 (m/m), Xe lamp (UVC-filter)	A	The proportion of Hg-O bonding increases as we move downwards, and so does the reaction rate.	−0.77 ± 0.18	−2.94	1.19 ± 0.02	MDF, (+)MgIE	Zheng & Hintelmann, 2009
		Quartz glass, ~6000 (m/m), Xe lamp (UVC-filter)			−0.72 ± 0.10	−4.12	1.22 ± 0.02		
~50 µM		Quartz glass, ~1200 (m/m), Xe lamp (UVC-filter)			−1.26 ± 0.07	−6.29	1.24 ± 0.02		
		Quartz glass, ~1200 (m/m), sunlight			−0.99 ± 0.02	−5.57	1.26 ± 0.01		
~500 µM		Quartz glass, ~120 (m/m), Xe lamp (UVC-filter)			−1.06 ± 0.02	−1.94	1.30 ± 0.02		
~50 µM					−1.09 ± 0.04	−1.99	1.31 ± 0.01		
29 nM (NO₃⁻)	Marine algal DOM (intracellular)	Teflon, 1.41 nmol chla⁻¹, UVB-light	O		−0.70	1.03	1.06	MDF, (−)MgIE	Kritee et al., 2018
82 nM (Cl⁻)	Water-soluble diesel soot extracts	Quartz glass, ~67:1 (M/M), Xe lamp, Instanteous removal of product (Hg⁰)	A		−1.30 ± 0.11	−2.49	1.15	MDF, (+)MgIE	Huang et al., 2021
10 nM (NO₃⁻)	Dissolved black carbon (< 0.45 µm)	Glass, ~42000:1 (M/M), Xe lamp	A				1.20 ± 0.10	MDF, (−)MgIE	Li et al., 2020b
Photoreduction of $MMHg^+$									
50 µM	CH₃HgCl	Hg-lamp (λ=254 nm), pH 4.0		CH₃HgCl	~−0.25	~−0.5	1.26 ±0.06	MDF, (+)MgIE	Malinovsky et al., 2010
	CH₃HgOH	Hg-lamp (λ=254 nm), pH 8.6		CH₃HgOH	~−0.3	<−0.06		MDF, supressed (+)MgIE	
0.3−0.5 µM?		Suwannee River fulvic acid, sunlight — 10 mg C/L	O		−1.70 ± 0.30	−7.9	1.36 ±0.02		Bergquist & Blum, 2007
		1 mg C/L			−1.30 ± 0.20	−3.3			
102 nM	CH₃Hg⁺ (Cl⁻)	Suwannee River fulvic acid, Xe lamp (UVC-filter) — 2.13[38]	O		−1.74 ±0.50	−0.9	1.30 ±0.07	MDF, (+)MgIE	Chandan et al., 2015
86 nM		0.72			−4.64 ±1.64	−5.0	1.28 ±0.09		
101 nM		0.42			−1.91 ±0.25	−7.2	1.32 ±0.03		
80 nM		0.17			−1.77 ±0.81	−7.2	1.30 ±0.03		
97 nM		0.10			−1.50 ±0.50	−13.4	1.40 ±0.03		
94 nM		0.07			−2.24 ±0.44	−16.2	1.37 ±0.03		

[35] Appears at 4 h photoreduction and beyond with a $\Delta^{199}Hg/\Delta^{201}Hg$ of 1.10–1.18
[36] Onset of (+)MgIE at $f_R = 0.40$–0.76 depending on reaction conditions.
[37] A single experiment (anoxic, pH 6) on oxalate indicates (+)MgIE at $f_R = 0.11$.
[38] MMHg/organic bound reduced sulfur (M/M)

96 nM		Pony Lake fulvic acid, Xe lamp (UVC-filter)	0.01			−1.13 ±0.36	−15.3	1.36 ±0.01		
104 nM		Nordic Lake DOM, Xe lamp (UVC-filter)	0.41			−1.33 ± 0.17	−1.3	1.17 ± 0.04		
95 nM			0.05			−2.23 ± 0.68	−14.6	1.41 ± 0.02		
Dark reduction of Hg^II										
1 μM (ClO$_4^-$)	Benzoquinone C$_6$H$_4$(OH)$_2$ QH$_2$	Pyrex, 300:1, dark, pH 4.6	O	Hg–QH$^+$?	−1.25 ±0.19	0.12	1.39 ±0.38	MDF, NVE	Zhao et al., 2021
0.5 μM NIST-3133 (Cl$^-$)	SnCl$_2$	Quartz, dark, low pH	A	HgCl$_4^{2-}$	−1.56 ±0.11	0.17	1.59 ±0.22		Zheng & Hintelmann, 2010a
1 μM (ClO$_4^-$)	Ascorbic acid	Pyrex, 300:1, dark, pH 5.1	O/A	?	−1.79 ±0.13	0.08	1.48 ±0.35		This work
NIST-3133 (Cl$^-$)	Dorset Lake bulk DOM	Quartz, dark, pH 6.5	A		−1.52 ± 0.06	0.19	1.54 ±0.34		Zheng & Hintelmann, 2009
1 μM NIST-3133 (NO$_3^-$)	FeCl$_2$	Glass, 12.5:1, dark, pH 6.5, 0.5 mM Cl$^-$	A	Hg(OH)$_2$	−2.20± 0.16 −2.44± 0.17[39]	0.21 0.34	1.58±0.08 1.60±0.05		Schwab et al., 2023
		Glass, 12.5:1, dark, pH 6.5, 10 mM Cl$^-$		HgCl$_2$, Hg(OH)Cl	−2.14± 0.09		0.24±0.01		
Methylation of Hg^II										
0.5 − 5 μM NIST-3133 (Cl$^-$)	Methylcobalamin	1000:1, pH 5, (UV–A lamp) (λ~325 nm)	O		~−1.5[40]	0.21[41]	1.20±0.17	MDF, (−)MgIE	Malinovsky & Vanhaecke, 2011
	Acetate					0.22	1.20±0.26		
Oxidation of Hg^0										
200 − 280 nM	Hydroxyl radicals	Pyrex, ≤ 600:1 (NaNO$_3$), pH 7, UV-lamp (λ > 300 nM)	A	Hg(OH)$_2$	1.20 ±0.14				Stathopoulos, 2014
~60 nM	Sulphanyl-acetic acid	Glass, 80:1 (M/M), dark, pH 7	A		1.25 ±0.11	−0.14	1.28 ±0.38	EIE-MDF, NVE	Zheng et al., 2019
	2-sulphanyl-propanoic acid		A		1.10 ±0.08				
115 nM	Reduced natural Elliott soil humic acid	Glass, ~0.6−1.2 S:Hg (M/M)	A		1.54 ±0.10	−0.18			

1775

As shown in **Table 8**, photo reduction of Hg^{2+} is often, but by no means always, associated with high odd-MIF. For macromolecular entities such as DOM and fulvic acids, and a selection of smaller organic ligands that use O−, N− and S-donor atoms to complex with Hg^{2+}, MgIE is induced initially in the photoreduction process, whereas for the amino acid serine, MgIE is triggered only after a significant turnover of Hg^{2+}, the onset of which varies significantly depending on the reaction conditions (Zheng and Hintelmann, 2010b; Motta et

1780 al., 2020b). The experimental Δ^{199}Hg/δ^{202}Hg data are described to follow the same trajectory, regardless of when MgIE kicks in during the serine-assisted photo-reduction. When oxalic acid was screened with a single light experiment (anoxic, pH 6, f$_R$ = 0.11), (+)MgIE was observed, while anoxic time series experiments with UV-B irradiation at pH 3.9 and 5.2 showed no evidence of MgIE in the range investigated down to f$_R$ = 0.01. This is evidence that Hg oxalate complexes can be directly photodegraded by homolysis (Hg(η^2−C$_2$O$_4$) $\xrightarrow{h\nu}$ Hg$^{\bullet+}$ + C$_2$O$_4^{\bullet-}$) as well as heterolysis (Hg(η^2−C$_2$O$_4$) $\xrightarrow{h\nu}$ Hg + 2 CO$_2$). Heterolytic photoreduction does not induce MgIE, but shows

1785 NFS with limited (−)odd-MIF, as is the case for ligation with the substituted aromatic carboxylic acids shown in the table. This also applies to thermal (dark) reduction by a uni− (e.g. Hg–QH$^+$ → Hg^0 + Q + H$^+$) or bimolecular (e.g. Hg^{2+} + Sn^{2+} → Hg^0 + Sn^{IV}) processes. Although the NFS is a general isotopic effect, its magnitude depends on the shift in the 6s orbital electron density, which is greater for a red-ox reaction than for ligand exchange or evaporation. In turn, ionic Hg complexes have a greater NFS than more covalent complexes upon reduction to Hg^0. NFS typically produces a characteristic Δ^{199}Hg/Δ^{201}Hg slope of ~1.54 to 1.66 as determined from experimental

1790 studies and theoretical calculations. However, the application of linear regression to NFS odd-MIF data (Δ^{199}Hg vs. Δ^{201}Hg) is limited in several cases because the observations are distributed over such a small range that it approaches the scale of the corresponding analytical precision. **Table 8** gives two standard deviations of the slope of the linear fits using York's regression, and intermittently the uncertainty is so large that it does not allow a definitive Δ^{199}Hg/Δ^{201}Hg ratio to be determined. In these cases, it has been suggested that a better indicator of NFS is instead to confirm that the patterns of Hg isotope fractionation observed mimic the odd-even staggering

1795 pattern of nuclear charge radii (Motta et al., 2020b). The description of NFS is limited to equilibrium fractionation (**Eq. 21**) and predicts,

---

[39] Refers to closed system
[40] iApplies to dark conditions, under UVA irradiation demethylation gradually counteracts MMHg$^+$ formation.
[41] Potentially explained by photo-degradation of MMHg$^+$

like EIE-MDF (**Eq. 19**), the enrichment of heavier isotopes in the oxidized fraction of the red-ox pair. Calculations performed for a series of Hg^{II} complexes, both binary and heterogeneous, containing simple hard and soft ligands relative to Hg^0, show that NFS makes the most significant contribution to $\varepsilon^{202}Hg_{NFS}$ in most cases (ranging in total from 46 to 85% at 25°C, Jiskra et al., 2012). The expected mass-independent enrichment $E^{199}Hg_{NFS}$ can be calculated based on the calculation of $\varepsilon^{202}Hg_{NFS}$, using the scale factors $\beta_{KIE-MDF}$ and β_{NFS}

1800 (Jiskra et al., 2012):

$$E^{199}Hg_{NFS} = \varepsilon^{202}Hg_{NFS} \cdot (\beta_{NFS} - \beta_{KIE-MDF}) \approx -0.2 \cdot \varepsilon^{202}Hg_{NFS} \qquad (23)$$

Reduction by Fe^{II} and p-substituted benzoic acids results in one of the highest magnitudes of experimentally observed kinetic MDF (**Table 8**). The former system has been studied anoxically both as an open and closed system (Schwab et al., 2023), where the fractionation is of Rayleighian model (kinetic) and equilibrium type, respectively. The closed system permits overprinting with the signature of isotopic equilibrium fractionation between Hg^0 and hydrolyzed Hg^{2+}, which has been consistently determined in two

1805 independent studies to be –2.63 (Wang et al., 2021) and –2.44‰ (Schwab et al., 2023), respectively. As will be demonstrated below, the magnitude of equilibrium isotope enrichment factors ($\varepsilon^{202}Hg$) between Hg^0 and thiol-bound Hg^{II} is significantly lower (1.1–1.6‰), as related to a lower vibrational energy in Hg-S bonds than in Hg-O/Cl bonds.

8.5 Isotope fractionation during complexation, sorption and surface-catalyzed reduction

8.5.1 Processes interfacing the aqueous phase

1810 Theoretical computations of EIE based on MDF and NVE generally agree with experimentally determined fractionation factors for complexation. Competitive complexation of Hg^{II} between one of the typical hard ligands HO^- and Cl^- and a soft one in the form of a thiol resin results in a lighter isotopic signature of the sulfur-bound Hg^{II} pool ($\varepsilon^{202}Hg$ of –0.62 and –0.53‰, respectively), which is related to increased covalent bonding and electron density in the 6s Hg orbital (Wiederhold et al., 2010). For the sorption of dissolved Hg^{II} on α-FeOOH, the observed isotopic fractionation ($\varepsilon^{202}Hg \sim -0.4$‰) is exclusively determined by the process in solution, where

1815 a vanishingly small pool (< 0.1%) of isotopically lighter cations is in equilibrium with a bulk of neutral Hg^{II} molecules, only the former being sorption active (Jiskra et al., 2012). Equilibration and kinetic fractionation have been reported to describe the precipitation process of β-HgS and HgO, respectively, from an initially acidic solution, with $\varepsilon^{202}Hg$ between precipitate and supernatant being –0.63‰ and –0.32‰, respectively (Smith et al., 2015). As with the adsorption on goethite, the observed fractionation during the precipitation of metacinnabar is interpreted as an effect of solution chemistry, in this case, a transition from

1820 O– to S–bonding for Hg^{II}. In addition to the homogeneous phase reduction of Hg^{II} by Fe^{II} in aqueous solutions (**Table 8**), the heterogeneous phase reduction of Hg^{II} by surface-bound (adsorbed Fe^{II} on goethite/boehmite) or structural Fe^{II} (magnetite $Fe^{II}Fe_2^{III}O_4$, Schwab et al., 2023 and siderite/green rust $FeCO_3$, Wang et al., 2021) has been studied isotopically. As shown in **Table 9**, the isotopic fractionation in heterogeneous reduction is well related in magnitude to that of the homogeneous one by Fe^{II} (**Table 8**), except in the case of magnetite (in whose structure iron is present in different oxidation states) with much more limited MDF and

1825 MIF ($\varepsilon^{202}Hg = -1.38$‰ and $E^{199}Hg = 0.13$‰, respectively). All these processes, when possible to be determined with confidence, demonstrate $\Delta^{199}Hg/\Delta^{201}Hg$ ratios within the range of 1.56 to 1.62, which indicates that the observed MIF ($E^{199}Hg$ in the range of 0.13 to 0.34‰) is caused by NVE.

8.5.2 Processes interfacing the gas phase

Section 8.4.1 and **Table 8** refer to a study of Hg^{II} photoreduction of aqueous diesel soot, which includes experiments with a stationary

1830 soot phase mixed with $HgCl_2$ on a quartz plate over which a slow flow of Ar gas passes, as discussed below (Huang et al., 2021). In comparison, photoreduction in aqueous and solid phase diesel soot shows equivalent enrichment of heavier isotopes in the Hg reactant of 1.26-1.75‰. This overlaps with the value typical of Hg redox chemistry (**Table 8**). In contrast to the aqueous phase, the photoreduction in the solid shows a continuous strong MIF (this time positive MgIE induced in the Hg^0 product) throughout the reaction, whereas in the latter case, a large MIF of opposite sign sets in only after ~60% of the reaction. Furthermore, the reduction

1835 rate increases with the carrier gas's humidity. The photo-triggered MgIE is highest when the carrier gas is dehumidified, but decreases rapidly as the RH increases (**Table 9**)

Table 9. Experimental fractionation factors determined for Hg^{II} complexation, sorption, surface-catalyzed reduction and processes interfacing the gas phase.

Initial Hg^{II} conc. (electrolyte)	Reactant	Experimental conditions: L/Hg ratio		Anoxic (A)/ Oxic (O)	$\varepsilon^{202}Hg$ (‰, ±2σ)	$E^{199}Hg$ (‰)	$\Delta^{199}Hg/\Delta^{201}Hg$	Isotope effects	Reference
Complexation, sorption, precipitation of aqueous Hg^{II}									
196 µM (Cl^-)	$HgCl_2$	Complexation between Hg^{II} and thiol resins		O	−0.53± 0.15			EIE-MDF, NVE	Wiederhold et al., 2010
207 µM (NO_3^-)	$Hg(OH)_2$				−0.62± 0.17				
5–25 µM	$HgOH^+$ $HgCl^+$	Hg^{II} sorption to α−FeOOH		O	−0.37± 0.03	−0.06			Jiskra et al., 2012
100 µM	$Hg(OAc)_2$	Sub-stoichiometric (10, 30, 50, 70%) amounts of S^{2-} added at a start pH of 2.3–3.0		A	−0.63± 0.04			KIE-MDF, NVE	Smith et al., 2015
	Hg^{2+}	Sub-stoichiometric (10, 30, 50, 70%) amounts of OH^- added at a start pH of 1.		A	−0.32				
Hg^{II} – Hg^0 equilibration									
300–328 nM Hg^{II}	$Hg(OH)_2/Hg^0$	Water		A	2.63± 0.37	0.28± 0.21	1.44	EIE-MDF, NVE	Wang et al., 2021
150–173 nM Hg^0	$HgCl_2/Hg^0$	10 mM NaCl			2.77± 0.70				
Heterogeneous Hg^{II} reduction by surface-bound and structural Fe^{II}									
285 nM (NO_3^-)	$Hg(OH)_2$	Hg^{II} reduction to Hg^0 by suspended $FeCO_3$ (s)	Siderite (0.1 g L^{-1}, pH 7.1)	A	2.43 ± 0.38	0.09		EIE–MDF NFS	Wang et al., 2021
			Green rust (0.01 g L^{-1}, pH 7.2)		2.28 ± 0.40				
1 µM (NO_3^-)	$Hg(OH)_2$	Hg^{II} reduction by suspended magnetite ($Fe^{II}Fe_2^{III}O_4$, surface area ~2 $m^2 L^{-1}$		A	−1.37 ± 0.07	0.13 ± 0.01	1.59 ± 0.09		Schwab et al., 2023
Photoreduction of Hg^{II} doped on a diesel soot matrix									
12 µM (Cl^-)		Hg/C 7.8×10^{-5} (M/M)	Relative humidity 28%	A	−1.75 ±0.05	2.43 ±0.19	1.15 ± 0.01	MDF, (−)MgIE	Huang et al., 2021
			Relative humidity 68%		−1.48 ±0.02	0.20 ±0.05			

8.6 Isotopic fractionation during air-surface Hg^0 gas exchange

The interaction between atmospheric Hg and the Earth's reservoirs has been discussed only briefly in **Section 4.2**, as this area has recently
1840 been covered by literature review (Sommar et al., 2020). It is crucial to acknowledge that the gas exchange of volatile Hg is bidirectional. Consequently, the net flux of Hg over an ecosystem may represent a delicate balance between opposing processes, including deposition/uptake versus re-emission. The end members of the Hg exchange between surface (biosphere, pedosphere, lithosphere, hydrosphere, and cryosphere) and atmosphere are all isotopically distinguishable (Liu et al., 2024). A combination of bulk measurements and analysis of stable Hg isotope composition allows to separate the contribution of, atmospheric Hg^{II} and Hg^0 deposition, as well as the
1845 local partitioning between Hg^0 deposition and re-emission. The isotopic composition of atmospheric Hg has been presented and discussed in **Section 8.2**. In addition to these data, an updated compilation of complementary isotopic Hg data for the reservoirs that are in contact with the atmosphere and thus can exert gas exchange has been produced during the preparation of this review (Liu et al., 2024).

8.6.1 Mixing and fractionation modeling of Hg^0 deposition and post-depositional processes

Deposition

1850 Isotope-based modeling by binary and ternary mixing with MDF, odd-MIF, and even-MIF signatures of atmospheric Hg^0 and other Hg pools as end members has been applied to distinguish the fraction of Hg^0 deposition via vegetated surfaces(Wang et al., 2020b; Enrico et al., 2016; Obrist et al., 2017; Wang et al., 2019b; Li et al., 2022a; Li et al., 2023a; Li et al., 2023b), soil (Zheng et al., 2016; Obrist et al., 2017; Wang et al., 2019b; Wang et al., 2020a), water (Jiskra et al., 2021; Zhang et al., 2023a), throughfall (Wang et al., 2020b) and snow run-off (Douglas and Blum, 2019), estimated to be 60–90%, 32–105%, 50–85%, 34–82% and >
1855 75% of total deposition, respectively. As a proxy for atmospheric Hg^0, foliage/litter Hg has been used as an end-member in mixing modeling of Hg^0 inputs to soil (Demers et al., 2013; Jiskra et al., 2015; Zhang et al., 2013), runoff (Jiskra et al., 2017), and stream water (Woerndle et al., 2018), which may introduce bias because a significant fraction of the gross air Hg^0 incorporated as Hg^{II} in foliage is re-emitted after photoreduction (Yuan et al., 2019b). The contribution of Hg^0 deposition to vegetation Hg uptake is greatest in foliage, followed by branches, bark, stem and roots (Wang et al., 2020b; Liu et al., 2021a; Sun et al., 2017). The new

1860 Hg isotope evidence has demonstrated that Hg throughfall via canopy and along stems, which were previously assumed to be derived mainly from wet and dry deposition of atmospheric RM (Wright et al., 2016), contains a larger proportion of Hg excreted from biomass, where it originated mainly from Hg^0 uptake followed by translocation.

Post-deposition

Isotopic and concentration measurements of Hg^0 jointly in near-surface air and surface pore air/water, in addition to other isotopic
1865 data, allow to infer processes by mass balance or Rayleigh-type models at the air-soil interface and in the surface soil (Jiskra et al., 2019; Li et al., 2023a; Yuan et al., 2021; Chen et al., 2023). For boreal poorly drained organic soil horizons (histosols), in contrast to podzols, mixing modeling indicates a significant reductive loss (24 – 33%) to the atmosphere by abiotic reduction (Jiskra et al., 2015). A further multi-process model is presented herewith, which is designed to elucidate the dynamic evolution of post-depositional Hg (>90% from litterfall) on subtropical forest floor over a period of 500 yr. (Yuan et al., 2020). The results indicate that photolytic and
1870 microbial reduction processes exert an influence during the initial few years, but are subsequently superseded by dark redox processes (exhibiting NVE) in the compost, where Hg^{II} became finally inert at depths of >10 cm in the horizon after approximately 420 years. Studies of forest soils in different climatic zones have shown that microbial reduction ($\varepsilon^{202}Hg$ = –0.4‰, $E^{199}Hg \approx 0$, Kritee et al., 2007) plays a dominant role (Yuan et al., 2021; Chen et al., 2023), which for rainforests can explain up to 90% of the Hg^{II} reduction in the upper soil horizon (Yuan et al., 2023b). In an open boreal peatland, photoreduction dominated the post-depositional process,
1875 accounting for the transformation of 30% of the annually deposited Hg (Li et al., 2023a).

8.6.2 Enclosure and related flux measurements

Experimental investigations employing dynamic flux chambers (DFCs) have been conducted in both ambient and controlled environments with the objective of elucidating the isotopic dynamics of Hg^0 exchange between the atmosphere and vegetation at the branch level (Yuan et al., 2019b; Chen et al., 2023), as well as between air and soil (Yuan et al., 2021; Chen et al., 2023; Zhu et al.,
1880 2022; Zhang et al., 2020), water (Zhang et al., 2023a), and snow (Sherman et al., 2010). For this application, in addition to traditional chambers (Demers et al., 2013; Chen et al., 2023; Zhu et al., 2024), a type was used that produces a uniform surface friction velocity over flat ground to couple with ambient shear conditions to scale to the ambient flux (Yuan et al., 2021; Yuan et al., 2023b; Lin et al., 2012). The surface-atmosphere Hg^0 flux is the result of complicated bidirectional processes, including Hg^0 efflux from surface and direct atmospheric Hg^0 deposition.

1885 **Deposition and sink processes**

When direct Hg^0 deposition is measured absolutely and isotopically with a DFC, enrichment factors for MDF ($\varepsilon^{202}Hg_{air/surface}$) and odd-MIF ($E^{199}Hg_{air/surface}$) may be calculated using a linearized Rayleigh fractionation model (Zhu et al., 2022; Mariotti et al., 1981):

$$\delta^{202}Hg^0_{DFC} - \delta^{202}Hg^0_{air} = \varepsilon^{202}Hg_{surface-air} \cdot \ln\left(c^{Hg^0}_{DFC}/c^{Hg^0}_{air}\right)$$
$$\Delta^{199}Hg^0_{DFC} - \Delta^{199}Hg^0_{air} = E^{199}Hg_{surface-air} \cdot \ln\left(c^{Hg^0}_{DFC}/c^{Hg^0}_{air}\right) \tag{24}$$

where c represents concentration and the indices air and DFC refers to the air entering and exiting the DFC, respectively. Alternatively, **Eq. 24** is applied for extracting $\varepsilon^{202}Hg_{surface-air}$ using measurements of c^{Hg^0} and $\delta^{202}Hg^0$ at two pristine sites with and without vegetation
1890 (Enrico et al., 2016) or using day vs. night-time segregated ambient air data at the same site (Jiskra et al., 2019). When direct deposition is measured isotopically with a DFC, the residual Hg^0 in the chamber outlet shifts to be preferentially isotopically heavier, with a large but variable discrimination observed over soils ($\varepsilon^{202}Hg_{soil-air}$ = ~0 to −5.8‰, Chen et al., 2023; Yuan et al., 2023b; Zhu et al., 2022) and over vegetation ($\varepsilon^{202}Hg_{foliage/air}$ = ~−1 to −4.2‰, Yuan et al., 2019b; Enrico et al., 2016; Demers et al., 2013; Jiskra et al., 2019; Chen et al., 2023). Deposition in contact with any surface does not result in a significant change in $\Delta^{199}Hg^0$, unlike the situation with $\delta^{202}Hg^0$.

1895 Information on the sink processes of Hg^0 in the soil can be obtained by pursuing measurements of isotopic Hg^0 in the soil pore air under sub-ambient concentration regimes. In tundra (Jiskra et al., 2019) and peatlands (Li et al., 2023a), isotopic difference between the ambient Hg^0 and pore gas Hg^0, whose concentration is sub-ambient (~0.4 – 0.6 and ~0.2 – ~0.7 ng m^{-3}) and therefore mediates Hg^0 net diffusion into the substrate, have via **Eq. 24** been linked to DOM-driven anaerobic oxidation in soil water exhibiting EIE (Zheng et al., 2019). Investigations of the Hg^0 level in the pore air of forest soils give a mixed picture, ranging from sites with highly
1900 depleted air (Obrist et al., 2014) to sites with up to ten times enriched pore air (Yuan et al., 2019a) compared to the above ambient concentrations. In subtropical (Yuan et al., 2019a) and subalpine (Chen et al., 2023) forest soils, the concentration of Hg^0 in pore air

is typically higher than in near-surface ambient air and shows seasonal isotopic variations (in MDF and odd-MIF), suggesting complexity in Hg^0 gas exchange between air and soil. In tropical forest soils, pore air shifts from being near-ambient during the rainy season to being markedly sub-ambient during the dry season (Yuan et al., 2023b). To resolve Hg^0 flux partitioning here, a

1905 combination of DFC measurements of net fluxes and forced unidirectional efflux, soil pore air, and Hg isotope composition in forest soil depth profiles are employed as input into isotope mass balance models based on odd-MIF (Yuan et al., 2021). Net fluxes measured by DFC are interpreted as a ternary mixing of deposition, Hg^0 losses from the surface soil via Hg^{II} photoreduction, and a term generated by Hg redox processes (dark/microbial reduction vs. oxidation) in the organic soil horizon. Although associated with considerable uncertainties, the estimated gross deposition to the forest floor is between -7.8 and -1.8 ng m^{-2} h^{-1} for the subtropical site

1910 (Yuan et al., 2021) and between -6.7 and -4.4 ng m^{-2} h^{-1} for the tropical site (Yuan et al., 2023b), depending on the season, and between -4.9 and -2.0 ng m^{-2} h^{-1} for the subalpine site, depending on the type of forest floor (Chen et al., 2023).
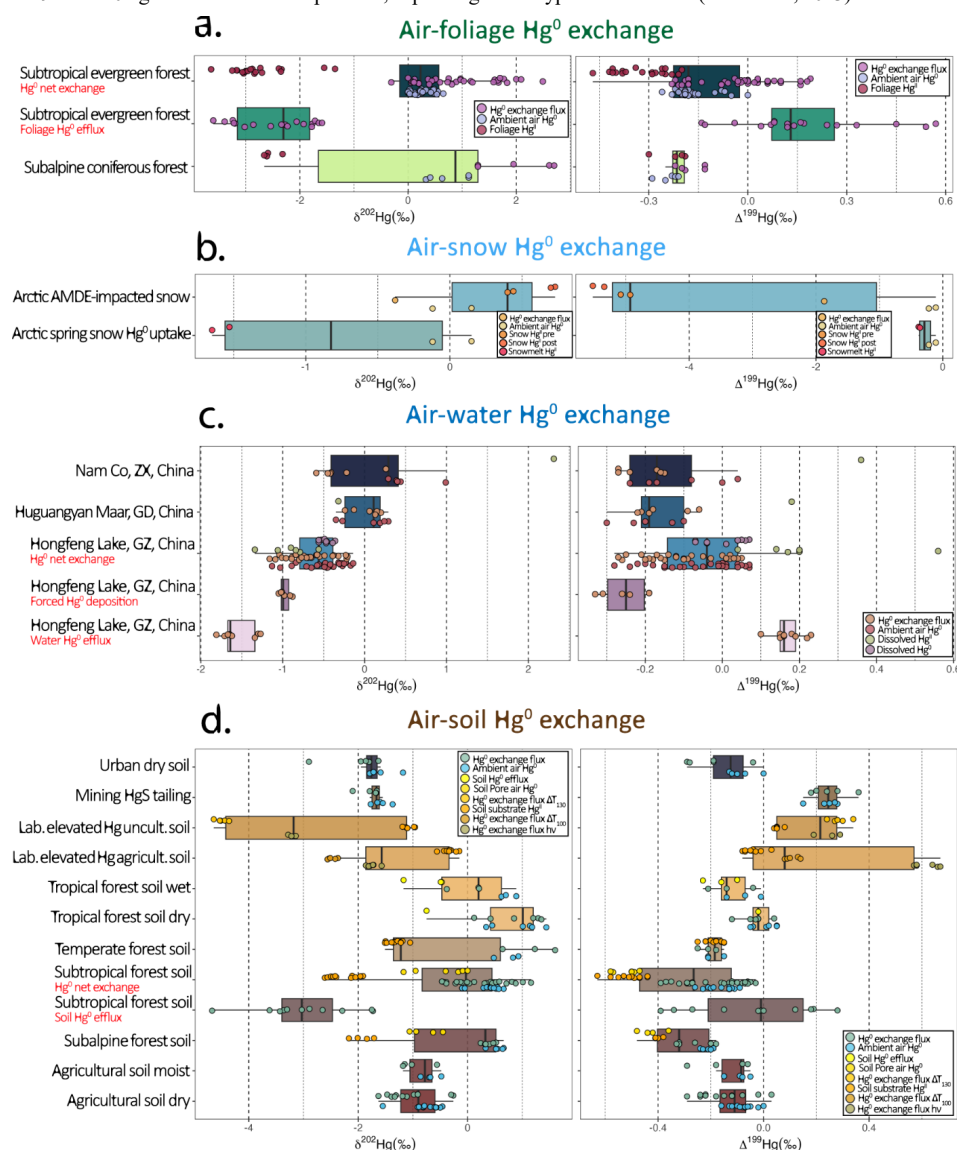
Figure 17. Statistical summary of observations from isotopic studies of Hg^0 exchange between the atmosphere and various groups of Earth's surface reservoirs. In the air-foliage group, data were taken from Yuan et al. (2019b) and Chen et al. (2023). In the air-snow group, data were taken from Sherman et

1915 al. (2010) and Douglas and Blum (2019). In the air-water group, data were taken from Zhang et al. (2023a; 2021a). In the air-soil group, data were taken from Zhang et al. (2020), Zhu et al. (2022), Yuan et al. (2021; 2023b) and Chen et al. (2023).

Foliar oxidation of Hg^0 drives its reactive uptake and is the most important step in the accumulation of initially dry deposited Hg^0 by plants (Liu et al., 2021b). Direct bio-oxidation from Hg^0 to Hg^{II} has been traced to heme enzymes that catalyze the degradation of H_2O_2, specifically to a ferryl ($O=Fe^{IV}$) catalase radical cation complex (Ogata and Aikoh, 1984) that swiftly oxidizes Hg^0 (1.4
1920 $\times 10^4$ M^{-1} s^{-1}, Wigfield and Tse, 1986):

$$H_2O_2 + \langle Fe^{II}–E^{\bullet+} \leftrightarrow Fe^{III}–E \rangle \longrightarrow H_2O + \langle O=Fe^{IV}–E^{+\bullet} \leftrightarrow O=Fe^{III}–E \rangle$$
$$Hg^0 + \langle O=Fe^{IV}–E^{+\bullet} \leftrightarrow O=Fe^{III}–E \rangle + 2\,H^+ \longrightarrow Hg^{2+} + \langle Fe^{II}–E^{+\bullet} \leftrightarrow Fe^{III}–E \rangle + H_2O \qquad \text{(Rxn 15)}$$
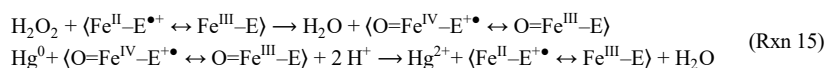
here, E represents the heme group attached to the enzyme, which can provide an electron, reducing the formal oxidation number of iron from five to four. The divalent Hg will readily bind to soft functional groups on the enzyme as soon as it is formed. MDF fractionation during oxidation of the absorbed isotopically light Hg^0 causes the product pool to be heavier than the reactant, consistent with observations that Hg^{II} incorporated into leaf shoots is only slightly lighter than Hg^0 in ambient air. Then it should be mentioned
1925   that, in contrast to the Hg pool in the leaf shoots, the Hg in the growing foliage of the current year shifts rapidly in the first months towards clearly negative $\delta^{202}Hg^{II}$ signatures, the causes of which have been discussed elsewhere (Yuan et al., 2019b).

In contrast to the observations regarding the air modified by interaction with soil and foliage, the residual Hg^0 in the outgoing air is significantly lighter than that in the incoming air ($\delta^{202}Hg^0_{air} - \delta^{202}Hg^0_{DFC} = 0.38‰$), as observed by DFC, for deposition regimes over freshwater surfaces (Zhang et al., 2023a). This may be interpreted as the dissolved $Hg^0(aq)$ being consumed by oxidation,
1930   whereby the rapid exchange of Hg isotopes between the remaining Hg^0 and the formed Hg^{II} (**Section 8.4.2**) causes the former, which is partially returned to the gas phase, to exhibit a more negative $\delta^{202}Hg^0$. In surface waters, photolytic re-reduction is also possible, which is another source involved in determining the isotopic composition of dissolved Hg^0 (Zhang et al., 2021a).

During colder seasons with limited solar radiation, there is a small but persistent net Hg^0 dry deposition over the snow-covered Arctic interior tundra (Obrist et al., 2017), whose interstitial snow air has sub-ambient concentrations (0.69 vs. 1.07 ng m^{-3}) with
1935   comparatively more positive $\delta^{202}Hg^0$-values (1.08 vs. 0.77‰, Jiskra et al., 2019). Using the exclusion method, this trajectory may reflect Hg^0 uptake by ground lichens (Olson et al., 2019). Compared to the hinterland (~50 ng m^{-2}), the Arctic coastal snowpack has regionally much higher Hg^{II} pools (>2000 ng m^{-2}), which are characteristically released as an ionic pulse in the runoff during snowmelt. High Hg^{II} concentrations in the coastal marine cryosphere are partially explained by AMDEs (described in **Section 5.1.1**, Douglas et al., 2017). However, most of the coastal AMDE deposition is re-emitted as Hg^0 to the atmosphere before the
1940   snow melts (see below). In contrast, the pulse in the runoff appears related mainly to the reactive uptake of Hg^0 on the marine snow, which is rich in halogen compounds and other reactive species (see **Section 7.3**) (Douglas et al., 2017). In support of a significant reactive uptake of Hg^0 on salt-laden snow, the analogous odd-MIF signatures between ambient air Hg^0 and snowmelt Hg^{II} have been referenced ($\Delta^{199}Hg$ values documented in **Fig. 17b**, Douglas and Blum, 2019).

Net exchange, source processes and flux partitioning

1945   Due to the length of time (typically a few days) required to accumulate sufficient Hg to perform isotopic analysis, samples from a DFC measurement are a composite of periods of net emission and net deposition, unless the Hg^0 concentration in the inlet is manipulated so that emission or deposition becomes persistent within the chamber. The MDF and odd-MIF signatures from DFC measurements in ambient air ("net Hg^0 exchange") are calculated as follows (Zhu et al., 2022):

$$\delta^{202}Hg^0_{exchange} = \left(\delta^{202}Hg^0_{DFC} \cdot c^{Hg^0}_{DFC} - \delta^{202}Hg^0_{air} \cdot c^{Hg^0}_{air} \right) / \left(c^{Hg^0}_{DFC} - c^{Hg^0}_{air} \right)$$
$$\Delta^{199}Hg^0_{exchange} = \left(\Delta^{199}Hg^0_{DFC} \cdot c^{Hg^0}_{DFC} - \Delta^{199}Hg^0_{air} \cdot c^{Hg^0}_{air} \right) / \left(c^{Hg^0}_{DFC} - c^{Hg^0}_{air} \right) \qquad (25)$$

In the special case of using Hg-free air (zero air) to feed the DFC, $\delta^{202}Hg^0_{emission}$ and $\Delta^{199}Hg^0_{emission}$ can be determined. The
1950   enrichment factors during net Hg^0 exchange and emission are calculated using the following set of equations:

$$\varepsilon^{202}Hg_{exchange} = \delta^{202}Hg^0_{exchange} - \delta^{202}Hg_{surface} \quad , \quad E^{199}Hg_{exchange} = \Delta^{199}Hg^0_{exchange} - \Delta^{199}Hg_{surface}$$
$$\varepsilon^{202}Hg_{emission} = \delta^{202}Hg^0_{emission} - \delta^{202}Hg_{surface}, \quad E^{199}Hg_{emission} = \Delta^{199}Hg^0_{emission} - \Delta^{199}Hg_{surface} \qquad (26)$$

In a series of light, temperature and substrate moisture controlled laboratory experiments with untilled (forest) and tilled (agricultural) soils, both with elevated Hg levels, enclosed in a DFC fed with Hg-free air, large Hg^0 fluxes (≥500 ng m^{-2} h^{-1}) were unanimously

with the most negative $\delta^{202}Hg^0_{emisson}$ (−2.9 to −2.2‰ and −4.4 to −4.2‰ for agricultural and forest soils, respectively) were observed when substrates were exposed to elevated temperatures in the dark (100-130 °C vs. 40 °C), while treatments with light, moisture, or a combination of both at room temperature produced more moderately negative $\delta^{202}Hg^0_{emisson}$ (−2.1 to −1.6‰ and −3.3 to −2.6‰ for agricultural and forest soils, respectively, Zhang et al., 2020). $E^{199}Hg_{emission}$ of agricultural and forest soils displays a value of approximately 0.2 ‰ and $\Delta^{199}Hg/\Delta^{201}Hg \sim 1.55$ in the temperature controls, suggesting that the treatment caused Hg^0 loss propelled by dark thermally driven Hg^{II} reduction (**Section 8.4.1**). In the light and light-moisture exposure controls, the substrates differed in the observed $E^{199}Hg_{emission}$, which for agricultural soils was 0.67 to 0.76‰ (mean) and for forest soils of a small magnitude, both positive and negative (−0.03 to 0.18‰, mean). The $E^{199}Hg_{emission}$ dichotomy may interpreted as deriving from a composite with $\Delta^{199}Hg$ contributions from both (−)MgIE and (+)MgIE inducing Hg^{II} photoreduction pathways, almost completely dominated by (−)MgIE processes (Hg^{II} bound to, e.g., N, S-containing ligands) for agricultural soils, and for forest soils with a larger contribution from (+)MgIE processes (Hg^{II} bound to e.g. O-containing ligands) balancing the odd-MIF fractionation from (−)MgIE processes. However, the aforementioned agricultural soil placed under water (rice paddy) photoemits Hg^0 characterized by negative $\Delta^{199}Hg^0$ ($\Delta^{199}Hg^0_{emission} = -0.38 \pm 0.18$‰, Zhang et al., 2024), which is indicative of all observed Hg^{II} photoreduction in natural freshwaters studied in the laboratory as well as in situ.

A field study with DFC of cultivated or managed soils measured exchange fluxes (an MDF Rayleigh model yielded 10-27 % contribution from deposition) that showed net Hg^0 emissions (fraction of) associated with average $\varepsilon^{202}Hg_{exchange}$ of −1.1 to −0.1‰ and −1.6 to −0.2‰ and average $E^{199}Hg_{exchange}$ of −0.27 to −0.13‰ and 0.00 to 0.14‰ for rural and urban soils, respectively. The above enrichment factors and $E^{199}Hg_{exchange} \approx E^{201}Hg_{exchange}$ indicate that the emitted Hg^0 comes mainly from the pool produced by photoreduction. The air concentration positively influences the magnitude of the deposition to soils so that at a critical concentration level (compensation point) the net flux tends to change direction. This is reflected in the apparent $\varepsilon^{202}Hg_{exchange}$, which varies with the ambient Hg^0 concentration (Zhu et al., 2022). Analogous to the laboratory experiments, in situ experiments on the subtropical forest floor show soil emissions of Hg^0 that have strongly negative $\delta^{202}Hg^0_{emission}$ (mean −3.0‰, Yuan et al., 2021), while the magnitude of $\delta^{202}Hg^0_{emission}$ for the tropical rainforest floor is much smaller, but still negative (mean −0.7‰, Yuan et al., 2023b). $E^{199}Hg_{emission}$ for subtropical forest soils exhibits positive values for all seasons over a considerable range (mean 0.1 – 0.7‰), whereas for rainforests, $E^{199}Hg_{emission}$ is consistently positive, albeit to a lesser extent (mean 0.2 – 0.3‰). Limited negative $\delta^{202}Hg^0_{exchange}$ (mean –0.26, –0.54, –0.07 and –0.09 ‰) and consistently positive $E^{199}Hg_{exchange}$ (mean 0.42, 0.23, 0.39 and 0.30 ‰) are observed in net Hg^0 gas exchange experiments over subtropical (Yuan et al., 2021), tropical (Yuan et al., 2023b), sub-alpine (Chen et al., 2023) and temperate (Demers et al., 2013) forest soils, respectively. In conclusion, bare or cultivated soils result in a greater degree of MDF isotope fractionation associated with Hg^0 gas exchange with the atmosphere, compared to forest soils, where the effect of photic and thermal processes is limited by canopy shading. Temporally extensive chamber measurements conducted globally over the forest floor indicate net emissions (Yuan et al., 2019a). For the first three forest soil studies mentioned above, the DFC data set also contains sufficient isotope data to enable the modeling of net flux partitioning into gross emission and gross deposition.

Re-emissions of Hg^0 from perennial foliage of three beech species show an average positive $\varepsilon^{202}Hg_{emission}$ and $E^{199}Hg_{emission}$ of 0.6 and 0.3‰, respectively. The studied net exchange of Hg^0 between foliage and air for the montane evergreen deciduous (Yuan et al., 2019b) and spruce (Chen et al., 2023) forests is mostly on the uptake side, which gives that $\delta^{202}Hg^0_{DFC}$ is generally more positive than that of ambient air (**Fig. 17a**, mean shift of 0.72‰ for the latter site). The presence of bidirectional fluxes is, however, reflected in the observation that the $E^{199}Hg_{exchange}$ for both sites is consistently positive (mean 0.08 and 0.13‰, respectively), albeit modestly, due to a contribution from Hg^0 emissions resulting from (−)MgIE-induced photoreduction.

Isotopic studies of air-snow Hg^0 interaction and post-depositional processes have typically been conducted in the Arctic (Araujo et al., 2022; Sherman et al., 2010; Zheng et al., 2021; Jiskra et al., 2019; Obrist et al., 2017; Douglas and Blum, 2019), with occasional studies at mid-latitudes (Kurz et al., 2021; Yuan et al., 2022). Hg in aging snowpack exhibits by far the most extensive distribution of $\Delta^{199}Hg^{II}$ among Earth's surface reservoirs, with observations of $\Delta^{199}Hg$ progression reported in both positive (Kurz et al., 2021) and negative (Sherman et al., 2010; Zheng et al., 2021; Douglas and Blum, 2019) directions relative to fresh snow. As previously

discussed in **Section 8.2.1**, the larger Δ^{199}Hg spread observed in polar airborne Hg (Hg^0 and RM) when compared to, for instance, high-altitude air from mid-latitudes, can be attributed to the influence of AMDEs (during spring after sunrise and during summer) on a significant proportion of the collected polar data. Snow(fall) during the polar night is characterized by positive or near-zero Δ^{199}Hg signatures, as is the case for most global precipitation data (**Fig. 13c**), while the Δ^{199}Hg of polar Hg^0 for the same period is all slightly

2000 negative, consistent with the global Hg^0 background pool (**Fig. 13a**). Only sporadic isotopic DFC measurements have been conducted over snow, yet ample measurements of the polar air and snow as endmembers still offer an understanding of air-surface Hg^0 exchange following Hg^{II} deposition associated with AMDE. A seminal set of isotope data (Sherman et al., 2010) demonstrating a substantial odd-MIF triggered as a consequence of Hg^{II} photoreduction in snow was obtained from samples collected during a 9-day AMDE at the Alaskan Arctic coastline in conjunction with periods of minimal snowfall carrying high concentrations of scavenged Hg^{II} (0.5 ± 0.4 µg

2005 L^{-1}, Johnson et al., 2008). Fresh snow, surface snow, and drifting snow showed, in order, rapidly increasing negative Δ^{199}Hg^{II} values of –0.95 to –1.20‰, –2.41 to –2.63‰, and –3.84 to –5.08‰, which, according to Rayleigh fractionation, can correspond to 5–30%, 35–50%, and 65–75% of photo-reduced Hg^{II}, respectively. A chamber measurement was conducted on AMDE-impacted drifting snow that had undergone substantial photoreduction (Δ^{199}Hg ~–5.0‰) for 10.5 h of sunlight. The total DFC throughput, inclusive of Hg^0 emissions corresponding to 6% of Hg^{II} in the snow plot (whose Δ^{199}Hg^{II} dropped to ~–5.4‰), exhibited a Δ^{199}Hg^0 of –1.87‰. A regression (-3.32

2010 ± 1.19, Kurz et al., 2021) corresponding to the Alaska DFC experiment Δ^{199}Hg plotted against δ^{202}Hg data (-3.44 ± 0.70, Sherman et al., 2010) has also been observed, given the uncertainty in the line fit, in mid-latitudinal snow (MI, USA) belonging to polar vortex transported air masses from subarctic regions where the presence of AMDEs is well known (Poissant et al., 2001).

Perennial data from the Canadian High Arctic show that Hg^{II} deposited on snow during the most frequent phase of AMDEs just after polar sunrise until early May, partly characterized by low temperatures and Arctic haze, has a significantly higher susceptibility to

2015 photoreduction and loss as Hg^0 (up to 60%) than that deposited later (<20%, Zheng et al., 2021). Regression of the Alaskan DFC experiment Δ^{199}Hg plotted against δ^{202}Hg data (–3.44 ± 0.70). As previously stated in **Section 5.1.4**, airborne Hg^{II} originating from high Arctic AMDEs undergoes rapid conversion to the particle phase between March and April, while unconverted GOM remains the dominant form between May and June. The cause of the reactivity of deposited Hg^{II} is unclear (Sherman et al., 2010; Kurz et al., 2021). It has been speculated that components of Arctic haze, such as black carbon, that cause photoreactivity of co-particulate Hg^{II}

2020 would be the cause of the observed (–)MgIE signature (Zheng et al., 2021), which is supported by water-phase experiments with Hg^{II} and dissolved black carbon (**Table 8**, Li et al., 2020b). Concurrently, the restricted Hg^{II} reduction observed in Arctic snow towards the conclusion of spring is consistent with concurrent observations of substantial reactive uptake of Hg^0 (see above; Douglas and Blum, 2019), indicating that the snowpack then contains species with a predominant oxidative capacity. However, during snowmelt on the inland tundra, net Hg^0 deposition is disrupted by shifts in isotopic signatures of snow interstitial air to those indicative of

2025 photoreduction, Δ^{199}Hg down to –1.37‰ in snow, –0.62‰ in snow interstitial air, consistently lower than in ambient air (–0.23 ± 0.06‰). In contrast to Arctic snow, snow sampling in the U.S. Great Lakes area (with the exceptions noted above) generally shows increasing positive Δ^{199}Hg^{II} values (up to 3.51‰) in aging snow (Kurz et al., 2021). Indicative of (–) and (+) MgIE triggering the photoreduction, respectively, the snow data from coastal Alaska (Sherman et al., 2010; Douglas and Blum, 2019) and the Great Lakes region (Kurz et al., 2021) show steeper Δ^{199}Hg/δ^{202}Hg trajectories than is the case for any of the well-studied Hg^{II} complex

2030 photoreductions in the laboratory (**Table 8 & 9**), leaving the question of which snow Hg^{II} complexes are involved.

The mean MIF values (Δ^{199}Hg^{II} and Δ^{200}Hg^{II}) in the pool of fresh and seawaters are situated between the mean values of global atmospheric Hg^0 and wet precipitation. However, the variation is particularly pronounced for Δ^{199}Hg^{II} in coastal seawater, lakes, and river water (Liu et al., 2024). After studying three different categories of lakes with DFC, a Δ^{200}Hg isotope mass balance model was used to partition the overall net emission fluxes into gross emission and deposition, which ranged from 2.1 to 4.2 ng m^{-2} h^{-1} and –2.3

2035 to –1.2 ng m^{-2} h^{-1}, depending on the lake (Zhang et al., 2023a). Hg^0 gross deposition exceeds the measured wet deposition over these lakes and is 56 - 85% of the total deposition (Feng et al., 2022). The anomalous observation of preferential deposition of heavier Hg isotopes over water has already been discussed. The results of the volatilization experiments of dissolved Hg^0 in water (DGM) indicate an MDF enrichment factor (ε^{202}Hg$^0_{air-water}$) of −0.45‰ and a negligible E^{199}Hg$^0_{air-water}$ (Zheng et al., 2007). Emission-

controlled experiments for one of the lakes give $E^{199}Hg_{emission}$ of –0.38‰ and $\varepsilon^{202}Hg_{emission}$ of –0.31‰, which are subject to large

2040 uncertainties, with a resulting $E^{199}Hg_{emission}/\varepsilon^{202}Hg_{emission}$ trajectory of 1.26 ± 0.72 that agrees within the margin of error with that for Hg^{II} photoreduction mediated by fulvic acids (1.15 ± 0.07, Bergquist and Blum, 2007). The isotopic tracing of the formation of dissolved Hg^0 in peat-covered groundwater from Hg^{II} in rainwater (1.24 ± 0.68) has also suggested that this process is of the same type of photoreduction (Li et al., 2023a). The $E^{199}Hg_{exchange}$ was between –0.76 and –0.32‰, with the highest absolute value for a clear mountain lake fed mainly by glacial water, indicating that (+)MgIE photoreduction plays an important role, as has been shown

2045 early on in laboratory experiments on natural freshwater (Bergquist and Blum, 2007; Zheng and Hintelmann, 2009). The observed substantial positive $\Delta^{199}Hg^{II}$ shift of sampled lake surface waters relative to Hg^{II} in precipitation can be interpreted as an effect of partial photoreduction of Hg^{II}. However, other sources, including MMHg photodegradation (Chen et al., 2016). As discussed in **Section 4.2**, Hg^0 emissions from the ocean represent a primary source of Hg in the atmosphere. However, the isotopic signatures of this emission source remain largely unknown. In the absence of in situ sampling, photoexperiments with Hg^{II} in the presence of DOM

2050 extracted from marine phytoplankton produce (–)MgIE during reduction, in contrast to freshwater DOM (Kritee et al., 2018).

9. Future perspectives

Knowledge of the atmospheric cycle of mercury has increased significantly in recent decades, as described in this paper. This is particularly evident in the field of computational chemistry, which has made seminal contributions to our understanding of gas-phase $Hg^{(I,II)}$ molecules in terms of their geometries, energies, UV-VIS spectra, and reaction kinetics. The treatment of strong relativistic

2055 effects, which largely determine the chemistry of Hg-containing species, is crucial for accurate results. Ab initio thermochemical calculations for atmospheric Hg species are performed at a higher level of theory, which incorporates core-valence electron correlation and extended basis sets (coupled-cluster methods). This approach yields more accurate results, with an accuracy of ≤1 kcal mol^{-1}, in accordance with high-quality experimental data. The undertaking of ab initio kinetics calculations is a considerably more arduous task than that of ab initio thermodynamics calculations. It is more challenging to calculate the energies of transition

2060 states (TS) with high accuracy than those of relative minima (meta-stable species). Furthermore, the rate is not solely dependent on the TS vs. reactant free energy difference, which can often be accurately calculated at sufficiently high levels. It is also essential to consider excited states when carrying out spectroscopic calculations (Ariya and Peterson, 2005; Ariya et al., 2009).

Absolute determination of rate constants experimentally with pulsed laser-assisted methods (reaction time typically < 0.1 ms) such as PLP-LIF is facilitated when secondary reactions are negligible and therefore do not contribute to the measured values. In general,

2065 the absolute determination is conducted by obtaining pseudo-first order conditions, whereby the more stable reactant is present in a density exceeding tenfold that of the other reactant. However, for Hg, this method is viable only for studies that are conducted at elevated temperatures. At standard atmospheric conditions, the relatively low vapor pressure of Hg^0 (in comparison to, for instance, DMHg) precludes the possibility of such experiments. Despite the challenges for Hg^0, a flow PLP-LIF system has many advantages, including the ability to measure the rate coefficient over a wide range of temperatures and pressures and to test the effect of a change

2070 in bath gas (third body). These advantages have been exploited by alternative methods where the Hg species is not in excess, but where the excess is X = Cl and Br in the study of the reaction $Hg + X^\bullet + M$, while this is instead Y = O_3, NO_2, NO and O_2 in the study of the interaction between $^\bullet Hg^I Br$ and Y. Despite being in excess, the $X^\bullet$ concentration decreases over time due to the rapid three-body recombination of the species to X_2 and M. This results in a non-trivial Hg^0 exponential decay. To achieve a fit to the observed Hg^0 time profiles, rate coefficients must be obtained through numerical integration. This requires monitoring both the $X^\bullet$

2075 and Hg^0 time profiles using LIF, with the absolute concentration of X atoms known with precision. The measurements of the rate coefficients for the $Hg + X^\bullet + M$ reaction experimentally by Donohoue et al. are in accordance with the findings of the theoretical computational studies. The study of the conversion of $^\bullet Hg^I Br$ by bimolecular elimination (reduction; Wu et al., 2020; Wu et al., 2022), addition (oxidation assisted by M, Wu et al., 2020), or abstraction (Gómez Martín et al., 2022) is constrained by the capacity to generate sufficiently high densities of $^\bullet Hg^I Br$ through the gas-phase photolysis of $HgBr_2$ in the deep UV. Because the vapor

2080 pressure over $HgBr_2$ is low (less than one-tenth that of Hg^0), it is necessary to keep the $HgBr_2$ source at least 30 ℃ and the flow tube reactor at least 10 ℃ higher to prevent vapor condensation. A higher temperature increases the thermal dissociation of $^\bullet Hg^I Br$ and

therefore a large excess of Y is required for the $^\bullet$Hg^{I}Br + Y reaction to completely dominate the conversion of $^\bullet$Hg^{I}Br. However, in the context of laboratory experiments necessitating deep UV irradiation, it is essential to consider that oxygen atoms are formed through the partial photolysis of O$_3$ and NO$_2$, thereby enabling O(^{3}P) to also react with $^\bullet$Hg^{I}Br (O + HgBr$^\bullet$ → Hg + BrO$^\bullet$). The

2085 experimentalists' intention to study the title reactions of $^\bullet$Hg^{I}Br with NO$_2$ and O$_3$ will inevitably result in the observation of a partially reversible oxidation process. This is due to the occurrence of secondary chemistry, including the reactions **G14**, **G23**, **G24**, and **G29**, which takes place concurrently with the title reactions Br7 and Br9. Furthermore, to elucidate the influence of secondary chemistry on the observed $^\bullet$Hg^{I}Br disappearance, a comprehensive series of experiments must be conducted, with pressure, temperature, [$^\bullet$Hg^{I}Br], [Y], and [O] as variables. Subsequently, numerical modeling is essential to isolate the individual rate constants. While the

2090 laboratory study of $^\bullet$Hg^{I}Br + O$_3$ gives an experimental rate constant for the reaction **G22** that is in good agreement with computational predictions (Castro Pelaez et al., 2022), experimental kinetic data for $^\bullet$Hg^{I}Br + NO$_2$ (**Rxn 20**), which must be decoupled in termolecular oxidation (**Rxn 20a**) and reduction (**Rxn 20b**), respectively, indicate that computational methods give overestimated rate constants for both channels (Wu et al., 2020). In the later experimental investigation it is however found that **Rxn 20** cannot fully account for observations, but that significant losses of $^\bullet$Hg^{I}Br must occur via side reactions, probably involving **Rxn G23**, which

2095 was unexplored at the time. In view of the above-mentioned intractable shortcomings, it is very challenging to validate the majority of the proposed reaction steps by computational quantum chemistry in the atmospheric Hg redox cycle, including YHg^{II}O$^\bullet$ chemistry, through experimental means. In fact, many of the proposed key intermediate Hg species lack any experimental characterization (such as spectral proofs). For example, apart from LDI-TOF MS experiments utilizing solid HgO as a source (Jayasekharan and Sahoo, 2014), there is a paucity of information of gaseous HgO. In order to assess the stability and potential reactions of HgO, it is necessary

2100 to employ advanced laser spectroscopic methods, which could potentially generate robust levels of HgO through the spin-allowed Hg(^{1}S) + O(^{1}D) reaction.

From a computational chemistry standpoint, the reaction between YHg^{II}O$^\bullet$ and CO has been identified as crucial in assessing the atmospheric burden of Hg^{II}. However, the calculated rate constant is subject to significant uncertainty, within a factor of 10 being a reasonable estimate. A direct reaction between water vapor and YHg^{II}O$^\bullet$ has recently been proposed for Y = OH (Saiz-Lopez et al.,

2105 2022). If this reaction is realized with the given rate expression in models, it will result in the conversion of essentially all HOHg^{II}O$^\bullet$ to the completely stable Hg(OH)$_2$ in the tropics. The question of whether iodine-induced Hg^0 oxidation is a significant process in the troposphere and lower stratosphere has been raised based on atmospheric observations (Murphy et al., 2006; Lee et al., 2024) and the emerging role that O$_3$ is thought to play in rapidly oxidizing $^\bullet$Hg^{I}X to XHg^{II}O$^\bullet$ species. As discussed in **Section 5.1.2**, the current evidence for $^\bullet$Hg^{I}I in terms of binding strength, thermal and photolytic stability is too uncertain to make an informed assessment.

2110 The current limitations and challenges to accurately measuring speciated atmospheric mercury (Gustin et al., 2024; **Section 4.1**) mean that the basis for verifying model studies is insufficient, despite generally reliable measurements of Hg^0 and Hg^{II} wet deposition. The difficulties of accurately determining the speciation of Hg^{II} in atmospheric water through equilibrium modelling, and thus identifying the pool of reducible complexes, have been elucidated (**Section 4.3**). Additionally, the potential for simulating the gas-particle distribution of atmospherically oxidized Hg has been explored (**Section 7.1.1**). The use of isotope data to constrain the Hg

2115 redox chemistry in the atmosphere has begun (Song et al., 2024; Zhen et al., 2024), but there are profound knowledge gaps that require state-of-the art theoretical and experimental investigations. The discovery, made over a decade ago, that atmospheric samples contain a significant level of the even-mass-number isotope MIF, which has been observed to exhibit seasonal and geospatial variations, has been a source of both benefit and puzzlement for scientists ever since (**Section 8.2.3 & -4**). As the even Hg MIF variation is limited to samples from a few localities so far (compare **Figs. 13 & 14**), Δ^{200}Hg & Δ^{204}Hg in the environment is considered

2120 a conservative tracer due to its generally narrow range, and values of Δ^{200}Hg & Δ^{204}Hg on the land surface and in water confine the relative contribution of Hg^0 to Hg^{II} exchange process with the atmosphere. Nevertheless, the underlying chemical processes that give rise to the anomalous MIF and the atmospheric conditions that facilitate its occurrence remain to be elucidated in greater detail. In addition to laboratory-based investigations, future field experiments that report on the vertical profiles of isotopic Hg^0 and Hg^{II} in the atmosphere may prove invaluable in further constraining the sources of even-MIF.

2125 **Author contribution**

J. O. S. prepared the manuscript with contributions from all co-authors.

Competing interests

The authors declare that they have no conflict of interest.

Financial support

2130 This work was supported by the National Natural Science Foundation of China (grant no. 42150710535, and 42373068).

References

Ababneh, F. A., Scott, S. L., Al-Reasi, H. A., and Lean, D. R. S.: Photochemical reduction and reoxidation of aqueous mercuric chloride in the presence of ferrioxalate and air, Science of the Total Environment, 367, 831-839, 10.1016/j.scitotenv.2006.02.018, 2006.

2135 Ahmed, S., Thomas, J. L., Angot, H., Dommergue, A., Archer, S. D., Bariteau, L., Beck, I., Benavent, N., Blechschmidt, A. M., Blomquist, B., Boyer, M., Christensen, J. H., Dahlke, S., Dastoor, A., Helmig, D., Howard, D., Jacobi, H. W., Jokinen, T., Lapere, R., Laurila, T., Quelever, L. L. J., Richter, A., Ryjkov, A., Mahajan, A. S., Marelle, L., Pfaffhuber, K. A., Posman, K., Rinke, A., Saiz-Lopez, A., Schmale, J., Skov, H., Steffen, A., Stupple, G., Stutz, J., Travnikov, O., and Zilker, B.: Modelling the coupled mercury-halogen-ozone cycle in the central Arctic during spring, Elementa-Science of the Anthropocene, 11, ARTN 2140 00129, 10.1525/elementa.2022.00129, 2023.

Ai, Y., Wang, C., Videen, G., and Pan, Y.-L.: Optically levitated, single-particle reactor for the study of surface and heterogeneous chemistry-reactions of particulate-bound mercury with ozone in air, Chemical Physics Letters, 817, 140428, 10.1016/j.cplett.2023.140428, 2023.

Akagi, H., Fujita, Y., and Tkabatake, E.: Photochemical Methylation of lnorganic Mercuric Compounds in Aqueous Acetic 2145 Acid Solutions, Nippon Kagaku Kaishi, 1974, 1180, 1974.

Alberts, J. J., Schindler, J. E., Miller, R. W., and Nutter, D. E.: Elemental Mercury Evolution Mediated by Humic Acid, Science, 184, 895-896, 1974.

Ambrose, J. L.: Improved methods for signal processing in measurements of mercury by Tekran® 2537A and 2537B instruments, Atmospheric Measurement Techniques, 10, 5063-5073, 10.5194/amt-10-5063-2017, 2017.

2150 Amirbahman, A., Kent, D. B., Curtis, G. P., and Marvin-DiPasquale, M. C.: Kinetics of Homogeneous and Surface-Catalyzed Mercury(II) Reduction by Iron(II), Environmental Science & Technology, 47, 7204-7213, 10.1021/es401459p, 2013.

Amos, H. M., Jacob, D. J., Holmes, C. D., Fisher, J. A., Wang, Q., Yantosca, R. M., Corbitt, E. S., Galarneau, E., Rutter, A. P., Gustin, M. S., Steffen, A., Schauer, J. J., Graydon, J. A., St Louis, V. L., Talbot, R. W., Edgerton, E. S., Zhang, Y., and Sunderland, E. M.: Gas-particle partitioning of atmospheric Hg(II) and its effect on global mercury deposition, Atmospheric 2155 Chemistry and Physics, 12, 591-603, 2012.

Amyot, M., Morel, F. M. M., and Ariya, P. A.: Dark Oxidation of Dissolved and Liquid Elemental Mercury in Aquatic Environments, Environmental Science & Technology, 39, 110-114, 10.1021/es035444k, 2005.

Andersson, M. E., Gårdfeldt, K., Wängberg, I., and Strömberg, D.: Determination of Henry's law constant for elemental mercury, Chemosphere, 73, 587-592, 10.1016/j.chemosphere.2008.05.067, 2008.

2160 Andrews, L., Wang, X., Gong, Y., Schloeder, T., Riedel, S., and Franger, M. J.: Spectroscopic Observation of a Group 12 Oxyfluoride: A Matrix-Isolation and Quantum-Chemical Investigation of Mercury Oxyfluorides, Angewandte Chemie-International Edition, 51, 8235-8238, 10.1002/anie.201204331, 2012.

Angot, H., Dastoor, A., De Simone, F., Gårdfeldt, K., Gencarelli, C. N., Hedgecock, I. M., Langer, S., Magand, O., Mastromonaco, M. N., Nordstrøm, C., Pfaffhuber, K. A., Pirrone, N., Ryjkov, A., Selin, N. E., Skov, H., Song, S., Sprovieri, F., 2165 Steffen, A., Toyota, K., Travnikov, O., Yang, X., and Dommergue, A.: Chemical cycling and deposition of atmospheric mercury in polar regions: review of recent measurements and comparison with models, Atmospheric Chemistry and Physics, 16, 10735-10763, 10.5194/acp-16-10735-2016, 2016.

Araujo, B. F., Osterwalder, S., Szponar, N., Lee, D., Petrova, M. V., Pernov, J. B., Ahmed, S., Heimburger-Boavida, L. E., Laffont, L., Teisserenc, R., Tananaev, N., Nordstrom, C., Magand, O., Stupple, G., Skov, H., Steffen, A., Bergquist, B., 2170 Pfaffhuber, K. A., Thomas, J. L., Scheper, S., Petaja, T., Dommergue, A., and Sonke, J. E.: Mercury isotope evidence for Arctic summertime re-emission of mercury from the cryosphere, Nature Communications, 13, ARTN 4956, 10.1038/s41467-022-32440-8, 2022.

Ariya, P. and Peterson, K. A.: Chemical transformation of gaseous elemental mercury in the atmosphere, in: Dynamics of Mercury Pollution on Regional and Global Scales: Atmospheric Processes and Human Exposures Around the World, edited by: 2175 Pirrone, N., and Mahaffey, K. R., Springer, 261-294, 2005.

Ariya, P. A., Khalizov, A., and Gidas, A.: Reactions of gaseous mercury with atomic and molecular halogens: Kinetics, product studies, and atmospheric implications, Journal of Physical Chemistry A, 106, 7310-7320, 2002.

Ariya, P. A., Peterson, K., Snider, G., and Amyot, M.: Mercury chemical transformations in the gas, aqueous and heterogeneous phases: state-of-the-art science and uncertainties, in: Mercury fate and transport in the global atmosphere. Emissions,
2180   measurements and models., edited by: Mason, R., and Pirrone, N., Springer, 459-501, 2009.

Ariya, P. A., Skov, H., Grage, M. M. L., and Goodsite, M. E.: Gaseous elemental mercury in the ambient atmosphere: Review of the application of theoretical calculations and experimental studies for determination of reaction coefficients and mechanisms with halogens and other reactants, in: Advances in Quantum Chemistry: Applications of Theoretical Methods to Atmospheric Science, edited by: Sabin, J. R., and Brandas, E. J., Academic Press, 43-55, 10.1016/s0065-3276(07)00204-3, 2008.

2185   Ariya, P. A., Amyot, M., Dastoor, A., Deeds, D., Feinberg, A., Kos, G., Poulain, A., Ryjkov, A., Semeniuk, K., Subir, M., and Toyota, K.: Mercury Physicochemical and Biogeochemical Transformation in the Atmosphere and at Atmospheric Interfaces: A Review and Future Directions, Chemical Reviews, 10.1021/cr500667e, 2015.

AuYang, D., Chen, J., Zheng, W., Zhang, Y., Shi, G., Sonke, J., Cartigny, P., Hongming, C., Yuan, W., Liu, L., Gai, P., and Liu, C.: South-hemispheric marine aerosol Hg and S isotope compositions reveal different oxidation pathways, National
2190   Science Open, 1, 20220014, 10.1360/nso/20220014, 2022.

Auzmendi-Murua, I., Castillo, Á., and Bozzelli, J. W.: Mercury Oxidation via Chlorine, Bromine, and Iodine under Atmospheric Conditions: Thermochemistry and Kinetics, Journal of Physical Chemistry A, 118, 2959-2975, 10.1021/jp412654s, 2014.

Åkerblom, S., Meili, M., and Bishop, K.: Organic Matter in Rain: An Overlooked Influence on Mercury Deposition,
2195   Environmental Science & Technology Letters, 2, 128-132, 10.1021/acs.estlett.5b00009, 2015.

Babaev, N. S., Cheltsov, A. N., Sazykin, A. A., Sosnin, L. Y., and Kuchelev, A. P.: Centrifugal enrichment of mercury isotopes, Nuclear Instruments and Methods in Physics Research Section A: Accelerators, Spectrometers, Detectors and Associated Equipment, 613, 473-476, 10.1016/j.nima.2009.10.006, 2010.

Balabanov, N. B. and Peterson, K. A.: Mercury and Reactive Halogens: The Thermochemistry of Hg + [Cl$_2$, Br$_2$, BrCl, ClO,
2200   and BrO], Journal of Physical Chemistry A, 107, 7465-7470, 2003.

Balabanov, N. B. and Peterson, K. A.: Accurate theoretical near-equilibrium potential energy and dipole moment surfaces of HgClO and HgBrO, Journal of Chemical Physics, 120, 6585-6592, 2004.

Balabanov, N. B., Shepler, B. C., and Peterson, K. A.: Accurate Global Potential Energy Surface and Reaction Dynamics for the Ground State of HgBr$_2$, Journal of Physical Chemistry A, 109, 8765-8773, 2005.

2205   Bartels-Rausch, T., Huthwelker, T., Jori, M., Gaggeler, H. W., and Ammann, M.: Interaction of gaseous elemental mercury with snow surfaces: laboratory investigation, Environmental Research Letters, 3, 10.1088/1748-9326/3/4/045009, 2008.

Bartels-Rausch, T., Krysztofiak, G., Bernhard, A., Schläppi, M., Schwikowski, M., and Ammann, M.: Photoinduced reduction of divalent mercury in ice by organic matter, Chemosphere, 82, 199-203, 2011.

Bash, J. O., Bresnahan, P., and Miller, D. R.: Dynamic surface interface exchanges of mercury: A review and
2210   compartmentalized modeling framework, Journal of Applied Meteorology and Climatology, 46, 1606-1618, 10.1175/jam2553.1, 2007.

Bash, J. O., Carlton, A. G., Hutzell, W. T., and Bullock, O. R.: Regional Air Quality Model Application of the Aqueous-Phase Photo Reduction of Atmospheric Oxidized Mercury by Dicarboxylic Acids, Atmosphere, 5, 1-15, 10.3390/atmos5010001, 2014.

2215   Bauer, D., Campuzano-Jost, P., and Hynes, A. J.: Rapid, ultra-sensitive detection of gas phase elemental mercury under atmospheric conditions using sequential two-photon laser induced fluorescence, Journal of Environmental Monitoring, 4, 339-343, 2002.

Bauer, D., D'Ottone, L., Campuzano-Jost, P., and Hynes, A. J.: Gas phase elemental mercury: a comparison of LIF detection techniques and study of the kinetics of reaction with the hydroxyl radical, Journal of Photochemistry and Photobiology, A:
2220   Chemistry, 157, 247-256, 2003.

Bauer, D., Everhart, S., Remeika, J., Tatum Ernest, C., and Hynes, A. J.: Deployment of a sequential two-photon laser-induced fluorescence sensor for the detection of gaseous elemental mercury at ambient levels: fast, specific, ultrasensitive detection with parts-per-quadrillion sensitivity, Atmospheric Measurement Techniques, 7, 4251-4265, 10.5194/amt-7-4251-2014, 2014.

Baxendale, J. H. and Bridge, N. K.: Photoreduction of Ferric Compounds in Aqueous Solution, The Journal of Physical
2225   Chemistry, 59, 783-788, 10.1021/j150530a022, 1955.

Baya, P. A., Gosselin, M., Lehnherr, I., St Louis, V. L., and Hintelmann, H.: Determination of Monomethylmercury and Dimethylmercury in the Arctic Marine Boundary Layer, Environmental Science & Technology, 49, 223-232, 2015.

Bencardino, M., D'Amore, F., Angot, H., Angiuli, L., Bertrand, Y., Cairns, W., Diéguez, M. C., Dommergue, A., Ebinghaus, R., Esposito, G., Komínková, K., Labuschagne, C., Mannarino, V., Martin, L., Martino, M., Neves, L. M., Mashyanov, N.,
2230   Magand, O., Nelson, P., Norstrom, C., Read, K., Sholupov, S., Skov, H., Tassone, A., Vítková, G., Cinnirella, S., Sprovieri, F., and Pirrone, N.: Patterns and trends of atmospheric mercury in the GMOS network: Insights based on a decade of measurements, Environmental Pollution, 363, 125104, 10.1016/j.envpol.2024.125104, 2024.

Bergquist, B. A. and Blum, J. D.: Mass-dependent and -independent fractionation of Hg isotopes by photoreduction in aquatic systems, Science, 318, 417-420, 2007.

2235 Berkovic, A. M., Bertolotti, S. G., Villata, L. S., Gonzalez, M. C., Pis Diez, R., and Mártire, D. O.: Photoinduced reduction of divalent mercury by quinones in the presence of formic acid under anaerobic conditions, Chemosphere, 89, 1189-1194, 2012.

Berkovic, A. M., Gonzalez, M. C., Russo, N., Del Carmen Michelini, M., Diez, R. P., and Mártire, D. O.: Reduction of mercury(II) by the carbon dioxide radical anion: A theoretical and experimental investigation, Journal of Physical Chemistry A, 114, 12845-12850, 2010.

2240 Bianco, A., Deguillaume, L., Vaïtilingom, M., Nicol, E., Baray, J.-L., Chaumerliac, N., and Bridoux, M.: Molecular Characterization of Cloud Water Samples Collected at the Puy de Dôme (France) by Fourier Transform Ion Cyclotron Resonance Mass Spectrometry, Environmental Science & Technology, 52, 10275-10285, 10.1021/acs.est.8b01964, 2018.

Bigeleisen, J. and Wolfsberg, M.: Theoretical and Experimental Aspects of Isotope Effects in Chemical Kinetics, in: Advances in Chemical Physics, 15-76, https://doi.org/10.1002/9780470143476.ch2, 1957.

2245 Bittrich, D. R., Chadwick, S. P., Babiarz, C. L., Manolopoulos, H., Rutter, A. P., Schauer, J. J., Armstrong, D. E., Collett, J., and Herckes, P.: Speciation of Mercury (II) and Methylmercury in Cloud and Fog Water, Aerosol and Air Quality Research, 11, 161-U181, Doi 10.4209/Aaqr.2010.08.0067, 2011.

Bloom, N. S., Grout, A. K., and Prestbo, E. M.: Development and complete validation of a method for the determination of dimethyl mercury in air and other media, Analytica Chimica Acta, 546, 92-101, 2005.

2250 Blum, J. D. and Bergquist, B. A.: Reporting of variations in the natural isotopic composition of mercury, Analytical and Bioanalytical Chemistry, 388, 353-359, 2007.

Blum, J. D. and Johnson, M. W.: Recent developments in mercury stable isotope analysis, Reviews in Mineralogy and Geochemistry, 82, 733-757, 2017.

Breitinger, D. and Brodersen, K.: Development of and Problems in the Chemistry of Mercury-Nitrogen Compounds,
2255 Angewandte Chemie International Edition in English, 9, 357-367, https://doi.org/10.1002/anie.197003571, 1970.

Brønsted, J. N. and de Hevesy, G.: The separation of the isotopes of mercury, Nature, 106, 144-144, 1921.

Buchachenko, A. L.: Mass-Independent Isotope Effects, Journal of Physical Chemistry B, 117, 2231-2238, 10.1021/jp308727w, 2013.

Buchachenko, A. L.: Mercury Isotopes in Earth and Environmental Chemistry, Russian Journal of Physical Chemistry B, 12,
2260 635-644, 10.1134/s1990793118040048, 2018.

Burkholder, J. B., Sander, S. P., Abbatt, J., Barker, J. R., Cappa, C., Crounse, J. D., Dibble, T. S., Huie, R. E., Kolb, C. E., Kurylo, M. J., Orkin, V. L., Percival, C. J., Wilmouth, D. M., and Wine, P. H.: Chemical Kinetics and Photochemical Data for Use in Atmospheric Studies, Evaluation No. 19, Jet Propulsion Laboratory, Pasadena, 2019.

Burnard, P.: The noble gases as geochemical tracers, Springer, 2013.

2265 Buxton, G. V., Mulazzani, Q. G., and Ross, A. B.: Critical Review of Rate Constants for Reactions of Transients from Metal Ions and Metal Complexes in Aqueous Solution, Journal of Physical and Chemical Reference Data, 24, 1055-1349, 10.1063/1.555966, 1995.

Byun, Y., Cho, M., Namkung, W., Lee, K., Koh, D. J., and Shin, D. N.: Insight into the Unique Oxidation Chemistry of Elemental Mercury by Chlorine-Containing Species: Experiment and Simulation, Environmental Science & Technology, 44,
2270 1624-1629, 2010.

Cai, H. and Chen, J.: Mass-independent fractionation of even mercury isotopes, Science Bulletin, 1-9, 10.1007/s11434-015-0968-8, 2015.

Callear, A. B.: Excited Mercury Complexes, Chemical Reviews, 87, 335-355, 1987.

Callear, A. B. and Shiundu, P. M.: Temperature-Dependence of the Hg 6s6p(^{3}P$_0$ → ^{3}P$_1$) Transition Induced by Nitrogen,
2275 Chemical Physics Letters, 136, 342-345, 10.1016/0009-2614(87)80263-4, 1987.

Callear, A. B., Patrick, C. R., and Robb, J. C.: Reaction of excited mercury (Hg 6^{3}P$_1$) with oxygen, Transactions of the Faraday Society, 55, 280 - 287, 1959.

Calvert, J. G. and Lindberg, S. E.: Mechanisms of mercury removal by O$_3$ and OH in the atmosphere, Atmospheric Environment, 39, 3355-3367, 2005.

2280 Calvert, J. G., Orlando, J. J., Stockwell, W. R., and Wallington, T. J.: The Mechanisms of Reactions Influencing Atmospheric Ozone, Oxford University Press, 2015.

Cardiano, P., Cucinotta, D., Foti, C., Giuffrè, O., and Sammartano, S.: Potentiometric, Calorimetric, and ^{1}H NMR Investigation on Hg^{2+}-Mercaptocarboxylate Interaction in Aqueous Solution, Journal of Chemical & Engineering Data, 56, 1995-2004, 10.1021/je101007n, 2011.

2285 Cario, G. and Franck, J.: Über Zerlegung von Wasserstoffmolekülen durch angeregte Quecksilberatome, Zeitschrift für Physik, 11, 161-166, 10.1007/BF01328410, 1922.

Carmona García, J.: Atmospheric chemistry of mercury and sulfur induced by sunlight: Quantum-chemical modelling and environmental implications, Ph D. thesis, Institut de Ciència Molecular, Universitat de València, 2024.

2290 Castro Pelaez, P., Kellö, V., Cernusak, I., and Dibble, T.: Together, Not Separately, OH and O_3 Oxidize $Hg^{(0)}$ to $Hg^{(II)}$ in the Atmosphere, The Journal of Physical Chemistry A, 126, 10.1021/acs.jpca.2c04364, 2022.

Chandan, P., Ghosh, S., and Bergquist, B. A.: Mercury Isotope Fractionation during Aqueous Photo-Reduction of Monomethylmercury in the Presence of Dissolved Organic Matter, Environmental Science & Technology, 49, 259-267, 10.1021/es5034553, 2015.

2295 Chen, C., Huang, J.-H., Li, K., Osterwalder, S., Yang, C., Waldner, P., Zhang, H., Fu, X., and Feng, X.: Isotopic Characterization of Mercury Atmosphere–Foliage and Atmosphere–Soil Exchange in a Swiss Subalpine Coniferous Forest, Environmental Science & Technology, 57, 15892-15903, 10.1021/acs.est.3c03576, 2023.

Chen, J., Pehkonen, S. O., and Lin, C. J.: Degradation of monomethylmercury chloride by hydroxyl radicals in simulated natural waters, Water Research, 37, 2496-2504, 2003.

2300 Chen, J., Hintelmann, H., Feng, X., and Dimock, B.: Unusual fractionation of both odd and even mercury isotopes in precipitation from Peterborough, ON, Canada, Geochimica et Cosmochimica Acta, 90, 3346, 2012.

Chen, J., Hintelmann, H., Zheng, W., Feng, X., Cai, H., Wang, Z., Yuan, S., and Wang, Z.: Isotopic evidence for distinct sources of mercury in lake waters and sediments, Chemical Geology, 426, 33-44, 10.1016/j.chemgeo.2016.01.030, 2016.

Chen, Y., Zhang, Q., Zhang, L., Liu, X., Li, Y., Liu, R., Wang, Y., Song, Y., Li, Y., Yin, Y., and Cai, Y.: Light-induced degradation of dimethylmercury in different natural waters, Journal of Hazardous Materials, 470, 2305 10.1016/j.jhazmat.2024.134113, 2024.

Chi, Y., Yan, N. Q., Qu, Z., Qiao, S. H., and Jia, J. P.: The performance of iodine on the removal of elemental mercury from the simulated coal-fired flue gas, Journal of Hazardous Materials, 166, 776-781, 10.1016/j.jhazmat.2008.11.130, 2009.

Cohen-Atiya, M. and Mandler, D.: Studying thiol adsorption on Au, Ag and Hg surfaces by potentiometric measurements, Journal of Electroanalytical Chemistry, 550, 267-276, 10.1016/S0022-0728(02)01145-2, 2003.

2310 Cole, A. S., Steffen, A., Pfaffhuber, K. A., Berg, T., Pilote, M., Poissant, L., Tordon, R., and Hung, H.: Ten-year trends of atmospheric mercury in the high Arctic compared to Canadian sub-Arctic and mid-latitude sites, Atmospheric Chemistry and Physics, 13, 1535-1545, 2013.

Cole, A. S., Steffen, A., Eckley, C. S., Narayan, J., Pilote, M., Tordon, R., Graydon, J. A., St Louis, V. L., Xu, X. H., and Branfireun, B. A.: A Survey of Mercury in Air and Precipitation across Canada: Patterns and Trends, Atmosphere, 5, 635-668, 2315 2014.

Conaway, C. H., Black, F. J., Weiss-Penzias, P., Gault-Ringold, M., and Flegal, A. R.: Mercury speciation in Pacific coastal rainwater, Monterey Bay, California, Atmospheric Environment, 44, 1788-1797, 2010.

Conaway, C. H., Black, F. J., Gault-Ringold, M., Pennington, J. T., Chavez, F. P., and Flegal, A. R.: Dimethylmercury in Coastal Upwelling Waters, Monterey Bay, California, Environmental Science & Technology, 43, 1305-1309, 2320 10.1021/es802705t, 2009.

Cremer, D., Kraka, E., and Filatov, M.: Bonding in Mercury Molecules Described by the Normalized Elimination of the Small Component and Coupled Cluster Theory, Physical Chemistry Chemical Physics, 9, 2510-2521, 2008.

Criss, R. E.: Principles of stable isotope distribution, Oxford University Press, 1999.

Custódio, D., Ebinghaus, R., Spain, T., and Bieser, J.: Source apportionment of atmospheric mercury in the remote marine 2325 atmosphere: Mace Head GAW station, Irish western coast, Atmospheric Chemistry and Physics, 20, 7929-7939, 10.5194/acp-20-7929-2020, 2020.

Deacon, G. B., Faulks, S. J., and Pain, G. N.: The Synthesis of Organometallics by Decarboxylation Reactions, in: Advances in Organometallic Chemistry, edited by: Stone, F. G. A., and West, R., Academic Press, 237-276, 10.1016/S0065-3055(08)60576-6, 1986.

2330 Deeds, D. A., Ghoshdastidar, A., Raofie, F., Guérette, É.-A., Tessier, A., and Ariya, P. A.: Development of a Particle-Trap Preconcentration-Soft Ionization Mass Spectrometric Technique for the Quantification of Mercury Halides in Air, Analytical Chemistry, 87, 5109-5116, 10.1021/ac504545w, 2015.

Demers, J. D., Blum, J. D., and Zak, D. R.: Mercury isotopes in a forested ecosystem: Implications for air-surface exchange dynamics and the global mercury cycle, Global Biogeochemical Cycles, 27, 222-238, 2013.

2335 Demers, J. D., Sherman, L. S., Blum, J. D., Marsik, F. J., and Dvonch, J. T.: Coupling atmospheric mercury isotope ratios and meteorology to identify sources of mercury impacting a coastal urban-industrial region near Pensacola, Florida, USA, Global Biogeochemical Cycles, 29, 1689-1705, 10.1002/2015GB005146, 2015.

Dibble, T. S. and Schwid, A. C.: Thermodynamics limits the reactivity of BrHg radical with volatile organic compounds, Chemical Physics Letters, 659, 289-294, 10.1016/j.cplett.2016.07.065, 2016.

2340 Dibble, T. S., Zelie, M. J., and Jiao, Y.: Quantum Chemistry Guide to PTRMS Studies of As-Yet Undetected Products of the Bromine-Atom Initiated Oxidation of Gaseous Elemental Mercury, Journal of Physical Chemistry A, 118, 7847-7854, 10.1021/jp5041426, 2014.

Dibble, T. S., Zelie, M. J., and Mao, H.: Thermodynamics of reactions of ClHg and BrHg radicals with atmospherically abundant free radicals, Atmospheric Chemistry and Physics, 12, 10271-10279, 2012.

2345   Dibble, T. S., Tetu, H. L., Jiao, Y. G., Thackray, C. P., and Jacob, D. J.: Modeling the OH-Initiated Oxidation of Mercury in the Global Atmosphere without Violating Physical Laws, Journal of Physical Chemistry A, 124, 444-453, 10.1021/acs.jpca.9b10121, 2020.

Dickinson, R. G. and Sherrill, M. S.: Formation of Ozone by Optically Excited Mercury Vapor, Proceedings of the National Academy of Sciences of the United States of America, 12, 175-178, 1926.

2350   Dommergue, A., Bahlmann, E., Ebinghaus, R., Ferrari, C., and Boutron, C.: Laboratory simulation of Hg^0 emissions from a snowpack, Analytical and Bioanalytical Chemistry, 388, 319-327, 2007.

Dong, W., Bian, Y., Liang, L., and Gu, B.: Binding Constants of Mercury and Dissolved Organic Matter Determined by a Modified Ion Exchange Technique, Environmental Science & Technology, 45, 3576-3583, 2011.

Donohoue, D. L.: Kinetic studies of the oxidation pathways of gaseous elemental mercury, Ph. D. Thesis, Department of
2355   Marine and Atmospheric Chemistry, University of Miami, Coral Gables, Florida, 261 pp., 2008.

Donohoue, D. L., Bauer, D., and Hynes, A. J.: Temperature and Pressure Dependent Rate Coefficients for the Reaction of Hg with Cl and the Reaction of Cl with Cl: A Pulsed Laser Photolysis-Pulsed Laser Induced Fluorescence Study, Journal of Physical Chemistry A, 109, 7732-7741, 2005.

Donohoue, D. L., Bauer, D., Cossairt, B., and Hynes, A. J.: Temperature and Pressure Dependent Rate Coefficients for the
2360   Reaction of Hg with Br and the Reaction of Br with Br: A Pulsed Laser Photolysis-Pulsed Laser Induced Fluorescence Study, Journal of Physical Chemistry A, 110, 6623-6632, 2006.

Donovan, P. M., Blum, J. D., Yee, D., Gehrke, G. E., and Singer, M. B.: An isotopic record of mercury in San Francisco Bay sediment, Chemical Geology, 349, 87 - 98, 2013.

Douglas, T. A. and Blum, J. D.: Mercury Isotopes Reveal Atmospheric Gaseous Mercury Deposition Directly to the Arctic
2365   Coastal Snowpack, Environmental Science & Technology Letters, 6, 235-242, 10.1021/acs.estlett.9b00131, 2019.

Douglas, T. A., Sturm, M., Blum, J. D., Polashenski, C., Stuefer, S., Hiemstra, C., Steffen, A., Filhol, S., and Prevost, R.: A Pulse of Mercury and Major Ions in Snowmelt Runoff from a Small Arctic Alaska Watershed, Environmental Science & Technology, 51, 11145-11155, 10.1021/acs.est.7b03683, 2017.

Dumarey, R., Dams, R., and Hoste, J.: Comparison of the collection and desorption efficiency of activated-charcoal, silver, and
2370   gold for the determination of vapor-phase atmospheric mercury, Analytical Chemistry, 57, 2638-2643, 1985.

Dunham-Cheatham, S. M., Lyman, S., and Gustin, M. S.: Comparison and calibration of methods for ambient reactive mercury quantification, Science of the Total Environment, 856, ARTN 159219, 10.1016/j.scitotenv.2022.159219, 2023.

Eder, J. M.: Ein neues chemisches Photometer mittelst Quecksilberoxalat zur Bestimmung der Intensität der ultravioletten Strahlen des Tageslichtes und Beiträge zur Photochemie des Quecksilberchlorides, Berichte der deutschen chemischen
2375   Gesellschaft, 13, 166-168, 10.1002/cber.18800130150, 1880.

Edirappulige, D. T. H., Cheng, L., and Dibble, T. S.: Computational chemistry re-interprets lab and field studies of nitrate radical initiation of oxidation of Hg(0), ACS Spring Meeting 2023, Indianapolis

Edirappulige, D. T. H., Kirby, I. J., Beckett, C. K., and Dibble, T. S.: Atmospheric Chemistry of $HOHg^{II}O\bullet$ Mimics That of a Hydroxyl Radical, Journal of Physical Chemistry A, 10.1021/acs.jpca.3c04159, 2023b.

2380   Enrico, M., Le Roux, G., Marusczak, N., Heimbürger, L. E., Claustres, A., Fu, X. W., Sun, R. Y., and Sonke, J. E.: Atmospheric Mercury Transfer to Peat Bogs Dominated by Gaseous Elemental Mercury Dry Deposition, Environmental Science & Technology, 50, 2405-2412, 2016.

Epov, V.: Mechanisms of Oxidation-Reduction Reactions Can Be Predicted by the Magnetic Isotope Effect, Advances in Physical Chemistry, 2011, 10.1155/2011/450325, 2011a.

2385   Epov, V. N.: Magnetic isotope effect and theory of atomic orbital hybridization to predict a mechanism of chemical exchange reactions, Physical Chemistry Chemical Physics, 13, 13222-13231, 10.1039/c1cp21012b, 2011b.

Faïn, X., Helmig, D., Hueber, J., Obrist, D., and Williams, M. W.: Mercury dynamics in the Rocky Mountain, Colorado, snowpack, Biogeosciences, 10, 3793-3807, 10.5194/bg-10-3793-2013, 2013.

Fang, Y., Liu, G., Wang, Y., Liu, Y., Yin, Y., Cai, Y., Mebel, A. M., and Jiang, G.: Transformation of Mercurous [Hg^I] Species
2390   during Laboratory Standard Preparation and Analysis: Implication for Environmental Analysis, Environmental Science & Technology, 58, 6825-6834, 10.1021/acs.est.4c00718, 2024.

Feinberg, A., Dlamini, T., Jiskra, M., Shah, V., and Selin, N. E.: Evaluating atmospheric mercury (Hg) uptake by vegetation in a chemistry-transport model, Environmental Science: Processes & Impacts, 24, 1303-1318, 10.1039/D2EM00032F, 2022.

Feinberg, A. I., Kurien, U., and Ariya, P. A.: The Kinetics of Aqueous Mercury(II) Reduction by Sulfite Over an Array of
2395   Environmental Conditions, Water Air and Soil Pollution, 226, 10.1007/s11270-015-2371-0, 2015.

Feldmann, J., Grumping, R., and Hirner, A. V.: Determination of Volatile Metal and Metalloid Compounds in Gases from Domestic Waste Deposits with GC ICP-MS, Fresenius Journal of Analytical Chemistry, 350, 228-234, 1994.

Feng, X., Li, P., Fu, X., Wang, X., Zhang, H., and Lin, C.-J.: Mercury pollution in China: implications on the implementation of the Minamata Convention, Environmental Science: Processes & Impacts, 24, 634-648, 10.1039/D2EM00039C, 2022.

2400   Filatov, M. and Cremer, D.: Revision of the dissociation energies of mercury chalcogendies - Unusual types of mercury

bonding, Chemical Physics Physical Chemistry, 5, 1547-1557, 10.1002/cphc.200301207, 2004.

Finlayson-Pitts, B. J. and Pitts, J. N.: Chemistry of the upper and lower atmosphere: theory, experiments and applications, 1st Ed., Academic Press, San Diego, 2000.

Foti, C., Giuffre, O., Lando, G., and Sammartano, S.: Interaction of Inorganic Mercury(II) with Polyamines, Polycarboxylates, and Amino Acids, Journal of Chemical and Engineering Data, 54, 893-903, 10.1021/je800685c, 2009.

Francés-Monerris, A., Carmona-García, J., Acuña, A. U., Dávalos, J. Z., Cuevas, C. A., Kinnison, D. E., Francisco, J. S., Saiz-Lopez, A., and Roca-Sanjuán, D.: Photodissociation Mechanisms of Major Mercury(II) Species in the Atmospheric Chemical Cycle of Mercury, Angewandte Chemie International Edition, 59, 7605-7610, 2020.

Fu, X., Maruszczak, N., Wang, X., Gheusi, F., and Sonke, J. E.: Isotopic Composition of Gaseous Elemental Mercury in the Free Troposphere of the Pic du Midi Observatory, France, Environmental Science & Technology, 10.1021/acs.est.6b00033, 2016a.

Fu, X., Zhang, H., Liu, C., Zhang, H., Lin, C.-J., and Feng, X.: Significant Seasonal Variations in Isotopic Composition of Atmospheric Total Gaseous Mercury at Forest Sites in China Caused by Vegetation and Mercury Sources, Environmental Science & Technology, 53, 13748-13756, 10.1021/acs.est.9b05016, 2019a.

Fu, X., Zhang, H., Feng, X., Tan, Q., Ming, L., Liu, C., and Zhang, L.: Domestic and Transboundary Sources of Atmospheric Particulate Bound Mercury in Remote Areas of China: Evidence from Mercury Isotopes, Environmental Science & Technology, 53, 1947-1957, 2019b.

Fu, X., Jiskra, M., Yang, X., Maruszczak, N., Enrico, M., Chmeleff, J., Heimbürger-Boavida, L.-E., Gheusi, F., and Sonke, J. E.: Mass-Independent Fractionation of Even and Odd Mercury Isotopes during Atmospheric Mercury Redox Reactions, Environmental Science & Technology, 55, 10164-10174, 2021.

Fu, X., Zhu, W., Zhang, H., Sommar, J., Yu, B., Yang, X., Wang, X., Lin, C. J., and Feng, X.: Depletion of atmospheric gaseous elemental mercury by plant uptake at Mt. Changbai, Northeast China, Atmospheric Chemistry and Physics, 16, 12861-12873, 10.5194/acp-16-12861-2016, 2016b.

Fu, X. W., Zhang, H., Yu, B., Wang, X., Lin, C. J., and Feng, X. B.: Observations of atmospheric mercury in China: a critical review, Atmospheric Chemistry and Physics, 15, 9455-9476, 10.5194/acp-15-9455-2015, 2015.

Fujita, S., Horii, H., and Taniguchi, S.: Pulse radiolysis of mercuric ion in aqueous solutions, The Journal of Physical Chemistry, 77, 2868-2871, 10.1021/j100642a009, 1973.

Fujita, S., Horii, H., Mori, T., and Taniguchi, S.: Pulse radiolysis of mercuric oxide in neutral aqueous solutions, Journal of Physical Chemistry, 79, 960-964, 10.1021/j100577a003, 1975.

Gačnik, J., Zivkovic, I., Guevara, S. R., Kotnik, J., Berisha, S., Nair, S. V., Jurov, A., Cvelbar, U., and Horvat, M.: Calibration Approach for Gaseous Oxidized Mercury Based on Nonthermal Plasma Oxidation of Elemental Mercury, Analytical Chemistry, 94, 8234-8240, 10.1021/acs.analchem.2c00260, 2022.

Gačnik, J., Lyman, S., Dunham-Cheatham, S. M., and Gustin, M. S.: Limitations and insights regarding atmospheric mercury sampling using gold, Analytica Chimica Acta, 1319, 342956, 10.1016/j.aca.2024.342956, 2024.

Gaffney, J. and Marley, N.: In-depth review of atmospheric mercury: sources, transformations, and potential sinks, Energy and Emission Control Technologies, 2, 10.2147/eect.s37038, 2014.

Gao, Z. Y., Bailey, N., and Wang, F. Y.: Experimental Determination of Mercury Photoreduction Rates in Cloudwater, Journal of Geophysical Research-Atmospheres, 128, 10.1029/2022jd038183, 2023.

Gao, Z. Y., Geilfus, N. X., Saiz-Lopez, A., and Wang, F. Y.: Reproducing Arctic springtime tropospheric ozone and mercury depletion events in an outdoor mesocosm sea ice facility, Atmospheric Chemistry and Physics, 22, 1811-1824, 10.5194/acp-22-1811-2022, 2022.

Gay, D. A., Schmeltz, D., Prestbo, E., Olson, M., Sharac, T., and Tordon, R.: The Atmospheric Mercury Network: Measurement and initial examination of an ongoing atmospheric mercury record across North America, Atmospheric Chemistry and Physics, 13, 11339-11349, 2013.

Gerson, J. R., Driscoll, C. T., Demers, J. D., Sauer, A. K., Blackwell, B. D., Montesdeoca, M. R., Shanley, J. B., and Ross, D. S.: Deposition of mercury in forests across a montane elevation gradient: Elevational and seasonal patterns in methylmercury inputs and production, Journal of Geophysical Research: Biogeosciences, 122, 1922-1939, 10.1002/2016JG003721, 2017.

Ghoshdastidar, A. J. and Ariya, P. A.: The Existence of Airborne Mercury Nanoparticles, Scientific Reports, 910733, 10.1038/s41598-019-47086-8, 9, 2019.

Ghoshdastidar, J., Ramamurthy, J., Morissette, M., and Ariya, P.: Development of methodology to generate, measure, and characterize the chemical composition of oxidized mercury nanoparticles, Analytical and Bioanalytical Chemistry, 10.1007/s00216-019-02279-y, 2019.

Giannakopoulos, E., Deligiannakis, Y., and Salahas, G.: Electrochemical interfacial adsorption mechanism of polyphenolic molecules onto Hanging Mercury Drop Electrode surface (HMDE), Journal of Electroanalytical Chemistry, 664, 117-125, 10.1016/j.jelechem.2011.11.008, 2012.

Gómez Martín, J. C., Lewis, T. R., Douglas, K. M., Blitz, M. A., Saiz-Lopez, A., and Plane, J. M. C.: The reaction between HgBr and O_3: kinetic study and atmospheric implications, Physical Chemistry Chemical Physics, 24, 12419-12432, 10.1039/D2CP00754A, 2022.

Goodsite, M., Plane, J. M. C., and Skov, H.: A Theoretical Study of the Oxidation of Hg^0 to $HgBr_2$ in the Troposphere, Environmental Science & Technology, 38, 2004.

2460 Goodsite, M. E., Plane, J. M. C., and Skov, H.: A Theoretical Study of the Oxidation of Hg0 to HgBr2 in the Troposphere (vol 38, pg 1772, 2004), Environmental Science & Technology, 46, 5262-5262, 10.1021/es301201c, 2012.

Gratz, L. E., Keeler, G. J., Blum, J. D., and Sherman, L. S.: Isotopic Composition and Fractionation of Mercury in Great Lakes Precipitation and Ambient Air, Environmental Science & Technology, 44, 7764-7770, 2010.

Gratz, L. E., Ambrose, J. L., Jaffe, D. A., Shah, V., Jaeglé, L., Stutz, J., Festa, J., Spolaor, M., Tsai, C., Selin, N. E., Song, S.,
2465 Zhou, X., Weinheimer, A. J., Knapp, D. J., Montzka, D. D., Flocke, F. M., Campos, T. L., Apel, E., Hornbrook, R., Blake, N. J., Hall, S., Tyndall, G. S., Reeves, M., Stechman, D., and Stell, M.: Oxidation of mercury by bromine in the subtropical Pacific free troposphere, Geophysical Research Letters, 2015GL066645, 10.1002/2015GL066645, 2015.

Greig, G., Gunning, H. E., and Strausz, O. P.: Reactions of Metal Atoms. II. The Combination of Mercury and Bromine Atoms and the Dimerization of HgBr, The Journal of Chemical Physics, 52, 3684, 10.1063/1.1673544, 1970.

2470 Greig, G., Young, P. J., and Strausz, O. P.: Reactions of Metal Atoms. IV. The uv Spectra of CdBr, CdI, ZnBr, and ZnI, The Journal of Chemical Physics, 54, 983 - 991, 1971.

Gruss, A. F., Rodriguez, R., and Mazyck, D. W.: Mercury Oxidation by UV Irradiation: Effect of Contact Time, UV Wavelength, and Moisture Content, Industrial & Engineering Chemistry Research, 56, 6131-6135, 10.1021/acs.iecr.7b00032, 2017.

2475 Gu, B. H., Bian, Y. R., Miller, C. L., Dong, W. M., Jiang, X., and Liang, L. Y.: Mercury reduction and complexation by natural organic matter in anoxic environments, Proceedings of the National Academy of Sciences of the United States of America, 108, 1479-1483, 2011.

Guérette, E.-A.: Kinetic and mass-spectrometric studies of atmospherically relevant mercury-bromine chemistry, M.Sc. thesis, Department of Chemistry, McGill University, Montreal, Canada, 114 pp., 2011.

2480 Gunning, H. E. and Strausz, O. P.: Isotopic Effects and the Mechanism of Energy Transfer in Mercury Photosensitization, in: Advances in Photochemistry Vol. 1, edited by: Noyes Jr, W. A., Hammond, G. S., and Pitts Jr, J. N., John Wiley & Sons, 209-274, 10.1002/9780470133316.ch7, 1963.

Gustin, M. S., Amos, H. M., Huang, J., Miller, M. B., and Heidecorn, K.: Measuring and modeling mercury in the atmosphere: A critical review, Atmospheric Chemistry and Physics, 15, 5697 - 5713, 2015.

2485 Gustin, M. S., Dunham-Cheatham, S. M., Huang, J. Y., Lindberg, S., and Lyman, S. N.: Development of an Understanding of Reactive Mercury in Ambient Air: A Review, Atmosphere, 12, ARTN 73, 10.3390/atmos12010073, 2021.

Gustin, M. S., Dunham-Cheatham, S. M., Allen, N., Choma, N., Johnson, W., Lopez, S., Russell, A., Mei, E. R., Magand, O., Dommergue, A., and Elgiar, T.: Observations of the chemistry and concentrations of reactive Hg at locations with different ambient air chemistry, Science of the Total Environment, 904, 166-184, 10.1016/j.scitotenv.2023, 2023.

2490 Gustin, M. S., Dunham-Cheatham, S. M., Lyman, S., Horvat, M., Gay, D. A., Gacnik, J., Gratz, L., Kempkes, G., Khalizov, A., Lin, C.-J., Lindberg, S. E., Lown, L., Martin, L., Mason, R. P., Macsween, K., Nair, S. V., Nguyen, L. S. P., O'Neil, T., Sommar, J., Zhang, L., Weiss-Penzias, P., and Zivkovic, I.: Measurement of Atmospheric Mercury: Current Limitations and Suggestions for Paths Forward, Environmental Science & Technology, 58, 12853-12864, 10.1021/acs.est.4c06011, 2024.

Guzman, F. J. and Bozzelli, J.: Thermodynamics of OHgX, XHgOH, XHgOCl, XHgOBr, and HOHgY Gaseous Oxidized
2495 Mercury Molecules from Isodesmic, Isogyric, and Atomization Work Reactions (X = Halogen, Y = OH, OCl, OBr), Journal of Physical Chemistry A, 123, 4452-4464, 10.1021/acs.jpca.9b01358, 2019.

Gårdfeldt, K. and Jonsson, M.: Is bimolecular reduction of Hg(II) complexes possible in aqueous systems of environmental importance?, Journal of Physical Chemistry A, 107, 4478- 4482, 2003.

Gårdfeldt, K., Munthe, J., Strömberg, D., and Lindqvist, O.: A kinetic study on the abiotic methylation of divalent mercury in
2500 the aqueous phase, Science of The Total Environment, 304, 127-136, https://doi.org/10.1016/S0048-9697(02)00562-4, 2003.

Gårdfeldt, K., Sommar, J., Strömberg, D., and Feng, X. B.: Oxidation of atomic mercury by hydroxyl radicals and photoinduced decomposition of methylmercury in the aqueous phase, Atmospheric Environment, 35, 3039-3047, 2001.

Görner, H.: Quinone Photochemistry, in: CRC Handbook of Organic Photochemistry and Photobiology, 3rd Ed. Volume 1, edited by: Griesbeck, A., Oelgemöller, M., and Ghetti, F., CRC Press, 683 - 714, 2019.

2505 Haitzer, M., Aiken, G. R., and Ryan, J. N.: Binding of Mercury(II) to Dissolved Organic Matter: The Role of the Mercury-to-DOM Concentration Ratio, Environmental Science & Technology, 36, 3564-3570, 10.1021/es025699i, 2002.

Hall, B.: An experimental study of mercury reactions in combustion flue gases, Ph. D. Thesis, Department of Inorganic Chemistry, Chalmers University of Technology and Göteborg University, Sweden, 76 pp., 1992.

Hall, B.: The gas-phase oxidation of elemental mercury by ozone, Water Air and Soil Pollution, 80, 301-315, 1995.

2510 Hall, B., Schager, P., and Weesmaa, J.: The Homogeneous Gas-Phase Reaction of Mercury with Oxygen, and the Corresponding Heterogeneous Reactions in the Presence of Activated Carbon and Fly-Ash, Chemosphere, 30, 611-627, 1995.

Hammerschmidt, C. R., Lamborg, C. H., and Fitzgerald, W. F.: Aqueous phase methylation as a potential source of methylmercury in wet deposition, Atmospheric Environment, 41, 1663-1668, 10.1016/j.atmosenv.2006.10.032, 2007.

Han, X. X., Li, Y. B., Li, D., and Liu, C.: Role of Free Radicals/Reactive Oxygen Species in MeHg Photodegradation: Importance of Utilizing Appropriate Scavengers, Environmental Science & Technology, 51, 3784-3793, 10.1021/acs.est.7b00205, 2017.

Harkins, W. D. and Mulliken, R. S.: The separation of mercury into isotopes, Nature, 108, 146, 10.1038/108146a0, 1921.

Hayashi, K., Kawai, S., Ohno, T., and Maki, Y.: Photomethylation of Inorganic Mercury by Aliphatic Alpha-Amino-Acids, Journal of the Chemical Society-Chemical Communications, 158-159, 10.1039/c39770000158, 1977.

He, F., Zhao, W., Liang, L., and Gu, B.: Photochemical oxidation of dissolved elemental mercury by carbonate radicals in water, Environmental Science & Technology Letters, 1, 499 - 503, 2014.

He, F., Zheng, W., Liang, L. Y., and Gu, B. H.: Mercury photolytic transformation affected by low-molecular-weight natural organics in water, Science of the Total Environment, 416, 429-435, 10.1016/j.scitotenv.2011.11.081, 2012.

He, Y. P. and Mason, R. P.: Comparison of reactive gaseous mercury measured by KCl-coated denuders and cation exchange membranes during the Pacific GEOTRACES GP15 expedition, Atmospheric Environment, 244, 10.1016/j.atmosenv.2020.117973, 2021.

He, Y. P., Shi, X. M., Huffman, W. W., Lamborg, C. H., and Mason, R. P.: Description of a Dimethylmercury Automatic Analyzer for the High-Resolution Measurement of Dissolved Gaseous Mercury Species in Surface Ocean Waters, Environmental Science & Technology, 10.1021/acs.est.2c02908, 2022.

Hepler, L. G. and Olofsson, G.: Mercury – thermodynamic properties, chemical equilibria, and standard potentials, Chemical Reviews, 75, 585-602, 10.1021/cr60297a003, 1975.

Hietanen, S. and Sillén, L. G.: On the standard potentials of mercury, and the equilibrium $Hg^{2+}+ Hg^0(l) = Hg_2^{2+}$ in nitrate and perchlorate solutions, Arkiv för Kemi, 10, 103-125, 1956.

Hintelmann, H. and Zheng, W.: Tracking Geochemical Transformations and Transport of Mercury through Isotope Fractionation, in: Environmental Chemistry and Toxicology of Mercury, edited by: Liu, G., Cai, Y., and O'Driscoll, N., John Wiley & Sons, 293 - 328, 2011.

Hippler, H., Wendt, H. R., and Hunziker, H. E.: Excited intermediates in Hg-photosensitized reaction of O_2 detected by energy-transfer, Journal of Chemical Physics, 68, 5103-5111, 1978.

Holmes, C. D., Jacob, D. J., Mason, R. P., and Jaffe, D. A.: Sources and deposition of reactive gaseous mercury in the marine atmosphere, Atmospheric Environment, 43, 2278-2285, 10.1016/j.atmosenv.2009.01.051, 2009.

Holmes, C. D., Jacob, D. J., Corbitt, E. S., Mao, J., Yang, X., Talbot, R., and Slemr, F.: Global atmospheric model for mercury including oxidation by bromine atoms, Atmospheric Chemistry and Physics, 10, 12037-12057, 2010.

Hong, Q., Xie, Z., Liu, C., Wang, F., Xie, P., Kang, H., Xu, J., Wang, J., Wu, F., He, P., Mou, F., Fan, S., Dong, Y., Zhan, H., Yu, X., Chi, X., and Liu, J.: Speciated atmospheric mercury on haze and non-haze days in an inland city in China, Atmospheric Chemistry and Physics, 16, 13807-13821, 10.5194/acp-16-13807-2016, 2016.

Horne, D. G., Gosavi, R., and Strausz, O. P.: Reactions of metal atoms. I. The combination of mercury and chlorine atoms and the dimerization of HgCl, The Journal of Chemical Physics, 48, 4758 - 4764, 1968.

Horowitz, H. M., Jacob, D. J., Zhang, Y. X., Dibble, T. S., Slemr, F., Amos, H. M., Schmidt, J. A., Corbitt, E. S., Marais, E. A., and Sunderland, E. M.: A new mechanism for atmospheric mercury redox chemistry: implications for the global mercury budget, Atmospheric Chemistry and Physics, 17, 6353-6371, 10.5194/acp-17-6353-2017, 2017.

Howard, D., Nelson, P. F., Edwards, G. C., Morrison, A. L., Fisher, J. A., Ward, J., Harnwell, J., van der Schoot, M., Atkinson, B., Chambers, S. D., Griffiths, A. D., Werczynski, S., and Williams, A. G.: Atmospheric mercury in the Southern Hemisphere tropics: seasonal and diurnal variations and influence of inter-hemispheric transport, Atmospheric Chemistry and Physics, 17, 11623-11636, 10.5194/acp-17-11623-2017, 2017.

Huang, J., Miller, M. B., Edgerton, E., and Sexauer Gustin, M.: Deciphering potential chemical compounds of gaseous oxidized mercury in Florida, USA, Atmospheric Chemistry and Physics, 17, 1689-1698, 10.5194/acp-17-1689-2017, 2017.

Huang, J., Kang, S., Tian, L., Guo, J., Zhang, Q., Cong, Z., Sillanpää, M., Sun, S., and Tripathee, L.: Influence of long-range transboundary transport on atmospheric water vapor mercury collected at the largest city of Tibet, Science of The Total Environment, 566-567, 1215-1222, 10.1016/j.scitotenv.2016.05.177, 2016a.

Huang, Q., He, X., Huang, W., and Reinfelder, J. R.: Mass-Independent Fractionation of Mercury Isotopes during Photoreduction of Soot Particle Bound Hg(II), Environmental Science & Technology, 55, 13783-13791, 10.1021/acs.est.1c02679, 2021.

Huang, Q., Liu, Y., Chen, J., Feng, X., Huang, W., Yuan, S., Cai, H., and Fu, X.: An improved dual-stage protocol to pre-concentrate mercury from airborne particles for precise isotopic measurement, Journal of Analytical Atomic Spectrometry, 30, 957-966, 10.1039/C4JA00438H, 2015.

Huang, Q., Chen, J., Huang, W., Reinfelder, J. R., Fu, P., Yuan, S., Wang, Z., Yuan, W., Cai, H., Ren, H., Sun, Y., and He, L.: Diel variation in mercury stable isotope ratios records photoreduction of PM2.5-bound mercury, Atmospheric Chemistry and Physics, 19, 315-325, 10.5194/acp-19-315-2019, 2019.

Huang, Q., Chen, J., Huang, W., Fu, P., Guinot, B., Feng, X., Shang, L., Wang, Z., Wang, Z., Yuan, S., Cai, H., Wei, L., and Yu, B.: Isotopic composition for source identification of mercury in atmospheric fine particles, Atmospheric Chemistry and

Physics, 16, 11773-11786, 10.5194/acp-16-11773-2016, 2016b.

Huber, M. L., Laesecke, A., and Friend, D. G.: Correlation for the Vapor Pressure of Mercury, Industrial & Engineering Chemistry Research, 45, 7351-7361, 10.1021/ie060560s, 2006.

Humphries, R. S., Schofield, R., Keywood, M. D., Ward, J., Pierce, J. R., Gionfriddo, C. M., Tate, M. T., Krabbenhoft, D. P.,
2575 Galbally, I. E., Molloy, S. B., Klekociuk, A. R., Johnston, P. V., Kreher, K., Thomas, A. J., Robinson, A. D., Harris, N. R. P., Johnson, R., and Wilson, S. R.: Boundary layer new particle formation over East Antarctic sea ice – possible Hg-driven nucleation?, Atmospheric Chemistry and Physics, 15, 13339-13364, 2015.

Hynes, A. J., Donohoue, D. L., Goodsite, M. E., and Hedgecock, I. M.: Our current understanding of major chemical and physical processes affecting mercury dynamics in the atmosphere and at the air-water/terrestrial interfaces, in: Mercury Fate and
2580 Transport in the Global Atmosphere - Emissions, Measurements and Models, edited by: Mason, R. P., and Pirrone, N., Springer, 427 - 457, 2009.

Hynes, A. J., Everhart, S., Bauer, D., Remeika, J., and Tatum Ernest, C.: In situ and denuder-based measurements of elemental and reactive gaseous mercury with analysis by laser-induced fluorescence – results from the Reno Atmospheric Mercury Intercomparison Experiment, Atmospheric Chemistry and Physics, 17, 465-483, 10.5194/acp-17-465-2017, 2017.

2585 Iverfeldt, A. and Lindqvist, O.: Atmospheric oxidation of elemental mercury by ozone in the aqueous phase, Atmospheric Environment, 20, 1567-1573, 10.1016/0004-6981(86)90245-3, 1986.

Jackson, T. A.: Long-range atmospheric transport of mercury to ecosystems, and the importance of anthropogenic emissions - a critical review and evaluation of the published evidence, Environmental Reviews, 5, 99-120, 1997.

Jackson, T. A.: Reply: Variations in the isotope composition of mercury in a freshwater sediment sequence and food web,
2590 Canadian Journal of Fisheries and Aquatic Sciences, 00058, 2312-2317, 2001.

Jaffe, D. A., Lyman, S., Amos, H. M., Gustin, M. S., Huang, J., Selin, N. E., Levin, L., ter Schure, A., Mason, R. P., Talbot, R., Rutter, A., Finley, B., Jaegle, L., Shah, V., McClure, C., Arnbrose, J., Gratz, L., Lindberg, S., Weiss-Penzias, P., Sheu, G.-R., Feddersen, D., Horvat, M., Dastoor, A., Hynes, A. J., Mao, H., Sonke, J. E., Slemr, F., Fisher, J. A., Ebinghaus, R., Zhang, Y., and Edwards, G.: Progress on Understanding Atmospheric Mercury Hampered by Uncertain Measurements, Environmental
2595 Science & Technology, 48, 7204-7206, 10.1021/es5026432, 2014.

Jayasekharan, T. and Sahoo, N. K.: Mercury mono oxide cluster ions $(HgO)_n^+$ by laser desorption ionization time of flight mass spectrometry, Journal of Mass Spectrometry, 49, 248-250, 2014.

Jerzykiewicz, M.: The effect of Hg(II) ions on the free radicals of humic substances and their model compounds, Chemosphere, 92, 445-450, 10.1016/j.chemosphere.2013.01.048, 2013.

2600 Jerzykiewicz, M., Witwicki, M., and Jezierska, J.: pH-dependent formation of Hg(II)-semiquinone complexes from natural phenols, Chemosphere, 138, 233-238, 10.1016/j.chemosphere.2015.06.006, 2015.

Jiang, H., Li, J., Tang, J., Cui, M., Zhao, S., Mo, Y., Tian, C., Zhang, X., Jiang, B., Liao, Y., Chen, Y., and Zhang, G.: Molecular characteristics, sources, and formation pathways of organosulfur compounds in ambient aerosol in Guangzhou, South China, Atmospheric Chemistry and Physics, 22, 6919-6935, 10.5194/acp-22-6919-2022, 2022.

2605 Jiao, Y. and Dibble, T. S.: Structures, Vibrational Frequencies, and Bond Energies of the BrHgOX and BrHgXO Species Formed in Atmospheric Mercury Depletion Events, The Journal of Physical Chemistry A, 121, 7976-7985, 10.1021/acs.jpca.7b06829, 2017a.

Jiao, Y. G. and Dibble, T. S.: First kinetic study of the atmospherically important reactions BrHg• + NO₂ and BrHg• + HOO, Physical Chemistry Chemical Physics, 19, 1826-1838, 10.1039/c6cp06276h, 2017b.

2610 Jimenez, J. L., Canagaratna, M. R., Donahue, N. M., Prevot, A. S. H., Zhang, Q., Kroll, J. H., DeCarlo, P. F., Allan, J. D., Coe, H., Ng, N. L., Aiken, A. C., Docherty, K. S., Ulbrich, I. M., Grieshop, A. P., Robinson, A. L., Duplissy, J., Smith, J. D., Wilson, K. R., Lanz, V. A., Hueglin, C., Sun, Y. L., Tian, J., Laaksonen, A., Raatikainen, T., Rautiainen, J., Vaattovaara, P., Ehn, M., Kulmala, M., Tomlinson, J. M., Collins, D. R., Cubison, M. J., E., Dunlea, J., Huffman, J. A., Onasch, T. B., Alfarra, M. R., Williams, P. I., Bower, K., Kondo, Y., Schneider, J., Drewnick, F., Borrmann, S., Weimer, S., Demerjian, K., Salcedo, D.,
2615 Cottrell, L., Griffin, R., Takami, A., Miyoshi, T., Hatakeyama, S., Shimono, A., Sun, J. Y., Zhang, Y. M., Dzepina, K., Kimmel, J. R., Sueper, D., Jayne, J. T., Herndon, S. C., Trimborn, A. M., Williams, L. R., Wood, E. C., Middlebrook, A. M., Kolb, C. E., Baltensperger, U., and Worsnop, D. R.: Evolution of Organic Aerosols in the Atmosphere, Science, 326, 1525-1529, 10.1126/science.1180353, 2009.

Jiskra, M., Wiederhold, J. G., Bourdon, B., and Kretzschmar, R.: Solution Speciation Controls Mercury Isotope Fractionation of
2620 Hg(II) Sorption to Goethite, Environmental Science & Technology, 46, 6654-6662, 10.1021/es3008112, 2012.

Jiskra, M., Sonke, J. E., Agnan, Y., Helmig, D., and Obrist, D.: Insights from mercury stable isotopes on terrestrial–atmosphere exchange of Hg⁰ in the Arctic tundra, Biogeosciences, 16, 4051-4064, 2019.

Jiskra, M., Wiederhold, J. G., Skyllberg, U., Kronberg, R.-M., and Kretzschmar, R.: Source tracing of natural organic matter bound mercury in boreal forest runoff with mercury stable isotopes, Environmental Science-Processes & Impacts, 19, 1235-
2625 1248, 10.1039/c7em00245a, 2017.

Jiskra, M., Wiederhold, J. G., Skyllberg, U., Kronberg, R. M., Hajdas, I., and Kretzschmar, R.: Mercury Deposition and Re-emission Pathways in Boreal Forest Soils Investigated with Hg Isotope Signatures, Environmental Science & Technology, 49, 7188-7196, 2015.

2630 Jiskra, M., Heimbürger-Boavida, L.-E., Desgranges, M.-M., Petrova, M. V., Dufour, A., Ferreira-Araujo, B., Masbou, J., Chmeleff, J., Thyssen, M., Point, D., and Sonke, J. E.: Mercury stable isotopes constrain atmospheric sources to the ocean, Nature, 597, 678-682, 10.1038/s41586-021-03859-8, 2021.

Jiskra, M., Sonke, J. E., Obrist, D., Bieser, J., Ebinghaus, R., Myhre, C. L., Pfaffhuber, K. A., Wängberg, I., Kyllönen, K., Worthy, D., Martin, L. G., Labuschagne, C., Mkololo, T., Ramonet, M., Magand, O., and Dommergue, A.: A vegetation control on seasonal variations in global atmospheric mercury concentrations, Nature Geoscience, 11, 244-251, 10.1038/s41561-018-
2635 0078-8, 2018.

Johnson, K. P., Blum, J. D., Keeler, G. J., and Douglas, T. A.: Investigation of the deposition and emission of mercury in arctic snow during an atmospheric mercury depletion event, Journal of Geophysical Research-Atmospheres, 113, 10.1029/2008jd009893, 2008.

Jones, C. P., Lyman, S. N., Jaffe, D. A., Allen, T., and O'Neil, T. L.: Detection and quantification of gas-phase oxidized
2640 mercury compounds by GC/MS, Atmospheric Measurement Techniques, 9, 2195-2205, 10.5194/amt-9-2195-2016, 2016.

Jordan, K. J., Bascal, H. A., Lipson, R. H., and Melchior, M.: The $B^2\Sigma^+ \leftarrow X^2\Sigma^+$ Transition of HgI, Journal of Molecular Spectroscopy, 159, 144-155, 10.1006/jmsp.1993.1113, 1993.

Knight Jr., L. B. and Lin, K. C.: ESR Spectroscopy and Chemical Bonding in CdCN and HgCN Molecules, The Journal of Chemical Physics, 56, 6044-6049, 10.1063/1.1677153, 1972.

2645 Knight Jr., L. B., Fisher, T. A., and Wise, M. B.: Photolytic codeposition generation of the HgF radical in an argon matrix at 12 K: An ESR investigation, The Journal of Chemical Physics, 74, 6009-6013, 10.1063/1.441040, 1981.

Jungbluth, H., Beyrich, J., and Asmus, K. D.: Reduction of mercuric halides and pseudohalides in aqueous solution. Formation and some physicochemical properties of HgCl, HgBr, HgI, HgSCN, and HgCN radical molecules, Journal of Physical Chemistry, 80, 1049-1053, 10.1021/j100551a004, 1976.

2650 Kallend, A. S. and Purnell, J. H.: Gas-Phase Thermal Decomposition of Dimethyl Mercury .2. Homogeneous Reaction, Transactions of the Faraday Society, 60, 103-&, 10.1039/tf9646000103, 1964.

Kaluza, U. and Boehm, H. P.: Titanium dioxide catalyzed photooxidation of mercury, Journal of Catalysis, 22, 347-358, 10.1016/0021-9517(71)90206-5, 1971.

Karakyriakos, E. and McKinley, A. J.: Matrix Isolated $HgCH_3$ Radical: An ESR Investigation, The Journal of Physical
2655 Chemistry A, 108, 4619-4626, 10.1021/jp0400925, 2004.

Khalizov, A. and Mao, N.: Heterogeneous Reaction of Gaseous Mercuric Chloride with Atmospherically Relevant Organic Films, ACS Earth and Space Chemistry, 7, 10.1021/acsearthspacechem.3c00268, 2023.

Khalizov, A., Guzman, F., Cooper, M., Mao, N., Antley, J., and Bozzelli, J.: Direct detection of gas-phase mercuric chloride by ion drift - Chemical ionization mass spectrometry, Atmospheric Environment, 238, 117687, 10.1016/j.atmosenv.2020.117687,
2660 2020.

Khalizov, A. F., Viswanathan, B., Larregaray, P., and Ariya, P. A.: A theoretical study on the reactions of Hg with halogens: Atmospheric implications, Journal of Physical Chemistry A, 107, 6360-6365, 2003.

Khiri, D., Louis, F., Cernusak, I., and Dibble, T. S.: BrHgO• + CO: Analogue of OH plus CO and Reduction Path for Hg(II) in the Atmosphere, ACS Earth and Space Chemistry, 4, 1777-1784, 2020.

2665 Kim, P. R., Han, Y. J., Holsen, T. M., and Yi, S. M.: Atmospheric particulate mercury: Concentrations and size distributions, Atmospheric Environment, 61, 94-102, 2012.

Kleszczewska, E.: The Spectrophotometry Determination of Chelate Complex: L-Ascorbic Acid with Cuprum (II) and Mercury (II) in Alkaline Solution, Polish Journal of Environmental Studies, 8, 313-318, 1999.

Kobayashi, T.: Oxidation of Metallic Mercury in Aqueous Solution by Hydrogen Peroxide and Chlorine, Journal of Japan
2670 Society of Air Pollution, 22, 230-236, 10.11298/taiki1978.22.230, 1987.

Koenig, A., Sonke, J., Magand, O., Andrade, M., Moreno R, C. I., Velarde, F., Forno, R., Gutierrez, R., Blacutt, L., Laj, P., Ginot, P., Bieser, J., Zahn, A., Slemr, F., and Dommergue, A.: Evidence for Interhemispheric Mercury Exchange in the Pacific Ocean Upper Troposphere, Journal of Geophysical Research: Atmospheres, 127, 10.1029/2021JD036283, 2022.

Kominar, R. J. and Price, S. J.: Determination of Bond Dissociation Energy $D(CH_3Hg-CH_3)$ by Toluene Carrier Method,
2675 Canadian Journal of Chemistry, 47, 991-&, 10.1139/v69-156, 1969.

Kornev, V. I. and Kardapol'tsev, A. A.: Heteroligand mercury(II) complexes with aspartic, tartaric, and citric acids, Russian Journal of Coordination Chemistry, 34, 896-900, 10.1134/s107032840812004x, 2008.

Kozin, L. F. and Hansen, S. C.: Mercury Handbook: Chemistry, Applications and Environmental Impact, Royal Society Of Chemistry, London, UK, 2013.

2680 Kramida, A., Ralchenko, Y., Reader, J., and Team, N. A.: NIST Atomic Spectra Database (version 5.11), 10.18434/T4W30F, 2023.

Kritee, K., Blum, J. D., Reinfelder, J. R., and Barkay, T.: Microbial stable isotope fractionation of mercury: A synthesis of present understanding and future directions, Chemical Geology, 336, 13-25, 10.1016/j.chemgeo.2012.08.017, 2013.

Kritee, K., Blum, J. D., Johnson, M. W., Bergquist, B. A., and Barkay, T.: Mercury Stable Isotope Fractionation during

2685   Reduction of Hg(II) to Hg(0) by Mercury Resistant Microorganisms, Environmental Science & Technology, 41, 1889-1895,
         2007.

         Kritee, K., Motta, L. C., Blum, J. D., Tsui, M. T. K., and Reinfelder, J. R.: Photomicrobial Visible Light-Induced Magnetic
         Mass Independent Fractionation of Mercury in a Marine Microalga, ACS Earth and Space Chemistry, 2, 432-440,
         10.1021/acsearthspacechem.7b00056, 2018.

2690   Kurien, U., Hu, Z., Lee, H., Dastoor, A. P., and Ariya, P. A.: Radiation enhanced uptake of $Hg^0(g)$ on iron (oxyhydr)oxide
         nanoparticles, RSC Advances, 7, 45010-45021, 10.1039/C7RA07401H, 2017.

         Kurz, A., Blum, J., Johnson, M., Nadelhoffer, K., and Zak, D.: Isotopic composition of mercury deposited via snow into mid-
         latitude ecosystems, Science of The Total Environment, 784, 147252, 10.1016/j.scitotenv.2021.147252, 2021.

         Kurz, A. Y., Blum, J. D., Gratz, L. E., and Jaffe, D. A.: Contrasting Controls on the Diel Isotopic Variation of Hg^0 at Two High
2695   Elevation Sites in the Western United States, Environmental Science & Technology, 54, 10502-10513, 2020.

         Kwon, S. Y., Blum, J. D., Yin, R., Tsui, M. T.-K., Yang, Y. H., and Choi, J. W.: Mercury stable isotopes for monitoring the
         effectiveness of the Minamata Convention on Mercury, Earth-Science Reviews, 203, 103-111, 2020.

         Lalonde, J. D., Poulain, A. J., and Amyot, M.: The role of mercury redox reactions in snow on snow-to-air mercury transfer,
         Environmental Science & Technology, 2002, 36, 174-178, 2002.

2700   Lalonde, J. D., Amyot, M., Doyon, M. R., and Auclair, J. C.: Photo-induced Hg(II) reduction in snow from the remote and
         temperate Experimental Lakes Area (Ontario, Canada), Journal of Geophysical Research-Atmospheres, 108, art. no.-4200,
         2003.

         Lalonde, J. D., Amyot, M., Kraepiel, A. M. L., and Morel, F. M. M.: Photooxidation of Hg(0) in artificial and natural waters,
         Environmental Science & Technology, 35, 1367-1372, 2001.

2705   Lam, K. T.: Chemistry and Implications of a Previously-Unknown Intermediate in the Atmospheric Mercury Oxidation, Ph. D.
         thesis, College of Environmental Science and Forestry, State University of New York, Syracuse, NY, 2019.

         Lam, K. T., Wilhelmsen, C. J., and Dibble, T. S.: $BrHgO^•$ + C_2H_4 and $BrHgO^•$ + HCHO in Atmospheric Oxidation of Mercury:
         Determining Rate Constants of Reactions with Prereactive Complexes and Bifurcation, Journal of Physical Chemistry A, 123,
         6045-6055, 10.1021/acs.jpca.9b05120, 2019a.

2710   Lam, K. T., Wilhelmsen, C. J., Schwid, A. C., Jiao, Y., and Dibble, T. S.: Computational Study on the Photolysis of BrHgONO
         and the Reactions of $BrHgO^•$ with CH_4, C_2H_6, NO, and NO_2: Implications for Formation of Hg(II) Compounds in the
         Atmosphere, The Journal of Physical Chemistry A, 123, 1637-1647, 2019b.

         Lan, X., Talbot, R., Castro, M., Perry, K., and Luke, W.: Seasonal and diurnal variations of atmospheric mercury across the US
         determined from AMNet monitoring data, Atmospheric Chemistry and Physics, 12, 10569-10582, 10.5194/acp-12-10569-2012,
2715   2012.

         Landis, M. S., Stevens, R. K., Schaedlich, F., and Prestbo, E. M.: Development and characterization of an annular denuder
         methodology for the measurement of divalent inorganic reactive gaseous mercury in ambient air, Environmental Science &
         Technology, 36, 3000-3009, 10.1021/es015887t, 2002.

         Lauretta, D. S., Klaue, B., Blum, J. D., and Buseck, P. R.: Mercury abundances and isotopic compositions in the Murchison
2720   (CM) and Allende (CV) carbonaceous chondrites, Geochimica et Cosmochimica Acta, 65, 2807-2818, 10.1016/S0016-
         7037(01)00630-5, 2001.

         Lee, C. F., Elgiar, T., David, L. M., Wilmot, T. Y., Reza, M., Hirshorn, N., McCubbin, I. B., Shah, V., Lin, J. C., Lyman, S. N.,
         Hallar, A. G., Gratz, L. E., and Volkamer, R.: Elevated Tropospheric Iodine Over the Central Continental United States: Is
         Iodine a Major Oxidant of Atmospheric Mercury?, Geophysical Research Letters, 51, e2024GL109247,
2725   10.1029/2024GL109247, 2024.

         Lee, H., Kurien, U., and Ariya, P. A.: Uptake of Hg^0 (g) on TiO_2, Al_2O_3, and Fe_2O_3 Nanoparticles: Importance in Atmospheric
         Chemical and Physical Processes, Journal of Physical Chemistry A, 10.1021/acs.jpca.2c03428, 2022.

         Lee, S., Kim, D.-H., and Kim, K.-W.: The enhancement and inhibition of mercury reduction by natural organic matter in the
         presence of Shewanella oneidensis MR-1, Chemosphere, 194, 515-522, 10.1016/j.chemosphere.2017.12.007, 2018.

2730   Lee, Y. H., Wangberg, I., and Munthe, J.: Sampling and analysis of gas-phase methylmercury in ambient air, Science of the
         Total Environment, 304, 107-113, 2003.

         Leonori, D. and Sturgeon, R. E.: A unified approach to mechanistic aspects of photochemical vapor generation, Journal of
         Analytical Atomic Spectrometry, 34, 636-654, 10.1039/c8ja00354h, 2019.

         Li, C., Enrico, M., Magand, O., Araujo, B., Le Roux, G., Osterwalder, S., Dommergue, A., Bertrand, Y., Brioude, J.,
2735   Vleeschouwer, F., and Sonke, J.: A peat core Hg stable isotope reconstruction of Holocene atmospheric Hg deposition at
         Amsterdam Island (37.8°S), Geochimica et Cosmochimica Acta, 341, 10.1016/j.gca.2022.11.024, 2022a.

         Li, C., Jiskra, M., Nilsson, M., Osterwalder, S., Zhu, W., Mauquoy, D., Skyllberg, U., Enrico, M., Haijun, P., Song, Y., Björn,
         E., and Bishop, K.: Mercury deposition and redox transformation processes in peatland constrained by mercury stable isotopes,
         Nature Communications, 14, 10.1038/s41467-023-43164-8, 2023a.

2740   Li, C., Chen, J., Angot, H., Zheng, W., Shi, G., Ding, M., Du, Z., Zhang, Q., Ma, X., Kang, S., Xiao, C., Ren, J., and Qin, D.:
         Seasonal Variation of Mercury and Its Isotopes in Atmospheric Particles at the Coastal Zhongshan Station, Eastern Antarctica,

Environmental Science & Technology, 54, 11344-11355, 10.1021/acs.est.0c04462, 2020a.

Li, L., Wang, X., Fu, H., Qu, X., Chen, J., Tao, S., and Zhu, D.: Dissolved Black Carbon Facilitates Photoreduction of Hg(II) to Hg(0) and Reduces Mercury Uptake by Lettuce (*Lactuca sativa L.*), Environmental Science & Technology, 54, 11137-11145, 10.1021/acs.est.0c01132, 2020b.

Li, M.-L., Kwon, S. Y., Poulin, B. A., Tsui, M. T.-K., Motta, L. C., and Cho, M.: Internal Dynamics and Metabolism of Mercury in Biota: A Review of Insights from Mercury Stable Isotopes, Environmental Science & Technology, 56, 9182-9195, 10.1021/acs.est.1c08631, 2022b.

Li, T., Wang, Y., Mao, H., Wang, S., Talbot, R. W., Zhou, Y., Wang, Z., Nie, X., and Qie, G.: Insights on Chemistry of Mercury Species in Clouds over Northern China: Complexation and Adsorption, Environmental Science & Technology, 52, 5125-5134, 10.1021/acs.est.7b06669, 2018.

Li, X., Wang, X., Zhang, H., and Lu, Z.: Mosses and lichens enhance atmospheric elemental mercury deposition in a subtropical montane forest†, Environmental Chemistry, 20, 105-113, 10.1071/EN22124, 2023b.

Li, X. S., Yan, M., Dibble, T. S., and Zhang, L. Q.: Reaction mechanism and kinetics of the important but neglected reaction of Hg with NO2 at low temperature, Chemical Engineering Journal, 432, 10.1016/j.cej.2021.134373, 2022c.

Lian, P., Guo, L., Devarajan, D., Parks, J. M., Painter, S. L., Brooks, S. C., and Smith, J. C.: The AQUA-MER databases and aqueous speciation server: A web resource for multiscale modeling of mercury speciation, Journal of Computational Chemistry, 41, 147-155, 10.1002/jcc.26081, 2020.

Lide, D. R. (Ed.) CRC Handbook of Chemistry and Physics, 89th Ed., CRC Press/Taylor and Francis, Boca Raton, FL, 2008.

Lin, C.-J., Singhasuk, P., and Pehkonen, S. O.: Atmospheric Chemistry of Mercury, in: Environmental Chemistry and Toxicology of Mercury, edited by: Liu, G., Cai, Y., and O'Driscoll, N., John Wiley & Sons, 113 - 154, 2011.

Lin, C.-J., Zhu, W., Li, X., Feng, X., Sommar, J., and Shang, L.: Novel Dynamic Flux Chamber for Measuring Air-Surface Exchange of Hg⁰ from Soils, Environmental Science & Technology, 46, 8910-8920, 10.1021/es3012386, 2012.

Lin, C. J. and Pehkonen, S. O.: Aqueous free radical chemistry of mercury in the presence of iron oxides and ambient aerosol, Atmospheric Environment, 31, 4125-4137, 1997.

Lin, C. J. and Pehkonen, S. O.: Two-phase model of mercury chemistry in the atmosphere, Atmospheric Environment, 32, 2543-2558, 1998a.

Lin, C. J. and Pehkonen, S. O.: Oxidation of elemental mercury by aqueous chlorine (HOCl/OCl⁻): Implications for tropospheric mercury chemistry, Journal of Geophysical Research-Atmospheres, 103, 28093-28102, 1998b.

Lin, C. J. and Pehkonen, S. O.: The chemistry of atmospheric mercury: A review, Atmospheric Environment, 33, 2067-2079, 1999.

Lin, C. J., Pongprueksa, P., Lindberg, S. E., Pehkonen, S. O., Byun, D., and Jang, C.: Scientific uncertainties in atmospheric mercury models I: Model science evaluation, Atmospheric Environment, 40, 2911-2928, 2006.

Lin, C. J., Pongprueksa, P., Russell Bullock Jr, O., Lindberg, S. E., Pehkonen, S. O., Jang, C., Braverman, T., and Ho, T. C.: Scientific uncertainties in atmospheric mercury models II: Sensitivity analysis in the CONUS domain, Atmospheric Environment, 41, 6544-6560, 2007.

Lin, M. and Thiemens, M. H.: 40 years of theoretical advances in mass-independent oxygen isotope effects and applications in atmospheric chemistry: A critical review and perspectives, Applied Geochemistry, 161, 10.1016/j.apgeochem.2023.105860, 2024.

Lindberg, S. E. and Stratton, W. J.: Atmospheric mercury speciation: Concentrations and behavior of reactive gaseous mercury in ambient air, Environmental Science & Technology, 32, 49-57, 1998.

Lindberg, S. E., Southworth, G., Prestbo, E. M., Wallschlager, D., Bogle, M. A., and Price, J.: Gaseous methyl- and inorganic mercury in landfill gas from landfills in Florida, Minnesota, Delaware, and California, Atmospheric Environment, 39, 249-258, 2005.

Lindqvist, O. and Rodhe, H.: Atmospheric Mercury - A Review, Tellus Series B, 37, 136-159, 1985.

Lindqvist, O., Johansson, K., Aastrup, M., Andersson, A., Bringmark, L., Hovsenius, G., Håkanson, L., Iverfeldt, Å., Meili, M., and Timm, B.: Mercury in the Swedish Environment - Recent Research on Causes, Consequences and Corrective Methods, Water Air and Soil Pollution, 55, 1-261, 1991.

Liu, E., Makarov, I. E., and Pikaev, A. K.: Pulse-radiolysis of alkaline aqueous-solutions of divalent mercury compounds, High Energy Chemistry, 17, 41-46, 1983.

Liu, K., Wu, Q., Wang, S., Chang, X., Tang, Y., Wang, L., Liu, T., Zhang, L., Zhao, Y., Wang, Q. g., and Chen, J.: Improved atmospheric mercury simulation using updated gas-particle partition and organic aerosol concentrations, Journal of Environmental Sciences, 119, 106-118, 10.1016/j.jes.2022.04.007, 2022.

Liu, Q. and Margerum, D. W.: Equilibrium and kinetics of bromine chloride hydrolysis, Environmental Science & Technology, 35, 1127-1133, 2001.

Liu, T.: Oxidation of aqueous elemental mercury through the Fenton reaction, M Sc. Thesis, Tennessee Technological University, USA, 106 pp., 2011.

Liu, Y., Lin, C.-J., Yuan, W., Lu, Z., and Feng, X.: Translocation and distribution of mercury in biomasses from subtropical forest ecosystems: evidence from stable mercury isotopes, Acta Geochimica, 40, 42-50, 10.1007/s11631-020-00441-3, 2021a.

2800   Liu, Y., Liu, H., Guo, Y., lu, D., Hou, X., Shi, J., Yin, Y., Cai, Y., and Jiang, G.: Atmospheric Hg(0) dry deposition over environmental surfaces: Insights from mercury isotope fractionation, Eco-Environment & Health, 10.1016/j.eehl.2024.04.009, 2024.

Liu, Y., Tao, H., Wang, Y., Fang, Y., Xiang, Y., Liu, G., Guo, Y., Liu, J., Yin, Y., Cai, Y., and Jiang, G.: Gaseous Elemental Mercury [Hg$^{(0)}$] Oxidation in Poplar Leaves through a Two-Step Single-Electron Transfer Process, Environmental Science & Technology Letters, 8, 1098-1103, 10.1021/acs.estlett.1c00735, 2021b.

Love, L. O.: Electromagnetic Separation of Isotopes at Oak Ridge, Science, 182, 343-352, 10.1126/science.182.4110.343, 1973.

Lu, X., Zhao, J., Liang, X., Zhang, L., Liu, Y., Yin, X., Li, X., and Gu, B.: The Application and Potential Artifacts of Zeeman Cold Vapor Atomic Absorption Spectrometry in Mercury Stable Isotope Analysis, Environmental Science & Technology Letters, 6, 165-170, 10.1021/acs.estlett.9b00067, 2019.

2810   Lyman, S. and Jaffe, D.: Formation and fate of oxidized mercury in the upper troposphere and lower stratosphere, Nature Geoscience, 5, 114 - 117, 2012.

Lyman, S. N., Jaffe, D. A., and Gustin, M. S.: Release of mercury halides from KCl denuders in the presence of ozone, Atmospheric Chemistry and Physics, 10, 8197-8204, 10.5194/acp-10-8197-2010, 2010.

Lyman, S. N., Cheng, I., Gratz, L. E., Weiss-Penzias, P., and Zhang, L.: An updated review of atmospheric mercury, Science of
2815   The Total Environment, 707, 135575, 2020a.

Lyman, S. N., Gratz, L. E., Dunham-Cheatham, S. M., Gustin, M. S., and Luippold, A.: Improvements to the Accuracy of Atmospheric Oxidized Mercury Measurements, Environmental Science & Technology, 54, 13379-13388, 10.1021/acs.est.0c02747, 2020b.

Lyman, S. N., Elgiar, T., Gustin, M. S., Dunham-Cheatham, S. M., David, L. M., and Zhang, L.: Evidence against Rapid
2820   Mercury Oxidation in Photochemical Smog, Environmental Science & Technology, 10.1021/acs.est.2c02224, 2022.

Maguire, R. J. and Anand, S.: Kinetics of Acidolysis of Dimethyl Mercury, Journal of Inorganic & Nuclear Chemistry, 38, 1167-1169, 1976.

Malcolm, E. G., Keeler, G. J., Lawson, S. T., and Sherbatskoy, T. D.: Mercury and trace elements in cloud water and precipitation collected on Mt. Mansfield, Vermont, Journal of Environmental Monitoring, 5, 584-590, 2003.

2825   Malcolm, E. G., Ford, A. C., Redding, T. A., Richardson, M. C., Strain, B. M., and Tetzner, S. W.: Experimental investigation of the scavenging of gaseous mercury by sea salt aerosol, Journal of Atmospheric Chemistry, 63, 221-234, 2009.

Malinovsky, D. and Vanhaecke, F.: Mercury isotope fractionation during abiotic transmethylation reactions, International Journal of Mass Spectrometry, 307, 214-224, 2011.

Malinovsky, D., Latruwe, K., Moens, L., and Vanhaecke, F.: Experimental study of mass-independence of Hg isotope
2830   fractionation during photodecomposition of dissolved methylmercury, Journal of Analytical Atomic Spectrometry, 25, 950-956, 2010.

Mangiante, D. M., Schaller, R. D., Zarzycki, P., Banfield, J. F., and Gilbert, B.: Mechanism of Ferric Oxalate Photolysis, ACS Earth and Space Chemistry, 1, 270-276, 10.1021/acsearthspacechem.7b00026, 2017.

Mao, H., Cheng, I., and Zhang, L.: Current understanding of the driving mechanisms for spatiotemporal variations of
2835   atmospheric speciated mercury: a review, Atmospheric Chemistry and Physics, 16, 12897-12924, 10.5194/acp-16-12897-2016, 2016.

Mao, H., Talbot, R. W., Sigler, J. M., Sive, B. C., and Hegarty, J. D.: Seasonal and diurnal variations of Hg^0 over New England, Atmospheric Chemistry and Physics, 8, 1401-1421, 2008.

Mao, N. and Khalizov, A.: Exchange Reactions Alter Molecular Speciation of Gaseous Oxidized Mercury, ACS Earth and
2840   Space Chemistry, 5, 10.1021/acsearthspacechem.1c00178, 2021.

Mao, N., Antley, J., Cooper, M., Shah, N., Kadam, A., and Khalizov, A.: Heterogeneous Chemistry of Mercuric Chloride on Inorganic Salt Surfaces, The Journal of Physical Chemistry A, 125, 10.1021/acs.jpca.1c02220, 2021.

Mariotti, A., Germon, J. C., Hubert, P., Kaiser, P., Letolle, R., Tardieux, A., and Tardieux, P.: Experimental-Determination of Nitrogen Kinetic Isotope Fractionation - Some Principles - Illustration for the Denitrification and Nitrification Processes, Plant
2845   and Soil, 62, 413-430, 10.1007/Bf02374138, 1981.

Martell, A. and Smith, R. M.: Critical stability constants: Other Organic Ligands, Critical stability constants, Springer, 495 pp.1977.

Martell, A. E. and Smith, R. M.: Critical stability constants: Vol. 4 Inorganic complexes, Plenum Pr., New York u.a.1976.

Martell, A. E. and Smith, R. M.: Critical stability constants: Vol. 5 First Supplement, 1982.

2850   Maya, J.: Ultraviolet-Absorption Cross-Sections of HgI$_2$, HgBr$_2$, and Tin(II) Halide Vapors, Journal of Chemical Physics, 67, 4976-4980, 1977.

McClure, C. D., Jaffe, D. A., and Edgerton, E. S.: Evaluation of the KCl denuder method for gaseous oxidized mercury using HgBr$_2$ at an in-service AMNet site, Environmental Science & Technology, 48, 11437-11444, 2014.

2855   McElroy, W. J. and Munthe, J.: The oxidation of mercury(I) by ozone in acidic aqueous solutions, Acta Chemica Scandinavica, 45, 254-257, 10.3891/acta.chem.scand.45-0254, 1991.

McKeown, F. P., Iyer, R. S., and Rowland, F. S.: Methyl fluoride formation from thermal ^{18}F reaction with dimethylmercury, Journal of Physical Chemistry, 87, 3972-3975, 10.1021/j100243a035, 1983.

Mead, C., Lyons, J. R., Johnson, T. M., and Anbar, A. D.: Unique Hg Stable Isotope Signatures of Compact Fluorescent Lamp-Sourced Hg, Environmental Science & Technology, 47, 2542-2547, 2013.

2860   Medhekar, A. K., Rokni, M., Trainor, D. W., and Jacob, J. H.: Surface Catalyzed Reaction of Hg + Cl$_2$, Chemical Physics Letters, 65, 600-604, 1979.

Miller, M. B., Dunham-Cheatham, S. M., Gustin, M. S., and Edwards, G. C.: Evaluation of cation exchange membrane performance under exposure to high Hg0 and HgBr2 concentrations, Atmospheric Measurement Techniques, 12, 1207-1217, 10.5194/amt-12-1207-2019, 2019.

2865   Morand, J.-P. and Nief, G.: Oxydation isotopique du mercure par l'oxygène moléculaire sous l'influence de la radiation 2357 Å, J. Chim. Phys., 65, 2058-2068, 10.1051/jcp/1968652058, 1968.

Morton, D. C.: Atomic-data for resonance absorption lines. II. Wavelengths longward of the lyman limit for heavy elements, Astrophysical Journal Supplement Series, 130, 403-436, 2000.

Moser, H. C. and Voigt, A. F.: Dismutation of the Mercurous Dimer in Dilute Solutions, Journal of the American Chemical
2870   Society, 79, 1837-1839, 10.1021/ja01565a019, 1957.

Motta, L. C., Chien, A. D., Rask, A. E., and Zimmerman, P. M.: Mercury Magnetic Isotope Effect: A Plausible Photochemical Mechanism, Journal of Physical Chemistry A, 124, 3711-3719, 2020a.

Motta, L. C., Kritee, K., Blum, J. D., Tsz-Ki Tsui, M., and Reinfelder, J. R.: Mercury Isotope Fractionation during the Photochemical Reduction of Hg(II) Coordinated with Organic Ligands, Journal of Physical Chemistry A, 124, 2842-2853,
2875   2020b.

Motta, L. C., Blum, J. D., Johnson, M. W., Umhau, B. P., Popp, B. N., Washburn, S. J., Drazen, J. C., Benitez-Nelson, C. R., Hannides, C. C. S., Close, H. G., and Lamborg, C. H.: Mercury Cycling in the North Pacific Subtropical Gyre as Revealed by Mercury Stable Isotope Ratios, Global Biogeochemical Cycles, 33, 777-794, 2019.

Mulliken, R. S.: The separation of isotopes application of systematic fractionation to mercury in a high-speed evaporation-
2880   diffusion apparatus, Journal of the American Chemical Society, 45, 1592-1604, 10.1021/ja01660a003, 1923.

Munthe, J.: The aqueous oxidation of elemental mercury by ozone, Atmospheric Environment. Part A, 26, 1461-1468, 10.1016/0960-1686(92)90131-4, 1992.

Munthe, J. and McElroy, W. J.: Some aqueous reactions of potential importance in the atmospheric chemistry of mercury, Atmospheric Environment Part A, 26, 553-557, 10.1016/0960-1686(92)90168-k, 1992.

2885   Munthe, J., Xiao, Z. F., and Lindqvist, O.: The Aqueous Reduction of Divalent Mercury by Sulfite, Water Air and Soil Pollution, 56, 621-630, 1991.

Murphy, D. M., Hudson, P. K., Thomson, D. S., Sheridan, P. J., and Wilson, J. C.: Observations of mercury-containing aerosols, Environmental Science & Technology, 40, 3163-3167, 2006.

Nazhat, N. B. and Asmus, K. D.: Reduction of Mercuric Chloride by Hydrated Electrons and Reducing Radicals in Aqueous-
2890   Solutions - Formation and Reactions of HgCl, Journal of Physical Chemistry, 77, 614-620, 1973.

Nerentorp Mastromonaco, M., Gårdfeldt, K., Jourdain, B., Abrahamsson, K., Granfors, A., Ahnoff, M., Dommergue, A., Méjean, G., and Jacobi, H. W.: Antarctic winter mercury and ozone depletion events over sea ice, Atmospheric Environment, 129, 125-132, 10.1016/j.atmosenv.2016.01.023, 2016.

Niki, H., Maker, P. D., Savage, C. M., and Breitenbach, L. P.: A Long-Path Fourier-Transform Infrared Study of the Kinetics
2895   and Mechanism for the HO-Radical Initiated Oxidation of Dimethylmercury, Journal of Physical Chemistry, 87, 4978-4981, 1983a.

Niki, H., Maker, P. S., Savage, C. M., and Breitenbach, L. P.: A Fourier-Transform Infrared Study of the Kinetics and Mechanism for the Reaction Cl + CH$_3$HgCH$_3$, Journal of Physical Chemistry, 87, 3722-3724, 1983b.

Niksa, S., Helble, J. J., and Fujiwara, N.: Kinetic modeling of homogeneous mercury oxidation: The importance of NO and H$_2$O
2900   in predicting oxidation in coal- derived systems, Environmental Science & Technology, 35, 3701-3706, 2001.

Nriagu, J. (Ed.) The biogeochemistry of mercury in the environment, Elsevier/North- Holland Biomedical Press, 671 pp., 1979.

O'Concubhair, R., O'Sullivan, D., and Sodeau, J. R.: Dark Oxidation of Dissolved Gaseous Mercury in Polar Ice Mimics, Environmental Science & Technology, 46, 4829-4836, 10.1021/es300309n, 2012.

Obrist, D., Pokharel, A. K., and Moore, C.: Vertical profile measurements of soil air suggest immobilization of gaseous
2905   elemental mercury in mineral soil, Environmental Science & Technology, 48, 2242-2252, 2014.

Obrist, D., Tas, E., Peleg, M., Matveev, V., Fain, X., Asaf, D., and Luria, M.: Bromine-induced oxidation of mercury in the mid-latitude atmosphere, Nature Geoscience, 4, 22-26, 2011.

Obrist, D., Agnan, Y., Jiskra, M., Olson, C. L., Colegrove, D. P., Hüber, J., Moore, C. W., Sonke, J. E., and Helmig, D.: Tundra uptake of atmospheric elemental mercury drives Arctic mercury pollution, Nature, 547, 201-204, 10.1038/nature22997, 2017.

2910   Obrist, D., Roy, E. M., Harrison, J. L., Kwong, C. F., Munger, J. W., Moosmüller, H., Romero, C. D., Sun, S., Zhou, J., and Commane, R.: Previously unaccounted atmospheric mercury deposition in a midlatitude deciduous forest, Proceedings of the National Academy of Sciences, 118, e2105477118, 10.1073/pnas.2105477118, 2021.

Ogata, M. and Aikoh, H.: Mechanism of metallic mercury oxidation in vitro by catalase and peroxidase, Biochemical Pharmacology, 33, 490-493, 10.1016/0006-2952(84)90246-6, 1984.

2915   Ogg, R. A., Martin, H. C., and Leighton, P. A.: Kinetics of the vapor phase reaction of mercury and halogens, Journal of the American Chemical Society, 58, 1922-1924, 10.1021/ja01301a026, 1936.

Olson, C. L., Jiskra, M., Sonke, J. E., and Obrist, D.: Mercury in tundra vegetation of Alaska: Spatial and temporal dynamics and stable isotope patterns, Science of the Total Environment, 660, 1502-1512, 10.1016/j.scitotenv.2019.01.058, 2019.

Osterwalder, S., Eugster, W., Feigenwinter, I., and Jiskra, M.: Eddy covariance flux measurements of gaseous elemental
2920   mercury over a grassland, Atmospheric Measurement Techniques, 13, 2057-2074, 10.5194/amt-13-2057-2020, 2020.

Osterwalder, S., Nerentorp, M., Zhu, W., Jiskra, M., Nilsson, E., Nilsson, M. B., Rutgersson, A., Soerensen, A. L., Sommar, J., Wallin, M. B., Wängberg, I., and Bishop, K.: Critical Observations of Gaseous Elemental Mercury Air-Sea Exchange, Global Biogeochemical Cycles, 35, e2020GB006742, 10.1029/2020GB006742, 2021.

Pal, B. and Ariya, P. A.: Gas-Phase HO-Initiated Reactions of Elemental Mercury: Kinetics, Product Studies, and Atmospheric
2925   Implications, Environmental Science & Technology, 38, 5555-5566, 2004a.

Pal, B. and Ariya, P. A.: Studies of ozone initiated reactions of gaseous mercury: kinetics, product studies, and atmospheric implications, Physical Chemistry Chemical Physics, 6, 572-579, 2004b.

Pankow, J. F.: An absorption model of the gas/aerosol partitioning involved in the formation of secondary organic aerosol, Atmospheric Environment, 41, 75-79, https://doi.org/10.1016/j.atmosenv.2007.10.060, 2007.

2930   Parks, J. M., Johs, A., Podar, M., Bridou, R., Hurt, R. A., Smith, S. D., Tomanicek, S. J., Qian, Y., Brown, S. D., Brandt, C. C., Palumbo, A. V., Smith, J. C., Wall, J. D., Elias, D. A., and Liang, L.: The Genetic Basis for Bacterial Mercury Methylation, Science, 339, 1332-1335, doi:10.1126/science.1230667, 2013.

Pasakarnis, T., Boyanov, M., Kemner, K., Mishra, B., O'Loughlin, E., Parkin, G., and Scherer, M.: Influence of Chloride and Fe(II) Content on the Reduction of Hg(II) by Magnetite, Environmental Science & Technology, 47, 10.1021/es304761u, 2013.

2935   Pehkonen, S. O. and Lin, C. J.: Aqueous photochemistry of mercury with organic acids, Journal of the Air & Waste Management Association, 48, 144-150, 1998.

Peleg, M., Tas, E., Obrist, D., Matveev, V., Moore, C., Gabay, M., and Luria, M.: Observational Evidence for Involvement of Nitrate Radicals in Nighttime Oxidation of Mercury, Environ. Sci. Technol., 49, 14008-14018, 10.1021/acs.est.5b03894, 2015.

Pertel, R. and Gunning, H. E.: Photochemical separation of mercury isotopes 2. The reaction of ^{202}Hg(6^3P_1) atoms, photoexcited
2940   in natural mercury vapor, with water vapor and other HgO-forming substrates, Canadian Journal of Chemistry-Revue Canadienne De Chimie, 37, 35-42, 1959.

Peterson, K. A., Shepler, B. C., and Singleton, J. M.: The group 12 metal chalcogenides: an accurate multireference configuration interaction and coupled cluster study, Molecular Physics, 105, 1139-1155, 2007.

Pikaev, A. K., Sibirskaya, G. K., and Spitsyn, V. I.: Pulse radiolysis of aqueous solutions of bivalent mercury compounds,
2945   Doklady Akademii Nauk SSSR, 224, 638-641, 1975.

Pleijel, K. and Munthe, J.: Modeling the atmospheric chemistry of mercury, Water, Air, & Soil Pollution, 80, 317324, 10.1007/BF01189681, 1995.

Pliss, E. M., Grobov, A. M., Kuzaev, A. K., and Buchachenko, A. L.: Magnetic field effect on the oxidation of organic substances by molecular oxygen, Journal of Physical Organic Chemistry, 32, 10.1002/poc.3915, 2019.

2950   Poissant, L., Amyot, M., Kwan, M., and Bégin, M.: Atmospheric mercury transport, oxidation and fallout in northern Québec (Nunavik): an important potential route of contamination., Environment Canada, Montréal, Northern Contaminants Program, Synopsis of Research 2000-2001, Indian and Northern Affairs Canada, 125-129, 2001.

Poissant, L., Pilote, M., Yumvihoze, E., and Lean, D.: Mercury concentrations and foliage/atmosphere fluxes in a maple forest ecosystem in Quebec, Canada, 10.1029/2007jd009510, 2008.

2955   Pongratz, R. and Heumann, K. G.: Production of methylated mercury, lead, and cadmium by marine bacteria as a significant natural source for atmospheric heavy metals in polar regions, Chemosphere, 39, 89-102, 1999.

Poulain, A. J., Lalonde, J. D., Amyot, M., Shead, J. A., Raofie, F., and Ariya, P. A.: Redox transformations of mercury in an Arctic snowpack at springtime, Atmospheric Environment, 38, 6763-6774, 10.1016/j.atmosenv.2004.09.013, 2004.

Powell, K. J., Brown, P. L., Byrne, R. H., Gajda, T., Hefter, G. T., Sjöberg, S., and Wanner, H.: Chemical speciation of
2960   environmentally significant heavy metals with inorganic ligands. Part 1: The Hg^{2+}– Cl^-, OH^-, CO_3^{2-}, SO_4^{2-}, and PO_4^{3-} aqueous systems, Pure and Applied Chemistry, 77, 739-800, 2005.

Puigdomenech, I.: SPANA and DATABASE (modified JAVA versions of earlier software MEDUSA, HYDRA and INPUT-SED-PREDOM) Dept. of Inorganic Chemistry, Royal Institute of Technology (KTH), 2013.

Pyykkö, P.: Relativistic Effects in Structural Chemistry, Chemical Reviews, 88, 10.1021/cr00085a006, 1988.

2965   Qiu, Y., Gai, P., Yue, F., Zhang, Y., He, P., Kang, H., Yu, X., Chen, J., and Xie, Z.: Potential factors impacting PM$_{2.5}$-Hg

during haze evolution revealed by mercury isotope: Emission sources and photochemical processes, Atmospheric Research, 277, 10.1016/j.atmosres.2022.106318, 2022.

Qu, Z., Yan, N. Q., Liu, P., Chi, Y. P., and Jia, J.: Bromine Chloride as an Oxidant to Improve Elemental Mercury Removal from Coal-Fired Flue Gas, Environmental Science & Technology, 43, 8610-8615, 10.1021/es901803s, 2009.

2970 Raofie, F. and Ariya, P. A.: Product study of the gas-phase BrO-initiated oxidation of Hg^0: evidence for stable Hg^{1+} compounds, Environmental Science & Technology, 38, 4319-4326, 2004.

Raofie, F., Snider, G., and Ariya, P. A.: Reaction of gaseous mercury with molecular iodine, atomic iodine, and iodine oxide radicals - Kinetics, product studies, and atmospheric implications, Canadian Journal of Chemistry-Revue Canadienne De Chimie, 86, 811-820, 10.1139/v08-088, 2008.

2975 Riccardi, D., Guo, H.-B., Parks, J. M., Gu, B., Summers, A. O., Miller, S. M., Liang, L., and Smith, J. C.: Why Mercury Prefers Soft Ligands, Journal of Physical Chemistry Letters, 4, 2317-2322, 10.1021/jz401075b, 2013.

Richard, J. H., Bischoff, C., Ahrens, C. G. M., and Biester, H.: Mercury (II) reduction and co-precipitation of metallic mercury on hydrous ferric oxide in contaminated groundwater, Science of the Total Environment, 539, 36-44, 10.1016/j.scitotenv.2015.08.116, 2016.

2980 Rolison, J. M., Landing, W. M., Luke, W., Cohen, M., and Salters, V. J. M.: Isotopic composition of species-specific atmospheric Hg in a coastal environment, Chemical Geology, 336, 37-49, 2013.

Rose, C. H., Ghosh, S., Blum, J. D., and Bergquist, B. A.: Effects of ultraviolet radiation on mercury isotope fractionation during photo-reduction for inorganic and organic mercury species, Chemical Geology, 405, 102-111, 10.1016/j.chemgeo.2015.02.025, 2015.

2985 Rosenthal, J. E. and Breit, G.: The isotope shift in hyperfine structure, Physical Review, 41, 459-470, 10.1103/PhysRev.41.459, 1932.

Rutter, A. P. and Schauer, J. J.: The impact of aerosol composition on the particle to gas partitioning of reactive mercury, Environmental Science & Technology, 41, 3934-3939, 2007a.

Rutter, A. P. and Schauer, J. J.: The effect of temperature on the gas-particle partitioning of reactive mercury in atmospheric 2990 aerosols, Atmospheric Environment, 41, 8647-8657, 10.1016/J.Atmosenv.2007.07.024, 2007b.

Rutter, A. P., Shakya, K. M., Lehr, R., Schauer, J. J., and Griffin, R. J.: Oxidation of gaseous elemental mercury in the presence of secondary organic aerosols, Atmospheric Environment, 59, 86-92, 10.1016/j.atmosenv.2012.05.009, 2012.

Saiz-Lopez, A., Sitkiewicz, S. P., Roca-Sanjuán, D., Oliva-Enrich, J. M., Dávalos, J. Z., Notario, R., Jiskra, M., Xu, Y., Wang, F., Thackray, C. P., Sunderland, E. M., Jacob, D. J., Travnikov, O., Cuevas, C. A., Acuña, A. U., Rivero, D., Plane, J. M. C., 2995 Kinnison, D. E., and Sonke, J. E.: Photoreduction of gaseous oxidized mercury changes global atmospheric mercury speciation, transport and deposition, Nature Communications, 9, 4796, 2018.

Saiz-Lopez, A., Ulises Acuna, A., Trabelsi, T., Carmona-Garcia, J., Davalos, J. Z., Rivero, D., Cuevas, C. A., Kinnison, D. E., Sitkiewicz, S. P., Roca-Sanjuan, D., and Francisco, J. S.: Gas-Phase Photolysis of Hg(I) Radical Species: A New Atmospheric Mercury Reduction Process, Journal of the American Chemical Society, 141, 8698-8702, 10.1021/jacs.9b02890, 2019.

3000 Saiz-Lopez, A., Travnikov, O., Sonke, J. E., Thackray, C. P., Jacob, D. J., Carmona-Garcia, J., Frances-Monerris, A., Roca-Sanjuan, D., Acuna, A. U., Davalos, J. Z., Cuevas, C. A., Jiskra, M., Wang, F., Bieser, J., Plane, J. M. C., and Francisco, J. S.: Photochemistry of oxidized Hg(I) and Hg(II) species suggests missing mercury oxidation in the troposphere, Proceedings of the National Academy of Sciences of the United States of America, 117, 30949-30956, 2020.

Saiz-Lopez, A., Acuña, A., Mahajan, A., Dávalos, J., Wuhu, F., Roca-Sanjuán, D., Carmona-García, J., Cuevas, C. A., 3005 Kinnison, D., Gomez Martin, J. C., Francisco, J., and Plane, J.: The Chemistry of Mercury in the Stratosphere, Geophysical Research Letters, 49, e2022GL097953, 10.1029/2022GL097953, 2022.

Saiz-Lopez, A., Cuevas, C. A., Acuña, A. U., Añel, J. A., Mahajan, A. S., de la Torre, L., Feng, W., Dávalos, J. Z., Roca-Sanjuán, D., Kinnison, D. E., Carmona-García, J., Fernandez, R. P., Li, Q., Sonke, J. E., Feinberg, A., Martín, J. C. G., Villamayor, J., Zhang, P., Zhang, Y., Blaszczak-Boxe, C. S., Travnikov, O., Wang, F., Bieser, J., Francisco, J. S., and Plane, J. M. C.: Role of 3010 the stratosphere in the global mercury cycle, Science Advances, 11, eads1459, 10.1126/sciadv.ads1459, 2025.

Salter, C., Tellinghuisen, P. C., Ashmore, J. G., and Tellinghuisen, J.: The emission spectrum of $^{200}Hg^{127}I$, Journal of Molecular Spectroscopy, 120, 334-358, 10.1016/0022-2852(86)90009-3, 1986.

Sander, R.: Modeling Atmospheric Chemistry: Interactions between Gas-Phase Species and Liquid Cloud/Aerosol Particles, Surveys in Geophysics, 20, 1-31, 10.1023/A:1006501706704, 1999.

3015 Sanemasa, I.: Solubility of Elemental Mercury-Vapor in Water, Bulletin of the Chemical Society of Japan, 48, 1795-1798, DOI 10.1246/bcsj.48.1795, 1975.

Schartup, A. T., Soerensen, A. L., and Heimburger-Boavida, L. E.: Influence of the Arctic Sea-Ice Regime Shift on Sea-Ice Methylated Mercury Trends, Environmental Science & Technology Letters, 7, 708-713, 10.1021/acs.estlett.0c00465, 2020.

Schauble, E. A.: Role of nuclear volume in driving equilibrium stable isotope fractionation of mercury, thallium, and other very 3020 heavy elements, Geochimica Et Cosmochimica Acta, 71, 2170-2189, 2007.

Schmolke, S. R., Schroeder, W. H., Kock, H. H., Schneeberger, D., Munthe, J., and Ebinghaus, R.: Simultaneous measurements of total gaseous mercury at four sites on a 800 km transect: spatial distribution and short-time variability of total gaseous

mercury over central Europe, Atmospheric Environment, 33, 1725-1733, 1999.

Schroeder, W. H. and Munthe, J.: Atmospheric mercury - An overview, Atmospheric Environment, 32, 809-822, 1998.

3025 Schroeder, W. H., Yarwood, G., and Niki, H.: Transformation Processes Involving Mercury Species in the Atmosphere - Results from a Literature Survey, Water Air and Soil Pollution, 56, 653-666, 1991.

Schroeder, W. H., Anlauf, K. G., Barrie, L. A., Lu, J. Y., Steffen, A., Schneeberger, D. R., and Berg, T.: Arctic springtime depletion of mercury, Nature, 394, 331-332, 1998.

Schwab, L., Gallati, N., Reiter, S. M., Kimber, R. L., Kumar, N., McLagan, D. S., Biester, H., Kraemer, S. M., and Wiederhold,
3030 J. G.: Mercury Isotope Fractionation during Dark Abiotic Reduction of Hg(II) by Dissolved, Surface-Bound, and Structural Fe(II), Environmental Science & Technology, 57, 15243-15254, 10.1021/acs.est.3c03703, 2023.

Schwartz, S. E.: Mass-transport considerations pertinent to aqueous phase reactions of gases in liquid-water clouds, in: Chemistry of Multiphase Atmospheric Systems, edited by: Jäschke, W., NATO ASI Series, G6, Springer-Verlag Berlin Heidelberg, 415-471, 1986.

3035 Scott, S. L., Yusuf, H., Lahoutifard, N., and Maunder, K.: Homogeneous and heterogeneous reactions of atmospheric mercury(II) with sulfur(IV), Journal De Physique IV, 107, 1201-1204, 2003.

Seigneur, C., Wrobel, J., and Constantinou, E.: A chemical kinetic mechanism for atmospheric inorganic mercury, Environmental Science & Technology, 28, 1589-1597, 1994.

Sexauer Gustin, M., Pierce, A. M., Huang, J., Miller, M. B., Holmes, H. A., and Loria-Salazar, S. M.: Evidence for Different
3040 Reactive Hg Sources and Chemical Compounds at Adjacent Valley and High Elevation Locations, Environmental Science & Technology, 50, 12225-12231, 10.1021/acs.est.6b03339, 2016.

Shah, V., Jacob, D., Thackray, C., Wang, X., Sunderland, E., Dibble, T., Saiz-Lopez, A., Cernusak, I., Kellö, V., Castro, P., Wu, R., and Wang, C.: Improved Mechanistic Model of the Atmospheric Redox Chemistry of Mercury, Environmental Science & Technology, 55, 14445 - 14456, 2021.

3045 Shah, V., Jaeglé, L., Gratz, L. E., Ambrose, J. L., Jaffe, D. A., Selin, N. E., Song, S., Campos, T. L., Flocke, F. M., Reeves, M., Stechman, D., Stell, M., Festa, J., Stutz, J., Weinheimer, A. J., Knapp, D. J., Montzka, D. D., Tyndall, G. S., Apel, E. C., Hornbrook, R. S., Hills, A. J., Riemer, D. D., Blake, N. J., Cantrell, C. A., and Mauldin, R. L.: Origin of oxidized mercury in the summertime free troposphere over the southeastern US, Atmospheric Chemistry and Physics, 16, 1511-1530, 10.5194/acp-16-1511-2016, 2016.

3050 Shepler, B. C.: Ab Initio Investigation of the thermochemistry, spectroscopy and dynamics of reactions between mercury and reactive halogen species, Ph. D. thesis, Department of Chemistry, Washington State University, Pullman, WA, 289 pp., 2006.

Shepler, B. C. and Peterson, K. A.: Mercury Monoxide: A Systematic Investigation of Its Ground Electronic State, Journal of Physical Chemistry A, 107, 1783-1787, 2003.

Shepler, B. C., Balabanov, N. B., and Peterson, K. A.: Ab Initio Thermochemistry Involving Heavy Atoms: An Investigation of
3055 the Reactions Hg + IX (X = I, Br, Cl, O), Journal of Physical Chemistry A, 109, 10363 - 10372, 2005.

Shepler, B. C., Balabanov, N. B., and Peterson, K. A.: Hg + Br → HgBr recombination and collision-induced dissociation dynamics, Journal of Chemical Physics, 127, 164304; 10.1063/1.27771422007, 2007.

Sherman, L. S., Blum, J. D., Dvonch, J. T., Gratz, L. E., and Landis, M. S.: The use of Pb, Sr, and Hg isotopes in Great Lakes precipitation as a tool for pollution source attribution, Science of the Total Environment, 502, 362-374, 2015.

3060 Sherman, L. S., Blum, J. D., Keeler, G. J., Demers, J. D., and Dvonch, J. T.: Investigation of Local Mercury Deposition from a Coal-Fired Power Plant Using Mercury Isotopes, Environmental Science & Technology, 46, 382-390, 2012.

Sherman, L. S., Blum, J. D., Johnson, K. P., Keeler, G. J., Barres, J. A., and Douglas, T. A.: Mass-independent fractionation of mercury isotopes in Arctic snow driven by sunlight., Nature Geoscience, 3, 173–177, 2010.

Sholupov, S., Pogarev, S., Ryzhov, V., Mashyanov, N., and Stroganov, A.: Zeeman atomic absorption spectrometer RA-
3065 915+for direct determination of mercury in air and complex matrix samples, Fuel Processing Technology, 85, 473-485, 2004.

Si, L. and Ariya, P.: Recent Advances in Atmospheric Chemistry of Mercury, Atmosphere, 9, 76, 2018.

Si, L. and Ariya, P. A.: Reduction of Oxidized Mercury Species by Dicarboxylic Acids (C$_2$−C$_4$): Kinetic and Product Studies, Environmental Science & Technology, 42, 5150-5155, 10.1021/es800552z, 2008.

Si, L. and Ariya, P. A.: Aqueous photoreduction of oxidized mercury species in presence of selected alkanethiols,
3070 Chemosphere, 84, 1079-1084, 2011.

Si, L. and Ariya, P. A.: Photochemical reactions of divalent mercury with thioglycolic acid: Formation of mercuric sulfide particles, Chemosphere, 119, 467-472, 10.1016/j.chemosphere.2014.07.022, 2015.

Siegler, R. W., Nierenberg, D. W., and Hickey, W. F.: Fatal poisoning from liquid dimethylmercury: A neuropathologic study, Human Pathology, 30, 720-723, 10.1016/s0046-8177(99)90101-6, 1999.

3075 Sitkiewicz, S. P., Rivero, D., Oliva-Enrich, J. M., Saiz-Lopez, A., and Roca-Sanjuán, D.: Ab initio quantum-chemical computations of the absorption cross sections of HgX$_2$ and HgXY (X, Y = Cl, Br, and I): molecules of interest in the Earth's atmosphere, Physical Chemistry Chemical Physics, 21, 455-467, 10.1039/C8CP06160B, 2019.

Skyllberg, U.: Chemical speciation of mercury in soil and sediment, in: Advances in environmental chemistry and toxicology of

mercury edited by: Liu, G., Cai, Y., and O'Driscoll, N., John Wiley & Sons, 218-258, 2011.

3080   Slemr, F., Schuster, G., and Seiler, W.: Distribution, speciation, and budget of atmospheric mercury, Journal of Atmospheric Chemistry, 3, 407-434, 1985.

Slemr, F., Martin, L., Labuschagne, C., Mkololo, T., Angot, H., Magand, O., Dommergue, A., Garat, P., Ramonet, M., and Bieser, J.: Atmospheric mercury in the Southern Hemisphere – Part 1: Trend and inter-annual variations in atmospheric mercury at Cape Point, South Africa, in 2007–2017, and on Amsterdam Island in 2012–2017, Atmospheric Chemistry and
3085   Physics, 20, 7683-7692, 10.5194/acp-20-7683-2020, 2020.

Slemr, F., Weigelt, A., Ebinghaus, R., Kock, H. H., Bödewadt, J., Brenninkmeijer, C. A. M., Rauthe-Schöch, A., Weber, S., Hermann, M., Becker, J., Zahn, A., and Martinsson, B.: Atmospheric mercury measurements onboard the CARIBIC passenger aircraft, Atmospheric Measurement Techniques, 9, 2291-2302, 10.5194/amt-9-2291-2016, 2016.

Slemr, F., Weigelt, A., Ebinghaus, R., Bieser, J., Brenninkmeijer, C. A. M., Rauthe-Schoch, A., Hermann, M., Martinsson, B.
3090   G., van Velthoven, P., Bonisch, H., Neumaier, M., Zahn, A., and Ziereis, H.: Mercury distribution in the upper troposphere and lowermost stratosphere according to measurements by the IAGOS-CARIBIC observatory: 2014-2016, Atmospheric Chemistry and Physics, 18, 12329-12343, 2018.

Smith, R. M., Martell, A. E., and Motekaitis, R. J.: NIST Critically Selected Stability Constants of Metal Complexes Database, 2004.

3095   Smith, R. S., Wiederhold, J. G., and Kretzschmar, R.: Mercury Isotope Fractionation during Precipitation of Metacinnabar (β-HgS) and Montroydite (HgO), Environmental Science & Technology, 49, 4325-4334, 2015.

Snelson, A.: Infrared Matrix Isolation Spectrum of Methyl Radical Produced by Pyrolysis of Methyl Iodide and Dimethyl Mercury, Journal of Physical Chemistry, 74, 537-&, 10.1021/j100698a011, 1970.

Snider, G., Raofie, F., and Ariya, P. A.: Effects of relative humidity and CO(g) on the O_3-initiated oxidation reaction of $Hg^0(g)$:
3100   kinetic & product studies, Physical Chemistry Chemical Physics, 10, 5616-5623, 10.1039/b801226a, 2008.

Soerensen, A. L., Sunderland, E. M., Holmes, C. D., Jacob, D. J., Yantosca, R. M., Skov, H., Christensen, J. H., Strode, S. A., and Mason, R. P.: An Improved Global Model for Air-Sea Exchange of Mercury: High Concentrations over the North Atlantic, Environmental Science & Technology, 44, 8574-8580, 10.1021/es102032g, 2010.

Sommar, J., Feng, X. B., and Lindqvist, O.: Speciation of volatile mercury species present in digester and deposit gases,
3105   Applied Organometallic Chemistry, 13, 441-445, 1999.

Sommar, J., Hallquist, M., and Ljungstrom, E.: Rate of reaction between the nitrate radical and dimethyl mercury in the gas phase, Chemical Physics Letters, 257, 434-438, 1996.

Sommar, J., Lindqvist, O., and Strömberg, D.: Distribution equilibrium of mercury (II) chloride between water and air applied to flue gas scrubbing, Journal of the Air & Waste Management Association, 50, 1663-1666, 2000.

3110   Sommar, J., Osterwalder, S., and Zhu, W.: Recent advances in understanding and measurement of Hg in the environment: Surface-atmosphere exchange of gaseous elemental mercury (Hg^0), Science of The Total Environment, 721, 137648, 10.1016/j.scitotenv.2020.137648, 2020.

Sommar, J., Gårdfeldt, K., Strömberg, D., and Feng, X. B.: A kinetic study of the gas-phase reaction between the hydroxyl radical and atomic mercury, Atmospheric Environment, 35, 3049-3054, 2001.

3115   Sommar, J., Hallquist, M., Ljungstrom, E., and Lindqvist, O.: On the gas phase reactions between volatile biogenic mercury species and the nitrate radical, Journal of Atmospheric Chemistry, 27, 233-247, 1997.

Sommar, J., Wängberg, I., Berg, T., Gårdfeldt, K., Munthe, J., Richter, A., Urba, A., Wittrock, F., and Schroeder, W. H.: Circumpolar transport and air-surface exchange of atmospheric mercury at Ny-Ålesund (79ºN), Svalbard, spring 2002., Atmospheric Chemistry and Physics, 7, 151-166, 2007.

3120   Song, Z. C., Huang, S. J., Zhang, P., Yuan, T. F., and Zhang, Y. X.: Isotope Data Constrains Redox Chemistry of Atmospheric Mercury, Environmental Science & Technology, 10.1021/acs.est.4c02600, 2024.

Sonke, J. E., Angot, H., Zhang, Y., Poulain, A., Björn, E., and Schartup, A.: Global change effects on biogeochemical mercury cycling, Ambio, 52, 853-876, 10.1007/s13280-023-01855-y, 2023.

Spicer, C. W., Satola, J., Abbgy, A. A., Plastridge, R. A., and Cowen, K. A.: Kinetics of Gas-Phase Elemental Mercury
3125   Reactions with Halogen Species, Ozone, and Nitrate Radical under Atmospheric Conditions, Florida Department of Environmental Protection, 2002.

Sprovieri, F., Pirrone, N., Ebinghaus, R., Kock, H., and Dommergue, A.: A review of worldwide atmospheric mercury measurements, Atmospheric Chemistry and Physics, 10, 8245-8265, 2010.

Sprovieri, F., Pirrone, N., Bencardino, M., D'Amore, F., Angot, H., Barbante, C., Brunke, E. G., Arcega-Cabrera, F., Cairns,
3130   W., Comero, S., Diéguez, M. D. C., Dommergue, A., Ebinghaus, R., Feng, X. B., Fu, X., Garcia, P. E., Gawlik, B. M., Hageström, U., Hansson, K., Horvat, M., Kotnik, J., Labuschagne, C., Magand, O., Martin, L., Mashyanov, N., Mkololo, T., Munthe, J., Obolkin, V., Ramirez Islas, M., Sena, F., Somerset, V., Spandow, P., Vardè, M., Walters, C., Wängberg, I., Weigelt, A., Yang, X., and Zhang, H.: Five-year records of mercury wet deposition flux at GMOS sites in the Northern and Southern hemispheres, Atmospheric Chemistry and Physics, 17, 2689-2708, 10.5194/acp-17-2689-2017, 2017.

3135   Sprovieri, F., Pirrone, N., Bencardino, M., D'Amore, F., Carbone, F., Cinnirella, S., Mannarino, V., Landis, M., Ebinghaus, R.,

Weigelt, A., Brunke, E.-G., Labuschagne, C., Martin, L., Munthe, J., Wängberg, I., Artaxo, P., Morais, F., Barbosa, J. H. d. M., Brito, J., Cairns, W., Barbante, C., del Carmen Dieguez, M., Garcia, P. E., Dommergue, A., Angot, H., Magand, O., Skov, H., Horvat, M., Kotnik, J., Read, K. A., Neves, L. M., Gawlik, B. M., Sena, F., Mashyanov, N., Obolkin, V., Wip, D., Feng, X., Zhang, H., Fu, X., Ramachandran, R., Cossa, D., Knoery, J., Maruszak, N., Nerentorp, M., and Norstrom, C.: Atmospheric mercury concentrations observed at ground-based monitoring sites globally distributed in the framework of the GMOS network, Atmospheric Chemistry and Physics, 16, 11915-11935, 10.5194/acp-16-11915-2016, 2016.

St Louis, V. L., Hintelmann, H., Graydon, J. A., Kirk, J. L., Barker, J., Dimock, B., Sharp, M. J., and Lehnherr, I.: Methylated mercury species in Canadian high arctic marine surface waters and snowpacks, Environmental Science & Technology, 41, 6433-6441, 10.1021/es070692s, 2007.

Stathopoulos, D.: Fractionation of mercury isotopes in an aqueous environment: Chemical oxidation, M. Sc. Thesis, Faculty of Arts and Science, Trent University, Peterborough, Canada, 77 pp., 2014.

Steffen, A., Schroeder, W., Bottenheim, J., Narayan, J., and Fuentes, J. D.: Atmospheric mercury concentrations: measurements and profiles near snow and ice surfaces in the Canadian Arctic during Alert 2000, Atmospheric Environment, 36, 2653-2661, 2002.

Steffen, A., Bottenheim, J., Cole, A., Ebinghaus, R., Lawson, G., and Leaitch, W. R.: Atmospheric mercury speciation and mercury in snow over time at Alert, Canada, Atmospheric Chemistry and Physics, 14, 2219-2231, 2014.

Steffen, A., Douglas, T. A., Amyot, M., Ariya, P. A., Aspmo, K., Berg, T., Bottenheim, J., Brooks, S., Cobbett, F., Dastoor, A., Dommergue, A., Ebinghaus, R., Ferrari, C. P., Gårdfeldt, K., Goodsite, M. E., Lean, D. R., Poulain, A. J., Scherz, C., Skov, H., Sommar, J., and Temme, C.: A synthesis of atmospheric mercury depletion event chemistry linking atmosphere, snow and water, Atmospheric Chemistry and Physics, 8, 1445-1482, 2008.

Stephan, T. and Trappitsch, R.: Reliable uncertainties: Error correlation, rotated error bars, and linear regressions in three-isotope plots and beyond, International Journal of Mass Spectrometry, 491, 117053, 10.1016/j.ijms.2023.117053, 2023.

Stowe, A. C. and Knight, L. B.: Electron spin resonance studies of [199]HgH, [201]HgH, [199]HgD and [201]HgD isolated in neon and argon matrices at 4K: an electronic structure investigation, Molecular Physics, 100, 353-360, 10.1080/00268970110096443, 2002.

Strand, R., Lund, W., and Aaseth, J.: Complex formation of zinc, cadmium, and mercury with penicillamine, Journal of Inorganic Biochemistry, 19, 301-309, 10.1016/0162-0134(83)80003-8, 1983.

Strömberg, D., Gropen, O., and Wahlgren, U.: Non-relativistic and relativistic calculations on some Zn, Cd and Hg complexes, Chemical Physics, 133, 207-219, 10.1016/0301-0104(89)80202-2, 1989.

Strömberg, D. and Wahlgren, U. First-order relativistic calculations on Au$_2$ and Hg$_2^{2+}$, Chemical Physics Letters, 169, 109-115, 10.1016/0009-2614(90)85174-B, 1990

Strömberg, D., Strömberg, A., and Wahlgren, U.: Relativistic quantum calculations on some mercury sulfide molecules, Water Air & Soil Pollution, 56, 681-695, 10.1007/BF00342309, 1991.

Subir, M., Ariya, P. A., and Dastoor, A. P.: A review of uncertainties in atmospheric modeling of mercury chemistry I. Uncertainties in existing kinetic parameters - Fundamental limitations and the importance of heterogeneous chemistry, Atmospheric Environment, 45, 5664-5676, 2011.

Subir, M., Ariya, P. A., and Dastoor, A. P.: A review of the sources of uncertainties in atmospheric mercury modeling II. Mercury surface and heterogeneous chemistry - A missing link, Atmospheric Environment, 46, 1-10, 2012.

Suda, I., Suda, M., and Hirayama, K.: Degradation of Methyl and Ethyl Mercury by Singlet Oxygen Generated from Sea-Water Exposed to Sunlight or Ultraviolet-Light, Archives of Toxicology, 67, 365-368, 10.1007/Bf01973709, 1993.

Sumner, A. L., Spicer, C. W., Satola, J., Mangaraj, R., Cowen, K. A., Landis, M. S., Stevens, R. K., and Atkeson, T.: Environmental chamber studies of mercury reactions in the atmosphere, in: Dynamics of Mercury Pollution on Regional and Global Scales: Atmospheric Processes and Human Exposures Around the World, edited by: Pirrone, N., and Mahaffey, K. R., Springer US, 193-212, 10.1007/b105709, 2005.

Sun, G.: Isotope fractionation during major chemical transformations of atmospheric mercury, Ph D. thesis, Institute of Geochemistry, Chinese Academy of Sciences, Guiyang, 2018.

Sun, G., Feng, X., Yin, R., Wang, F., Lin, C.-J., Li, K., and Sommar, J. O.: Dissociation of Mercuric Oxides Drives Anomalous Isotope Fractionation during Net Photo-oxidation of Mercury Vapor in Air, Environmental Science & Technology, 55, 13428–13438, 10.1021/acs.est.2c02722, 2022.

Sun, G., Sommar, J., Feng, X., Lin, C.-J., Ge, M., Wang, W., Yin, R., Fu, X., and Shang, L.: Mass -dependent and -independent fractionation of mercury isotope during gas-phase oxidation of elemental mercury vapor by atomic Cl and Br, Environmental Science & Technology, 50, 9232 - 9241, 2016.

Sun, L., Lu, B., Yuan, D., Hao, W., and Zheng, Y.: Variations in the isotopic composition of stable mercury isotopes in typical mangrove plants of the Jiulong estuary, SE China, Environmental Science and Pollution Research, 24, 1459-1468, 10.1007/s11356-016-7933-1, 2017.

Sun, R., Sonke, J. E., Heimbürger, L.-E., Belkin, H. E., Liu, G., Shome, D., Cukrowska, E., Liousse, C., Pokrovsky, O. S., and Streets, D. G.: Mercury stable isotope signatures of world coal deposits and historical coal combustion emissions,

Environmental Science & Technology, 48, 7660, 2014.

Sun, R. Y., Jiskra, M., Amos, H. M., Zhang, Y. X., Sunderland, E. M., and Sonke, J. E.: Modelling the mercury stable isotope distribution of Earth surface reservoirs: Implications for global Hg cycling, Geochimica Et Cosmochimica Acta, 246, 156-173, 2019.

Sun, R. Y., Cao, F., Dai, S. F., Shan, B., Qi, C. C., Xu, Z. J., Li, P. F., Liu, Y., Zheng, W., and Chen, J. B.: Atmospheric Mercury Isotope Shifts in Response to Mercury Emissions from Underground Coal Fires, Environmental Science & Technology, 57, 8638-8649, 10.1021/acs.est.2c08637, 2023.

Svanberg, S.: Geophysical gas monitoring using optical techniques: Volcanoes, geothermal fields and mines, Optics and Lasers in Engineering, 37, 245-266, 2002.

Swartzendruber, P. C., Jaffe, D. A., and Finley, B.: Development and First Results of an Aircraft-Based, High Time Resolution Technique for Gaseous Elemental and Reactive (Oxidized) Gaseous Mercury, Environmental Science & Technology, 43, 7484-7489, Doi 10.1021/Es901390t, 2009.

Symons, M. C. R. and Yandell, J. K.: Unstable intermediates. Part LXXXVII. The dipositive radical cations of gallium, thallium, and mercury derived from aqueous solutions of gallium(III), thallium(III), and mercury(II) salts at 77 K by γ-irradiation, Journal of the Chemical Society A: Inorganic, Physical, Theoretical, 760-762, 10.1039/J19710000760, 1971.

Szponar, N., McLagan, D. S., Kaplan, R. J., Mitchell, C. P. J., Wania, F., Steffen, A., Stupple, G. W., Monaci, F., and Bergquist, B. A.: Isotopic Characterization of Atmospheric Gaseous Elemental Mercury by Passive Air Sampling, Environmental Science & Technology, 54, 10533-10543, 10.1021/acs.est.0c02251, 2020.

Tacey, S. A., Xu, L., Mavrikakis, M., and Schauer, J. J.: Heterogeneous Reduction Pathways for Hg(II) Species on Dry Aerosols: A First-Principles Computational Study, Journal of Physical Chemistry A, 120, 2106-2113, 10.1021/acs.jpca.5b12769, 2016.

Tacey, S. A., Szilvási, T., Xu, L., Schauer, J. J., and Mavrikakis, M.: The role of iron-oxide aerosols and sunlight in the atmospheric reduction of Hg(II) species: A DFT+U study, Applied Catalysis B, 234, 347-356, 10.1016/j.apcatb.2018.04.049, 2018a.

Tacey, S. A., Xu, L., Szilvási, T., Schauer, J. J., and Mavrikakis, M.: Quantum chemical calculations to determine partitioning coefficients for $HgCl_2$ on iron-oxide aerosols, Science of The Total Environment, 636, 580-587, 10.1016/j.scitotenv.2018.04.289, 2018b.

Tas, E., Obrist, D., Peleg, M., Matveev, V., Faïn, X., Asaf, D., and Luria, M.: Measurement-based modelling of bromine-induced oxidation of mercury above the Dead Sea, Atmospheric Chemistry and Physics, 12, 2429-2440, 2012.

Tate, M. T., Janssen, S. E., Lepak, R. F., Flucke, L., and Krabbenhoft, D. P.: National-Scale Assessment of Total Gaseous Mercury Isotopes Across the United States, Journal of Geophysical Research-Atmospheres, 128, e2022JD038276, 10.1029/2022JD038276, 2023.

Taylor, P. H., Mallipeddi, R., and Yamada, T.: LP/LIF study of the formation and consumption of mercury (I) chloride: Kinetics of mercury chlorination, Chemosphere, 61, 685-692, 2005.

Tellinghuisen, J. and Ashmore, J. G.: Mixed representations for diatomic spectroscopic data: application to mercury(I) bromide, Chemical Physics Letters, 102, 10-16, 1983.

Tellinghuisen, J., Tellinghuisen, P. C., Davies, S. A., Berwanger, P., and Viswanathan, K. S.: B → X transitions in HgCl and HgI, Applied Physics Letters, 41, 789-791, 10.1063/1.93704, 1982.

Terenin, A.: Photo-Dissociation of the Vapors of Organo-Metallic Compounds, The Journal of Chemical Physics, 2, 441-442, 10.1063/1.1749505, 1934.

Terenin, A. and Prileshajewa, N.: Photodissociation of the vapors of some organo metallic compounds, Acta Physicochimica URSS, 1, 759-776, 1935.

Thomsen, E. L. and Egsgaard, H.: Rate of reaction of dimethylmercury with oxygen atoms in the gas phase, Chemical Physics Letters, 125, 378-382, 1986.

Tong, Y., Eichhorst, T., Olson, M. R., Rutter, A. P., Shafer, M. M., Wang, X., and Schauer, J. J.: Comparison of heterogeneous photolytic reduction of Hg(II) in the coal fly ashes and synthetic aerosols, Atmospheric Research, 138, 324-329, 10.1016/j.atmosres.2013.11.015, 2014.

Tong, Y., Eichhorst, T., Olson, M. R., McGinnis, J. E., Turner, I., Rutter, A. P., Shafer, M. M., Wang, X., and Schauer, J. J.: Atmospheric photolytic reduction of Hg(II) in dry aerosols, Environmental Science-Processes & Impacts, 15, 1883-1888, 10.1039/c3em00249g, 2013.

Tong, Y. D., Zhang, H. F., Lin, H. M., de Foy, B., Chen, L., Zhang, W., Wang, X. J., and Guan, C. F.: A potential route for photolytic reduction of $HgCl_2$ and $HgBr_2$ in dry air and analysis about the impacts from ozone, Atmospheric Research, 249, 10.1016/j.atmosres.2020.105310, 2021.

Tossell, J. A.: Theoretical study of the photodecomposition of methyl Hg complexes, Journal of Physical Chemistry A, 102, 3587-3591, 10.1021/jp980244u, 1998.

Tossell, J. A.: Calculation of the energetics for oxidation of gas-phase elemental Hg by Br and BrO, Journal of Physical Chemistry A, 107, 7804-7808, 2003.

3250   Tossell, J. A.: Calculation of the energetics for the oligomerization of gas phase HgO and HgS and for the solvolysis of crystalline HgO and HgS, Journal of Physical Chemistry A, 110, 2571-2578, 2006.

Tossell, J. A. and Vaughan, D. J.: Relationships between Valence Orbital Binding-Energies and Crystal-Structures in Compounds of Copper, Silver, Gold, Zinc, Cadmium, and Mercury, Inorganic Chemistry, 20, 3333-3340, 10.1021/ic50224a038, 1981.

3255   Toyota, K., Dastoor, A. P., and Ryzhkov, A.: Air-snowpack exchange of bromine, ozone and mercury in the springtime Arctic simulated by the 1-D model PHANTAS - Part 2: Mercury and its speciation, Atmospheric Chemistry and Physics, 14, 4135-4167, 2014.

Tsui, M. T.-K., Blum, J. D., and Kwon, S. Y.: Review of stable mercury isotopes in ecology and biogeochemistry, Science of The Total Environment, 716, 135386, 2020.

3260   Turro, N. J.: Influence of nuclear spin on chemical reactions: Magnetic isotope and magnetic field effects (A Review), Proceedings of the National Academy of Sciences, 80, 609-621, 1983.

Ullrich, S. M., Tanton, T. W., and Abdrashitova, S. A.: Mercury in the aquatic environment: A review of factors affecting methylation, Critical Reviews in Environmental Science and Technology, 31, 241-293, 2001.

UNEP: Global Mercury Assessment 2018: Sources, Emissions, Releases and Environmental Transport, UNEP Chemicals
3265   Branch, Geneva, Switzerland, 2018.

van Der Linden, W. E. and Beers, C.: Determination of composition and stability-constants of complexes of mercury(II) with amino-acids, Analytica Chimica Acta, 68, 143-154, 10.1016/s0003-2670(01)85155-2, 1974.

van der Linden, W. E. and Beers, C.: Formation constants of mercury(II) with some buffer/masking agents and the formation of mixed-ligand complexes, Talanta, 22, 89-92, 10.1016/0039-9140(75)80148-2, 1975.

3270   van Loon, L. L., Mader, E. A., and Scott, S. L.: Reduction of the aqueous mercuric ion by sulfite: UV spectrum of $HgSO_3$ and its intramolecular redox reaction, Journal of Physical Chemistry A, 104, 1621-1626, 2000.

van Loon, L. L., Mader, E. A., and Scott, S. L.: Sulfite stabilization and reduction of the aqueous mercuric ion: Kinetic determination of sequential formation constants, Journal of Physical Chemistry A, 105, 3190-3195, 2001.

Velivetskaya, T. A., Ignatiev, A. V., Yakovenko, V. V., and Vysotskiy, S. V.: Experimental studies of the oxygen isotope
3275   anomalies ($\Delta^{17}O$) of H_2O_2 and their relation to radical recombination reactions, Chemical Physics Letters, 693, 107-113, 10.1016/j.cplett.2018.01.012, 2018.

Velivetskaya, T. A., Ignatiev, A. V., Budnitskiy, S. Y., Yakovenko, V. V., and Vysotskiy, S. V.: Mass-independent fractionation of oxygen isotopes during H_2O_2 formation by gas-phase discharge from water vapour, Geochimica et Cosmochimica Acta, 193, 54-65, 10.1016/j.gca.2016.08.008, 2016.

3280   Volman, D. H.: Reaction of Optically Excited Mercury Vapor with Oxygen, Journal of Chemical Physics, 21, 2086-2087, 10.1063/1.1698769, 1953.

Vyazovetskii, Y. V.: Photochemical production of the ^{204}Hg isotope, Technical Physics, 57, 603-607, 2012.

Wallschläger, D., Hintelmann, H., Evans, R. D., and Wilken, R. D.: Volatilization of demethylmercury and elemental mercury from river Elbe floodplain soils, Water, Air, and Soil Pollution, 80, 1325-1329, 10.1007/BF01189798, 1995.

3285   Wang, B., Yuan, W., Wang, X., Li, K., Lin, C.-J., Li, P., Lu, Z., Feng, X., and Sommar, J.: Canopy-Level Flux and Vertical Gradients of Hg^0 Stable Isotopes in Remote Evergreen Broadleaf Forest Show Year-Around Net Hg^0 Deposition, Environmental Science & Technology, 56, 5950-5959, 10.1021/acs.est.2c00778, 2022.

Wang, S., McNamara, S. M., Moore, C. W., Obrist, D., Steffen, A., Shepson, P. B., Staebler, R. M., Raso, A. R. W., and Pratt, K. A.: Direct detection of atmospheric atomic bromine leading to mercury and ozone depletion, Proceedings of the National
3290   Academy of Sciences, 116, 14479-14484, 10.1073/pnas.1900613116, 2019a.

Wang, X., Yuan, W., Lin, C.-J., Zhang, L., Zhang, H., and Feng, X.: Climate and Vegetation As Primary Drivers for Global Mercury Storage in Surface Soil, Environmental Science & Technology, 53, 10665-10675, 10.1021/acs.est.9b02386, 2019b.

Wang, X., Luo, J., Yuan, W., Lin, C.-J., Wang, F., Liu, C., Wang, G., and Feng, X.: Global warming accelerates uptake of atmospheric mercury in regions experiencing glacier retreat, Proceedings of the National Academy of Sciences of the United
3295   States of America, 117, 2049-2055, 10.1073/pnas.1906930117, 2020a.

Wang, X., Yuan, W., Lin, C.-J., Luo, J., Wang, F., Feng, X., Fu, X., and Liu, C.: Underestimated Sink of Atmospheric Mercury in a Deglaciated Forest Chronosequence, Environmental Science & Technology, 54, 8083-8093, 10.1021/acs.est.0c01667, 2020b.

Wang, X. F. and Andrews, L.: Infrared spectrum of $Hg(OH)_2$ in solid neon and argon, Inorganic Chemistry, 44, 108-113, 2005.

3300   Wang, Y., Liu, G., Fang, Y., Liu, P., Liu, Y., Guo, Y., Shi, J., Hu, L., Cai, Y., Yin, Y., and Jiang, G.: Dark oxidation of mercury droplet: Mercurous Hg(I) species controls transformation kinetics, Water Research, 244, 10.1016/j.watres.2023.120472, 2023.

Wang, Y. W., Bartov, G., Wang, T., Reinfelder, J. R., Johnson, T. M., and Yee, N.: Rapid Attainment of Isotopic Equilibrium after Mercury Reduction by Ferrous Iron Minerals and Isotopic Exchange between Hg(II) and Hg(0), ACS Earth and Space Chemistry, 5, 1384-1394, 10.1021/acsearthspacechem.1c00026, 2021.

3305   Wang, Z. and Pehkonen, S. O.: Oxidation of elemental mercury by aqueous bromine: atmospheric implications, Atmospheric

Environment, 38, 3675-3688, 2004.

Wang, Z., Sun, T., Driscoll, C. T., Zhang, H., and Zhang, X.: Dimethylmercury in Floodwaters of Mercury Contaminated Rice Paddies, Environmental Science & Technology, 53, 9453-9461, 10.1021/acs.est.8b07180, 2019c.

Warneck, P. (ed.) Sulfur Compounds in the Atmosphere, in: Chemistry of the Natural Atmosphere, International Geophysics
3310 vol. 71, Academic Press, 484-542, 10.1016/S0074-6142(08)60637-3, 1988.

Warneck, P.: In-cloud chemistry opens pathway to the formation of oxalic acid in the marine atmosphere, Atmospheric Environment, 37, 2423-2427, 10.1016/s1352-2310(03)00136-5, 2003.

Washburn, S. J., Blum, J. D., Johnson, M. W., Tomes, J. M., and Carnell, P. J.: Isotopic Characterization of Mercury in Natural Gas via Analysis of Mercury Removal Unit Catalysts, ACS Earth and Space Chemistry, 2, 462-470,
3315 10.1021/acsearthspacechem.7b00118, 2018.

Washburn, S. J., Blum, J. D., Motta, L. C., Bergquist, B. A., and Weiss-Penzias, P.: Isotopic Composition of Hg in Fogwaters of Coastal California, Environmental Science & Technology Letters, 8, 3-8, 2021.

Weigelt, A., Ebinghaus, R., Pirrone, N., Bieser, J., Bodewadt, J., Esposito, G., Slemr, F., van Velthoven, P. F. J., Zahn, A., and Ziereis, H.: Tropospheric mercury vertical profiles between 500 and 10,000 m in central Europe, Atmospheric Chemistry and
3320 Physics, 16, 4135-4146, 10.5194/acp-16-4135-2016, 2016.

Weiss-Penzias, P., Sorooshian, A., Coale, K., Heim, W., Crosbie, E., Dadashazar, H., MacDonald, A. B., Wang, Z., and Jonsson, H.: Aircraft Measurements of Total Mercury and Monomethyl Mercury in Summertime Marine Stratus Cloudwater from Coastal California, USA, Environmental Science & Technology, 52, 2527-2537, 10.1021/acs.est.7b05395, 2018.

Weiss-Penzias, P. S., Ortiz, C., Acosta, R. P., Heim, W., Ryan, J. P., Fernandez, D., Collett, J. L., and Flegal, A. R.: Total and
3325 monomethyl mercury in fog water from the central California coast, Geophysical Research Letters, 39, L03804, 10.1029/2011gl050324, 2012.

West, J., Gindorf, S., and Jonsson, S.: Photochemical Degradation of Dimethylmercury in Natural Waters, Environmental Science & Technology, 56, 5920-5928, 10.1021/acs.est.1c08443, 2022.

Wiederhold, J. G.: Metal Stable Isotope Signatures as Tracers in Environmental Geochemistry, Environmental Science &
3330 Technology, 49, 2606-2624, 2015.

Wiederhold, J. G., Cramer, C. J., Daniel, K., Infante, I., Bourdon, B., and Kretzschmar, R.: Equilibrium Mercury Isotope Fractionation between Dissolved Hg(II) Species and Thiol-Bound Hg, Environmental Science & Technology, 44, 4191-4197, 10.1021/es100205t, 2010.

Wigfield, D. C. and Perkins, S. L.: Oxidation of elemental mercury by hydroperoxides in aqueous solution, Canadian Journal of
3335 Chemistry, 63, 275-277, 10.1139/v85-045, 1985a.

Wigfield, D. C. and Perkins, S. L.: Oxidation state analysis of mercury: evidence of the formation of mercurous ion in the oxidation of mercury by peracetic acid, Journal of Applied Toxicology, 5, 339-341, 10.1002/jat.2550050514, 1985b.

Wigfield, D. C. and Tse, S.: The mechanism of biooxidation of mercury, Journal of Applied Toxicology, 6, 73-74, 10.1002/jat.2550060115, 1986.

3340 Wilcox, J.: A Kinetic Investigation of High-Temperature Mercury Oxidation by Chlorine, Journal of Physical Chemistry A, 113, 6633-6639, 10.1021/jp901050d, 2009.

Williston, S. H.: Mercury in atmosphere, Journal of Geophysical Research, 73, 7051-&, 1968.

Woerndle, G. E., Tsui, M. T. K., Sebestyen, S. D., Blum, J. D., Nie, X. P., and Kolka, R. K.: New Insights on Ecosystem Mercury Cycling Revealed by Stable Isotopes of Mercury in Water Flowing from a Headwater Peatland Catchment,
3345 Environmental Science & Technology, 52, 1854-1861, 10.1021/acs.est.7b04449, 2018.

Wolfe, N. L., Zepp, R. G., Gordon, J. A., and Baughman, G. L.: Chemistry of methylmercurials in aqueous solution, Chemosphere, 2, 147-152, 1973.

Won, A. Y., Kim, M. K., and Zoh, K. D.: Characteristics of total and methyl mercury in precipitation in Seoul, Korea, Atmospheric Pollution Research, 10, 493-500, 10.1016/j.apr.2018.10.001, 2019.

3350 Wright, L. P., Zhang, L., and Marsik, F. J.: Overview of mercury dry deposition, litterfall, and throughfall studies, Atmospheric Chemistry and Physics, 16, 13399-13416, 10.5194/acp-16-13399-2016, 2016.

Wu, L., Mao, H., Ye, Z., Dibble, T. S., Saiz-Lopez, A., and Zhang, Y.: Improving Simulation of Gas-Particle Partitioning of Atmospheric Mercury Using CMAQ-newHg-Br v2, Journal of Advances in Modeling Earth Systems, 16, e2023MS003823, 10.1029/2023MS003823, 2024a.

3355 Wu, P., Song, Z., Zhang, P., Huang, S., Yuan, T., and Zhang, Y.: Atmospheric monomethylmercury: Inferred sources constrained by observations and implications for human exposure, Environment International, 193, 109-127, 10.1016/j.envint.2024.109127, 2024b.

Wu, R., Wang, C., and Dibble, T. S.: First experimental kinetic study of the atmospherically important reaction of BrHg + NO$_2$, Chemical Physics Letters, 759, 137928, 10.1016/j.cplett.2020.137928, 2020.

3360 Wu, R. R., Castro, P. J., Gaito, C., Beiter, K., Dibble, T. S., and Wang, C. J.: Combined Experimental and Computational Kinetics Studies for the Atmospherically Important BrHg Radical Reacting with NO and O$_2$, Journal of Physical Chemistry A,

126, 3914-3925, 10.1021/acs.jpca.2c02531, 2022.

Wu, X., Fu, X. W., Zhang, H., Tang, K. H., Wang, X., Zhang, H., Deng, Q. W., Zhang, L. M., Liu, K. Y., Wu, Q. R., Wang, S. X., and Feng, X. B.: Changes in Atmospheric Gaseous Elemental Mercury Concentrations and Isotopic Compositions at Mt. Changbai During 2015-2021 and Mt. Ailao During 2017-2021 in China, Journal of Geophysical Research-Atmospheres, 128, 10.1029/2022jd037749, 2023a.

Wu, Y. R., Mao, Y. X., Liu, G. L., Li, Y. B., Guo, Y. Y., Liu, Y. W., Yin, Y. G., Cai, Y., and Jiang, G. B.: Analytical Methods, Occurrence, Fate, and Toxicity of Ethylmercury in the Environment: Review and Outlook, Reviews of Environmental Contamination and Toxicology, 261, 10.1007/s44169-023-00037-x, 2023b.

Wängberg, I., Munthe, J., Pirrone, N., Iverfeldt, A., Bahlman, E., Costa, P., Ebinghaus, R., Feng, X., Ferrara, R., Gardfeldt, K., Kock, H., Lanzillotta, E., Mamane, Y., Mas, F., Melamed, E., Osnat, Y., Prestbo, E., Sommar, J., Schmolke, S., Spain, G., Sprovieri, F., and Tuncel, G.: Atmospheric mercury distribution in Northern Europe and in the Mediterranean region, Atmospheric Environment, 35, 3019-3025, 2001.

Xiao, Z., Munthe, J., Strömberg, D., and Lindqvist, O.: Photochemical behaviour of inorganic mercury compounds in aqueous solution, in: Mercury pollution: Integration and synthesis, edited by: Watras, C. J., and Huckabee, J. W., Lewis Publishers, 581-594, 1994.

Xiao, Z., Sommar, J., Wei, S., and Lindqvist, O.: Sampling and determination of gas phase divalent mercury in the air using a KCl coated denuder, Fresenius Journal of Analytical Chemistry, 358, 386-391, 1997.

Xie, Z. Q., Sander, R., Pöschl, U., and Slemr, F.: Simulation of atmospheric mercury depletion events (AMDEs) during polar springtime using the MECCA box model, Atmospheric Chemistry and Physics, 8, 7165 - 7180, 2008.

Yamakawa, A., Moriya, K., and Yoshinaga, J.: Determination of isotopic composition of atmospheric mercury in urban-industrial and coastal regions of Chiba, Japan, using cold vapor multicollector inductively coupled plasma mass spectrometry, Chemical Geology, 448, 84-92, 10.1016/j.chemgeo.2016.11.010, 2017.

Yamakawa, A., Luke, W., Kelley, P., Ren, X., and Iaukea-Lum, M.: Unraveling atmospheric mercury dynamics at Mauna Loa through the isotopic analysis of total gaseous mercury, Ecotoxicology and Environmental Safety, 284, 116993, 10.1016/j.ecoenv.2024.116993, 2024.

Yang, J., Kim, J., Soerensen, A. L., Lee, W., and Han, S.: The role of fluorescent dissolved organic matter on mercury photoreduction rates: A case study of three temperate lakes, Geochimica Et Cosmochimica Acta, 277, 192-205, 2020a.

Yang, M., Rasche, B., and Compton, R. G.: Acoustic cavitation generates molecular mercury(II) hydroxide, Hg(OH)₂, from biphasic water/mercury mixtures, Chemical Science, 11, 556-560, 10.1039/C9SC04743C, 2020b.

Yang, S. and Liu, Y.: Nuclear volume effects in equilibrium stable isotope fractionations of mercury, thallium and lead, Scientific Reports, 5, 12626, 10.1038/srep12626, 2015.

Yang, X., Jiskra, M., and Sonke, J. E.: Experimental rainwater divalent mercury speciation and photoreduction rates in the presence of halides and organic carbon, Science of The Total Environment, 697, 133821, 10.1016/j.scitotenv.2019.133821, 2019.

Yin, Y., Chen, B., Mao, Y., Wang, T., Liu, J., Cai, Y., and Jiang, G.: Possible alkylation of inorganic Hg(II) by photochemical processes in the environment, Chemosphere, 88, 8-16, 2012.

Young, E. D., Galy, A., and Nagahara, H.: Kinetic and equilibrium mass-dependent isotope fractionation laws in nature and their geochemical and cosmochemical significance, Geochimica et Cosmochimica Acta, 66, 1095-1104, 10.1016/S0016-7037(01)00832-8, 2002.

Yu, B., Yang, L., Liu, H., Yang, R., Fu, J., Wang, P., Li, Y., Xiao, C., Liang, Y., Hu, L., Zhang, Q., Yin, Y., Shi, J., and Jiang, G.: Katabatic Wind and Sea-Ice Dynamics Drive Isotopic Variations of Total Gaseous Mercury on the Antarctic Coast, Environmental Science & Technology, 55, 6449-6458, 10.1021/acs.est.0c07474, 2021.

Yuan, S., Chen, J., Hintelmann, H., Cai, H., Yuan, W., He, S., Zhang, K., Zhang, Y., and Liu, Y.: Event-Based Atmospheric Precipitation Uncovers Significant Even and Odd Hg Isotope Anomalies Associated with the Circumpolar Vortex, Environmental Science & Technology, 56, 12713-12722, 10.1021/acs.est.2c02613, 2022.

Yuan, S., Zhang, Y., Chen, J., Kang, S., Zhang, J., Feng, X., Cai, H., Wang, Z., Wang, Z., and Huang, Q.: Large Variation of Mercury Isotope Composition During a Single Precipitation Event at Lhasa City, Tibetan Plateau, China, Procedia Earth and Planetary Science, 13, 282-286, 10.1016/j.proeps.2015.07.066, 2015.

Yuan, T. F., Zhang, P., Song, Z. C., Huang, S. J., Wang, X., and Zhang, Y. X.: Buffering effect of global vegetation on the air-land exchange of mercury: Insights from a novel terrestrial mercury model based on CESM2-CLM5, Environment International, 174, 10.1016/j.envint.2023.107904, 2023a.

Yuan, W., Wang, X., Lin, C.-J., Sommar, J., Lu, Z., and Feng, X.: Process factors driving dynamic exchange of elemental mercury vapor over soil in broadleaf forest ecosystems, Atmospheric Environment, 219, 117047, 10.1016/j.atmosenv.2019.117047, 2019a.

Yuan, W., Wang, X., Lin, C.-J., Sommar, J. O., Wang, B., Lu, Z., and Feng, X.: Quantification of Atmospheric Mercury Deposition to and Legacy Re-emission from a Subtropical Forest Floor by Mercury Isotopes, Environmental Science & Technology, 55, 12352-12361, 10.1021/acs.est.1c02744, 2021.

3420 Yuan, W., Wang, X., Lin, C.-J., Song, Q., Zhang, H., Wu, F., Liu, N., Lu, H., and Feng, X.: Deposition and Re-Emission of Atmospheric Elemental Mercury over the Tropical Forest Floor, Environmental Science & Technology, 57, 10686-10695, 10.1021/acs.est.3c01222, 2023b.

Yuan, W., Wang, X., Lin, C.-J., Wu, C., Zhang, L., Wang, B., Sommar, J., Lu, Z., and Feng, X.: Stable Mercury Isotope Transition during Postdepositional Decomposition of Biomass in a Forest Ecosystem over Five Centuries, Environmental Science & Technology, 54, 8739-8749, 10.1021/acs.est.0c00950, 2020.

3425 Yuan, W., Sommar, J., Lin, C.-J., Wang, X., Li, K., Liu, Y., Zhang, H., Lu, Z., Wu, C., and Feng, X.: Stable Isotope Evidence Shows Re-emission of Elemental Mercury Vapor Occurring after Reductive Loss from Foliage, Environmental Science & Technology, 53, 651-660, 10.1021/acs.est.8b04865, 2019b.

Zacharewski, T. R. and Cherniak, E. A.: FTIR investigation of the heterogeneous reaction of HgO (s) with SO$_2$(g) at ambient temperature, Atmospheric Environment, 21, 2327-2332, 1987.

3430 Zerkle, A. L., Yin, R., Chen, C., Li, X., Izon, G. J., and Grasby, S. E.: Anomalous fractionation of mercury isotopes in the Late Archean atmosphere, Nature Communications, 11, 1709, 2020.

Zhang, H., Wang, Z. W., and Zhang, X. S.: Methylmercury concentrations and potential sources in atmospheric fine particles in Beijing, China, Science of the Total Environment, 681, 183-190, 10.1016/j.scitotenv.2019.05.128, 2019a.

Zhang, H., Tan, Q., Zhang, L., Fu, X., and Feng, X.: A Laboratory Study on the Isotopic Composition of Hg(0) Emitted From 3435 Hg-Enriched Soils in Wanshan Hg Mining Area, Journal of Geophysical Research: Atmospheres, 125, 10.1029/2020JD032572, 2020.

Zhang, H., Wu, X., Deng, Q., Zhang, L., Fu, X., and Feng, X.: Extraction of ultratrace dissolved gaseous mercury and reactive mercury in natural freshwater for stable isotope analysis, Journal of Analytical Atomic Spectrometry, 36, 1921-1932, 10.1039/D1JA00212K, 2021a.

3440 Zhang, H., Yin, R. S., Feng, X. B., Sommar, J., Anderson, C. W. N., Sapkota, A., Fu, X. W., and Larssen, T.: Atmospheric mercury inputs in montane soils increase with elevation: Evidence from mercury isotope signatures, Scientific Reports, 3, 3322, 2013.

Zhang, H., Fu, X., Wu, X., Deng, Q., Tang, K., Zhang, L., Sommar, J., Sun, G., and Feng, X.: Using Mercury Stable Isotopes to Quantify Bidirectional Water-Atmosphere Hg(0) Exchange Fluxes and Explore Controlling Factors, Environmental Science & 3445 Technology, 10.1021/acs.est.3c01273, 2023a.

Zhang, K., Pu, Q., Liu, J., Hao, Z., Zhang, L., Zhang, L., Fu, X., Meng, B., and Feng, X.: Using Mercury Stable Isotopes to Quantify Directional Soil–Atmosphere Hg(0) Exchanges in Rice Paddy Ecosystems: Implications for Hg(0) Emissions to the Atmosphere from Land Surfaces, Environmental Science & Technology, 58, 11053-11062, 10.1021/acs.est.4c02143, 2024.

Zhang, K., Zheng, W., Sun, R., He, S., Shuai, W., Fan, X., Yuan, S., Fu, P., Deng, J., Li, X., Wang, S., and Chen, J.: Stable 3450 Isotopes Reveal Photoreduction of Particle-Bound Mercury Driven by Water-Soluble Organic Carbon during Severe Haze, Environmental Science & Technology, 56, 10619-10628, 10.1021/acs.est.2c01933, 2022.

Zhang, L., Wright, L. P., and Blanchard, P.: A review of current knowledge concerning dry deposition of atmospheric mercury, Atmospheric Environment, 43, 5853-5864, 2009.

Zhang, L., Lyman, S., Mao, H., Lin, C.-J., Gay, D. A., Wang, S., Gustin, M. S., Feng, X., and Wania, F.: A synthesis of 3455 research needs for improving the understanding of atmospheric mercury cycling, Atmospheric Chemistry and Physics, 17, 9133-9144, 10.5194/acp-17-9133-2017, 2017.

Zhang, P. and Zhang, Y. X.: Earth system modeling of mercury using CESM2-Part 1: Atmospheric model CAM6-Chem/Hg v1.0, Geoscientific Model Development, 15, 3587-3601, 10.5194/gmd-15-3587-2022, 2022.

Zhang, T. and Hsu-Kim, H.: Photolytic degradation of methylmercury enhanced by binding to natural organic ligands, Nature 3460 Geoscience, 3, 473-476, 10.1038/ngeo892, 2010.

Zhang, Y., Horowitz, H., Wang, J., Xie, Z., Kuss, J., and Soerensen, A. L.: A Coupled Global Atmosphere-Ocean Model for Air-Sea Exchange of Mercury: Insights into Wet Deposition and Atmospheric Redox Chemistry, Environmental Science & Technology, 10.1021/acs.est.8b06205, 2019b.

Zhang, Y., Song, Z., Huang, S., Zhang, P., Peng, Y., Wu, P., Gu, J., Dutkiewicz, S., Zhang, H., Wu, S., Wang, F., Chen, L., 3465 Wang, S., and Li, P.: Global health effects of future atmospheric mercury emissions, Nature Communications, 12, 3035, 10.1038/s41467-021-23391-7, 2021b.

Zhang, Y. X., Zhang, P., Song, Z. C., Huang, S. J., Yuan, T. F., Wu, P. P., Shah, V. R., Liu, M. D., Chen, L., Wang, X. J., Zhou, J., and Agnan, Y.: An updated global mercury budget from a coupled atmosphere-land-ocean model: 40% more re-emissions buffer the effect of primary emission reductions, One Earth, 6, 316-325, 10.1016/j.oneear.2023.02.004, 2023b.

3470 Zhao, H., Meng, B., Sun, G., Lin, C.-J., Feng, X., and Sommar, J.: Chemistry and Isotope Fractionation of Divalent Mercury during Aqueous Reduction Mediated by Selected Oxygenated Organic Ligands, Environmental Science & Technology, 55, 13376-13386, 2021.

Zhao, Y., Hallar, A. G., and Mazzoleni, L. R.: Atmospheric organic matter in clouds: exact masses and molecular formula identification using ultrahigh-resolution FT-ICR mass spectrometry, Atmospheric Chemistry and Physics, 13, 12343-12362, 3475 10.5194/acp-13-12343-2013, 2013.

Zhen, J., Li, T., Cai, H., Nie, X., He, S., Meng, M., Wang, Y., and Chen, J.: Photoreduction and origin of dissolved and particulate mercury in cloud water: Insights from stable mercury isotopes, Journal of Hazardous Materials, 474, 134654, 10.1016/j.jhazmat.2024.134654, 2024.

3480 Zhen, J., Li, T., Xu, X., Du, P., Song, Y., Nie, X., Liu, X., Liu, H., Bi, Y., Wang, X., Xue, L., and Wang, Y.: Changed mercury speciation in clouds driven by changing cloud water chemistry and impacts on photoreduction: Field evidence at Mt. Tai in eastern China, Water Research, 244, 120402, 10.1016/j.watres.2023.120402, 2023.

Zheng, W. and Hintelmann, H.: Mercury isotope fractionation during photoreduction in natural water is controlled by its Hg/DOC ratio, Geochimica et Cosmochimica Acta, 73, 6704-6715, 2009.

Zheng, W. and Hintelmann, H.: Nuclear Field Shift Effect in Isotope Fractionation of Mercury during Abiotic Reduction in the
3485 Absence of Light, Journal of Physical Chemistry A, 114, 4238-4245, 10.1021/jp910353y, 2010a.

Zheng, W. and Hintelmann, H.: Isotope Fractionation of Mercury during Its Photochemical Reduction by Low-Molecular-Weight Organic Compounds, Journal of Physical Chemistry A, 114, 4246-4253, 2010b.

Zheng, W., Foucher, D., and Hintelmann, H.: Mercury isotope fractionation during volatilization of Hg(0) from solution into the gas phase, Journal of Analytical Atomic Spectrometry, 22, 1097-1104, 10.1039/B705677j, 2007.

3490 Zheng, W., Liang, L. Y., and Gu, B. H.: Mercury Reduction and Oxidation by Reduced Natural Organic Matter in Anoxic Environments, Environmental Science & Technology, 46, 292-299, 2012.

Zheng, W., Obrist, D., Weis, D., and Bergquist, B. A.: Mercury isotope compositions across North American forests, Global Biogeochemical Cycles, 30, 2015GB005323, 10.1002/2015GB005323, 2016.

Zheng, W., Lin, H., Mann, B. F., Liang, L., and Gu, B.: Oxidation of Dissolved Elemental Mercury by Thiol Compounds under
3495 Anoxic Conditions, Environmental Science & Technology, 47, 12827-12834, 10.1021/es402697u, 2013.

Zheng, W., Demers, J. D., Lu, X., Bergquist, B. A., Anbar, A. D., Blum, J. D., and Gu, B. H.: Mercury Stable Isotope Fractionation during Abiotic Dark Oxidation in the Presence of Thiols and Natural Organic Matter, Environmental Science & Technology, 53, 1853-1862, 10.1021/acs.est.8b05047, 2019.

Zheng, W., Chandan, P., Steffen, A., Stupple, G., De Vera, J., Mitchell, C., Wania, F., and Bergquist, B.: Mercury stable
3500 isotopes reveal the sources and transformations of atmospheric Hg in the high Arctic, Applied Geochemistry, 131, 10.1016/j.apgeochem.2021.105002, 2021.

Zhou, J. and Obrist, D.: Global Mercury Assimilation by Vegetation, Environmental Science & Technology, 55, 14245-14257, 10.1021/acs.est.1c03530, 2021.

Zhou, J., Obrist, D., Dastoor, A., Jiskra, M., and Ryjkov, A.: Vegetation uptake of mercury and impacts on global cycling,
3505 Nature Reviews Earth & Environment, 2, 269-284, 10.1038/s43017-021-00146-y, 2021.

Zhu, W., Fu, X., Zhang, H., Liu, C., Skyllberg, U., Sommar, J., Yu, B., and Feng, X.: Mercury Isotope Fractionation during the Exchange of Hg(0) between the Atmosphere and Land Surfaces: Implications for Hg(0) Exchange Processes and Controls, Environmental Science & Technology, 56, 1445-1457, 10.1021/acs.est.1c05602, 2022.

Zhu, W., Li, Z., Li, P., Sommar, J., Fu, X., Feng, X., Yu, B., Zhang, W., Reis, A. T., and Pereira, E.: Legacy Mercury Re-
3510 emission and Subsurface Migration at Contaminated Sites Constrained by Hg Isotopes and Chemical Speciation, Environmental Science & Technology, 58, 5336-5346, 10.1021/acs.est.3c07276, 2024.